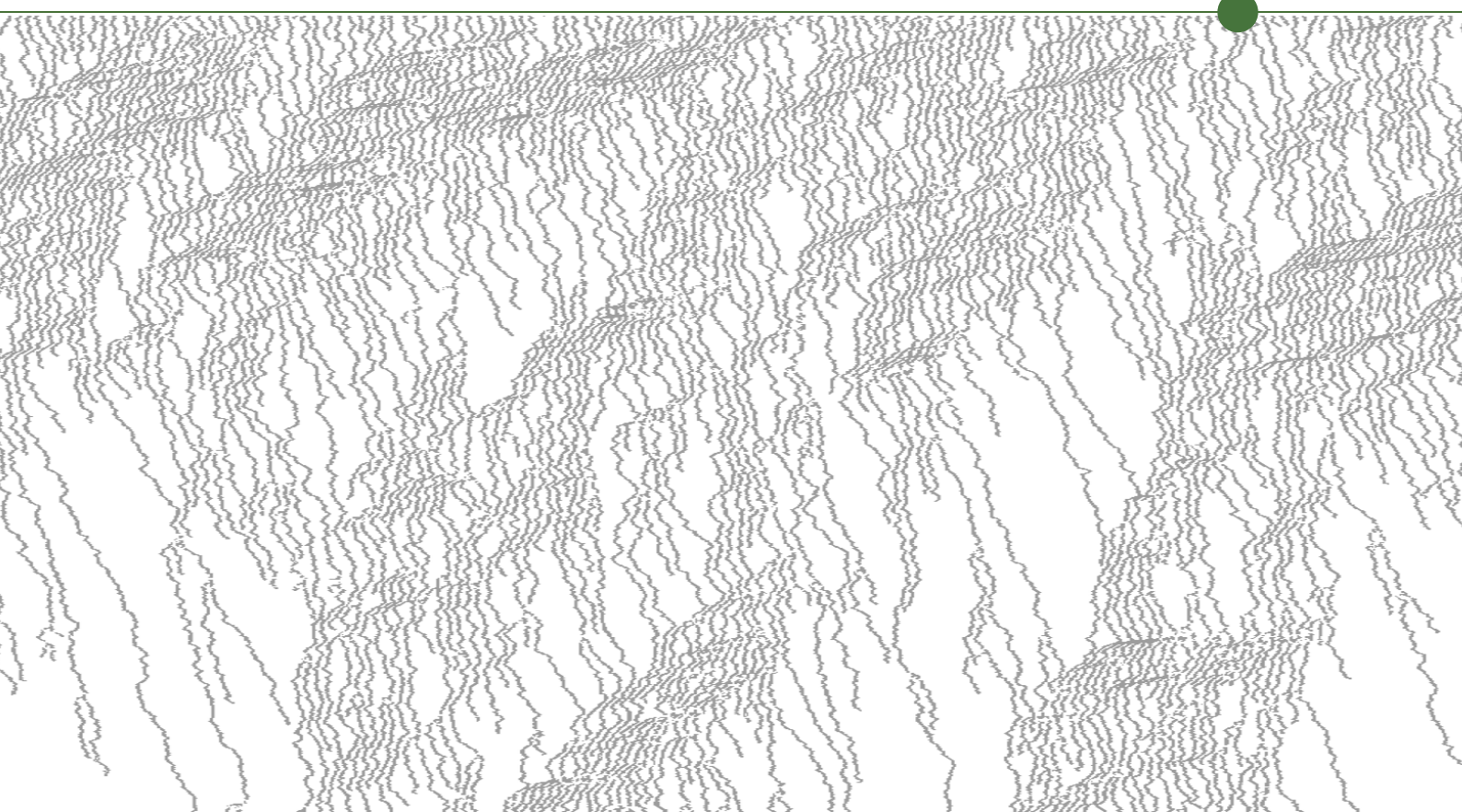


UNIVERSITY OF COPENHAGEN  
FACULTY OF SCIENCE



Gaute Linga

# Fluid Flows with Complex Interfaces: Modelling and Simulation from Pore to Pipe

Thesis submitted to the PhD School of The Faculty of Science,  
University of Copenhagen, for the degree of Doctor of Philosophy

Advisor: Joachim Mathiesen

Submitted: August 2, 2018



## ABSTRACT

---

In this thesis, aspects of fluid flow with disordered interfaces are investigated by numerical and theoretical means, and their relations to geophysically relevant systems are discussed. The research output consists of physical models, numerical methods and tools, and applications of the models and methods to problems ranging from the pore to the pipe scale.

A part of the work focuses on single-phase fluid flow. In order to address the universality class of the laminar–turbulent transition in pipe flow, particle-based models for the interaction between turbulent domains are introduced. To illuminate the joint effects of a disordered geometry and fluid inertia on macroscopic transport properties, transitional flow in rough fractures is investigated by direct numerical simulations. In the limit of creeping flow, the coupling between flow and stress in dissolving porous rock is studied.

The remainder of the work concerns flows where the effects of a second phase, chemical transport, and electric fields, are included. Models for such electrohydrodynamic and two-phase flows are analysed herein. Furthermore, efficient numerical methods are developed both for single- and two-phase electrohydrodynamic flow, and a simulation framework, based on a diffuse-interface model, is introduced to facilitate simulation of phenomena including wetting at the pore scale and microfluidic devices.

## DANSK RESUMÉ

I denne afhandling undersøges aspekter af væskestrømning med uordnede grænseflader i numeriske og teoretiske termer. Forskningsresultaterne består af fysiske modeller, numeriske metoder og værktøjer samt anvendelser af modellerne og metoderne til problemer, der spænder fra pore- til rørskala.

En del af arbejdet fokuserer på enfasestrømning. For at undersøge universalitetsklassen for overgangen fra laminær til turbulent strømning i rør, introduceres partikelbaserede modeller for interaktionen mellem turbulente domæner. For at belyse den koblede virkning af en uordnet geometri og væskens inertie på de makroskopiske transportegenskaber, undersøges strømning ved den turbulente overgang i ru sprække ved hjælp af direkte numerisk simulering. I grensen af krybende strømning undersøges forbindelsen mellem strømning og spænding i porøse stenarter der undergår oplosning.

Resten af arbejdet besæftiger sig med strømning, hvor virkningerne af en anden fase, kemisk transport og elektriske felter er inkluderet. Modeller af sådan elektrohydrodynamisk strømning og tofasestrømning analyseres. Yderligere udvikles effektive numeriske metoder til både en og to faser, og et simuleringsværktøj baseret på en diffus-grænseflademodel, indført for at muliggøre simulering af fænomener som vædning på poreskala og mikrofluidiske indretninger.



## ACKNOWLEDGEMENTS

---

First of all, I acknowledge financial support from the European Union’s Horizon 2020 research programme under the Marie Skłodowska-Curie grant agreement No. 642976 (Initial Training Network “NanoHeal”). The following industry partners are acknowledged: Chemiplastica, Dynea, Iris, Lafarge, Total, and NNL.

I would like to thank my advisor, Joachim Mathiesen, for giving me the opportunity to take on this PhD project, and for both allowing me and (at times when I did not believe in them myself) encouraging me to pursue my own ideas. I would like to express my gratitude to my collaborators at the Niels Bohr Institute, including Asger Bolet, Anier Hernandez-Garcia, and Mads Madsen. I am sincerely grateful to François Renard and Luiza Angheluta at the University of Oslo for good collaboration and for always providing an open door at the Physics building. Thanks are due also to other collaborators, including Tore Flåtten and Halvor Lund, former colleagues at Sintef, and to Nigel Goldenfeld and Hong-Yan Shih, University of Illinois at Urbana-Champaign, for a fruitful autumn of 2017. Further, I thank my colleagues and friends at NBI and in NanoHeal network for making my PhD period a predominantly joyful experience.

I would also like to thank my friends in Copenhagen, Oslo, Trondheim, Bergen, and Paris, for providing supplementary perspectives on life to that of science. Sincere thanks are due to my family for keeping me warm and well fed during my formative years (which continue to this day), and for teaching me the value of the saying “perfect is the enemy of good.”

Finally, I would like to express my gratitude to Linn Helmich Pedersen for displaying terrific patience and enduring support during the past three years, and for being an inexhaustible source of joy in my life.

Copenhagen, August 2018  
Gaute Linga



## LIST OF PAPERS

---

The thesis is comprised by results included the following publications.

- PAPER 1: Statistical mechanics of puff-splitting in the transition to pipe turbulence  
Hong-Yan Shih, Gaute Linga, Grégoire Lemoult, Mukund, Vasudevan, Björn Hof, Joachim Mathiesen, and Nigel Goldenfeld  
In preparation (2018)
- PAPER 2: Self-similar distributions of fluid velocity and stress heterogeneity in a dissolving porous limestone  
Gaute Linga, Joachim Mathiesen, and François Renard  
*Journal of Geophysical Research: Solid Earth* **122**, 1726–1743 (2017)
- PAPER 3: Transitional flow in self-affine rough fractures  
Gaute Linga, Luiza Angheluta, and Joachim Mathiesen  
In preparation (2018).
- PAPER 4: Electrohydrodynamic channeling effects in narrow fractures and pores  
Asger Bolet, Gaute Linga, and Joachim Mathiesen  
*Physical Review E* **97**, 043114 (2018)
- PAPER 5: Transient electrohydrodynamic flow with concentration-dependent fluid properties: modelling and energy-stable numerical schemes  
Gaute Linga, Asger Bolet, and Joachim Mathiesen  
Submitted to *Journal of Computational Physics* (2018)
- PAPER 6: Bernaise: A flexible framework for simulating two-phase electrohydrodynamic flows in complex domains  
Gaute Linga, Asger Bolet, and Joachim Mathiesen  
Submitted (2018)
- PAPER 7: Controlling wetting with electrolytic solutions: Phase-field simulations of a droplet-conductor system  
Gaute Linga, Asger Bolet, and Joachim Mathiesen  
*Physical Review E* **98**, 013101 (2018)
- PAPER 8: A hierarchy of non-equilibrium two-phase flow models  
Gaute Linga and Tore Flåtten  
Submitted to *ESAIM: Proceedings & Surveys* (2018).
- PAPER 9: A two-fluid model for vertical flow applied to CO<sub>2</sub> injection wells  
Gaute Linga and Halvor Lund  
*International Journal of Greenhouse Gas Control* **51**, 71–80 (2016)

The following papers were published during the course of the PhD period, but are not included in the thesis.

- Creep rupture of fiber bundles: A molecular dynamics investigation.  
Gaute Linga, Pietro Ballone, and Alex Hansen.  
*Physical Review E* **92**, 022405 (2015).
- Two-phase nozzle flow and the subcharacteristic condition.  
Gaute Linga, Peder Aursand, and Tore Flåtten.  
*Journal of Mathematical Analysis and Applications* **426**, 917–934 (2015).
- Thermodynamic modeling with equations of state: present challenges with established methods.  
Øivind Wilhelmsen, Ailo Aasen, Geir Skaugen, Peder Aursand, Anders Austegard, Eskil Aursand, Magnus Aa. Gjennestad, Halvor Lund, Gaute Linga, and Morten Hammer.  
*Industrial & Engineering Chemistry Research* **56** (13), 3503–3513 (2017).

## CONTENTS

---

ABSTRACT	i
ACKNOWLEDGEMENTS	iii
LIST OF PAPERS	v
1 INTRODUCTION	3
1.1 A contemporary survey of <i>fluid</i> natural resources . . . . .	3
1.2 Scope and objectives . . . . .	4
1.3 Applications to other fields . . . . .	6
1.4 Structure of the thesis . . . . .	7
2 BACKGROUND	9
2.1 Brief historical development and phenomenology . . . . .	9
2.2 State of the art . . . . .	19
3 PHYSICAL MODELLING	31
3.1 Single-phase flow . . . . .	31
3.2 Two-phase flow . . . . .	36
3.3 Single-phase electrohydrodynamics . . . . .	43
3.4 Two-phase electrohydrodynamics . . . . .	48
4 NUMERICAL METHODOLOGY	55
4.1 The finite element method . . . . .	55
4.2 A numerical scheme for transient flow . . . . .	59
4.3 Steady-state schemes . . . . .	69
4.4 Numerical software and tools . . . . .	71
5 SUMMARY OF PAPERS	75
5.1 Turbulent fronts in pipe flow . . . . .	75
5.2 Flow in fractured and porous media . . . . .	80
5.3 Electrohydrodynamics . . . . .	84
5.4 Homogenized models for two-phase flow . . . . .	88
6 CLOSING REMARKS	89
6.1 Outlook . . . . .	90
BIBLIOGRAPHY	93
A RESEARCH ARTICLES	119



# 1

## INTRODUCTION

---

### 1.1 A CONTEMPORARY SURVEY OF FLUID NATURAL RESOURCES

How do fluids flow through rocks? Answers to this blunt question are not simple and straightforward, but the advances made by humanity in addressing this question has had widespread consequences for the standard of living in the 21<sup>st</sup> century. From the moment you wake up in the morning and brew yourself a cup of coffee, you enjoy the fruits of fluid flow in porous media.

From a purely geophysical perspective, fluid circulation from the mantle to the atmosphere shapes the world around us. In porous rocks, fluid flow is an important factor for pattern formation and rock weathering<sup>[215]</sup>, as it controls mineral transport and heat flow from the nanoscale to the field scale<sup>[359]</sup>. Deformation coupled to fluid flow is also tightly connected with the triggering of earthquakes<sup>[171,303,384,409]</sup>. Hence, understanding the intimate coupling between fluid flow, reaction and deformation of rocks is crucial for understanding how patterns form in nature and how sceneries are sculpted.

From a more industrial point of view, many of the Earth's most desired natural resources are found below the surface, in a liquid state of matter in porous rock formations. Freshwater stored in aquifers, i.e. underground water-bearing rock formations, is an essential natural resource. Groundwater accounts for roughly a third of the available freshwater resources in the world<sup>[407]</sup>, and has served to keep the author, among others, hydrated during the last three years. Due to food production requirements for a rapidly growing global population, many groundwater resources are becoming depleted<sup>[114]</sup>. Unsustainable harvesting of groundwater may not only have dire consequences for drinking and irrigation purposes, but may also reduce the integrity of rock formations<sup>[12]</sup>. Simultaneously, human activity has led to unintended groundwater contamination<sup>[103]</sup>.<sup>1</sup> In fact, the scarcity of drinkable water (being in surface or subsurface reservoirs) represents such a fundamental issue that it can trigger future wars.<sup>2</sup> In this respect, technological progress in *desalination*—roughly speaking, turning seawater into freshwater—could prevent future conflicts. The downside with many current methods is that they are highly energy consuming.

In this respect, petroleum (oil and natural gas)—another important fluid resource found in porous geological formations—has been a major contributor to covering the Earth's exploding energy consumption during the last century. At the time of writing, petroleum accounts for more than half of the total global energy usage<sup>[65]</sup>. Many renewable energy sources, such as wind and solar energy, cannot produce energy *on-demand*, as both wind and sun conditions fluctuate in time and space. The only completely renewable energy source that can be used to provide a base load in the global electrical grid is hydroelectricity. However, in many developed countries, the majority of available waterfalls are already exploited<sup>[469]</sup>, at least to the point where they pose a threat to biological diversity in and around the affected drainage systems. It thus seems clear that hydroelectricity alone cannot compensate for the soaring demand for (green) energy in

<sup>1</sup> As anyone knows who has seen the movie *Erin Brockovich* (2000).

<sup>2</sup> Like it has in the past, see e.g. <sup>[348]</sup>.

*Geothermics* is another practically renewable energy resource, where water heated deep in the Earth's crust is pumped from reservoirs to either drive power plants or directly heat buildings.

the world. An alternative candidate for providing a base load is nuclear energy, where the basic energy production process does not release CO<sub>2</sub>. Despite large reserves, unfortunate accidents, most recently caused by earthquakes (Fukushima, 2011), have degraded public and political opinion on nuclear energy and stalled development<sup>[469]</sup>.

In the advent of *sufficiently* large-scale renewable energy production, petroleum will therefore remain a major source of energy. If coal is the direct alternative (as with Germany's phase-out of nuclear plants), oil and (in particular) natural gas appear to be the lesser of evils. In this respect, basic knowledge of how fluid flows from the nanometer to the basin scale is essential. A contrasting *laissez-faire* attitude likely leads to unforeseen consequences such as, e.g., induced seismicity<sup>[173,434]</sup> (generation of earthquakes by human activity), and land lowering or groundwater contamination due to shale gas extraction<sup>[98]</sup>.

The Paris Agreement from 2015 states that global warming should be limited to 1.5 °C above pre-industrial levels—a goal which seems to be at odds with current trends in energy consumption. A possible remedy from the dire consequences of continued reliance on fossile fuels, is to reduce the net release of CO<sub>2</sub> by means of carbon capture, transport and storage (CCS)<sup>[204]</sup>. The idea behind CCS is to capture the CO<sub>2</sub> where it is released, typically at an industrial site; transport it to suitable storage sites, e.g. saline aquifers or depleted petroleum reservoirs; and inject it into the formation through injection wells<sup>[203,260,328]</sup>. Injected CO<sub>2</sub> should then bind to the rock<sup>[291]</sup>, and by that and other trapping mechanisms<sup>[112,203]</sup> remain permanently stored in the geological formations. Although CCS is already being carried out in practice (e.g. in Norwegian deep saline aquifers since 1996), many fundamental processes are not fully understood<sup>[203]</sup>. Injection of CO<sub>2</sub> into petroleum reservoirs can be used to increase the amount of oil that can be harnessed—called *enhanced oil recovery*—closing the circle between CCS and petroleum production. Enhanced oil recovery is, however, usually carried out using other fluids and water of varying salinity, surfactants, or other chemicals<sup>[382]</sup>.

<sup>3</sup> And is, of course, interesting *in itself*.

Taken together, fluid natural resources are essential to our existence. Knowing how fluids flow in rocks, pipes, fractures, and other geophysical systems, can improve safety and efficiency of energy harnessing and transport and storage of CO<sub>2</sub>.<sup>3</sup> While the applications differ, the underlying physical mechanisms, the resulting equations, and the methods used to investigate them, are largely similar. In these cases the results are not limited to, e.g., a given type of rock or fluid composition, but universal or general properties can be found which have consequences for a broad range of systems. Thus, it makes sense to address these topics in a unified way.

## 1.2 SCOPE AND OBJECTIVES

The survey in the previous section is not intended to be complete, but merely to motivate why fluid flow in disordered geometries—and in particular why the question asked at the beginning of the chapter—is relevant.

The present thesis does not mainly concern specific applications, but addresses instead the general physical concepts *behind* the applications, using theory and numerical simulations. A recurrent theme in this thesis is flow resistance, or conversely, *permeability*. In most applications, it is desirable to minimize the driving force needed to sustain a certain flow rate; that is, to maximize the permeability. This holds valid for flow across several scales; from the pore scale, through networks of pores and fractures, to the corrugated internal surface of a pipe. Complex interfaces, between either a solid and a fluid phase, or between two fluid phases, also have consequences for flow resistance on macroscopic scales, and are not fully understood. Physical processes such as ion migration and surface charges inducing an electric field, may influence flow properties

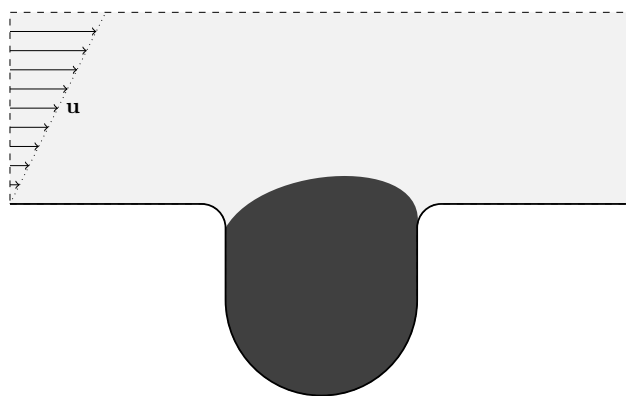


**FIGURE 1.1:** A conceptual dead-end pore filled with conceptual oil, while water is flowing above. A slight distortion of the oil surface is observed, but the oil remains stuck in the pore. (Figure courtesy of A. Bolet.)

even on large scales.

As an illustrative example, consider Fig. 1.1 where we show a schematic dead-end pore wherein an amount of “oil” is stuck. Above the pore, another phase a shear flow of “water” is imposed, and the two phases are taken to be immiscible. This is a basic example of a multiphase system with complex interfaces, where a solid phase provides a disordered confining geometry and the two liquid phases interact nonlinearly.

To both a petroleum engineer (seeking to harness the oil) and an environmental remediator (seeking to decontaminate the soil), it would be desirable to get the oil out of the pore. As the water flows above it, however, the droplet remains stuck in its dead-end pore. Two apparent suggestions on how to get the droplet out are the following:

- Increase the flow rate, i.e., the effect of *inertia*.
- Account for the effect of ions in the solution and the electric field due to surface charges on the pore walls, i.e., include electrohydrodynamics (EHD).

The scope of this thesis is rather broad, and it aims to address effects on flow typically present in geologically relevant systems—in particular, the roles of inertia, disordered interfaces, and the effect of surface charges and ionic solutions.

Using continuum-scale descriptions, these effects are investigated on scales from a single pore, through fractures and pore networks, to pipe flow. As these scales span roughly from sub-micrometer to the kilometer scale, it is clear that this thesis cannot cover all aspects of flow in this range. Hence, the objectives can (in some retrospect) be summarized as the following:

1. Develop and analyse physically consistent continuum-scale models for single- and two-phase flow in geophysically relevant systems, including solute transport and electric fields.
2. Develop methods for simulating such models, predominantly using the finite element method.
3. Apply the developed models and methods to studying flows with complex interfaces.

In particular, both models and methods are developed, and studies are carried out.

Although the broad, overarching question was posed already in the first sentence of this chapter, the more specific *physical* research questions in this thesis include the following:

- How does a disordered geometry influence the macroscopic transport properties of geophysically relevant media?

- What is the combined effect of inertia and a disordered geometry?
- How do charged surfaces and ions in solution influence the wetting behaviour and macroscopic flow properties in disordered geometries?

Progress towards answering these questions is presented in this thesis. Moreover, numerical methods and software are developed that can help gaining even more insights into these questions in the future.

The results are primarily given in the papers that make up the thesis. Summaries of these and more specified research questions are given in chapter 5, along with some complementary information. In Table 1.1, the interested reader will find a simple overview of how the appended papers relate to each other.

TABLE 1.1: How the different papers comprising this thesis relate to each other. The overview indicates included physical effects and novelties in the appended papers. The papers are grouped according to the summary in chapter 5.

Paper	Phases		Scale			Including		Novelty		
	1	2	Pore	Fracture	Pipe	Inertia	EHD	Model	Method	Study
<i>Turbulent fronts in pipe flow (section 5.1)</i>										
1	✓				✓	✓		✓	✓	✓
<i>Flow in fractured and porous media (section 5.2)</i>										
2	✓		✓					✓	✓	
3	✓			✓		✓				✓
<i>Electrohydrodynamics (section 5.3)</i>										
4	✓		✓	✓			✓		✓	✓
5	✓		✓	✓		✓	✓	✓	✓	✓
6	✓	✓	✓	✓		✓	✓		✓	
7	✓	✓					✓	✓		✓
<i>Homogenized models for two-phase flow (section 5.4)</i>										
8		✓			✓	✓		✓		
9		✓			✓	✓		✓	✓	✓

### 1.3 APPLICATIONS TO OTHER FIELDS

Obviously, although the results presented in this thesis have in common that they are related to geophysics, the results are by no means limited to such systems. Below follows a brief and incomplete list of topics to which the results presented here may be of relevance.

- **Microfluidics:** The coupling of two-phase fluid flow and electrochemistry probably has even more applications within micro-<sup>[74,418]</sup> and nanofluidics<sup>[400]</sup> than in geophysics. Technological applications span from fabricating microelectromechanical devices<sup>[249,361,419]</sup>, electronic displays<sup>[37,38,183,210]</sup>, desalination devices<sup>[411]</sup>, inkjet printing, and more.
- **Phase separation:** Two-phase systems with electric fields and chemical effects have applications to electrocoalescers, i.e., devices used to separate water and crude oils in emulsions<sup>[135,280]</sup>.
- **Biology:** Unsteady, inertial flow in disordered geometries, e.g. rough pipes, has applications to how blood flows in our bodies. In particular, inertial effects are important in the larger arteries; in the aorta the Reynolds number (see next

chapter) is around 4000<sup>[238]</sup>, which is far beyond the point where turbulence arises in smooth pipes or tubes<sup>[23]</sup>.

Moreover, electrohydrodynamic (or at least electrokinetic) effects control how fluid is transported in the brain<sup>[198]</sup>, and how neural signals propagate<sup>[281,416]</sup>. As another unexpected link, the Barkley model<sup>[28–30]</sup> that describes the turbulent transition in pipe flow as an excitable medium, is inspired by models for nerve signals.

Multiphase porous flows and poroelasticity is also relevant in biological tissue, e.g. in the dynamics of cancerous invasions<sup>[461]</sup>.

- **Nuclear engineering:** Many of the models for two-phase flow that are now extensively used for petroleum and CO<sub>2</sub> transport, have not only applications to, but actually their origin in, nuclear engineering<sup>[24,46]</sup>; where they describe the flow of the working fluid (heated in the nuclear reactors) used to drive the steam turbines that produce electricity.
- **Semiconductor physics:** The equations of electrohydrodynamics, in particular the Nernst–Planck equations, find wide use in semiconductor physics<sup>[91,268]</sup>. At least through the use and development of numerical methods, these fields could find common ground.
- **Food industry:** Foams, sauces (some of which are oil-in water emulsions), milk, etc., are all realizations of two-phase flow with chemical interactions, and thus relevant to the present work.

Finally, we return to the first paragraph of the chapter, and to the freshly brewed cup of coffee that you might enjoy in the morning. Consolidated, grinded coffee is perhaps the archetypical example of a porous medium. In the art of coffee making, a multitude of physical and chemical processes are at play and must be controlled. Influenced by gravity, one fluid (water) intrudes and displaces the other (air) within the porous medium, the porous medium deforms, chemical reactions and diffusion (extraction) occur, and heat flows through the system; but still you are likely left with a reproducible cup of coffee.<sup>4</sup> Adding the socio-economic aspects of cultivating coffee to the picture (e.g. freshwater requirements, global export), makes it clear that coffee brewing is a far too complicated task to take on in this project. We will therefore leave it to the baristas, for now.<sup>5</sup>

#### 1.4 STRUCTURE OF THE THESIS

The structure of this thesis is as follows. Chapter 1, which you are now reading, is an attempt to put the topics of this thesis into a broader context, without diving into too specific details; and in a broad sense to motivate the work presented. Chapter 2 gives an overview of historical development, phenomenology, and the state of the art of the topics involved. Chapter 3 deals with the physical models employed in the present work. In chapter 4, an overview is given of the numerical methods, spatial and temporal discretization strategies, and numerical software employed and developed in this work. In chapter 5, brief summaries of the research articles that comprise the results of this thesis are given. Finally, chapter 6 concludes and points to future avenues of research. The research papers are collated in appendix A.

<sup>4</sup> For a popular-science based introduction to coffee brewing, see<sup>[185]</sup>.

<sup>5</sup> Perhaps, some day, coffee brewing will be the subject of a Horizon 2020 Initial Training Network.



# 2

## BACKGROUND

---

### 2.1 BRIEF HISTORICAL DEVELOPMENT AND PHENOMENOLOGY

The Navier–Stokes equations, which can be stated for an incompressible fluid evolving in space  $\mathbf{x}$  and time  $t$ , as

$$\rho (\partial_t \mathbf{u} + \mathbf{u} \cdot \nabla \mathbf{u}) - \mu \nabla^2 \mathbf{u} = -\nabla p, \quad (2.1a)$$

$$\nabla \cdot \mathbf{u} = 0, \quad (2.1b)$$

are at the heart of this thesis. Equation (2.1) describes the velocity  $\mathbf{u}(\mathbf{x}, t)$  and pressure  $p(\mathbf{x}, t)$  of a fluid of constant density  $\rho$  and dynamic viscosity  $\mu$ . The left hand side of eq. (2.1a) constitutes a balance between inertial forces, represented by the parenthesis term, and viscous forces, represented by the last term. Roughly speaking, the viscous term dampens out fluctuations, and when it dominates over the inertial term, the flow field tends to be smooth and predictable, i.e. *laminar*, much like the flow of syrup under calm breakfast conditions. Conversely, when the inertial term dominates, fluctuations may be enhanced rather than damped, eventually leading to unsteady and irregular flow patterns—colloquially termed *turbulence*. Such flows can be observed (under the same breakfast conditions) by vigorously pouring milk into your coffee, leading to the formation of unsteady swirls, or turbulent *eddies*. This simple physical experiment is shown in fig. 2.1 (b). The eddies eventually decay, as the viscous term takes its toll, when you stop injecting energy.



**FIGURE 2.1:** Different flow regimes related to coffee. (a) Creeping flow ( $Re \ll 1$ ) through a consolidated porous medium during the brewing process. (b) Turbulent flow ( $Re \gg 1$ ) triggered by pouring of milk into a cup of coffee. Turbulent eddies can be observed. (Photos by Linn Helmich Pedersen.)

Building on work by, among others, Euler<sup>[138]</sup>, Navier<sup>[330]</sup> with the improvements of Stokes<sup>[102,423]</sup> arrived at the equations (2.1) which bear their name. However, scientific investigations of fluid dynamics predate these, as will become apparent below. As an example, the first recorded sketch and description of turbulent eddies is due to da Vinci<sup>[202]</sup>. The following account is neither complete (reference is given to more elaborate

texts where appropriate) nor chronological, but gives a primer on the phenomenology and history of the themes encountered in this thesis.

In 1883, Reynolds<sup>[380]</sup> set out to investigate the “circumstances which determine whether the motion of water shall be direct or sinuous,” or in modern terms, what conditions determine whether flow in pipes is laminar or turbulent. The investigation led to the identification of a dimensionless number, now called the *Reynolds number*,

$$\text{Re} = \frac{\rho u d}{\mu}, \quad (2.2)$$

where  $u$  is the mean axial velocity and  $d$  is the pipe diameter. The number Re roughly measures the ratio of inertial to viscous forces. Reynolds identified Re, as the sole parameter determining the flow regime: when Re was below a “critical” value  $\text{Re}_c \simeq 2000$ , the flow was laminar, whereas above, it could become turbulent. In a transitional region around  $\text{Re}_c$ , the turbulence would appear as intermittent flashes, being neither fully laminar nor turbulent. We will revisit this transitional region in section 2.1.2.

As we will see, the Reynolds number is an extremely useful quantity for all aspects of fluid flow, giving a simple criterion for which flow regimes are relevant, and which approximations can be made.

### 2.1.1 Flow in disordered media

Due to its ubiquity, flow in *porous media* has been a subject of scientific investigations since the days of Euler<sup>[111,139,140]</sup>. Two examples of porous media are shown in fig. 2.1 (a) and in fig. 2.2 (b). A porous medium can arise as an aggregation of solid particles and by chemical or biological processes. The resulting solid matrix contains pores that, if connected from inlet to outlet, can allow a macroscopic flow through the system. As a lowest-order description of its geometry, a porous medium can be characterised by its porosity  $\phi$ . Due to the unfeasibility of analytically solving the equations of fluid motion within the pore, much of the theory of porous media flow has been focused on obtaining macroscopic equations for flow through representative elementary volumes. A basic question (in e.g. hydrogeology) has thus been how to relate the *flow rate*  $\mathbf{q}$ , i.e. volumetric discharge per unit area, through a porous medium, to the imposed pressure gradient  $\nabla p$ . Following pioneering work by Woltmann<sup>[468]</sup>, Delesse<sup>[117]</sup>, and Fick<sup>[149]</sup>, Darcy<sup>[106]</sup> came up with his celebrated law,

$$\mathbf{q} = -\frac{k}{\mu} \nabla p, \quad (2.3)$$

where  $k$  is the *permeability* of the porous medium. This linear relationship has a direct link from the  $\text{Re} \ll 1$  limit of the Navier–Stokes eq. (2.1), where the inertial part can be neglected, leading to the Stokes equations,

$$\mu \nabla^2 \mathbf{u} = \nabla p, \quad \nabla \cdot \mathbf{u} = 0. \quad (2.4)$$

This is often a good approximation in porous media, where the characteristic pore diameter  $d$  is exceedingly small. For a more complete historical account of the development of the theory for porous media, see e.g.<sup>[111]</sup>. Herein, of particular relevance to the present thesis might be the work of Biot concerning the mechanical behaviour of fluid-saturated solids, called *poroelasticity*<sup>[49–52,384,459]</sup>.

Historically, much effort has been devoted to relating the permeability,  $k$  in eq. (2.3), to quantities such as the porosity  $\phi$ <sup>[99,292]</sup>. The arguably most popular such relation is the Kozeny–Carman equation<sup>[84,85,237]</sup>,

$$k \propto \frac{\phi^3 d^2}{(1 - \phi)^2}. \quad (2.5)$$

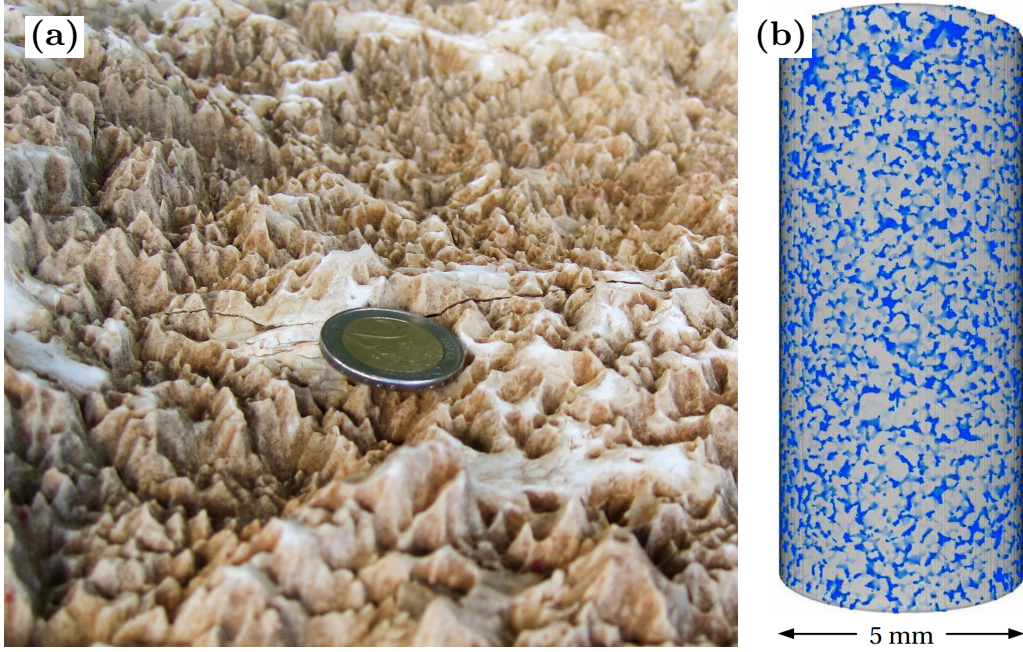


FIGURE 2.2: Examples of rough and porous systems in nature. (a) Rough stylolite surface. (b) Sample of a reservoir rock (Fontainebleau sandstone), imaged by X-ray microtomography. The blue color indicates porosity. (Courtesy of François Renard.)

where  $d$  is a characteristic pore diameter. The relation (2.5) is typically applicable to packed beds. Other common modelling choices is to use empirical power laws,  $k \sim \phi^m$  (with high exponents  $m$ ) suitable for soils<sup>[159]</sup>, or exponential forms, cf.<sup>[131]</sup>.

Darcy obtained eq. (2.3) (in a one-dimensional form) by empirically-based considerations, but both eq. (2.3) and improvements thereof have been found by systematic means. Homogenization techniques (e.g. volume averaging) can be used, as demonstrated by Whitaker<sup>[465]</sup>, to derive from first principles a generalized version of eq. (2.3),

$$\mathbf{q} = -\frac{\mathbf{k}}{\mu} \nabla p, \quad (2.6)$$

where  $\mathbf{k}$  is the permeability tensor, reflecting the fact that the discharge need not be directed parallel to the pressure gradient. For non-negligible inertia (moderate  $Re$ ), empirical corrections eq. (2.3) are due to e.g. Forchheimer<sup>[156]</sup> and Ergun<sup>[134]</sup>, who both on empirical grounds proposed to add a positive term  $\propto \rho|\mathbf{q}|\mathbf{q}$  (where  $\rho$  is still the density), to the left hand side of eq. (2.3)<sup>[159,412]</sup>. A more general power-law description  $\propto \rho|\mathbf{q}|^n \mathbf{q}$  (where  $n$  is an empirical exponent) is due to Izbash<sup>[209]</sup>. Correction terms can also be found by homogenization, see e.g.<sup>[466]</sup> for the Forcheimer term above, which is valid for strong inertia. For weaker inertia, Mei and Auriault<sup>[298]</sup> found a correction term  $\propto |\mathbf{q}|^2 \mathbf{q}$ <sup>[412]</sup>. Early disputes concerned whether the departure from the linear Darcy law was due to turbulence, but careful analysis has shown that this is not a necessity (see section I in<sup>[243]</sup>).

In crustal rock, the permeability is often so low that the fluid transport is not controlled by the microscopic pore size distribution, but takes place mainly in fracture networks spanning large scales<sup>[36,297,390]</sup>. To estimate the macroscopic permeability of such rocks, a description of both the fracture network topology and of the single fractures is necessary. An intriguing property of fracture surfaces is that they display *scale-invariance*. In particular, they are *self-affine*<sup>[61]</sup>, i.e. the fracture surface  $z = h(x, y)$  is *statistically invariant* under the transformation

$$x \rightarrow \lambda x, \quad y \rightarrow \lambda y, \quad z \rightarrow \lambda^H z, \quad (2.7)$$

or  $h(x, y) \sim \lambda^{-H} h(\lambda x, \lambda y)$  in a statistical sense<sup>[26,146]</sup>. Here,  $H$  is called the Hurst exponent, characterizing how correlated the surface is, and  $\lambda$  is a real number. The exponent  $H = 0.8$  has been shown to hold for both synthetic and natural three-dimensional

When both the porous rock and the fracture network contribute to permeability, so-called *dual-porosity models* are often applied, where voids can correspond to either pores or fractures<sup>[120]</sup>.

fractures in a wide range of materials<sup>[61,62,282,398]</sup>. There are, however, notable exceptions, such as in sandstones ( $H \simeq 0.6$ )<sup>[364]</sup>, and in glassy ceramics ( $H \simeq 0.4$ )<sup>[59,333]</sup>.

Classically, a fracture geometry was approximated by two parallel plates separated by a constant separation  $d$ , which amounts to so-called plane Poiseuille flow where an analytical solution is available—often termed the parallel plate law. Improvements to the latter can be found when the flow is creeping ( $\text{Re} \ll 1$ ), and the in-plane length scale of the height variations is much larger than the *local* fracture aperture  $d(x, y)$  (here, the local distance between the upper surface  $z_{\max}$  and the lower surface  $z_{\min}$ ). In particular, the *lubrication approximation* can be used. Defining the aperture-averaged flux by  $\mathbf{Q} = \int_{z_{\min}(x,y)}^{z_{\max}(x,y)} \mathbf{u}(x, y, z) dz$ , a variant of the Darcy equation (cf. eq. (2.3)) arises<sup>[336]</sup>,

$$\mathbf{Q} = -\frac{d^3(x, y)}{12\mu} \nabla p. \quad (2.8)$$

Equation (2.8) is commonly termed the local cubic law (LCL)<sup>[40]</sup> due to the (local) presence of the  $d^3$  term. The parallel plate law is given by eq. (2.8) with a constant  $d$ . Generalizations to eq. (2.8) for the case of non-negligible inertia in the lines of Forchheimer<sup>[156]</sup> are commonly applied<sup>[412]</sup>. By imposing conservation of mass, i.e.  $\nabla \cdot \mathbf{Q} = 0$ , the velocity can be eliminated, which yields the Reynolds equation<sup>[381]</sup>

$$\nabla \cdot (d^3(x, y) \nabla p) = 0, \quad (2.9)$$

which has been of extensive use in the literature. However, once the roughness varies abruptly over small length scales, the lubrication approximation is inapplicable. Modelling approaches for flow in fractured rock were reviewed by Zimmerman and Yeo<sup>[484]</sup>, and on somewhat larger scales by Berre et al.<sup>[42]</sup>.

In general, increasing inertia, and decreasing permeability, is associated with increased energy dissipation or equivalently pressure loss (or hydraulic head loss). Since this is often unsought in industrial settings, flow in fractures is scientifically closely connected to flow in pipes, with smooth or rough internal surfaces. All industrial pipes are rough on some microscopic scale<sup>[9]</sup>, and in many cases (such as in geothermics) transport supersaturated aqueous solutions that lead to precipitation patterns on the pipe walls; a phenomenon known as *scaling*<sup>[174]</sup>. Scaling increases flow resistance and can lead to clogging.<sup>6</sup>

<sup>6</sup> Similar to the effect that can lead to atherosclerosis in arteries.

Efforts to estimate the friction loss, or conversely, the permeability, in pipes and channels date back at least to measurements by French hydrologists Chézy and Prony in the early 18th century (see<sup>[71]</sup>). Poiseuille<sup>[360]</sup> and Hagen<sup>[177]</sup> independently empirically found the relation between flow rate, pressure gradient, and tube dimensions for laminar flow in smooth tubes (now known as Hagen–Poiseuille flow, see<sup>[429]</sup> for a more complete historical account), which can be summarized as

$$u = \frac{d^2}{32\mu} |\nabla p|, \quad (2.10)$$

where  $u$  is the mean velocity and  $R$  is the tube radius. Weisbach<sup>[464]</sup> collected results from several experiments and proposed to write the relation in the following form, known as the Darcy–Weisbach equation,

$$|\nabla p| = f_D \frac{\frac{1}{2}\rho u^2}{d} \quad (2.11)$$

where the dimensionless quantity  $f_D$  is called the Darcy friction factor (due to improved experiments by Darcy<sup>[107]</sup>). The Fanning<sup>[144]</sup> friction factor  $f_F$ , which is also often used,

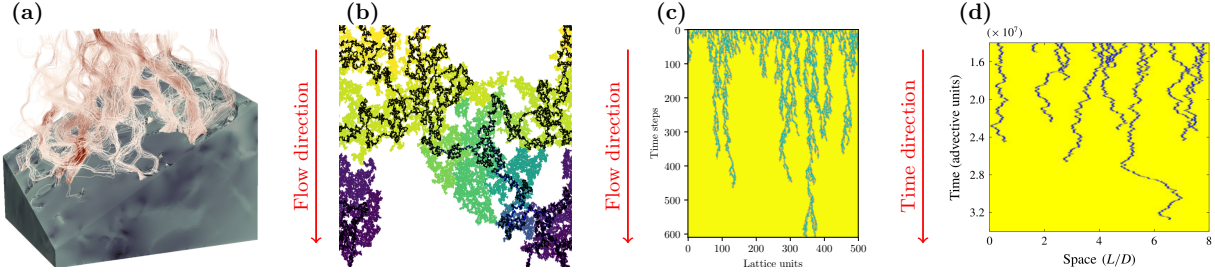


**FIGURE 2.3:** Variations over percolation. (a) Numerically resolved flow through a porous rock sample, from<sup>[261]</sup>. (b) Bond percolation on a hexagonal lattice, slightly above the percolation threshold. The percolating cluster was extracted, Darcy’s law was assumed to hold for each bond, and a pressure drop was imposed from top to bottom. The pressure is shown in the background color coding (lighter is higher). The collection of squiggly dark lines is the conducting part of the cluster, i.e. the percolation backbone. (c) Directed percolation model, below the critical point (blue are active sites). (d) Spatio-temporal dynamics of puffs (blue), slightly below criticality, in the experiments by Mukund and Hof<sup>[327]</sup>. (Reprinted from<sup>[327]</sup>.)

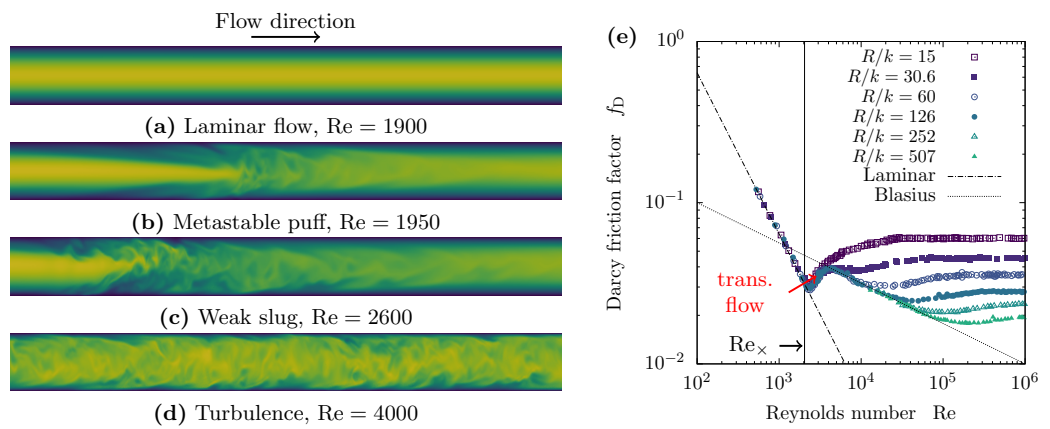
is simply  $f_F = f_D/4$ . For turbulent flow in smooth pipes, Blasius, a student of Prandtl, found the scaling  $f \sim Re^{-1/4}$  for large  $Re$ . Rough pipes turned out to be more elusive. Nikuradse<sup>[339]</sup>, another student of Prandtl, carried out an impressive range of experiments, where the interior of pipes were coated with sand of a characteristic particle size, i.e. roughness size,  $r$ . From his data, spanning many decades in  $Re$  and several roughness sizes, it could be seen that the friction factor  $f_D$  stabilized at a certain value for high  $Re$ . This asymptotic value displays the Strickler scaling  $f_D \sim (r/d)^{1/3}$ <sup>[164,424]</sup>. In the years following, e.g., Colebrook and White<sup>[96]</sup> provided experiments with less uniform roughness. With the introduction and resultant popularity of the Moody diagram<sup>[316]</sup> (which plots  $f_D$  as a function of  $Re$ ), the Darcy–Weisbach equation (2.11) and the Darcy friction factor  $f_D$  became the accepted way of expressing friction in pipe flow<sup>[71]</sup>. The data from Nikuradse’s experiments are plotted in a Moody diagram in fig. 2.4 (e), showing the friction factor  $f_D$  as a function of  $Re$  for varying roughness. Much research has been directed into attempts to connect the empirical laws to *fully developed* turbulence; in particular recently due to the evident connection to dynamical critical phenomena from statistical physics<sup>[164,165]</sup>. The fully-developed limit will not be a focus of this thesis; rather we will be focused in coming sections on the *transition region* from laminar flow to turbulence. This region is indicated as the crossover region between laminar and Blasius scaling in fig. 2.4 (e).

Having taken a detour into high-velocity flows with disordered boundaries, we now return to the pore network scale. The perhaps most obvious contribution from the statistical physics community to flow in porous and fractured media has been to draw attention towards spatial (or temporal) fluctuations, e.g. in porosity and velocity, instead of the average quantities. In this respect, *percolation* is a conceptually important class of models. These models were originally devised by Flory<sup>[155]</sup> and Stockmayer<sup>[422]</sup> to describe polymers. The application to porous flows was pioneered by Broadbent and Hammersley<sup>[70]</sup>, who coined the name due to its resemblance to the phenomena taking place in a coffee percolator<sup>[390]</sup>. The basic variant of percolation considers a lattice with sites (site percolation) or bonds (bond percolation) that all can be open with a probability  $s$ . The analogy to a porous medium is striking, both on the level of pores and single fractures in a fracture network— $s$  being analogous to porosity. A comparison between flow in porous rock and a percolation cluster is shown in fig. 2.3 (a) and (b). At a certain value  $s = s_c$ , there appears a connected path through the system from one end to the other, and the system is permeable. Continuing the analogy to porous media flow, it is clear (from conservation of mass) that the same flux of fluid must pass through any cross-section, implying that in such systems, close to  $s_c$ , the local velocities will vary by orders of magnitude. This is illustrated in fig. 2.3 (b). Considering  $s$  as a control parameter, and the percolation probability  $P(s)$  as the order parameter, the system exhibits a continuous phase transition at  $s_c$ , with associated critical exponents. A thorough introduction to percolation can be found in the book by Stauffer and Aharony<sup>[420]</sup> and their many applications and implications for flow in rocks have been reviewed by Sahimi<sup>[390,391]</sup>.

Several versions of percolation models beyond the basic ones apply to porous media, such as invasion percolation (one phase displacing another), or gradient percolation (in the presence of an external field). In this work, we shall mainly be acquainted with directed percolation (DP), which is a variant of bond percolation where the bonds are *directed*. Typically, one considers a  $45^\circ$  tilted square lattice, where the “fluid” is only allowed to flow downwards. A realisation of directed percolation is shown in fig. 2.3 (c), and is seen to yield a different pattern than regular percolation, cf. fig. 2.3 (c). Percolation models have in general had important consequences for understanding fluctuations in two-phase flow (e.g. related to imbibition and drainage) in porous media, but we will not consider that here. For overviews of such studies, the reader is referred to the recent thesis of Moura<sup>[322]</sup> and references therein, or the review of pore network models by Joekar-Niasar and Hassanizadeh<sup>[225]</sup>.

### 2.1.2 Pipe flow phenomenology

**FIGURE 2.4:** From laminar to turbulent flow in pipes. Figures (a)–(d) show the four flow regimes of single phase pipe flow, for increasing Reynolds number  $Re$ . Figure (e) shows the data from the seminal experiments by Nikuradse<sup>[339]</sup> re-plotted in a Moody diagram. Here, the Darcy friction factor  $f_D$  is plotted against  $Re$ ,  $k$  is a roughness amplitude and  $R$  is the pipe radius. The laminar scaling  $f_D \sim Re^{-1}$ , corresponding to (a), and the Blasius scaling  $f_D \sim Re^{-1/4}$  corresponding to (d) are indicated as dashed lines. Additionally, the region of transitional flow, where (b) and (c) belong, is indicated, along with the critical point  $Re_x$ , measured by Avila et al.<sup>[23]</sup>, where solitary puffs are equally likely to split as to decay.



We now return to Reynolds’ experiments on transitional flow in smooth pipes. Although his investigations led to the estimate of a critical  $Re$ , the picture of the transition between laminar flow and turbulence was not complete—and remains incomplete to this day<sup>[29,327]</sup>. Nevertheless, he noted that depending on how carefully the inlet conditions were prepared, laminar flow (see fig. 2.4 (a)) could be sustained up to  $Re \simeq 13000$ . That, along with the identification of a critical  $Re$  below which turbulence would ultimately decay, pointed to the fact that he already *then* identified the transition to turbulence as *subcritical*: *finite* perturbations are required to trigger turbulence, and nonlinearity drives the instability that ultimately leads to turbulence. It is now generally believed that the laminar Hagen–Poiseuille solution (see fig. 2.4 (a)) to the Navier–Stokes equation is linearly stable for all  $Re$ —as demonstrated in simulations up to  $Re \simeq 10^7$ <sup>[300,392]</sup>, and underpinned by experiments<sup>[105,470]</sup>. This supports the view of the transition as a subcritical one, and also helps explain why approaches to account for this transition using hydrodynamic stability theory (Orr–Sommerfeld method) have been fruitless<sup>[129]</sup>. Other shear flows, such as that in a Taylor–Couette cell (shear flow between counter-moving cylinders), *does* exhibit a linear instability at finite  $Re$ , and for such systems, the global ‘period doubling’ route to turbulence by chaos theorists proved successful (see e.g.<sup>[430]</sup>). Here, we will consider only the transition to turbulence in pipe flow. For fully developed turbulence, consider standard textbooks on the topic (e.g.<sup>[313,440]</sup>), and for the transition in shear flows in general, consider the reviews by Manneville<sup>[283,284]</sup>.

Reynolds noted that around the critical point, turbulence did not rise uniformly, but occurred as intermittent “flashes,” which are now usually termed turbulent *puffs* and *slugs*. These structures are shown, respectively, in fig. 2.4 (b) and (c). This underpins the notion that transitional flow does not consist of a diffuse mix of laminar flow and turbulence,

but rather as a spatial and temporal distribution of relatively sharply separated domains of *either* turbulence or laminar flow. *Puffs* are arrowhead-shaped patches of localized turbulence that travel downstream at approximately the mean velocity of the flow. A turbulent puff is separated upstream from laminar flow by a sharp interface, leading to early analogies to gas–liquid phase transitions<sup>[29,97,470]</sup>. At the downstream front the flow more gradually relaminarises, eventually reaching the Hagen–Poiseuille profile (unless a trailing puff comes along). The puffs may either *split* or *decay* spontaneously. During puff splitting, a daughter puff is created at the downstream end of a mother puff<sup>[23,29,471]</sup>, leading to two coexisting puffs, and accordingly a higher fraction of the pipe being in a turbulent state. At low  $Re$ , puffs are more likely to decay than to split, whereas for higher  $Re$ , they are more likely to split than to decay. Evidently, for (spatially localized) puffs, the upstream front travels at the same net speed as the downstream one. At a certain *second* critical  $Re$ , the downstream puff starts to move faster than the upstream front, and single puffs start to expand. These expanding puffs are known as *slugs*. When the downstream front is characterized by gradual relaminarization, the slugs are termed *weak slugs*, whereas when the  $Re$  is sufficiently high for the downstream edge to invade the laminar flow as aggressively as the upstream front, the slugs are termed *strong slugs*. At the Reynolds where slugs are present, the entire system will be filled with turbulence; see fig. 2.4 (d). A clear description of the transition of turbulence in pipe flow is given by Barkley<sup>[29]</sup>, and, in particular, the Barkley model<sup>[28–30]</sup> has given a near complete understanding—at least qualitatively—of the dynamics that gives rise to turbulence in a smooth pipe.

### 2.1.3 Two-phase flow

Two-phase flow in pipes and tubes, typically of two immiscible fluids (e.g. gas and liquid), displays a significantly more complex phase diagram than what does single-phase flow in the same geometries. These flows can, for example, be classified into the following categories<sup>[6,104,197]</sup>, which are also shown schematically in fig. 2.5:

- **Stratified flow:** The lighter phase (e.g. gas) floats on top of the liquid, and there is a clear interface separating the phases. Such flows occur when gravity is important and the pipe is horizontal or inclined from vertical.
- **Dispersed flow:** One of the phases is dispersed in the other, as small bubbles, drops or droplets.<sup>7</sup>
- **Annular flow:** The lighter phase flows through the center of the pipe, while the other phase flows along the walls.
- **Slug flow:** Alternating, unsteady, intermittent flow of extended bubbles of one fluid, interspersed by the other phase.

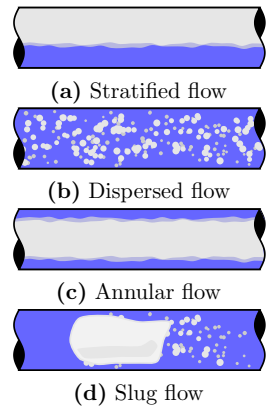
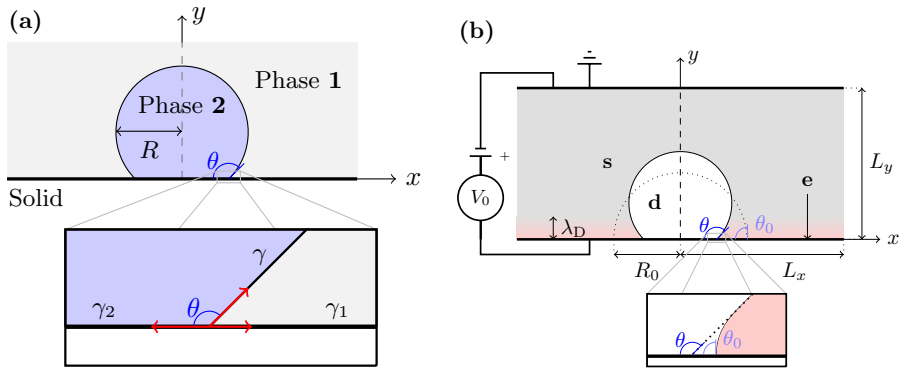


FIGURE 2.5: The author's impression of the four flow regimes listed in the text.

In addition to the fact that turbulence can occur in both phases, the phenomena are further complicated by the existence of surface forces on the fluid-fluid interface. Nevertheless, accurate phenomenological descriptions of the thermophysical properties of two-phase mixtures transported in tubes is of critical importance for an impressively wide range of applications, including nuclear reactors<sup>[46]</sup>, heat exchangers, petroleum production<sup>[1]</sup> and  $CO_2$  transport<sup>[328]</sup>. As a first-principles simulation of the complex interface is generally unachievable for large systems, experimentally based correlations are usually employed in simulations<sup>[266]</sup>. These correlations are algebraic expressions that relate the macroscopic heat transfer, friction, etc., to dimensionless parameters describing the flow. In two-phase flow, there can be several other dimensionless parameters than the Reynolds number  $Re$  which control the flow. Some of these are:

<sup>7</sup> *Droplet* means ‘small drop’ and typically refers to a drop less than 500  $\mu m$  in size.

**FIGURE 2.6:** Wetting. (a) A droplet wetting a substrate, where the contact angle  $\theta$  is indicated. A close-up of the force balance at the contact line is shown. (b) An electrowetting setup, reprinted from<sup>[264]</sup>. The setup corresponds to (a), but an electrolyte is added to the surrounding phase, and an electric field is applied across the system. The close-up shows that the *apparent* (on scales beyond  $\lambda_D$ ) contact angle differs from the local one,  $\theta_0$ .



- The Weber number,  $We$ : inertia to surface forces,
- The Capillary number,  $Ca$ : viscous to surface forces,
- The Bond number  $Bo$  or Eötvös number  $Eo$ : buoyant to surface forces.

At smaller scales, such as in porous media (where two-phase flow was briefly introduced in section 2.1.1) or when modelling individual droplets, the Reynolds number will often be small, and a more important control parameter will then be the capillary number  $Ca$ . As mentioned above, it measures the ratio of viscous to surface forces, and it is defined by

$$Ca = \frac{u\mu}{\gamma}, \quad (2.12)$$

where  $u$  is a characteristic velocity, and  $\gamma$  is the fluid–fluid interface tension. For flow near solid boundaries, an essential concept is *wetting*, which is the ability of a liquid phase to adhere to the surface. The wetting properties of two-phase flows are of importance in a wealth of applications (see e.g.<sup>[60]</sup>), including in geophysics, as they are a controlling factor e.g. oil recovery<sup>[44]</sup>. Observations of wetting and capillarity date, at least, back to da Vinci, and the foundations of its theoretical understanding were laid by, among others, Hauksbee<sup>[180]</sup>, Young<sup>[478]</sup>, Laplace<sup>[242]</sup>, Plateau<sup>[357]</sup>, and Gibbs<sup>[162]</sup> (see<sup>[251]</sup>).

For a static droplet (or drop) immersed in another liquid, the Young–Laplace law states

$$\Delta p = \gamma\kappa, \quad (2.13)$$

where  $\Delta p$  is the pressure difference between the inside and the outside of the droplet, and  $\kappa$  is the curvature, which for a spherical droplet with radius  $R$  (in 3D) is given by  $\kappa = 2/R$ . The *wettability* is often quantified through the *spreading parameter*  $S$ :

$$S = \gamma_1 - (\gamma + \gamma_2), \quad (2.14)$$

where  $\gamma_1$  is the surface tension between the solid and the surrounding phase and  $\gamma_2$  is that between the solid and the droplet. If  $S > 0$ , it is energetically favoured for the droplet to wet the entire solid; in practice a thin (nanometer-sized) film will remain. If  $S < 0$ , the droplet is partially wetting. Then, in equilibrium, the contact angle  $\theta_{eq}$ , which quantifies partial wettability, is given by the energy balance—or alternatively force balance—at the three-phase contact line. This balance gives Young’s law,

$$\cos \theta_{eq} = \frac{\gamma_1 - \gamma_2}{\gamma}. \quad (2.15)$$

A droplet wetting a solid substrate is shown in fig. 2.6 (a), along with the force balance, and the contact angle, at the contact line.

Out of equilibrium, e.g. when a glass plate is slowly lifted out of a water bath, the contact line may be forced to move along the solid substrate. Huh and Scriven<sup>[201]</sup> demonstrated that blindly assuming that there is no hydrodynamic slip (which is common, and usually valid, for the single phase case) leads to a logarithmically diverging energy dissipation near the contact line. Thus, in their words, “not even Herakles could a sink a solid”<sup>[60,201]</sup>. The no-slip Navier–Stokes equations are therefore not directly compatible with a moving contact line (MCL). Near the moving contact line, a more precise *microscopic* description is needed to supplement the purely hydrodynamic model. One way is to abandon the no-slip condition and regularize the microscopic length scale that leads to the divergence, with a slip length; referred to as a Navier slip boundary condition. This is compatible with the Voinov–Tanner–Cox law for  $\text{Ca} \ll 1$ <sup>[81,101,435,455]</sup>,

$$\theta \sim \text{Ca}^{1/3}, \quad R(t) \sim t^{1/10}. \quad (2.16)$$

Here,  $R$  is the radius of a droplet spreading on a substrate in time  $t$ , and  $\theta$  is an *apparent* contact angle, valid on scales beyond the moving contact line. Equation (2.16) also has experimental support for a range of systems<sup>[60]</sup>. Other models for the moving contact line include molecular kinetic theory<sup>[54]</sup>, and evaporation and condensation at the fronts, which is particularly relevant for a moving liquid droplet surrounded by its vapour<sup>[60]</sup>. Another complicating factor is that surfaces usually have a micro- to macroscopic roughness or chemical inhomogeneities, which means that in the static case there are several metastable states that locally minimize the energy, imparting hysteresis effects<sup>[374]</sup>. For a broader introduction to the field of wetting, consider the seminal reviews by de Gennes<sup>[113]</sup>, Leger and Joanny<sup>[251]</sup>, and Bonn et al.<sup>[60]</sup>, as well as that by Snoeijer and Andreotti<sup>[415]</sup> for modelling contact line motion.

#### 2.1.4 Electrohydrodynamics

Loosely speaking, *electrohydrodynamics* constitutes the joint effects of fluid flow and solute transport in the presence of electric fields. Such effects are important within geophysics<sup>[207]</sup>, because charged surfaces appear naturally as rocks are exposed to water. Electrohydrodynamic effects can be harnessed for detecting seismic events or earthquakes<sup>[35,310,442]</sup>, and have been suggested as a source of increased dissipation during seismic activity<sup>[366]</sup>. Moreover, electrohydrodynamics is of relevance e.g. for geothermics<sup>[379]</sup> and environmental remediation of soils or aquifers<sup>[163]</sup>. In addition to being important for the permeability of reservoirs, electrokinetic effects may be of importance for two-phase flow, as surface charges and electric fields are known to change the wetting properties of fluids<sup>[145,382]</sup>. Electrohydrodynamic effects could thus be instrumental in the explanation of why and how oil recovery can be enhanced by injecting water of a particular salinity<sup>[179,192]</sup>.

The possibly first report of electric fields generating fluid motion was given by Reuss<sup>[378]</sup>, who observed that clay particles moved relative to the fluid when subjected to an electric field; an effect now known as *electrophoresis*. The *streaming potential*, i.e. the build-up of an electric potential due to the flow of an electrolyte solution through a charged channel, was first observed by Quincke<sup>[375]</sup>. von Helmholtz<sup>[457,458]</sup> provided early theoretical results explaining the ‘double layer’ at the electrolyte-solid interface, and its role as a capacitor. Separate from this, Nernst<sup>[331,332]</sup> and Planck<sup>[355,356]</sup> worked, albeit not together (see the review<sup>[281]</sup>), on the problem of electrodiffusion. Not long after, Smoluchowski modelled electrophoresis and streaming potential<sup>[413,414]</sup>. Gouy<sup>[167,168]</sup>, and later Chapman<sup>[90]</sup>, derived the Poisson–Boltzmann equation, which gave an expression for the extent of the electrical double layer. The latter is termed the *Debye length*  $\lambda_D$ , named after Debye, who rederived it in his work with Hückel<sup>[115,116]</sup>. These theoretical

descriptions formed the basis for refinements by Stern<sup>[421]</sup>, Grahame<sup>[169]</sup>, and others. A more complete historical review can be found e.g., in<sup>[34]</sup>, and introductions to the broader field of electrochemistry can be found in several books, see for example<sup>[27,233,367]</sup>.

Observations of electrohydrodynamics in two-phase fluid systems date back to the seminal experiments by Lippmann<sup>[267]</sup> in 1875, where he pioneered the field of *electro-capillarity*, or, the study of the relationship between capillarity and electric fields<sup>[325]</sup>.<sup>8</sup> Lippmann observed that the contact angle of mercury in contact with an electrolytic solution in a capillary could be modified by applying a potential difference  $V_0$  between the mercury and the electrolyte. In particular, he found the quadratic relation

$$\cos \theta = \cos \theta_{\text{eq}} + \frac{1}{2} BV_0^2, \quad (2.17)$$

where  $\theta$  is the observed (apparent) contact angle,  $\theta_{\text{eq}}$  is the equilibrium contact angle without any applied field, typically given by eq. (2.15), and  $B$  is a phenomenological parameter. A similar setup (on an electrode instead of in a capillary), demonstrating the effect of imposing an electric field on the wetting properties of a single droplet, is sketched in fig. 2.6 (b). Eq. (2.17) can also be inferred from Gibbs' adsorption isotherm<sup>[257,314]</sup>. This discovery not only led to the first electrocardiograph by Waller in 1887<sup>[45,462]</sup>, but also laid the foundation for the field of electrowetting. Further studies were carried out by Pellat<sup>[350,351]</sup>. Frumkin et al.<sup>[160]</sup> studied wetting of an oil droplet sitting on a mercury electrode. More recently, electrowetting-on-dielectric (EWOD) was pioneered by Berge<sup>[39,450]</sup> and this technology has since found wide use in e.g. electronic displays<sup>[37,38,183,210]</sup>. For a more complete overview of the state-of-the-art of electrowetting, the reader is referred to the reviews by Mugele and coworkers<sup>[324–326]</sup>.

Around 1905, it was discovered that applying electric fields to water-in-oil emulsions (i.e. dispersed flows, cf. the start of section 2.1.3) could help speed up the deemulsification process<sup>[135]</sup> needed for the oil to become usable as fuel. This led to the invention of the electrocoalescer by Cottrell and Speed<sup>[100]</sup> (see<sup>[135]</sup> for a brief history of the latter invention). Recent reviews of electrocoalescence are available in the literature<sup>[280,302]</sup>.

In 1913, Millikan<sup>[304]</sup> published the findings from his and Fletcher's elegant oil drop experiment. Oil droplets were charged and sprayed into a chamber, and by measuring the terminal velocity with and without an electric field, they could find the charge of a droplet. This charge turned out always to be an integer multiplet of the elementary charge,  $q_e$ , which they could measure with (overly) high precision. This led to Millikan receiving the Nobel prize in 1923.

Much of the early theoretical work on two-phase electrohydrodynamics was, if not directly motivated by electrocoalescers, at least applicable to such configurations, as it was concerned with the physics of single droplets of one liquid suspended in another. The early models assumed that the two phases were either perfectly dielectric (non-conductive) or perfectly conductive materials. Both these models predict a prolate deformation of the droplet in the direction normal to the applied electric field<sup>[8,345]</sup>. Careful experiments by Allan and Mason<sup>[8]</sup>, on the other hand, showed that the deformation could be either prolate or oblate depending on the conductivities in the two phases. The conundrum was partly resolved by Taylor<sup>[436]</sup>. In his “leaky-dielectric” model, the phases were assumed to be weakly conducting, thus allowing a net current through the system including droplets. This, in turn, could drive a circulation in the droplet and gives rise to interfacial stresses that enables the oblate shape, which was shown analytically for small displacements. The main approximation behind Taylor's model is (1) that the electric field is strong, and (2) that the electric double layer is vanishingly thin compared to the droplet; hence the conductivity is taken to be constant and net charges are confined to the interface, i.e., diffusion of charges is neglected. When either of these assumptions are not satisfied, the

<sup>8</sup> Lippmann later went on to win the Nobel prize for inventing color photography.

The controversy regarding the share of labour between Millikan and Fletcher is not entered here; it suffices to state that Fletcher's own recollection<sup>[154]</sup> is an interesting read.

model cannot be expected to hold quantitatively. This concerns in particular situations with mobile charge carriers, where there can be regions of net charge, and where the conductivity is not uniform<sup>[43,88]</sup>. Phenomena such as concentration polarization cannot be captured by such models.<sup>9</sup> As an improvement over Taylor's analytical solution to the leaky-dielectric model, Zholkovskij et al.<sup>[483]</sup> developed analytical expressions for droplets with arbitrarily thick Debye layers in one of the phases (but still for small perturbations). The latter could interpolate between the asymptotic solutions for a perfectly dielectric and a leaky-dielectric model. Saville<sup>[396]</sup> outlined how the leaky-dielectric model can be derived from the basic electrokinetic equations, illuminating the assumptions made in the process. Schnitzer and Yariv<sup>[399]</sup> showed rigorously, building on the work by Baygents and Saville<sup>[32]</sup>, how the leaky-dielectric model can be seen as a limit of the full model.

## 2.2 STATE OF THE ART

### 2.2.1 Direct simulation of flow in disordered geophysical media

#### Pore scale simulations

The search for macroscopic transport properties such as porosity, permeability and tortuosity from a pore-scale description has recently become possible to address numerically, through the development of numerical methods and improved computational facilities. The development of the field of *digital rock physics* imparts calculation of flow properties, as well as mechanical properties, from 3D images of porous samples obtained using X-ray microtomography or other imaging techniques<sup>[14,20,56,76,488]</sup>. Methods for numerically simulating such flow, reviewed by Meakin and Tartakovsky<sup>[294]</sup>, has enabled simulation of solute transport<sup>[47,48,226,307]</sup>, multiphase flow<sup>[308]</sup>, and time-dependent evolution of the microstructure e.g. through dissolution and precipitation kinetics<sup>[341]</sup>. Simulations have revealed that the macroscopic behaviour is controlled by local heterogeneities<sup>[41]</sup>. Computed elastic properties depend on the initial microstructure and change during rock transformation processes<sup>[467]</sup>, and the preferred dissolution patterns impact the mechanical properties and seismic wave velocities<sup>[21]</sup>.

Pore-scale simulations have revealed that there exists large (several orders of magnitude) variations in local flow velocities in porous networks<sup>[48,110,247]</sup> and in fracture joints<sup>[72]</sup>. Much of the information that is contained in the Eulerian velocity field can be captured by the probability distribution function (PDF) sampled uniformly over the pore space. Recent simulations of ensembles of synthetically generated porous media have suggested that the velocity PDFs can be captured by either a stretched exponential<sup>[95,199,410]</sup> or a 'power-exponential' distribution<sup>[293]</sup>

$$P(u) = \begin{cases} a \left( \frac{u}{u_s} \right)^{\eta-1} \exp \left[ - \left( \frac{u}{u_s} \right)^\eta \right] & \text{(stretched exponential),} \\ a \exp \left[ - \left( \frac{u-u_0}{u_s} \right)^\eta \right] & \text{(power-exponential).} \end{cases} \quad (2.18)$$

Here  $u_0$  (peak),  $u_s$  (spread) and  $\eta$  (exponent) are fitted parameters that depend on the geometry,  $a$  is a normalization factor, and  $u \geq 0$  can refer to both the (absolute) transversal and longitudinal component of the velocity field  $\mathbf{u}$ , as well as to its absolute value. Note that the two distributions have the same asymptotic behaviour for  $u \gg u_s$ , i.e.  $P(u) \sim \exp[-(u/u_s)^\eta]$ . In particular, Matyka et al.<sup>[293]</sup> found the exponent  $\eta$  in the power-exponential distributions for the longitudinal component and the absolute value to be an increasing function of the porosity which interpolates between a broad distribution ( $\eta < 1/2$ ) at (relatively) low porosity, through exponential ( $\eta \simeq 1$ ) and a Gaussian distribution ( $\eta \simeq 2$ ) at high porosity. Here, the considered porosities were

<sup>9</sup> That being said, neither could Millikan's experiment, since in Taylor's model, no droplet can have a net charge.

in the range  $\phi > 0.4$ , as compared to  $0.2 < \phi < 0.6$  in the study of Siena et al.<sup>[410]</sup>, who suggested a stretched exponential distribution. The latter study also encompassed a different porous medium generation protocol. A stretched exponential distribution can be theoretically inferred by heuristically assuming the medium to be a collection of cylindrical pores with exponentially distributed radii, wherein the flow is given by the Hagen–Poiseuille solution, as demonstrated by<sup>[199]</sup>. Other studies have suggested both exponential and Gaussian distributions for different porous systems<sup>[48,108,223,248,285]</sup>. Close to the percolation threshold, the velocity PDF obeys a power-law distribution over several orders of magnitude, as shown in Navier–Stokes simulations in the backbone of a site percolation network<sup>[15]</sup>. These observations together suggest that (i) the velocity distributions are not a simple function of porosity alone, but that (ii) a general trend is that a broad (power-law) distribution at low porosity (the percolation threshold) is gradually turned into a more narrow stretched exponential, exponential, and finally Gaussian distribution as the porosity is increased. However, these observations apply only for porous media when flow and deformation are decoupled.

### *Mechanical coupling*

Voronov et al.<sup>[460]</sup> considered the viscous stress associated with the flow field in a highly porous medium, and proposed a gamma distribution to describe the PDF of the largest eigenvalue of the rate of strain tensor for the bulk. Pham et al.<sup>[354]</sup> performed a similar study on packed beds and Berea sandstone, and found a lognormal distribution of stress. For assessing the impact of fluid stress on the state of stress in the solid, the pore-wall stress would be more relevant. In deformable porous media, numerical simulations have suggested that the relationship between the imposed pressure gradient and velocity flux becomes non-linear and saturates for large pressure gradients<sup>[189]</sup>, and can impart hysteresis effects<sup>[176]</sup>. Saenger et al.<sup>[389]</sup> studied the effect of fluid viscosity on the effective elastic parameters of rocks. Nonetheless, rocks can usually only deform very slightly (less than 1%) before they are irreversibly damaged. Opening of microfractures and collapse of pores lead to a non-linear evolution of porosity and permeability with the pore pressure gradient<sup>[109]</sup>. Jasinski et al.<sup>[219]</sup> considered the evolution of elastic parameters and permeability of a Bentheim sandstone under small deformations, through experiments and simulations. Lan et al.<sup>[239]</sup> found normal (within grains) and bimodal (at grain boundaries) distributions of principal stress in 2D discrete simulations of compressing granite rock. Laubie et al.<sup>[244]</sup> studied the stress distributions in 2D artificial “swiss cheese” porous media. The probability density functions were found to decay as stretched exponentials for high stresses, and the distributions broadened with the degree of disorder. They also observed the formation of stress chains analogously to what are known for granular packings. Other researchers have considered transient coupling between the fluid flow and solid matrix through precipitation<sup>[222]</sup>, dissolution<sup>[352]</sup> (thermodynamically driven morphology evolution), erosion and deposition<sup>[213,214]</sup>.

### *Fracture flow*

Most numerical studies of flow in rough fractures, up until about a decade ago, have been carried out in the regime of creeping flow, often using a lubrication approximation (i.e. the local cubic law, eq. (2.8))<sup>[40]</sup>. The main challenge is then to relate the permeability to the aperture field<sup>[358,432]</sup>. The default assumption is to use the distance between boundaries along the normal direction to the flow plane<sup>[40]</sup>, but this is clearly unsuitable for situations e.g. where the surface varies sharply over short distances, or perfect fracture joints resulting from ‘mode 1’ fracture (no shear displacement). To compensate for this discrepancy, Mourzenko et al.<sup>[323]</sup> suggested the method of fitting the largest possible

spheres at each point in the fracture to calculate the effective aperture. Brown<sup>[72]</sup> solved the Reynolds equation (2.9) in a synthetic rough fracture and showed that wall roughness strongly affected the transport. Méheust and Schmittbuhl<sup>[295, 296]</sup> showed experimentally and numerically (in the same lubrication paradigm) that the heterogeneity of the rough surfaces can lead to both enhanced and inhibited flow compared to parallel plates with the same mean separation, and is moreover dependent on the orientation of the pressure gradient. Further, long-range correlations in the aperture fields are transmitted to the flow fields, leading to flow channeling<sup>[297]</sup>.

Gutfaind and Hansen<sup>[175]</sup> and Zhang et al.<sup>[482]</sup> simulated flow in 2D and 3D fractures, respectively, beyond the lubrication approximation, considering creeping flow in 2D self-affine channels. Drazer and Koplik<sup>[121]</sup> studied flow in self-affine fractures, and the analysis was extended to 3D and compared to effective medium theory<sup>[122]</sup>. Through direct 3D simulations, Brush and Thomson<sup>[73]</sup> evaluated the effect of roughness and Re on the validity of the lubrication approximation, giving explicit bounds (on Re and roughness) on the validity range of the latter. Previous such analyses were based on an order-of-magnitude analysis<sup>[346]</sup>. Lo and Koplik<sup>[269, 270]</sup> considered both pure fluid and suspension flow in similar geometries. Jin et al.<sup>[224]</sup> investigated the role of roughness in 2D simulation, and found, following Talon et al.<sup>[433]</sup>, three regimes for the permeability dependency on roughness. In particular, it has been found that the permeability is often dominated by the narrowest constriction, but this effect is more pronounced in 2D than in 3D<sup>[412, 432]</sup>.

Auradou et al.<sup>[22]</sup> investigated the effect of a shear displacement on fracture walls, comparing experiments to numerical simulations, and found that the permeability depended linearly on the variance in local aperture. This effect was previously estimated by geometric considerations<sup>[386]</sup>, and may reduce permeability by several orders of magnitude, as shown in laboratory experiments<sup>[125]</sup>. Flow in rough fractures imposes a significant stress on the solid walls, as numerically demonstrated by Lo and Koplik<sup>[270]</sup>. Boundary roughness also leads to increased solute dispersion<sup>[64]</sup>. Other lines of research concern the coupling of fluid flow to heat transfer in fractures<sup>[333–335]</sup>, solute transport<sup>[64]</sup>, and flow in propped fractures<sup>[218]</sup>.

Inertial effects on the flow properties in porous media have been considered in 2D geometries<sup>[15, 16, 130, 385]</sup> and in 3D spherical packings<sup>[157, 190, 191]</sup>, suggesting that for moderate Re, steady eddies are responsible for the quadratic deviation from Darcy flow. Lo Jacono et al.<sup>[271]</sup> simulated weak inertial flow (first-order correction to Poiseuille flow) in a rough channel, verifying the initial cubic deviation. Gutfaind and Hansen<sup>[175]</sup> simulated flow in a channel with one self-affine wall. High-velocity flow in a 2D self-affine fracture joint was simulated by Skjetne et al.<sup>[412]</sup> up to Re = 52, who found that the relation between pressure gradient and velocity was well described by a weak inertial correction at low Re and a Forchheimer equation at higher Re. Cardenas et al.<sup>[80]</sup> simulated flow and solute transport in a 2D asymmetric fracture, paying particular attention to the role of eddies. A similar study for a larger range in Re, and for several values of the Hurst exponent  $H$ , was carried out by Briggs et al.<sup>[69]</sup>, but display only a weak nonlinearity and an Izbash (power-law) equation provided a better fit than a Forchheimer equation. The Forchheimer equation also appears to be applicable to flow of non-Newtonian fluids in 2D fractures<sup>[474]</sup>. Zou et al.<sup>[486]</sup> studied unsteady flow in 2D fractures up to Re = 1000. The same authors studied steady flow in 3D fractures up to Re = 400<sup>[487]</sup> (see also<sup>[485]</sup>), while Wang et al.<sup>[463]</sup> studied steady flow in self-affine fractures for somewhat lower Reynolds numbers. On the experimental side, laboratory experiments<sup>[220, 448]</sup> yield good agreement with the phenomenological Forchheimer equation. Experimental studies of flow in fractures indicate that turbulence sets in at lower Re for rougher fractures<sup>[369, 370]</sup>. In general, a “critical” Reynolds number,

where either (i) laminar non-linear effects (steady eddies) become apparent, or (ii) the laminar flow field becomes linearly unstable, seems to be highly sample-dependent. Conceptually, this is understandable for 2D geometries, where the flow is limited by the narrowest passage along the path. In 3D, however, the flow will tend to pass around obstacles, yielding lesser impact<sup>[412]</sup>. The comparative investigation of (i) and (ii) above have been largely omitted in the literature, particularly in 3D, where most studies have been carried out by solving the time-independent Navier–Stokes equations. On the other hand, the spatiotemporal dynamics of the transition to turbulence in rough channels was recently investigated numerically by Ishida et al.<sup>[206]</sup>. These simulations were concerned with homogeneous small-scale roughness that could be numerically incorporated as an effective body force near the domain walls<sup>[77]</sup>, thus not enabling the possibility of eddies detaching from the boundary and entering into the bulk flow. Nevertheless, their results showed spatially localized turbulent structures similar, and complementary, to the stripes and bands observed for transitional plane Poiseuille flows. Thus, they provide a first link between the studies of the transition to turbulence in shear flows and the field of fracture flow, briefly introduced above.

### *Electrohydrodynamics in disordered media*

Due to the strong inherent nonlinearity that arises when coupling the Navier–Stokes equations to electrokinetic transport, computational studies of such phenomena have been largely limited to two-dimensional<sup>[150,151]</sup> or axisymmetric geometries<sup>[286,287]</sup>. Recently, a method to simulate steady-state electrohydrodynamic phenomena in nanopores was presented by Mitscha-Baude et al.<sup>[309]</sup>. As an alternative, Obliger et al.<sup>[344]</sup> studied the transport properties of a pore-network model of electrokinetic flow.

#### *2.2.2 Directed percolation and the transition to turbulence in pipe flow*

Since Reynolds performed his pipe experiment, much experimental effort has been invested into determining the precise value of the critical Reynolds number  $Re_c$  (see<sup>[327]</sup> for a concise historical overview). However, it was not until the work of Avila et al.<sup>[23]</sup> that an unambiguous value, (approximately) free of finite-size effects and other systematic errors, could be determined. This was done solely based on single-puff statistics. The ‘life times’ of uncorrelated single puffs are distributed exponentially, so the probability distribution can be expressed as  $P_d(t) \sim \exp(-t/\tau_d)$  where  $\tau_d(Re)$  is a function of  $Re$ . An equivalent distribution holds for the characteristic splitting times  $\tau_s$ . By fitting to experimental data, precise values of  $\tau_s$  and  $\tau_d$  could be obtained for a wide range of  $Re$ . It turns out that both these characteristic times depend superexponentially on the Reynolds number, i.e. like  $\tau_i \sim \exp(\exp(a_i Re + b_i))$ , where  $i \in \{s, d\}$  and  $a_i, b_i$  are empirically determined numerical prefactors. The dependence of the lifetime  $\tau_d$  on  $Re$  can be inferred from extreme value statistics<sup>[166]</sup>. When the two values are equal, i.e. when a single puff is equally likely to decay as to spread, a critical Reynolds number  $Re_x$  can be defined. Avila et al.<sup>[23]</sup> found a value  $Re_x \simeq 2040$ , strikingly close to the value  $Re \simeq 2000$  estimated by Reynolds. The transition is, however, not fully quantified by simply locating a critical value of the control parameter.

Pomeau<sup>[362]</sup> first pointed out that the spreading of turbulent spots in pipe flow had a striking analogue to directed percolation (DP, described in section 2.1.1). In this picture, the downward (‘flow propagation’) direction in DP must be identified as the time axis, and the horizontal direction corresponds to the flow direction (in a co-moving reference frame). Here, an occupied site corresponds to a coarse-grained region of turbulence, i.e. a puff, while unoccupied sites correspond to laminar regions. This analogy between the rise of turbulence in pipe flow and directed percolation is seen by comparing fig. 2.3 (c) and

(d). Like in DP, there is in transitional pipe flow a spatio-temporal competition between an *active* (turbulent) state and an absorbing *inactive* (laminar) state. The absorbing property of laminar flow is given by its linear stability: a laminar region must by contaminated by a nearby puff to become turbulent; it does not turn turbulent by itself.

As a universality class, DP models have proven to be robust with respect to the details of the microscopic interaction rules. Janssen and Grassberger<sup>[170,193,216]</sup> conjectured that models should belong to the DP universality class provided that they possess the following necessary ingredients:

1. The system exhibits a continuous phase transition from a fluctuating active state to a unique absorbing state,
2. the system is characterised by a positive one-component order parameter,
3. the system has no additional symmetries or quenched randomness,
4. there are only short-range interaction rules.

In this picture, the turbulent fraction  $F$ , i.e. the fraction of the pipe occupied by turbulence,<sup>10</sup> fulfils the condition for being the order parameter, and the other conditions seem also to be satisfied. Hence, Pomeau's conjecture—a view that since has been advocated by several others<sup>[283,284]</sup>—is that pipe flow belongs to the universality class of 1+1 DP (which refers to 1 spatial and 1 temporal dimension). If this conjecture holds true, the *instantaneous* turbulent fraction  $F_t$ , i.e., the fraction of the pipe that is occupied by turbulence at any time  $t$ , should display the dynamic power-law scaling

$$F_t \sim t^\alpha \quad (2.20)$$

at the critical  $\text{Re}$ . Close to criticality, the order parameter  $F = \lim_{t \rightarrow \infty} F_t$  should obey the scaling

$$F \sim (\text{Re} - \text{Re}_c)^\beta, \quad (2.21)$$

close to the critical point. Moreover, the distributions of laminar gaps in space ( $\ell_x$ ) and time ( $\ell_t$ ) should display the scalings

$$P(\ell_x) \sim \ell_x^{\nu_x} \quad \text{and} \quad P(\ell_t) \sim \ell_t^{\nu_t} \quad (2.22)$$

at the critical point. The critical exponents  $\alpha$ ,  $\beta$ ,  $\nu_x$ , and  $\nu_t$  given here should be those of 1+1 DP, which are listed in table 2.1.

Finding experimental realizations of DP, even in other systems than pipe flow, has proven to be a delicate matter.<sup>11</sup> Lemoult et al.<sup>[252]</sup> provided strong evidence that Couette flow (countermoving plates, or actually countermoving cylinders with large radii and small gap size) belongs to the 1+1 DP universality class. Experiments by Sano and Tamai<sup>[393]</sup> indicated that plane Poiseuille flow (PPF) belongs to the universality class of 2+1 DP (two spatial dimensions). The latter experiments hinged on grid-generated turbulence at the inlet and were far from reaching a steady state<sup>[327]</sup> and reported a critical  $\text{Re}$  in disagreement with more elaborate studies<sup>[472]</sup>. Hence the quality of their observations is dubious. On the other hand, Chantry et al.<sup>[89]</sup> recently provided clear evidence that a reduced-order model of Navier–Stokes PPF, Waleffe flow, belongs to 2+1 DP. This type of flow, though less computationally requiring, contains the essential self-sustaining mechanisms of turbulence and provides strong hints to what should be expected in experiments.

With regard to pipe flow, Shih et al.<sup>[406]</sup> provided a conceptual link between transitional flow and predator-prey models, where *zonal flow* takes on the role as predator,

<sup>10</sup> In DNS or experiments, the square of the non-axial part of the velocity vector averaged over the cross section, *viz.*

$$q = \langle u_r^2 + u_\theta^2 \rangle_{r,\theta} \quad (2.19)$$

makes up a good indicator for whether a region is turbulent or not.

TABLE 2.1: Critical exponents in 1+1 directed percolation. Values taken from<sup>[221]</sup>.

Exponent	Value
$\beta$	0.276 486(8)
$\nu_x$	1.733 847(6)
$\nu_t$	1.096 854(4)
$\alpha = \frac{\beta}{\nu_x}$	0.159 464(6)

<sup>11</sup> Despite the theoretical success, experimental observations of DP were lacking<sup>[194]</sup> until 2+1 DP scaling was displayed for electrohydrodynamic convection in nematic liquid crystals by Takeuchi et al.<sup>[431]</sup>.

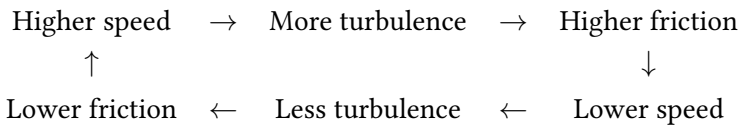
which could be shown to belong to DP by renormalization group methods. However, the numerical simulations on which their model was based were incomprehensive, and the significance of zonal flow is generally believed to be minor<sup>[29]</sup>.<sup>12</sup> Using his model for pipe flow, Barkley<sup>[28, 29]</sup> performed simulations which are consistent with 1+1 DP, whereas a validation using experiments or DNS is still lacking. Mukund and Hof<sup>[327]</sup> observed in  $7800d$  long pipe experiments a discontinuous transition without signs of scale invariance. Instead, above criticality, the system was jammed in a ‘crystalline’ state, where puffs were approximately equidistantly spaced (at  $\text{Re} \simeq 2060$ ). Below, the system would always die out (at  $\text{Re} \simeq 2020$ ). This points to two possible explanations:

- The DP scaling range in  $\text{Re}$  is extremely narrow, i.e. smaller than  $2020 \lesssim \text{Re} \lesssim 2060$  (within 2 %); or
- the transition to turbulence in pipe flow is not in the DP universality class.

<sup>12</sup> The predator-prey oscillations they observe are not unlikely to be the result of the feedback between friction factor and mean flow, which is a pronounced finite size effect that is ubiquitous for periodic pipes with short lengths—see the discussion near the end of this section.

The latter position was advocated by Pomeau<sup>[363]</sup>, against his own conjecture<sup>[362]</sup>, 30 years after he posed it. A reason for the transition not being in the DP universality class, could be the asymmetric *interaction* observed between puffs. As noted already by Hof et al.<sup>[195]</sup> and Barkley<sup>[29]</sup>, the interaction between two puffs manifests itself in the properties of the downstream puff, while the upstream puff remains unaffected<sup>[327]</sup>. As the downstream puff is fed less energetic flow, i.e. a more flattened profile than that of Hagen–Poiseuille flow, the closer to the upstream puff it is, it will be more likely to decay and less likely to split. Additionally, it will travel at a faster speed downstream, moving away from the upstream puff. Furthermore, in the crystalline puff state, downstream waves, originating from colliding puffs, were observed, representing an emergent property of puff–puff interactions.

A final point in this section concerns the friction factor for transitional flow. At the same  $\text{Re}$ , pipe flow completely contaminated by turbulence will exhibit a higher friction than what will a completely laminar flow. This is connected to the transitional region in the Moody diagram, where the friction factor  $f_D$  crosses over from the laminar branch, where  $f_D^{(\text{lam})} \sim \text{Re}^{-1}$ , to the turbulent branch, where  $f_D^{(\text{turb})} \sim \text{Re}^{-1/4}$ . For flow in finite tubes driven by a constant body force (or pressure gradient), this gives rise to a negative feedback loop between friction and flow velocity; shown schematically:



This leads to the instantaneous  $\text{Re}$  being a fluctuating quantity. For sufficiently long pipes, i.e. in the thermodynamic limit, these fluctuations should vanish and the  $\text{Re}$  number can be considered as the prescribed control parameter. For DNS, this effect must however be accounted for.

Recent experimental work by Cerbus et al.<sup>[87]</sup> has shown that the friction factor in transitional flow can be written as the linear combination

$$f_D(\text{Re}) = F_t f_D^{(\text{turb})}(\text{Re}) + (1 - F_t) f_D^{(\text{lam})}(\text{Re}), \quad (2.23)$$

where  $F_t \in [0, 1]$  is (still) the instantaneous turbulent fraction, which they could measure directly from experiments. Thus, the transitional region in the Moody diagram in reality appears directly from the spatial mixture of turbulent and laminar patches. In the steady state, in particular close to the critical point, the behaviour of  $F$  is expected to be described by the universal exponents (table 2.1). This illustrates also a practical need for a first-principles description and understanding of the dynamics, and in particular, knowledge of whether the transition belongs to the DP universality class.

### 2.2.3 Models and methods for two-phase flow

#### Overview of methods

Methods for modelling the flow of two immiscible fluids (components or phases) where the detailed interface is resolved, can be classified into two groups: interface-*tracking* and interface-*capturing* methods. In general, these methods adopt a “one-fluid” formulation, such that the governing equations are written in terms of one continuous field<sup>[368]</sup>. Some of the most popular methods are the following:

- The *volume-of-fluid* (VOF) method<sup>[397]</sup>, an improvement of the now obsolete marker-in-cell method by Harlow and Welch<sup>[178]</sup>, is perhaps the most widely used method for the computation of multiphase flows. Here, a marker function (the volume fraction of one of the phases) which takes the value zero or one, is advected in a conservative manner. The surface is then reconstructed typically using piecewise linear interface calculation. Surface forces typically depend on the curvature (which is found from the reconstructed surface), and are often implemented using the continuous surface force (CSF) approach, which means that the singular (‘delta function’) force on an interface is replaced by a surface force that is smeared over a finite “interface thickness”<sup>[66]</sup>. VOF conserves mass locally very well, but provides inaccurate curvature calculation<sup>[427]</sup>.
- The *front-tracking* method for multiphase flow belongs to the class of interface-tracking methods. Pioneered by Unverdi and Tryggvason<sup>[449]</sup>, the methods consists of representing the interface as a collection of connected Lagrangian markers, i.e. a mesh of codimension 1, which is advected with the flow<sup>[368]</sup>. This method is closely linked to the immersed boundary method, which was originally developed for fluid-structure interaction in the heart (see<sup>[353]</sup>). Hence, such methods may be particularly suitable for elastic interfaces<sup>[137]</sup>, and can simulate, for example, very low capillary number flows<sup>[4]</sup>. The method can be highly accurate, but topological changes, such as bubble splitting and collapse, are not easily handled. This is particularly true in 3D, where the required remeshing can be cumbersome and deteriorate the solution. The method is also prone to numerical instabilities.
- The *level-set* (LS) method<sup>[347,428]</sup> (see also the review<sup>[401]</sup>) describes the interface as the zero-level of a level-set function which is defined in the whole domain. This method handles topological changes automatically, provided that the level-set function is well-behaved. In order to do this, it must be reinitialized every few time steps (which is based on heuristics and tends to degrade the solution)<sup>[368]</sup>. Further, robust curvature calculations can be challenging<sup>[136,253]</sup>. Interface forces can be included either using the ghost-fluid method (sharp inclusion of forces) or by using the continuous surface force approach. A weakness of the level-set method is that it does not properly conserve mass, although mitigation strategies have been proposed.
- *Lattice Boltzmann* methods (LBM)<sup>[425]</sup>, founded on statistical mechanics and developed as a refinement of lattice-gas automata, represent a completely different class of methods. Rather than approximating the Navier–Stokes equations, fluid dynamics is simulated by collisions of particle distributions which obey Boltzmann statistics (with a discrete set of velocities). Several methods are available that extend the lattice Boltzmann method to multiple phases. One advantage of the lattice Boltzmann method is that it is trivially parallelizable as all interactions are local; another is that it easily handles complex boundaries. Hence, it has been applied to,

for example, porous media flows, and constitutes thus another important contribution from the statistical physics community to flow in porous media. However, time step limitations are more restricted than in other methods, as the method is (at least in principle) fully explicit. In industrial settings unstructured meshes are often used, and the unstructured lattice Boltzmann method (ULBM) for both single and multiphase flow has been a research topic in the group of the author (see<sup>[186,288–290,307,308]</sup>). However, some of the intuitiveness and efficiency contained in the (structured) lattice Boltzmann method is lost through this generalization.

- The *phase-field* (or diffuse-interface) method (see<sup>[13]</sup> for an early review, and<sup>[232]</sup> for a more recent one) represents the interface implicitly by the phase field  $\phi$  which interpolates the fluid parameters smoothly between the phases, and includes the interface forces through a phase field chemical potential derived from a free energy. This method has been used in the present thesis, and is discussed in more depth below.

In addition, less established methods such as smoothed particle hydrodynamics (see e.g. the review<sup>[312]</sup>), and stochastic rotation dynamics<sup>[205]</sup>, are available, but these are not discussed here. Moreover, there exist methods that attempt to exploit the strengths and eliminate the shortcomings of the different methods, such as the combined level-set/volume-of-fluid (CLSOV) method<sup>[427]</sup>. More extensive overviews than presented here are found in e.g. several books<sup>[368,447]</sup> and reviews<sup>[306,365,397,426]</sup>.

### *Phase-field models*

Phase-field models can typically be derived as a gradient flow of a free energy functional describing the system, imparting that interface forces can be included directly in a thermodynamically consistent way. Typically, the order parameter, or phase field,  $\phi$ , equals 1 in one phase, and  $-1$  in the other. At the interface, the phase field interpolates between the two values. The gradient flow can be taken in  $L^2$  or  $H^{-1}$ , which leads to a non-conserved and conserved order parameter, respectively. We will in this work consider the latter, which, coupled to hydrodynamics, typically results in variations over the Cahn–Hilliard–Navier–Stokes system.

In phase-field models, topological changes are handled automatically without reinitialization. Provided that all relevant physical terms are included in the free energy functional, the topological changes should also be physically sound. In practical simulations, however, the interface width must be chosen to be much higher than the *physical* interface width (which is typically a few molecules wide), and it is not clear whether the thermodynamic consistency represents an advantage over other methods when the interface is unrealistically thick. On the other hand, it has become standard for many of the sharp-interface methods to incorporate the interface forces in a continuous way over a smoothed interface (cf. the continuous surface force approach in volume-of-fluid or level-set methods). Sharp jumps in physical quantities such as density and viscosity also represent a numerical challenge, and smoothing is often done in other methods (e.g. smoothed Heaviside function). Thus the conceptual difference is not all different.

The phase-field model generally conserves mass globally well, but the phase field is allowed to move by diffusion in addition to advection, and thus larger droplets will grow at the expense of smaller ones (Ostwald ripening)<sup>[479]</sup>. However, this can be mitigated by using a phase-field mobility that makes this time scale much longer than the simulation time. On the other hand, standard phase-field models may give equilibrium solutions where  $|\phi| > 1$  in the pure phases, which can be catastrophic if the density ratio is large<sup>[306,479]</sup>. Mitigations exist, but however they mean that the model is no longer a gradient flow.

Other advantages of phase-field methods is that they are relatively easy to implement in any finite element framework, and that it is possible to rigorously prove stability and convergence of numerical schemes.

In general, it is probably not possible to find a method that is entirely satisfactory, and it is hard to find completely fair comparisons between methods in the literature. An important advantage of phase-field methods over other methods, however, is the way complex boundaries are handled. The phase-field model can be easily implemented in finite-element methods, and can thus operate on unstructured meshes representing complex geometries. Moreover, implementation of moving contact line models does not require any additional ad-hoc modelling, in contrast to most other methods. The contact line moves by diffusion, but contact line dissipation can be introduced in different ways, which reproduces experimental results both in the nanoscale<sup>[371,373]</sup> and at the continuum scale<sup>[83]</sup>.

We now focus on the phase-field models directly applicable to the purposes of this thesis. Phase-field models have a long history in fluid mechanics, as the concept of a diffuse interface dates back to Lord Rayleigh<sup>[376]</sup> and van der Waals<sup>[454]</sup>. However, they have only relatively recently appeared as a serious tool for *quantitative* simulation, notably starting with the work by Jacqmin<sup>[211, 212]</sup>. The basic phase-field model is the ‘Model H’ by Hohenberg and Halperin<sup>[196]</sup>, which was introduced to describe phase separation of binary fluids near the critical point. This model consists of the coupled Cahn–Hilliard–Navier–Stokes equations and describes fluids with matched densities and viscosities. Lowengrub and Truskinovsky<sup>[276]</sup> derived a thermodynamically consistent generalization of Model H for fluids with different densities in the two phases, however with the numerical difficulty that the velocity field was not divergence free. In contrast, the model by Ding et al.<sup>[118]</sup> is a straightforward generalization of Model H, where a constant density is replaced by a phase dependent one, while the velocity field remains solenoidal. That model does not appear to be thermodynamically consistent, as it seems unfeasible to construct a free energy functional for the model that decays in time. To circumvent these issues, Shen and Yang<sup>[403]</sup> heuristically added a term proportional to  $\partial_t \rho + \nabla \cdot (\rho \mathbf{u})$  (which vanishes in the bulk but contributes at the interface) to the momentum equation; and found an associated energy dissipation law. From a more fundamental starting point, Abels et al.<sup>[2]</sup> developed a thermodynamically consistent, frame invariant model for two-phase flow with density contrast. In contrast to the model by Lowengrub and Truskinovsky<sup>[276]</sup>, the velocity field in the latter three models<sup>[2,118,403]</sup> is divergence free, allowing for the use of efficient numerical methods.

### *Electrohydrodynamic simulations*

Most simulations of electrohydrodynamics have been concerned with the leaky-dielectric model or perfect dielectrics. In this respect, Fernández et al.<sup>[147]</sup> extended the front-tracking method by Unverdi and Tryggvason<sup>[449]</sup> to include electric forces at the fluid-fluid interface. Zhang and Kwok<sup>[481]</sup> developed a lattice Boltzmann method with the same capabilities. Tomar et al.<sup>[443]</sup> developed a combined level-set/volume-of-fluid (CLSVOF) method to simulate the aforementioned mentioned models. López-Herrera et al.<sup>[274]</sup> developed a charge-conservative CLSVOF as an enhancement to the model by Tomar et al.<sup>[443]</sup>. As a refinement to the model by López-Herrera et al.<sup>[274]</sup>, Berry et al.<sup>[43]</sup> developed a CLSVOF method that resolves the full electrokinetic problem, where ions were allowed to dissolved in only one of the phases. Bjørklund<sup>[53]</sup>, Teigen and Munkejord<sup>[437, 438]</sup> developed a LS method for a leaky-dielectric model including surfactants. The possibly first phase-field model for such phenomena was introduced by<sup>[277]</sup>, but their model was limited to Hele–Shaw cells, using a Darcy equation to

describe the hydrodynamics, and the electric effects were only effectively modelled. Eck et al.<sup>[128]</sup> presented a charge conservative phase-field model of the dielectric type with the purpose of studying electrowetting, and Nohetto et al.<sup>[340]</sup> followed thereafter with a similar model which included a generalized Navier boundary condition and density contrast. Lin et al.<sup>[258]</sup> presented a leaky-dielectric phase-field model which is a straightforward simplification of the model by Eck et al.<sup>[128]</sup>. A thermodynamically consistent phase-field model which fully accounts for electrokinetic effects, based on the model by Abels et al.<sup>[2]</sup>, was derived by Campillo-Funollet et al.<sup>[79]</sup>. This model is of central importance to the electrohydrodynamic simulations in this thesis, as its single-phase limit is consistent with standard electrokinetic description. Numerical resolution of these models is addressed in chapter 4.

### *Homogenized models*

We now move to several orders of magnitude larger scales. A whole different class of methods for two-phase flows are those that deal with transport of compressible fluids over large scales, where the interface and the flow patterns are so complex that it is impossible to resolve the full interface in practical situations. As indicated previously, this is typically the case for flows in industrial pipelines. Although early models were purely empirical, it has been recognized that physical modelling strategies are needed e.g. to better predict operating conditions.

In order to obtain models that are tractable, and that simultaneously contain the essential physics, homogenization techniques (much like those that can be employed to derive Darcy's law in a porous medium<sup>[465]</sup>) are employed; see Drew and Passman<sup>[124]</sup>. Thus, by averaging either over a representative elementary volume, over time<sup>[208]</sup>, over ensembles, or simply over cross sections, one ends up with a set of equations that describes each phase without any notion of an interface. The resulting *two-fluid models* are derived from such considerations, and are distinguished from one-fluid models in that both fluids are governed by a separate set of quantities, including velocity, occupying the same space<sup>[123]</sup>.<sup>13</sup> Additionally, a separately governed volume fraction (which summed over phases must add up to 1) of each phase is added to the description. The detailed description of the interaction between the two phases is replaced by (more or less empirical) source terms, typically driving the phases towards thermodynamic equilibrium, and effectively introducing dissipation due to friction between the phases or between the fluid and the pipe wall. Since diffusive processes are slow, second order differential terms are typically omitted (with coarse grids, they will often be dominated by numerical diffusion anyway), and we are left with models that can be written as first-order hyperbolic systems with source terms<sup>[279,317]</sup>.

One such averaged model is the Baer–Nunziato model<sup>[24]</sup>, originally developed to model the detonation-to-deflagration transition in solid-gas systems. This model was revived and stated in a more practical form for the purpose of modelling compressible multiphase flow by Saurel and Abgrall<sup>[394]</sup>, and has since found wide use. The Baer–Nunziato model describes two phases which are not in equilibrium with each other, in the sense that all thermodynamic quantities are governed separately in each phase. However, for many practical purposes, it is both physically and numerically sound to simplify by imposing *partial* equilibrium between the two phases, e.g. in temperature, pressure, chemical potential, or velocity.<sup>14</sup> Combination of zero or more of these partial equilibrium conditions leads to a possible hierarchy of models, one model for each combination. The assumption of equilibrium in velocity leads to the branch of the hierarchy denoted as *homogeneous flow models*, which was studied by Flåtten and Lund<sup>[153]</sup>, Lund<sup>[278]</sup>. For an overview of models studied by other authors, see the introduction of Paper 8<sup>[259]</sup>.

<sup>13</sup> Separate velocities allows, for example, a coarse-grained dispersed phase to move in the opposite direction of the other phase within the same computational cell.

<sup>14</sup> That is, imposing equal phase velocities, which can be valid e.g. for well-mixed flows.

Accurate prediction of the fluid-mechanical speed of sound (in practice, the velocity of information propagation) is important for many purposes—from preventing running ductile fracture of pipelines<sup>[317]</sup> to constructing efficient numerical schemes. It has long been folklore knowledge in the community that equilibrium constraints tend to decrease the speed of sound in the resulting models. In the terminology of hyperbolic relaxation systems (see the review by Natalini<sup>[329]</sup>), this corresponds to the *subcharacteristic condition*, which is closely linked to the stability of such systems. By building on results from the literature, Flåtten and Lund<sup>[153]</sup>, Lund<sup>[278]</sup> showed that this condition was satisfied for the entire homogeneous flow branch of the hierarchy. Other authors<sup>[148,318]</sup> have shown this condition to hold also for two-fluid models. The reader is referred to recent theses<sup>[279,317]</sup> or to the appended article<sup>[259]</sup> (Paper 8), for a broader overview of the topic. A continuation of this discussion is found in section 5.4.



## 3.1 SINGLE-PHASE FLOW

In reality, fluids are composed of discrete atoms and molecules that attract and repel each other. In practice, however, the basic assumption underpinning most of fluid mechanics, and the work presented in this thesis, is *the continuum assumption*, i.e., that all matter can, beyond a certain scale, be assumed to be continuous. On the one hand, the success of continuum mechanics in describing physical phenomena and enabling industrial applications is a testimony of the validity of this assumption. On the other hand, the macroscopic equations of fluid flow can be formally derived from kinetic theory (see for example,<sup>[425]</sup> Chapter 5). For our purposes, not much is gained from the latter procedure compared to the macroscopic approach, which we will adopt in the following.

We assume for now that the fluid we consider is a pure phase and that in the region it occupies, it is completely space-filling, described by a continuous velocity field  $\mathbf{u}$ , density  $\rho$ , dynamic viscosity  $\mu$ , etc. For macroscopic derivations of the equations of fluid flow, e.g. using the Reynolds transport theorem, consider standard textbooks on the topic, e.g.<sup>[245]</sup>.

3.1.1 *Fundamental principles*

Now, we consider a fixed domain  $\Omega$ , with a boundary  $\partial\Omega$ , which does not vary in time. For a closed system, the following fundamental physical principles should be satisfied:

- Conservation of mass,
- conservation of momentum (in the absence of friction),
- conservation of (total) energy,
- the second law of thermodynamics, i.e. that the global entropy should be non-decreasing.

We next present the fundamental compressible flow model and show that the above points are satisfied.

*The equation of state*

Generally, fluids, and in particular gases, are compressible. We assume the fluid to be in *local thermodynamic equilibrium*, such that the thermodynamic quantities, e.g. pressure  $p$ , temperature  $T$ , and chemical potential  $\mu$ , are state functions. In particular they are related by an *equation of state*. Thus all thermodynamic quantities can be found as differentials of a thermodynamic Helmholtz free energy  $a$ . Given that we are by definition in a pure stable phase (not on the spinodal), any thermodynamic quantity can then be found by knowledge of exactly two others.<sup>15</sup>

<sup>15</sup> This is not strictly necessary, but will suffice for the arguments made here.

For real fluids, their ‘real’ equations of state must be approximated by algebraic expressions with complexity and parameter values that depend on the physical parameter ranges of interest. Examples of equations of state often employed in simulations, ordered by increasing complexity, are (i) the ideal gas, (ii) the stiffened gas, (iii) van der Waals<sup>[453]</sup> and other cubic equations of state, and (iv) the Span–Wagner equation of state for CO<sub>2</sub><sup>[417]</sup>. The latter expression contains a total of 51 terms, including exponentials and

<sup>16</sup> Which illustrates the importance of universality classes in practical settings.

The following variables are of central to the thermodynamic description of a compressible single-phase fluid:

- $\rho$  – density [kg m<sup>-3</sup>],
- $p$  – pressure [Pa],
- $e$  – specific internal energy [J kg<sup>-1</sup>],
- $T$  – temperature [K],
- $s$  – specific entropy [J K<sup>-1</sup> kg<sup>-1</sup>],
- $g$  – specific chemical potential [J kg<sup>-1</sup>].

### Compressible flow

The archetypal model of compressible fluid flow can be stated as the following set of equations:

$$\partial_t \rho + \nabla \cdot (\rho \mathbf{u}) = 0, \quad (3.1a)$$

$$\partial_t(\rho \mathbf{u}) + \nabla \cdot (\rho \mathbf{u} \otimes \mathbf{u}) + \nabla p - \nabla \cdot \boldsymbol{\sigma}_{\text{visc}} = \mathbf{0}, \quad (3.1b)$$

$$\partial_t E + \nabla \cdot ((E + p)\mathbf{u}) - \nabla \cdot (\mathbf{h} + \boldsymbol{\sigma}_{\text{visc}}\mathbf{u}) = 0. \quad (3.1c)$$

Here,  $\boldsymbol{\sigma}_{\text{visc}}$  is the (objective and symmetric) viscous stress tensor. For a Newtonian fluid, where the stress is linear in the velocity field  $\mathbf{u}$ , the following stress–strain rate relationship holds:

$$\boldsymbol{\sigma}_{\text{visc}} = 2\mu \mathbf{D}\mathbf{u} + \lambda \mathbf{I} \nabla \cdot \mathbf{u}, \quad (3.2)$$

where the symmetric rate-of-strain tensor is given by  $\mathbf{D}\mathbf{u} = (\nabla \mathbf{u} + \nabla \mathbf{u}^\top)/2$ , and  $\mu, \lambda > 0$  are viscosity parameters. Further, the total energy per volume is defined by

$$E = \frac{1}{2} \rho \mathbf{u}^2 + \rho e. \quad (3.3)$$

The heat flux,  $\mathbf{h}$ , is proportional to the temperature gradient, and given by

$$\mathbf{h} = K_T \nabla T \quad (3.4)$$

where  $K_T > 0$  is the thermal diffusivity. As noted above, the internal specific energy  $e$  is assumed to be a thermodynamic state variable. Thus it is specified by any two other thermodynamic variables, such as the pair  $(\rho, T)$ . Note that in the absence of any viscous dissipation and heat transfer,  $\boldsymbol{\sigma}_{\text{visc}}, \mathbf{h} \rightarrow \mathbf{0}$ , and we arrive at the classical Euler equations.

### Boundary conditions

In addition to bulk equations, boundary conditions for  $\mathbf{x} \in \partial\Omega$  must be specified. The no-slip boundary condition  $\mathbf{u} = \mathbf{0}$  is usually applied. The latter is valid down to the

nanometer scale, but for certain materials it be replaced by the more general Navier slip condition (see e.g.<sup>[31]</sup>),

$$\mathbf{u} \cdot \hat{\mathbf{n}} = 0, \quad [\boldsymbol{\sigma}_{\text{visc}} \hat{\mathbf{n}} + l \mathbf{u}] \times \hat{\mathbf{n}} = \mathbf{0}, \quad (3.5)$$

where  $l$  is a slip coefficient. In the limit  $l \rightarrow 0$ , a shear-free boundary condition is achieved, while the no-slip condition is recovered in the limit  $l \rightarrow \infty$ .

### *Conservation laws*

Local mass conservation is given by eq. (3.1a). The total mass  $\mathcal{M} = \int_{\Omega} \rho$  is conserved:

$$\frac{d\mathcal{M}}{dt} = \int_{\Omega} \partial_t \rho = - \int_{\Omega} \nabla \cdot (\rho \mathbf{u}) = - \int_{\partial\Omega} \rho \hat{\mathbf{n}} \cdot \mathbf{u} = 0, \quad (3.6)$$

where  $\hat{\mathbf{n}}$  is the outward directed normal of the domain, and we have used that the velocity flux vanishes at the boundary. For a thermally insulated system,  $\hat{\mathbf{n}} \cdot \mathbf{h} = 0$  can be set on the boundary; otherwise Dirichlet boundary conditions on  $T$  can be imposed.

The evolution of momentum is governed by eq. (3.1b). Note that due to the presence of viscous dissipation, the global momentum  $\mathcal{P} = \int_{\Omega} \rho \mathbf{u}$  is *not* generally conserved.

Energy balance can in general be written as eq. (3.1c). The global energy  $\mathcal{E} = \int_{\Omega} E$  is conserved:

$$\frac{d\mathcal{E}}{dt} = \int_{\Omega} \partial_t E = 0, \quad (3.7)$$

given that either the shear stress or the tangential velocity vanishes at the boundary, and that the heat flux across the boundary,  $\hat{\mathbf{n}} \cdot \mathbf{h} = 0$ .

### *Entropy production*

The global entropy is given by  $\mathcal{S} = \int_{\Omega} \rho s$ . Now, the second law of thermodynamics states that the entropy should be non-decreasing. The fundamental thermodynamic differential can be written as

$$ds = T ds + \frac{p}{\rho^2} d\rho. \quad (3.8)$$

Using eqs. (3.1a) to (3.1c) and (3.8), we find, with some calculation, that the time derivative of the global entropy can be written as

$$\frac{d\mathcal{S}}{dt} = \int_{\Omega} \frac{2\mu|\mathbf{D}\mathbf{u}|^2}{T} d\Omega + \int_{\Omega} \frac{\lambda|\nabla \cdot \mathbf{u}|^2}{T} d\Omega + \int_{\Omega} K_T |\nabla \ln T|^2 d\Omega, \quad (3.9)$$

which, given that  $\mu, \lambda, T > 0$  on physical grounds, must be non-negative. Hence, the second law of thermodynamics is satisfied. It is worth noting that when no diffusive processes (viscous damping and heat transfer) are present in the system, the entropy is conserved.

#### 3.1.2 Approximations

##### *Isothermal flow*

In many physical applications, the temperature can be taken to be constant. This amounts to assuming that the heat generated externally or internally, i.e. by viscous dissipation, is negligible, or that temperature equilibrium with the surroundings is enforced instantaneously. The energy equation eq. (3.1c) can then be replaced directly by the condition

$T = T_0$ , where  $T_0$  is a specified temperature. In this case, the thermodynamic pressure, density, internal energy, and so forth, becomes dependent on a single variable.

It is clear that in the case of thermal equilibrium with the surroundings, the energy conservation principle will not be satisfied. The laws of thermodynamics require that<sup>[373]</sup>

$$\frac{d\mathcal{F}}{dt} = -T \frac{dS}{dt} + \frac{dW}{dt}, \quad (3.10)$$

where  $\mathcal{W}$  denotes work and  $\mathcal{F}$  is a free energy. In the absence of external work, it can be seen that the equivalent to entropy increase, in the case of isothermal flow, is a decrease in the free energy. This is a relevant quantity to inspect for many of the models presented in this work.

### Incompressible flow

In many cases, in particular those considered herein, the flow can be considered to be incompressible, i.e., the density is constant:

$$\rho = \text{constant}. \quad (3.11)$$

This is a good approximation for most liquids. A more general condition can be found based on the Mach number  $\text{Ma} = u/c$ , i.e. the ratio of the fluid speed  $u$  to the speed of sound  $c$ . The incompressibility assumption is physically justified when  $\text{Ma}^2 \ll 1$  (see<sup>[446], sec. 5.8</sup>).

Using eq. (3.11), we find from eq. (3.1a):

$$\nabla \cdot \mathbf{u} = 0, \quad (3.12)$$

i.e., the velocity field is *solenoidal*, or divergence free. In particular, the condition eq. (3.12) imparts that information propagates infinitely fast, i.e. all points in the domain affect each other instantly. This is because the pressure wave associated with eq. (3.1a) travels with the speed  $c \rightarrow \infty$  in an incompressible (infinitely stiff) medium.<sup>17</sup>

Now, the momentum eq. (3.1b) can be written as

$$\rho (\partial_t \mathbf{u} + \mathbf{u} \cdot \nabla \mathbf{u}) + \nabla p - \nabla \cdot (2\mu \mathbf{D}\mathbf{u}) = \mathbf{0} \quad (3.13)$$

and the energy eq. (3.1c) becomes decoupled from the mass and momentum equations, and is thus superfluous to the flow description. The only thermodynamic *variable* left now is the pressure, which can be seen as a Lagrange multiplier that makes the velocity field solenoidal. All other thermodynamic quantities, although uncoupled from the flow, are given by  $p$  alone.

Taking now the viscosity  $\mu$  to be constant, which is valid approximation unless temperature or pressure variations are too large, we obtain the classical incompressible Navier–Stokes equations,

$$\rho (\partial_t \mathbf{u} + \mathbf{u} \cdot \nabla \mathbf{u}) + \nabla p - \mu \nabla^2 \mathbf{u} = \mathbf{0}, \quad (3.14a)$$

$$\nabla \cdot \mathbf{u} = 0. \quad (3.14b)$$

### Laminar and creeping flow

As introduced in the previous chapter, an important dimensionless quantity that arises in the study of fluid flow is the Reynolds number  $\text{Re}$ , defined as the ratio of inertial to viscous forces in eq. (3.14),

$$\text{Re} = \frac{\rho u d}{\mu} \simeq \frac{\rho |\mathbf{u} \cdot \nabla \mathbf{u}|}{\mu |\nabla^2 \mathbf{u}|}, \quad (3.15)$$

<sup>17</sup> From a numerical standpoint, the velocity field being divergence free can be both advantageous and disadvantageous. On the one hand, it is a simplification, as one does not have to resolve the fast pressure wave. On the other hand, the infinitely fast information propagation means that no interactions are local, yielding possible issues with parallel scalability. Further, incompressible flow is prone to numerical instabilities; see the Babuska–Brezzi criterion in section 4.3.

where  $d$  is a typical length scale, and  $u$  is a characteristic velocity.

Laminar flow is a regime associated with low  $\text{Re}$ , where the fluid travels in a smooth and predictable way, and there is essentially no transfer of energy across scales. Since perturbations have a tendency to decay in such flows, such flows can often be taken to be time-independent. Still assuming incompressibility, the flow can then be described by the time-independent Navier–Stokes equations, obtained by imposing steady-state flow,  $\partial_t \mathbf{u} = 0$ , in eqs. (3.14a) and (3.14b):

$$\rho \mathbf{u} \cdot \nabla \mathbf{u} + \nabla p - \mu \nabla^2 \mathbf{u} = \mathbf{0}, \quad \nabla \cdot \mathbf{u} = 0. \quad (3.16)$$

With the presence of the advective term  $\mathbf{u} \cdot \nabla \mathbf{u}$ , the time-symmetry is broken, and standing vortices may be present e.g. behind obstacles.

When the characteristic velocity and the length scale is so small that  $\text{Re} \ll 1$ , the flow is not only laminar, but *creeping*.<sup>18</sup> That is, the viscous forces completely dominate over the inertial forces and eqs. (3.14a) and (3.14b) simplifies to

$$\mu \nabla^2 \mathbf{u} = \nabla p, \quad \nabla \cdot \mathbf{u} = 0 \quad (3.17)$$

<sup>18</sup> This can be shown by nondimensionalization of eq. (3.16), and matching the ‘Lagrange multiplier’  $p$  to the dominating term.

which are known as the Stokes equations. As can be seen from eq. (3.17), the equation is linear and the solution is completely specified by the boundary conditions.<sup>19</sup> In fact, the flow field becomes—up to a scaling with the value of the forcing—a purely geometric property. To see this, consider a domain  $\Omega$  with the no-slip condition  $\mathbf{u} = \mathbf{0}$  imposed on the boundary  $\partial\Omega$ , except at an inlet  $\partial\Omega_{\text{in}}$ , where an inlet pressure  $p_{\text{in}}$  is specified, and an outlet  $\partial\Omega_{\text{out}}$ , where an outlet pressure  $p_{\text{out}}$  is specified. We can then introduce the dimensionless variables  $\tilde{\mathbf{u}}$ ,  $\tilde{p}$ ,  $\tilde{\mathbf{x}}$ , defined by:

$$\tilde{\mathbf{u}} = \frac{\mu}{L(p_{\text{in}} - p_{\text{out}})} \mathbf{u}, \quad \tilde{p} = \frac{p - \frac{1}{2}(p_{\text{in}} + p_{\text{out}})}{p_{\text{in}} - p_{\text{out}}}, \quad \tilde{\mathbf{x}} = \frac{\mathbf{x}}{L}. \quad (3.18)$$

<sup>19</sup> Since the equation is invariant under the transformation  $(\mathbf{u}, p) \rightarrow (-\mathbf{u}, -p)$ , the flow field is reversible. The implications of this can be observed in captivating experiments on ‘reversible mixing’ of tracer dyes in a Taylor–Couette cell. See e.g. [https://www.youtube.com/watch?v=p08\\_KITKP50](https://www.youtube.com/watch?v=p08_KITKP50).

The scaled problem (3.17) then becomes

$$\tilde{\nabla}^2 \tilde{\mathbf{u}} = \tilde{\nabla} \tilde{p}, \quad \text{with} \quad \tilde{p} = \begin{cases} \frac{1}{2} & \text{for } \tilde{\mathbf{x}} \in \partial\tilde{\Omega}_{\text{in}} \quad \text{and} \\ -\frac{1}{2} & \text{for } \tilde{\mathbf{x}} \in \partial\tilde{\Omega}_{\text{out}}, \end{cases} \quad (3.19)$$

where  $\partial\tilde{\Omega}$  is the boundary of the scaled domain. Clearly, the solution  $(\tilde{\mathbf{u}}, \tilde{p})$  is *independent* of the inlet/outlet pressures  $p_{\text{in}}, p_{\text{out}}$ , the viscosity  $\mu$  and the scale  $L$  of the system. Thus, the flow field inherently only depends on the shape of the domain, including the location of the inlet and outlet. The flux  $Q$  is proportional to the magnitude of the physical flow field, and hence we can write down the relation

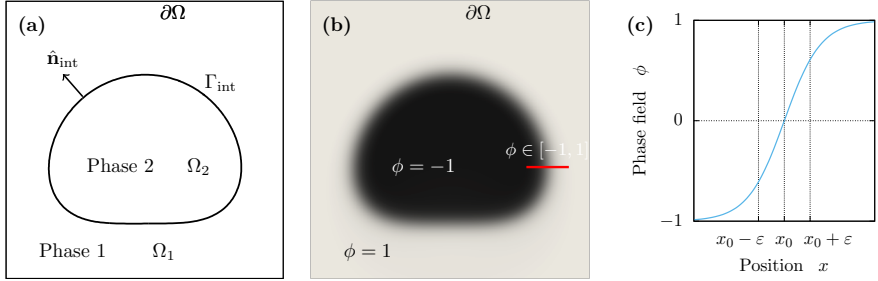
$$Q = kA \frac{p_{\text{in}} - p_{\text{out}}}{L\mu}, \quad (3.20)$$

where the permeability  $k$  is a function of the shape of the domain, and  $A$  is a cross-sectional area. Heuristically taking the continuum limit, i.e. letting  $(p_{\text{in}} - p_{\text{out}})/L \rightarrow |\nabla p|$  and  $Q \rightarrow A|\mathbf{q}|$ , we find that this is consistent with Darcy’s law,

$$\mathbf{q} = -\frac{k}{\mu} \nabla p, \quad (3.21)$$

where  $\mathbf{q}$  is the discharge per area. This invariance is heavily exploited in Paper 2<sup>[261]</sup>, which will be summarized in section 5.2.

FIGURE 3.1: Two phase flow modelling. (a) The sharp-interface description. (b) A diffuse-interface model meant to represent (a). The red line corresponds to (c). (c) Profile of the phase field  $\phi$  across the interface.



### 3.2 TWO-PHASE FLOW

Having established the fundamental equations for the continuum description of single-phase flow, we proceed now to describing the concurrent flow of two fluid phases. Equations (3.1a) to (3.1c) describe a single phase, and these equations are expected to hold in the *bulk* of the two phases; but the sets of parameters in the two phases will be separate. Therefore, we can replace  $\rho$  by  $\rho_i$ , and correspondingly for the other quantities, where  $i = 1, 2$  denotes either of the two phases. However, the bulk phases are separated by an interface which requires an explicit description. For simplicity, we will consider, in the bulk of this section, isothermal and incompressible flow. Under the same conditions as with single-phase flow, this is usually a good approximation at scales where the interface is explicitly modelled. We briefly return to compressible two-phase flow in section 3.2.3.

#### 3.2.1 Interface conditions

<sup>20</sup> At least far from the gas–liquid critical point, where the interface thickness diverges.

As mentioned briefly already, the two-phase interface is not sharp on the molecular scale, but rather a diffuse one. However, this thickness is usually only a few molecular layers thick<sup>[475]</sup> (i.e.  $\sim 10^{-9}$  m),<sup>20</sup> and thus already below the micrometer scale ( $\sim 10^{-6}$  m) it is perfectly valid to view it as an infinitely thin region where the physical properties change sharply and local interface forces are acting. A sharp-interface two-phase domain is sketched in fig. 3.1 (a).

We denote the jump in a physical quantity  $\chi_i$  across the interface by  $[\chi_i]_-^+$ . That is, assuming that the interface is located at  $x = 0$ , and that phase 1 is in the subdomain  $x < 0$  and phase 2 in the subdomain  $x > 0$ :

$$[\chi_i]_-^+ = \chi_2|_{x \rightarrow 0^+} - \chi_1|_{x \rightarrow 0^-}. \quad (3.22)$$

Further, we take  $\hat{\mathbf{n}}_{\text{int}}$  to be the unit vector normal to the interface.

Due to the incompressibility condition (3.14b), the continuity condition holds for the velocity field:

$$[\mathbf{u}]_-^+ = 0. \quad (3.23)$$

Further, the interface stress condition is given by

$$[p]_-^+ \hat{\mathbf{n}}_{\text{int}} - [2\mu_i \mathbf{D}\mathbf{u}]_-^+ \cdot \hat{\mathbf{n}}_{\text{int}} = \gamma\kappa \hat{\mathbf{n}}_{\text{int}}, \quad (3.24)$$

where  $\kappa$  is the curvature. In equilibrium, shear stresses vanish, and this condition trivially reduces to the Young–Laplace law (2.13), which in the new notation reads  $[p]_-^+ = \gamma\kappa$ .

#### Boundary conditions

At the solid–fluid interface, i.e. the boundary of the domain  $\partial\Omega$ , the no-slip condition is still expected to hold in the bulk of each phase. However, as mentioned in section 2.1.3,

the hydrodynamic theory with a no-slip condition predicts a non-integrable stress singularity at the MCL (the Huh–Scriven paradox<sup>[201]</sup>). By some physical means, this must be regularized; and as listed by Bonn et al.<sup>[60]</sup> several mechanisms have been proposed and are relevant in different settings. In particular, hydrodynamic *slip* at the contact line was proposed by Huh and Scriven<sup>[201]</sup> (see also<sup>[126]</sup>) as a mitigation strategy, and it has since been shown in molecular dynamics simulations that this slip is physically justified, and moreover extends a significant distance from the contact line<sup>[371,372,377,426]</sup>. Ren and E<sup>[377]</sup> proposed a boundary condition for the sharp-interface contact line motion, which amounts to imposing the Navier slip condition, cf. eq. (3.5),

$$l_i u_x = \mu_i \partial_y u_x \quad \text{away from the contact line, and} \quad (3.25a)$$

$$l_{\text{CL}} u_{x,\text{CL}} = \gamma (\cos \theta_{\text{eq}} - \cos \theta), \quad \text{at the contact line.} \quad (3.25b)$$

Here, the surface is oriented along  $x$ , and the surface normal is in the  $y$  direction,  $\theta_{\text{eq}}$  is the equilibrium contact angle given by Young's law (2.15),  $\theta$  is the instantaneous *dynamic* contact angle, and  $l_i, l_{\text{CL}}$  are the slip coefficients in the bulk phases and at the contact line, respectively. It is, however, not straightforward to implement such a boundary condition numerically.

### 3.2.2 Phase-field modelling

Phase-field modelling is a way to avoid the numerical difficulties associated with satisfying the jump conditions at the fluid–fluid interface (eqs. (3.23) and (3.24)), and is on sound physical grounds, as the interface on the microscopic scale *is* diffuse. Early phase-field models included compressibility and an energy equation, and were reviewed by Anderson et al.<sup>[13]</sup>, but as noted by Kim<sup>[232]</sup>, much progress has taken place since then.<sup>21</sup>

Here we focus on the fully incompressible formulation by Abels et al.<sup>[2]</sup>, and compare it to other formulations. A phase-field model is characterized by the order parameter field, i.e. the phase field,  $\phi$ , which typically takes the value 1 in one phase, and  $-1$  in the other.<sup>22</sup> At the interface,  $\phi \in (-1, 1)$ . In the forthcoming, the value  $\phi = 1$  corresponds to phase  $i = 1$  (with the associated phasic quantities), while  $\phi = -1$  corresponds to phase  $i = 2$ .

The thermodynamically consistent and frame indifferent model by Abels et al.<sup>[2]</sup> is given by

$$\rho(\phi) \partial_t (\mathbf{u}) + (\mathbf{m} \cdot \nabla) \mathbf{u} - \nabla \cdot [2\mu(\phi) \mathbf{D}\mathbf{u}] + \nabla p = -\phi \nabla g_\phi, \quad (3.26a)$$

$$\nabla \cdot \mathbf{u} = 0, \quad (3.26b)$$

$$\partial_t \phi + \mathbf{u} \cdot \nabla \phi = \nabla \cdot (M(\phi) \nabla g_\phi), \quad (3.26c)$$

$$g_\phi = \chi \gamma [\varepsilon^{-1} W'(\phi) - \varepsilon \nabla^2 \phi]. \quad (3.26d)$$

<sup>21</sup> Much progress has occurred also since the latter review<sup>[232]</sup>, as briefly surveyed in section 2.1.3.

<sup>22</sup> It is also commonplace to let it denote a local phase fraction, so that  $\phi \in [0, 1]$  but the difference is trivial.

Here, eqs. (3.26a) and (3.26b) are the Navier–Stokes equations, but augmented by a body force and a few new factors, which are explained below. Equations (3.26c) and (3.26d) govern the conservative evolution of the phase field, and represent the Cahn–Hilliard equation coupled to an advective field. Thus the system (3.26) is called the (augmented) Navier–Stokes–Cahn–Hilliard system.

The following new quantities have been introduced:

$\rho(\phi)$  – the phase-dependent density, which interpolates between the phasic values such that  $\rho(1) = \rho_1$  and  $\rho(-1) = \rho_2$ . Here, we use the arithmetic average:

$$\rho(\phi) = \frac{1+\phi}{2} \rho_1 + \frac{1-\phi}{2} \rho_2, \quad (3.27)$$

which is the only average that ensures global mass conservation; as realized by integrating over the domain and using that the flux of the phase field vanishes at the boundary.

- $\mu(\phi)$  – the phase-dependent dynamic viscosity. It interpolates between the phasic values, corresponding to  $\rho(\phi)$  above; an arithmetic average is usually used, but again a harmonic or geometric average may be more suitable if the viscosity contrast is large.
- $g_\phi$  – the phase-field chemical potential [ $\text{N m}^{-2}$ ]. It contains  $W(\phi)$ , a double well-potential, which has minima at  $\phi = \pm 1$ . Here, we use the Ginzburg–Landau potential

$$W(\phi) = \frac{1}{4}(1 - \phi^2)^2. \quad (3.28)$$

Moreover,  $\chi$  is a numerical prefactor to ensure the correct surface energy<sup>[211]</sup> given by  $\chi = 3/\sqrt{8} \simeq 1.06$ .

$\varepsilon$  – the interface thickness [m].

$\mathbf{m}$  – the advecting momentum, given by:

$$\mathbf{m} = \rho(\phi)\mathbf{u} - \rho'(\phi)M(\phi)\nabla g_\phi, \quad (3.29)$$

which only differs from the canonical momentum  $\rho\mathbf{u}$  at the interface, since  $g_\phi$  is constant in the bulk.

- $M(\phi)$  – The phase-field mobility function [ $\text{m}^3 \text{s kg}^{-1}$ ]. Two common alternatives are given by:

$$M(\phi) = \varepsilon M_0, \quad (3.30a)$$

$$M(\phi) = M_0(1 - \phi^2)_+, \quad (3.30b)$$

where  $M_0$  is a constant parameter, and  $(\cdot)_+ = \max(\cdot, 0)$ . An aim of these mobility functions is to reduce the diffusive mass currents that lead to unphysical (numerical) Ostwald ripening effects. To the author's knowledge, there have been few comparative studies of the effect of various mobility functions.

Abels et al.<sup>[2]</sup> showed through a matched asymptotic expansion that the model (3.26) reduces to the correct sharp-interface description (see previous section) in the limit where the interface thickness  $\varepsilon \rightarrow 0$ , provided that the phase-field mobility is modelled as in eq. (3.26). In particular, the correct fluid–fluid interface conditions are contained in the model, provided that the interface is sufficiently thin. The model by Ding et al.<sup>[118]</sup> is simply (3.26) with  $\mathbf{m} = \rho(\phi)\mathbf{u}$  instead of eq. (3.29). This formulation is not thermodynamically consistent (see below), but reduces to the correct interface description. The model by Shen and Yang<sup>[403]</sup> is similar to the model by Ding et al.<sup>[118]</sup> in that  $\mathbf{m} = \rho(\phi)\mathbf{u}$ , but additionally a term

$$\frac{\mathbf{u}}{2} (\partial_t \rho + \nabla \cdot (\rho \mathbf{u})) \quad (3.31)$$

is added to the left hand side of eq. (3.26a). This admits an energy dissipation law (thermodynamic consistency), but the model does not appear to be frame invariant. It is not known (at least to the author) whether this model reduces to the correct sharp-interface limit.

Note that the weighted arithmetic average (WAA), e.g. as in eq. (3.27), is not the only interpolation function that can be used for phasic quantities across the interface. Two

common alternatives are the weighted harmonic (WHA) and the weighted geometric average (WGA). For a general quantity  $A$ , these three averages are defined by

$$A_j(\phi) = \begin{cases} A_{j,1}\frac{1+\phi}{2} + A_{j,2}\frac{1-\phi}{2} & (\text{WAA}), \\ \left[ A_{j,1}^{-1}\frac{1+\phi}{2} + A_{j,2}^{-1}\frac{1-\phi}{2} \right]^{-1} & (\text{WHA}), \\ A_{j,1}^{\frac{1+\phi}{2}} \cdot A_{j,2}^{\frac{1-\phi}{2}} & (\text{WGA}). \end{cases} \quad (3.32)$$

and they are compared as a function of  $\phi$  in fig. 3.2. A problem with the WAA, and to some extent the WHA, is that for values of  $|\phi|$  numerically only slightly above 1 (which can occur in phase-field simulations), is that the value of the interpolated quantity may become negative. This is also seen in fig. 3.2 and can lead to ill-posed problems. The WGA avoids this, but is more costly to compute. Some authors claim that using the WHA instead of the WAA for the density, yields more accurate computations<sup>[232,476,477]</sup>, but this strictly imparts to violate mass conservation (however, the phase-field is conserved).

### Boundary conditions

A boundary condition directly on the contact angle and contact line motion, as that specified in the sharp-interface limit, i.e. eq. (3.25), cannot be directly applied to a diffuse interface. The static contact angle  $\theta_{\text{eq}}$  can be imposed through the condition

$$\chi\epsilon\hat{\mathbf{n}} \cdot \nabla\phi = \cos(\theta_{\text{eq}})f'_w(\phi), \quad \hat{\mathbf{n}} \cdot \nabla g_\phi = 0, \quad (3.33)$$

where the wall energy function

$$f_w(\phi) = \frac{1}{4}(2 + 3\phi - \phi^3) \quad (3.34)$$

interpolates smoothly between 0 (at  $\phi = -1$ ) and 1 (at  $\phi = 1$ ). Note that other forms of  $f_w(\phi)$  that satisfy the criterion  $f_w(1) - f_w(-1) = 1$  (and are smooth) are viable options, as discussed by Huang et al.<sup>[200]</sup>. However, the formulation (3.34) is the only one that is compatible with the equilibrium solution to eqs. (3.26c) and (3.26d), i.e.  $g_\phi = \text{constant}$ .

Due to the presence of a diffuse interface, the contact line will move even when eq. (3.33) is coupled to a no-slip condition on the velocity, due to interface diffusion. This can be admissible when the dynamics are governed by processes away from the contact line, but is not satisfactory on the microscopic scale. A remedy is due to Qian et al.<sup>[371,373]</sup>, who extracted phase-field parameters from carefully executed molecular dynamics simulations, and proposed a generalized Navier boundary condition (GNBC)<sup>[5]</sup> valid for  $\mathbf{x} \in \partial\Omega$ :

$$\mathbf{u} \cdot \hat{\mathbf{n}} = 0, \quad [\boldsymbol{\sigma}_{\text{visc}}\hat{\mathbf{n}} + l(\phi)\mathbf{u} - L[\phi]\nabla\phi] \times \hat{\mathbf{n}} = \mathbf{0}, \quad \text{on the velocity field,} \quad (3.35a)$$

$$\partial_t\phi + \mathbf{u} \cdot \nabla\phi = -\Gamma L[\phi], \quad \hat{\mathbf{n}} \cdot \nabla g_\phi = 0, \quad \text{on the phase field,} \quad (3.35b)$$

where

$$L[\phi] = \gamma [\chi\epsilon\hat{\mathbf{n}} \cdot \nabla\phi + \cos(\theta_{\text{eq}})f'_w(\phi)], \quad (3.35c)$$

$$l(\phi) = l_1\frac{1+\phi}{2} + l_2\frac{1-\phi}{2}. \quad (3.35d)$$

Here,  $l(\phi)$  can be interpreted as an inverse slip length, interpolating between the values in the two phases, and  $\Gamma$  is a phenomenological parameter. It should be noted that the simulations supporting the GNBC were carried out in a slow wetting regime<sup>[82]</sup>, and the

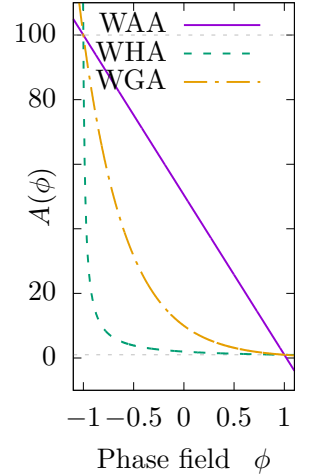


FIGURE 3.2: A comparison of three ways to interpolate a phasic quantity across the phase-field interface: Weighted arithmetic average (WAA), weighted harmonic average (WHA), and weighted geometric average (WGA).

interface width was matched to the actual, molecular one. It is less clear how well the GNBC works outside this domain.

An important limit to the GNBC is that of short slip length, which is obtained by letting  $l_1, l_2 \rightarrow \infty$  in eq. (3.35). Then the no-slip boundary condition  $\mathbf{u} = \mathbf{0}$  is recovered, along with the phase-field boundary condition

$$\Gamma^{-1} \partial_t \phi = \gamma \left[ -\chi \epsilon \hat{\mathbf{n}} \cdot \nabla \phi + \cos(\theta_e) f'_w(\phi) \right], \quad (3.36)$$

which was obtained by Carlson et al.<sup>[82]</sup> on phenomenological grounds, and previously proposed by Jacqmin<sup>[211]</sup>. Here,  $\tau_w = \epsilon / (\Gamma \gamma)$  can be interpreted as a characteristic relaxation time. It was shown e.g. in Refs.<sup>[82,83]</sup> that the condition (3.36) is fully capable of modelling rapid non-equilibrium wetting at the millimeter scale. In the limit  $\tau_w \rightarrow 0$  ( $\Gamma \rightarrow \infty$ ), the static condition eq. (3.33) is recovered.

### *Free energy*

Fundamental to most phase-field models is that they can be derived as the gradient flow of some energy functional. The system eq. (3.26) is associated with the energy functional

$$\mathcal{F} = \mathcal{F}_\phi + \mathcal{F}_w + \mathcal{F}_u, \quad (3.37)$$

where the Cahn–Hilliard free energy<sup>[78]</sup> is given by:

$$\mathcal{F}_\phi = \int_\Omega \chi \gamma \left[ \epsilon^{-1} W(\phi) + \frac{1}{2} \epsilon |\nabla \phi|^2 \right]. \quad (3.38)$$

The fluid-solid interface energy is given by:

$$\mathcal{F}_w = \int_{\partial\Omega} [\gamma_2 + (\gamma_1 - \gamma_2) f_w(\phi)], \quad (3.39)$$

where Young's law eq. (2.15) gives  $\gamma_1 - \gamma_2 = \gamma \cos \theta_{eq}$ . The kinetic energy is given by

$$\mathcal{F}_u = \int_\Omega \frac{1}{2} \rho(\phi) |\mathbf{u}|^2. \quad (3.40)$$

The time evolution of  $\mathcal{F}$  is given by using eqs. (3.26a) to (3.26c), along with the GNBC (3.35), and yields

$$\frac{d\mathcal{F}}{dt} = - \int_\Omega [M(\phi) |\nabla g_\phi|^2 + 2\mu(\phi) |\mathbf{D}\mathbf{u}|^2] - \int_{\partial\Omega} [l(\phi) |\mathbf{u}|^2 + \Gamma |L[\phi]|^2]. \quad (3.41)$$

In particular, all terms within brackets are squares with positive coefficients, i.e. the conditions  $M, \mu, l, \Gamma \geq 0$  ensure that the model is dissipative.

### 3.2.3 Homogenized models

We now return to two-phase flow in pipes. In typical phenomena of interest to these flows, such as rapid decompression, running ductile fracture<sup>[317]</sup>, the phenomena of interest occur at  $Ma \sim 1$ ; i.e. incompressibility cannot be justified. Thus, fully compressible models must be employed. Instead of resolving the interface, the Baer–Nunziato model<sup>[24]</sup> is based on averaged equations where the interaction between the phases across the interface is modelled effectively. The model is widely used in practice and extensively studied in the literature<sup>[480]</sup>. These effective interaction processes, that should drive the phases towards equilibrium (i) with each other, and (ii) with the surroundings, can be modelled as relaxation source terms.

The following processes can be physically motivated to take place:

- $p$  – **Volume transfer:** Relaxation towards mechanical equilibrium due to pressure differences between the phases, i.e. expansion or compression.
- $T$  – **Heat transfer:** Relaxation towards thermal equilibrium, due to temperature differences between the phases.
- $g$  – **Mass transfer:** Relaxation towards chemical equilibrium due to differences between the phases in chemical potential.
- $\mathbf{u}$  – **Momentum transfer:** Relaxation towards equal velocities, which occurs through momentum transfer due to interface friction when the phasic velocities are different.

Additionally, heat and momentum transfer can occur due to interaction with the surroundings, e.g. the confining pipe.

With all possible relaxation terms, the Baer–Nunziato model<sup>[24]</sup>, formulated in the lines of Saurel and Abgrall<sup>[394]</sup>, can be stated compactly as

$$\partial_t \alpha_k + \mathbf{u}_{\text{int}} \cdot \nabla \alpha_k = I_k, \quad (3.42a)$$

$$\partial_t (\alpha_k \rho_k) + \nabla \cdot (\alpha_k \rho_k \mathbf{u}_k) = K_k, \quad (3.42b)$$

$$\begin{aligned} \partial_t (\alpha_k \rho_k \mathbf{u}_k) + \nabla \cdot (\alpha_k \rho_k \mathbf{u}_k \otimes \mathbf{u}_k + \alpha_k p_k \mathbf{I}) - p_{\text{int}} \nabla \alpha_k &= \mathbf{u}_{\text{int}} K_k + \mathbf{M}_k \\ &\quad + \mathbf{M}_{k,\text{ext}}, \end{aligned} \quad (3.42c)$$

$$\begin{aligned} \partial_t E_k + \nabla \cdot (E_k \mathbf{u}_k + \alpha_k p_k \mathbf{u}_k) - p_{\text{int}} \mathbf{u}_{\text{int}} \cdot \nabla \alpha_k &= -p_{\text{int}} I_k + \mathbf{u}_{\text{int}} \cdot \mathbf{M}_k \\ &\quad + (g_{\text{int}} + \frac{1}{2} \mathbf{u}_{\text{int}}^2) K_k \\ &\quad + H_k + H_{k,\text{ext}}, \end{aligned} \quad (3.42d)$$

for each phase  $k \in \{g, \ell\}$ , where  $g$  denotes gas and  $\ell$  denotes liquid. Here,  $p_{\text{int}}$ ,  $g_{\text{int}}$ ,  $\mathbf{u}_{\text{int}}$  are interface quantities that result from the homogenization procedure and must be explicitly modelled in a physically consistent way. Moreover,  $\alpha_k$  denotes the volume fraction of the phase  $k$ , such that the condition  $\alpha_g + \alpha_\ell = 1$  makes eq. (3.42a) for one of the phases superfluous. Thus, we are left with 7 independently governed partial differential equations (where two are vectorial).

In the model (3.42), the relaxation source terms  $I_k$ ,  $K_k$ ,  $H_k$  and  $M_k$ , are modelled as the following:

- $I_g = -I_\ell = \mathcal{J}(p_g - p_\ell)$  drives the phases towards equal pressure through volume transfer,
- $K_g = -K_\ell = \mathcal{K}(g_\ell - g_g)$  drives the phases towards equal chemical potential through mass transfer,
- $H_g = -H_\ell = \mathcal{H}(T_\ell - T_g)$  drives the phases towards equal temperature through heat transfer,
- $\mathbf{M}_g = -\mathbf{M}_\ell = \mathcal{M}(\mathbf{u}_\ell - \mathbf{u}_g)$  drives the phases towards equal velocities through momentum transfer.
- $\mathbf{M}_{k,\text{ext}} = \alpha_k \rho_k \mathbf{a}_{\text{grav}} - f_{k,D} \mathbf{u}$  represents momentum transfer due to external sources; here  $\mathbf{a}_{\text{grav}}$  represents the gravitational acceleration, and  $f_{k,D}$  represents friction with the pipe wall (proportional to a Darcy friction factor for phase  $k$ ).
- $H_{k,\text{ext}}$  represents the heat transfer from surroundings.

The quantities  $\mathcal{J}, \mathcal{K}, \mathcal{H}, \mathcal{M}$  can be interpreted as coefficients that can depend on thermophysical properties of the flow, e.g. flow regime or temperature. On physical grounds, they must all be non-negative; see e.g. [153,259,278].

It should be noted that the model (3.42) in practice is comprised of the Euler equations for each of the phases, supplemented by interface interaction terms and source terms. In the absence of external source terms, the model (3.42) conserves

- total mass,  $\mathcal{M} = \int_{\Omega} (\alpha_g \rho_g + \alpha_\ell \rho_\ell)$ , which is realized by summing eq. (3.42b) over the phases  $k$ ;
- total momentum,  $\mathcal{P} = \int_{\Omega} (\alpha_g \rho_g \mathbf{u}_g + \alpha_\ell \rho_\ell \mathbf{u}_\ell)$ , as seen by summing (3.42c) over  $k$ ; and
- total energy,  $\mathcal{E} = \int_{\Omega} (E_g + E_\ell)$ , as seen by summing eq. (3.42d) over  $k$ .

Moreover, a second law analysis similar to that shown in section 3.1.1, but by combining the two phases, can be used to determine the interface parameters such that the model is thermodynamically consistent [259].

Writing out the differentials and for simplicity assuming a one-dimensional description along  $x$  (which is currently of most practical importance), eq. (3.42) can be written in the quasilinear form

$$\partial_t \mathbf{U} + \mathbf{A}(\mathbf{U}) \partial_x \mathbf{U} = \sum_i \frac{1}{\tau_i} \mathbf{Q}_i(\mathbf{U}), \quad (3.43)$$

Here,  $\mathbf{U}$  is the (seven-dimensional) vector of unknowns, the matrix  $\mathbf{A}$  is denotes the Jacobian of the system, and  $\mathbf{Q}_i$  contains the relaxation terms for each relaxation process  $i$ , with the associated characteristic timescale  $\tau_i$  (explicit expressions are omitted here). The eigenvalues of  $\mathbf{A}$  are independent of the choice of  $\mathbf{U}$  and determine the propagation velocities, i.e. the fluid-mechanical sound velocities, of the system.

### Partial equilibrium

When one or more of the timescales  $\tau_i$  are much faster than other time scales involved in the problem, it may be physically valid and practically advantageous to *directly* enforce equilibrium in one or more of the aforementioned processes. For example, pressure equilibrium imparts that

$$p_k \equiv p, \quad \text{which corresponds to} \quad \mathcal{J} \rightarrow \infty, \quad (3.44)$$

and similarly for the other processes. Enforcing eq. (3.44) effectively removes one unknown from the problem, so that one of the 7 equations in eq. (3.42) becomes superfluous. Typically, eq. (3.42a) is removed for such  $p$ -relaxation. Evidently, all the combinations of equilibrium conditions lead to different models, as mentioned in section 2.2.3. When all equilibrium are enforced, the *homogeneous equilibrium model* arises, which is basically the Euler equations supplied with a two-phase equation of state.

Zein et al. [480] discuss the physical mechanisms of the involved relaxation processes, arguing that pressure relaxation is much faster than temperature relaxation, which again is faster than chemical potential relaxation; i.e.

$$\tau_p \ll \tau_T \ll \tau_g, \quad (3.45)$$

which are also common assumptions in the literature. The velocity relaxation time  $\tau_u$  is expected to depend strongly on the flow regime. For stratified flow, the phase velocities

can be very different, while for dispersed flow it is reasonable to assume that the velocity relaxation is fast<sup>[279]</sup>. On the other hand, for these processes, full equilibrium in pressure will not be achieved. This is due to (i) gravity, which in stratified flow gives a pressure difference between the upper and lower phase, and (ii) surface tension, which through the Young–Laplace law (2.13) gives a higher pressure inside droplets in dispersed flow.

It is evident that replacing a PDE in eq. (3.42) by a functional relationship, such as eq. (3.44), changes the eigenstructure of the problem. Thereby, the propagation velocities, i.e. the fluid-mechanical speeds of sound, of the system change. In particular, it can be shown in the limit of equal phase velocities, that any equilibrium assumption reduces the fluid-mechanical speed of sound of such models<sup>[153,259,278]</sup>. This supports the folklore knowledge in the compressible multiphase flow community that the *equilibrium* speed of sound is always lower than the *frozen* speed of sound.

### 3.3 SINGLE-PHASE ELECTROHYDRODYNAMICS

The previous section concerned how to extend the modelling of single-phase flow to including a second phase. In this and the next section, we discuss the extension to modelling electrohydrodynamics, i.e. how to include the joint effects of dissolved ions and applied electric fields. The present section considers single-phase electrohydrodynamics, while in section 3.4 electrohydrodynamics in two phases is described.

The archetypical model for electrohydrodynamic flow, with  $N$  chemical species, is given by the following set of equations. The flow is assumed to be incompressible, isothermal and the electric currents are (safely) assumed to be sufficiently small for magnetic forces to be neglected.

$$\rho(\partial_t \mathbf{u} + \mathbf{u} \cdot \nabla \mathbf{u}) + \nabla p - \mu \nabla^2 \mathbf{u} = - \sum_{j=1}^N c_j \nabla g_{c_j}, \quad (3.46a)$$

$$\nabla \cdot \mathbf{u} = 0, \quad (3.46b)$$

$$\partial_t c_j + \mathbf{u} \cdot \nabla c_j = \nabla \cdot \left( \frac{D_j c_j}{k_B T} \nabla g_{c_j} \right), \quad (3.46c)$$

$$g_{c_j} = k_B T \ln \left( \frac{c_j}{c_j^{\text{ref}}} \right) + q_e z_j V, \quad (3.46d)$$

$$\epsilon_0 \epsilon_r \nabla^2 V = -\rho_e. \quad (3.46e)$$

In the literature, the terms *electrohydrodynamics* (EHD), *electrokinetics* (EK) and (to some extent) *electro-fluid-dynamics* are often used interchangably. Bazant<sup>[33]</sup> uses electrokinetics to refer to models which explicitly take into account ion transport, while electrohydrodynamics refers to modelling weakly conducting liquids with charged interfaces. The reason for the separate terminology is, in part, that the two fields have evolved separately and only recently are starting to become unified. Bruus<sup>[74]</sup>, pp. 141 uses electrohydrodynamics in a broad sense, *including* electrokinetic effects. We have in this work opted for the latter definition; in particular electrokinetics refers to the part of electrohydrodynamics where diffusion of ions is important.

Herein, the following physical quantities are introduced:

$c_j$  — number density, i.e. concentration, of species  $j \in \{1, \dots, N\}$  [ $\text{m}^{-3}$ ].

$g_{c_j}$  — chemical potential of species  $j$  [J].

$k_B$  — The Boltzmann constant [ $\text{J K}^{-1}$ ].

$D_j$  — diffusivity of species  $j$  [ $\text{m}^2 \text{s}^{-1}$ ].

$c_j^{\text{ref}}$  — reference concentration for species  $c_j$  [ $\text{m}^{-3}$ ].

$q_e$  — the elementary charge [C],

$V$  — electric potential [V]. The electric field is given by  $\mathbf{E} = -\nabla V$ .

$z_j$  — valency of ionic species  $j$  [-],

$\epsilon_0$  — the vacuum permittivity [ $\text{C V}^{-1} \text{ m}^{-1}$ ],

$\epsilon_r$  — the relative permittivity [-],

$\rho_e$  – the charge density field [ $\text{C m}^{-3}$ ]. It is given by:

$$\rho_e = q_e \sum_{j=1}^N z_j c_j. \quad (3.47)$$

Above, eqs. (3.46a) and (3.46b) are the Navier–Stokes equations (3.14), where the momentum equation (3.46a) is augmented, on the right hand side, by an ‘electrochemical’ body force.

The form of the body force is somewhat unconventional. In most studies, the term on the right hand side of eq. (3.46a) is taken to be  $\mathbf{f} = -\rho_e \nabla V$ . This formulation is related to the form stated in eq. (3.46a) by a redefinition of the pressure to include an osmotic contribution, i.e. the thermodynamical pressure (in the conventional form)  $p_{\text{therm}} = p + k_B T \sum_{j=1}^N c_j$  (where  $p$  is the same as in eq. (3.46a)). The adopted form has advantages over the conventional one, e.g. as it avoids pressure build-up in the electrical double layers<sup>[337]</sup>. In this redefinition, care must primarily be taken in applying pressure conditions at boundaries with different concentrations, but not otherwise, since the role of the pressure in incompressible flow is to keep the velocity divergence free.

Equation (3.46c), with (3.46d) inserted, is the Nernst–Planck equation. The two terms in eq. (3.46d) represent the contribution to the flux from, in written order, diffusion and migration. Equation (3.46e) is the Poisson equation for electrostatic equilibrium (Gauss’ law).

In Paper 5 (ref.<sup>[265]</sup>), a generalized version of the model (3.46) is presented, where fluid parameters such as density, viscosity and permittivity, are allowed to depend on the local concentrations. Additionally, a source term in the concentration equation, allowing for chemical reactions to occur, term is included. This is discussed in more depth in section 5.3.

### Boundary conditions

The same boundary conditions as for single-phase flow are expected to apply to the velocity field as before. Here, we assume the standard Navier slip boundary condition (3.5).

For the concentration fields, the constant concentrations can be set at inlet and outlet parts of the domain  $\partial\Omega$ , alternatively a no-flux condition is set by imposing  $\hat{\mathbf{n}} \cdot \nabla g_{c_j} = 0$ . The electric potential can e.g. be set to a fixed value  $V_0$  on a part of the boundary. In the presence of a surface charge, the boundary condition

$$\hat{\mathbf{n}} \cdot \nabla V = \frac{\sigma_e}{\epsilon_0 \epsilon_r}, \quad (3.48)$$

where  $\sigma_e$  is the surface charge [ $\text{C m}^{-2}$ ].

### Free energy

The free energy functional associated with eq. (3.46) is given by

$$\mathcal{F} = \mathcal{F}_{\mathbf{u}} + \sum_{j=1}^N \mathcal{F}_{c_j} + \mathcal{F}_V, \quad (3.49)$$

where the kinetic energy  $\mathcal{F}_{\mathbf{u}}$  is given by eq. (3.40), the chemical energy is given by

$$\mathcal{F}_{c_j} = \int_{\Omega} k_B T c_j \left( \ln \left( \frac{c_j}{c_j^{\text{ref}}} \right) - 1 \right), \quad (3.50)$$

and the electric field energy is given by

$$\mathcal{F}_V = \int_{\Omega} \frac{1}{2} \epsilon_0 \epsilon_r |\nabla V|^2. \quad (3.51)$$

Assuming no-flux boundary conditions and a Navier slip condition, the time derivative becomes:

$$\frac{d\mathcal{F}}{dt} = - \int_{\Omega} \left[ 2\mu |\mathbf{D}\mathbf{u}|^2 + \sum_{j=1}^N \frac{D_j c_j}{k_B T} |\nabla g_{c_j}|^2 \right] - \int_{\partial\Omega} l |\mathbf{u}|^2. \quad (3.52)$$

Hence, the model is dissipative, and thus thermodynamically consistent.

### *Creeping flow and steady-state*

For microscale flows, the assumption  $\text{Re} \ll 1$  is usually justified. In this case, the inertial term of eq. (3.46a) can be neglected. Further, we are often interested in the *steady-state* transport through microchannels, and hence all time derivatives vanish. The steady-state equations for creeping flow can be summarized as:

$$\nabla p - \mu \nabla^2 \mathbf{u} = - \sum_{j=1}^N c_j \nabla g_{c_j}, \quad (3.53a)$$

$$\nabla \cdot \mathbf{u} = 0, \quad (3.53b)$$

$$\nabla \cdot (c_j \mathbf{u}) = D_j \nabla^2 c_j + \nabla \cdot \left( \frac{D_j q_e z_j c_j}{k_B T} \nabla V \right), \quad (3.53c)$$

$$\epsilon_0 \epsilon_r \nabla^2 V = -\rho_e. \quad (3.53d)$$

Despite the simplification, this is a strongly coupled non-linear system, which can only be solved analytically in particular limits and simple geometries.

### *Equilibrium*

In equilibrium, all fluxes should vanish, including the one that is proportional to  $\nabla g_{c_i}$ . Thus, the chemical potential defined in eq. (3.46d) must be constant:

$$g_{c_i} = k_B T \ln \left( \frac{c_j}{c_j^{\text{ref}}} \right) + q_e z_i V = k_B T \ln \left( \frac{c_i^0}{c_i^{\text{ref}}} \right), \quad (3.54)$$

where we have implicitly defined a reference concentration  $c_i^0$  at a grounded part of the boundary. Solving this for  $c_i$  yields

$$c_i = c_i^0 e^{-\frac{q_e z_i V}{k_B T}}, \quad (3.55)$$

i.e., the concentrations follow the Boltzmann distribution. We can now insert the distributions eq. (3.55) into eq. (3.53d):

$$\nabla^2 V = -\frac{q_e}{\epsilon_0 \epsilon_r} \sum_{i=1}^N z_i c_i^0 e^{-\frac{q_e z_i V}{k_B T}}, \quad (3.56)$$

which is a non-linear equation to be solved for the single variable  $V$ . The latter becomes particularly appealing when considering a binary symmetric electrolyte, i.e.,  $i \in \{\pm\}$

and  $z_{\pm} = \pm z$ , which is taken to be neutral at the reference point, such that  $c_{\pm}^0 = c^0$ . Then, we obtain the classical nonlinear Poisson–Boltzmann equation

$$\nabla^2 V = \frac{2q_e z c^0}{\epsilon_0 \epsilon_r} \sinh \left( \frac{q_e z V}{k_B T} \right). \quad (3.57)$$

Here, we can identify the *thermal voltage*  $V_T$  and the Debye length  $\lambda_D$ , respectively defined by

$$V_T = \frac{k_B T}{q_e z}, \quad \text{and} \quad \lambda_D = \sqrt{\frac{k_B T \epsilon_0 \epsilon_r}{2 z^2 q_e^2 c^0}}. \quad (3.58)$$

Equations (3.57) and (3.58) yield an equation for the scaled electric potential  $\varphi = V/V_T$ :

$$\nabla^2 \varphi = \frac{1}{\lambda_D^2} \sinh \varphi. \quad (3.59)$$

The concentrations can subsequently be found from eq. (3.55) as  $c_{\pm} = c^0 e^{\mp \varphi}$ . Equation (3.59) can be solved exactly in the one-dimensional case, considering a semi-infinite domain. The so-called Gouy–Chapman solution, given in the domain  $\Omega = \{x \in [0, \infty)\}$ , with the potential  $\varphi = \varphi_0$  prescribed at  $x = 0$ , is given by<sup>[74]</sup>

$$\varphi = 4 \tanh^{-1} \left[ \tanh \left( \frac{\varphi_0}{4} \right) e^{-x/\lambda_D} \right]. \quad (3.60)$$

Clearly, the magnitude of  $|\varphi_0|$  determines the ‘nonlinearity’ of the potential distribution. In many practical settings, the magnitude of the scaled surface potential  $\varphi_0$  is so small that eq. (3.59) (and (3.60)) can be linearized. In this limit, the so-called Debye–Hückel approximation,  $|\varphi| \ll 1$  ( $|V| \ll V_T$ ), yields the *linearized* Poisson–Boltzmann equation,

$$\nabla^2 \varphi = \frac{1}{\lambda_D^2} \varphi, \quad (3.61)$$

where the corresponding solution to (3.60) is  $\varphi = \varphi_0 e^{-x/\lambda_D}$ . Thus, it is clearly seen that the Debye length  $\lambda_D$  is a characteristic length of the diffusive layer, i.e. it measures the extent of the electric double layer (EDL).

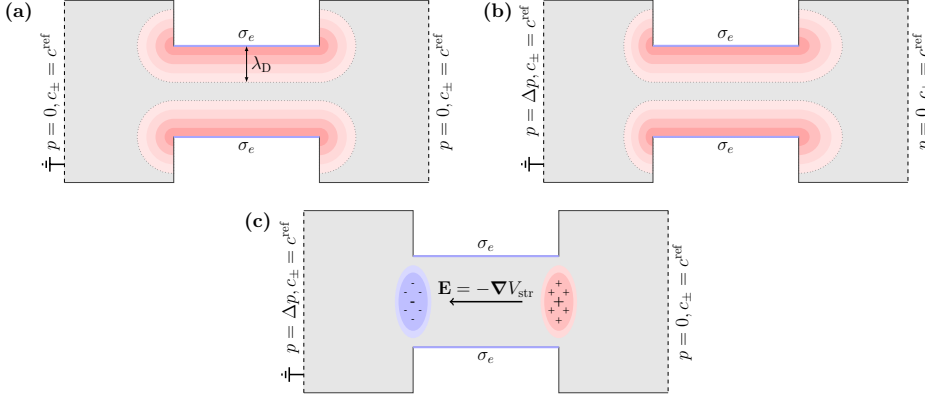
In many applications, a surface charge is prescribed instead of a surface potential. In the general nonlinear case, these are related through eq. (3.60). By using the surface-charge boundary condition  $\sigma_e = -\hat{\mathbf{n}} \cdot \mathbf{E}$  at the surface, we can obtain the Grahame equation,

$$\sigma_e = \frac{2\epsilon_0 \epsilon_r V_T}{\lambda_D} \sinh \left( \frac{\zeta}{2V_T} \right) = \sqrt{8k_B T \epsilon_0 \epsilon_r c^0} \sinh \left( \frac{\zeta}{2V_T} \right), \quad (3.62)$$

which relates the surface charge to the *surface potential*  $\zeta = \varphi_0 V_T$ , often referred to as the *zeta potential*.

### Streaming potential and the electroviscous effect

We now have a basic understanding of the electrokinetic effects present in the absence of fluid flow. A qualitative impression of the effect of coupling to fluid flow becomes apparent by inspecting fig. 3.3. Here, we consider a capillary of finite length, where a surface charge is applied to the capillary walls. In fig. 3.3 (a), there is no pressure difference between inlet and outlet, and hence, in equilibrium, the surface charge is screened by counterions. In fig. 3.3 (c) a pressure difference is applied across the system. In the steady state, the ion distributions are continuously advected by the velocity field,



which means that the electrical double layer is distorted and ions are moved away from the inlet side and spill out on the outlet side. This, as shown in fig. 3.3 (c) effectively induces a dipole moment and sets up an electric field  $\mathbf{E}$  due to the difference in net charge at each end. This electric field can be attributed to a streaming potential  $V_{\text{str}}$ , i.e.  $\mathbf{E} = -\nabla V_{\text{str}}$ . The associated electric field will act on the fluid, which has a net charge, effectively inhibiting the flow.

This effect can be quantified through the Helmholtz–Smoluchowski relation. For flow in an infinite cylindrical pore (oriented along  $z$ , with radius  $R$ ), it may heuristically be derived by considering symmetric binary electrolyte. Then, the total charge flux can be written using eqs. (3.46c), (3.46d) and (3.47):

$$\mathbf{J}_e = \rho_e \mathbf{u} - D \nabla \rho_e + K \mathbf{E}, \quad (3.63)$$

such that  $\partial_t \rho_e = \nabla \cdot \mathbf{J}_e$ . Here, we have identified the conductivity  $K = D z^2 q_e^2 (c_+ + c_-)/(k_B T)$ . Further, we assume the flux to be given by the Hagen–Poiseuille solution:

$$\mathbf{u} = u_z(r) \hat{\mathbf{z}} = \frac{f_z}{4\mu} (R^2 - r^2) \hat{\mathbf{z}}, \quad (3.64)$$

where  $f_z = -\partial p / \partial z + f_e$  is the total average driving force on the fluid, composed by the constant average pressure gradient,  $\partial p / \partial z$ , and the induced electric force,  $f_e$ . In the steady state, the cross sectional integral of  $\mathbf{J}_e$  must vanish, and so must the integral of the diffusive term; i.e. the second term on the right of eq. (3.63). By taking the cross-sectional integrals of eq. (3.63), we find

$$I_{\text{str}} + I_{\text{cond}} = 0, \quad (3.65)$$

where we have identified the streaming current  $I_{\text{str}}$  and the conducting current  $I_{\text{cond}}$  respectively as

$$I_{\text{str}} = 2\pi \int_0^R \rho_e(r) u_z(r) r dr \quad \text{and} \quad I_{\text{cond}} = 2\pi \int_0^R K E_z r dr \quad (3.66)$$

Within the realm of the linearized Poisson–Boltzmann equation (3.61), we may approximate  $c_+ + c_- \simeq 2c^0$  and thus  $K$  can be taken constant. Further, in the expression for  $I_{\text{str}}$ , we may introduce the new coordinate  $\xi = R - r$ , linearize the resulting expression in  $\xi$  (assuming  $\lambda_D \ll R$ ), insert eq. (3.46e) and integrate by parts. We thus obtain

$$I_{\text{str}} = -\frac{f_z \epsilon_0 \epsilon_r \zeta}{\mu} \quad \text{and} \quad I_{\text{cond}} = K E_z = \frac{2D z^2 q_e^2 c^0}{k_B T} E_z. \quad (3.67)$$

Using eqs. (3.58) and (3.65) we find

$$E_z = -\frac{\lambda_D^2 \zeta}{D \mu} f_z. \quad (3.68)$$

**FIGURE 3.3:** Streaming potential, electric double layer, and the electroviscous effect. Red indicates positive net charge, and blue indicates negative net charge. (a) The charge distribution in a model capillary with surface charges on the wall, where the pressure is the same at inlet and outlet. (b) Same as (a), but a pressure difference is imposed across the system, skewing the electric double layer. (c) The streaming potential effectively resulting from the skewed electrical double layers in (b). A net negative charge builds up to the left, and a net positive charge builds up to the right, which sets up an electric field counteracting fluid motion. (Courtesy of Asger Bolet.)

Using the fact that  $|f_e| \ll |f_z|$ , and the relation  $E_z = \partial V_{\text{str}} / \partial z$ , we find the Helmholtz-Smoluchowski relation:

$$\frac{\partial V_{\text{str}} / \partial z}{\partial p / \partial z} = -\frac{\lambda_D^2 \zeta}{\mu D}. \quad (3.69)$$

We are, however, interested in an approximation of the flow resistance in the capillary. Thus we retain eq. (3.68) and seek an approximation of  $f_e$ , i.e. we take the cross-sectional average over  $\mathbf{f}_e = -\rho_e \mathbf{E}$ :

$$f_e \simeq \frac{2}{R^2} \int_0^R \rho_e(r) E_z r \, dr \simeq 2E_z \frac{\epsilon_0 \epsilon_r \zeta}{R \lambda_D} = -\frac{2\epsilon_0 \epsilon_r \zeta^2}{D\mu} \frac{\lambda_D}{R} f_z, \quad (3.70)$$

where we have integrated by parts using eq. (3.46e), used the linearized Grahame eq. (3.62), and finally inserted eq. (3.68) in the last equality. Solving for  $f_z$ , we obtain

$$f_z = \frac{-\partial p / \partial z}{1 + \Xi}, \quad \text{where} \quad \Xi = \frac{2\epsilon_0 \epsilon_r \zeta^2}{D\mu} \frac{\lambda_D}{R}. \quad (3.71)$$

Clearly, the actual driving force that acts on the fluid in the capillary is *less* than the average pressure gradient,  $-\partial p / \partial z$ , since  $\Xi \geq 0$  on physical grounds. Now, interpreting this expression in terms of an effective *electric viscosity*  $\mu_e$  as a proportionality factor between flow rate and imposed pressure (see e.g. eq. (2.10)), gives the following relation:

$$\mu_e = (1 + \Xi)\mu, \quad (3.72)$$

which is larger than the viscosity in the absence of electrokinetic effects,  $\mu$ . While the derivation of eq. (3.72) was heuristic, it suffices to illustrate the *electroviscous effect*, which in practice quantifies the increased flow resistance due to surface charges and ions in solution. A more general version of eq. (3.72), using a more elaborate derivation with less restrictive assumptions, was presented by Rice and Whitehead<sup>[383]</sup> and later by Mansouri et al.<sup>[286, 287]</sup>. Here, e.g. the distortion of the velocity profile due to the electric force near the boundary is taken into account.

In Paper 4<sup>[58]</sup> (see also<sup>[57]</sup>), corresponding expressions to those in Refs.<sup>[286, 287]</sup> are found for plane Poiseuille flow. These expressions are mainly used for the purpose of validating a numerical code. Clearly, the assumption of infinitely long capillaries is highly idealized, and the results are expected to differ for finite and less ideal geometries. The main purpose of Paper 4<sup>[58]</sup> is to investigate electroviscous effects beyond those present in the simplest geometries—we will revisit these in section 5.3.

Much is known about electrical double layers at solid-fluid interfaces. However, at fluid-fluid interfaces double layers have been less studied, although an overview for oil–water interfaces can be found in<sup>[456]</sup>. Depending on the concentration, the Debye length  $\lambda_D$  can generally stretch from (roughly)  $10^{-10}$ – $10^{-6}$  m, meaning that the clear separation of scales which is usually the case in the study of droplets/two-phase flow is less clear here, since the EDL and the physical interface thickness *can* have comparable size.

### 3.4 TWO-PHASE ELECTROHYDRODYNAMICS

We now consider electrohydrodynamics in two phases. In this respect, we will first present the sharp-interface relations that we expect to hold when the interface thickness becomes vanishingly thin, and thereafter present the related phase-field modelling approach. We assume the single-phase description (3.46) to hold within the bulk of each fluid. At the interface, however, new conditions must be supplied.

#### 3.4.1 Sharp-interface conditions

The same continuity in the velocity field should hold as without any electric fields, namely  $[\mathbf{u}]_-^+ = 0$ . The stress balance at the interface changes from eq. (3.73), in that the electric stresses must be included:

$$[p]_-^+ \hat{\mathbf{n}}_{\text{int}} - [2\mu_i \mathbf{D}\mathbf{u}]_-^+ \cdot \hat{\mathbf{n}}_{\text{int}} - [\epsilon_0 \epsilon_{r,i} \mathbf{E} \otimes \mathbf{E} - \frac{1}{2} \epsilon_0 \epsilon_{r,i} |\mathbf{E}|^2 \mathbf{I}]_-^+ \cdot \hat{\mathbf{n}}_{\text{int}} = \gamma \kappa \hat{\mathbf{n}}_{\text{int}}, \quad (3.73)$$

where  $\mathbf{E} = -\nabla V$  is (still) the electric field. The Maxwell stress tensor,

$$\boldsymbol{\sigma}_M = \epsilon_0 \epsilon_{r,i} \mathbf{E} \otimes \mathbf{E} - \frac{1}{2} \epsilon_0 \epsilon_{r,i} |\mathbf{E}|^2 \mathbf{I} \quad (3.74)$$

is included in the above expression, and should balance the viscous and pressure forces at the interface. Here,  $\epsilon_{r,i}$  denotes the relative permittivity of phase  $i$ . Note that an osmotic contribution (see section 3.3) has been integrated in the definition of the pressure  $p$  above.

In general, the same ionic species  $j$  can be present in both phases, such that it can cross the interface. However, the ionic species will have a different solubility and diffusivity in the two phases. Similar to what is done with other phasic quantities, such as density and viscosity, the latter can be included by generalizing (i) the reference concentration  $c_j^{\text{ref}}$  to  $c_{j,i}^{\text{ref}}$ , denoting reference concentration of species  $j$  in phase  $i$ ; and (ii) the diffusivity  $D_j$  to  $D_{j,i}$ , denoting the diffusivity of species  $j$  in phase  $i$ .

Now, the missing pieces is the continuity of the electric potential  $V$  across the interface (in the absence of any accumulated charges) and the continuity of the normal component of the displacement field:

$$[V]_-^+ = 0, \quad \text{and} \quad \hat{\mathbf{n}}_{\text{int}} \cdot [\epsilon_{r,i} \mathbf{E}]_-^+ = 0. \quad (3.75)$$

Finally, the chemical potential  $g_{c_j}$  must be continuous across the interface:

$$[g_{c_j}]_-^+ = 0. \quad (3.76)$$

Using eqs. (3.46d), (3.75) and (3.76), the following relation is shown to hold at the interface:

$$\frac{c_j|_{x \rightarrow 0^+}}{c_j|_{x \rightarrow 0^-}} = \frac{c_{j,2}^{\text{ref}}}{c_{j,1}^{\text{ref}}}, \quad (3.77)$$

which gives a direct interpretation of the quantities involved at the right hand side. Alternatively, the quantities  $c_j$  can be related via a Henry jump condition<sup>[2]</sup>:

$$\frac{c_{j,2}^{\text{ref}}}{c_{j,1}^{\text{ref}}} = \exp \left( -\frac{\beta_{j,2} - \beta_{j,1}}{k_B T} \right), \quad (3.78)$$

where

$$\beta_{j,i} = -k_B T \ln \left( \frac{c_{j,i}^{\text{ref}}}{c^{\text{ref}}} \right) \quad (3.79)$$

can be interpreted physically as an energy penalty for dissolving species  $j$  in phase  $i$ , i.e. a *solubility energy*. In eq. (3.79),  $c^{\text{ref}}$  is an arbitrary global reference concentration (to make the units consistent). With eq. (3.79) inserted, eq. (3.46d) becomes

$$g_{c_j} = k_B T \ln \left( \frac{c_j}{c^{\text{ref}}} \right) + \beta_{j,i} + q_e z_j V. \quad (3.80)$$

The energetic approach to the solubility of a species in a phase differs from the approach by Berry et al.<sup>[43]</sup>, who, in their sharp-interface model, strictly assumed the ionic species to be confined to one of the phases. Nonetheless, such immiscibility can be captured efficiently with the energetic approach, as demonstrated e.g. in Refs.<sup>[263,264,301]</sup>.

### 3.4.2 Phase-field modelling

Campillo-Funollet et al.<sup>[79]</sup> presented an extension of the two-phase flow model by Abels et al.<sup>[2]</sup> (which was presented in the previous section), by including electrokinetic transport. The model is given by the following set of equations:

$$\rho(\phi)\partial_t \mathbf{u} + \mathbf{m} \cdot \nabla \mathbf{u} + \nabla p - \nabla \cdot (2\mu(\phi)\mathbf{D}\mathbf{u}) = -\phi\nabla g_\phi - \sum_{j=1}^N c_j \nabla g_{c_j}, \quad (3.81a)$$

$$\nabla \cdot \mathbf{u} = 0, \quad (3.81b)$$

$$\partial_t \phi + \mathbf{u} \cdot \nabla \phi = \nabla \cdot (M(\phi) \nabla g_\phi), \quad (3.81c)$$

$$g_\phi = \chi\gamma [\varepsilon^{-1}W'(\phi) - \varepsilon \nabla^2 \phi] + \sum_{j=1}^N \beta'_j(\phi) c_j - \frac{1}{2}\epsilon_0\epsilon_r'(\phi)|\nabla V|^2, \quad (3.81d)$$

$$\partial_t c_j + \mathbf{u} \cdot \nabla c_j = \nabla \cdot \left( \frac{D_j(\phi)c_j}{k_B T} \nabla g_{c_j} \right), \quad (3.81e)$$

$$g_{c_j} = k_B T \ln \left( \frac{c_j}{c_j^{\text{ref}}} \right) + \beta_j(\phi) + q_e z_j V, \quad (3.81f)$$

$$\nabla \cdot (\epsilon_0 \epsilon_r(\phi) \nabla V) = -\rho_e. \quad (3.81g)$$

Here, we have introduced interpolation functions for the diffusivities  $D_j$ , the solubility energies  $\beta_j$ , and the relative permittivities  $\epsilon_r(\phi)$ . For the diffusivity, both weighted arithmetic average (WAA) and the weighted geometric average (WGA) are viable options; see eq. (3.32) for their definitions. The advantage of using the latter, is that this prevents leakage of ions across the interface if the associated ionic diffusivity is much lower in one phase than in the other (see<sup>[263]</sup>). Further, it *strictly* does not allow negative values of the interpolated function (if  $|\phi| > 1$  numerically), which would lead to ill-posedness of the discretized problem. For the solubility energy  $\beta_j$  and the relative permittivity  $\epsilon_r$ , we use the WAA:

$$\beta_j(\phi) = \beta_{j,1} \frac{1+\phi}{2} + \beta_{j,2} \frac{1-\phi}{2}, \quad (3.82a)$$

$$\epsilon_r(\phi) = \epsilon_{r,1} \frac{1+\phi}{2} + \epsilon_{r,2} \frac{1-\phi}{2}. \quad (3.82b)$$

By considering the averaging eq. (3.82a) in terms of the reference concentration,  $c_j^{\text{ref}}$ , instead, using the definition (3.79) and eq. (3.82a), we find that

$$c_j^{\text{ref}}(\phi) = c^{\text{ref}} \exp \left( -\frac{\beta_j(\phi)}{k_B T} \right) = \left( c_{j,1}^{\text{ref}} \right)^{\frac{1+\phi}{2}} \cdot \left( c_{j,2}^{\text{ref}} \right)^{\frac{1-\phi}{2}}, \quad (3.83)$$

which is exactly a WGA, ideal for preserving the physically required positivity of  $c_j^{\text{ref}}$ . Choosing the arithmetic averages also simplifies the numerical treatment of the equations above, as the derivatives with respect to their arguments,  $\beta'_j$  and  $\epsilon'_r$ , simply become constants and do not require matrix assembly (in the finite element method, see section 4.1) at each time step.

Other choices for interpolating the permittivity have been reported in the literature. Tomar et al.<sup>[443]</sup> found, for their combined level-set/volume-of-fluid leaky-dielectric and perfect-dielectric models with smoothed interfacial properties, that a weighted harmonic average (WHA) gave more accurate computations of the electric field than what the

WAA did. However, for a model including free charges, López-Herrera et al.<sup>[274]</sup> found no evidence that WHA was superior.

The model stated in eq. (3.81) is a unification of the two-phase model eq. (3.26), and the single-phase electrohydrodynamics model eq. (3.46). The eqs. (3.81a) and (3.81b) are the incompressible Navier–Stokes equations with variable density, augmented by a body force that accounts for the interface forces *and* the chemical forces.<sup>23</sup> The eqs. (3.81c) and (3.81d) are the Cahn–Hilliard equations, where two new terms have been added in eq. (3.81d) due to the chemical transport, compared to the formulation without electrohydrodynamics, eq. (3.26d). These give, effectively, rise to new force contributions in the momentum eq. (3.81a). The third term in eq. (3.81d) gives an osmotic contribution, while the last term yields a Helmholtz force, which arises due to permittivity gradients. The eqs. (3.81e) to (3.81g) are the Poisson–Nernst–Planck system, where the permittivity and solubility now depends on the phase  $\phi$ .

<sup>23</sup> Accordingly, the pressure  $p$  is not the thermodynamic one here, either. But as before, for incompressible flow, it only imparts that care must be taken at the pressure boundaries.

Campillo-Funollet et al.<sup>[79]</sup> showed that the model reduced to the correct sharp-interface description in the limit  $\varepsilon \rightarrow 0$  by a matched asymptotic expansion. The same boundary conditions as for the pure two-phase problem, and the single-phase electrohydrodynamic problem, apply to this model.

### Free energy

Associated with the model (3.81), we have the free energy functional

$$\mathcal{F} = \mathcal{F}_u + \mathcal{F}_\phi + \mathcal{F}_w + \sum_{j=1}^N \mathcal{F}_{c_j} + \mathcal{F}_V. \quad (3.84)$$

Here,  $\mathcal{F}_u$  is given by eq. (3.40), the phase-field energy  $\mathcal{F}_\phi$  is given by eq. (3.38), and the fluid-solid interface energy is given by eq. (3.39). The chemical free energy (3.50) can be written in terms of the solubility energy  $\beta_j(\phi)$  as

$$\mathcal{F}_{c_j} = k_B T c_j \left[ \ln \left( \frac{c_j}{c_j^{\text{ref}}} \right) - 1 \right] + \beta_j(\phi) c_j, \quad (3.85)$$

while  $\mathcal{F}_V$  is given by eq. (3.51).

With the general GNBC boundary condition, the time evolution of the free energy can be written as

$$\begin{aligned} \frac{d\mathcal{F}}{dt} = & - \int_{\Omega} \left[ 2\mu(\phi)|\mathbf{Du}|^2 + M(\phi)|\nabla g_\phi|^2 + \sum_{j=1}^N \frac{D_j c_j}{k_B T} |\nabla g_{c_j}|^2 \right] \\ & - \int_{\partial\Omega} [l(\phi)|\mathbf{u}|^2 + \Gamma|L[\phi]|^2]. \end{aligned} \quad (3.86)$$

Thus, the model is dissipative.

### Comparison to other models

Several authors have noted the need to connect the electrokinetic description of two-phase flow to the leaky-dielectric description<sup>[396,399,445,483]</sup>. Taylor's original assumption<sup>[436]</sup> was to impose an instantaneous steady-state charge distribution in the system, neglecting the diffusive and convective contributions and the continuity of the displacement field. Through the solution of the Poisson eq. (3.81g), this gives rise to charge accumulation at the interface. Melcher and Taylor<sup>[299]</sup> reviewed the latter model, and included in their updated model the effect of convection of charges located at the interface.

Baygents and Saville<sup>[32]</sup> outlined the analysis of how electrokinetic effects could alter the leaky-dielectric results. Zholkovskij et al.<sup>[483]</sup> considered the electrokinetic description for two phases, and assumed that no solute could be adsorbed to the interface. They obtained an expression for infinitesimal droplet deformation under a weak field approximation, which was shown to reduce to the leaky-dielectric result<sup>[436]</sup> in the limit of vanishingly thin Debye layers, and to the perfect dielectric result<sup>[8,345]</sup> in the opposite limit. Schnitzer and Yariv<sup>[399]</sup> considered a binary electrolyte and included rates for the adsorption of charges at the interface, meaning that a net charge would generally accumulate there in a steady-state. They showed rigorously that the model using for electrokinetics for each phase, in the limit of strong fields and thin Debye layers, reduced to the original model of Taylor<sup>[436]</sup>. In particular, the convection of charge at the interface was found to be insignificant to the lowest order in their expansion.

In the model (3.81), ions are not allowed to be adsorbed *at* the interface, although they may accumulate in thin layers on either side. It is possible that a phase contrast in  $\beta_j$  could suffice to model these effects. On the other hand, using ideas from the related topic of surfactants—molecules that tend to stick to the interface and change the surface tension<sup>[135,438]</sup>—it may be possible to extend the model to incorporate this effect.

Several phase-field models for soluble surfactants have been proposed, see e.g.<sup>[3,4,7,133,161,439]</sup>. Engblom et al.<sup>[133]</sup> discuss well-posedness of such models derived from a variational principle, i.e. as a gradient flow. A surfactant species can be included in the model by endowing the surfactant concentration  $\psi$  with the free energy functional

$$\mathcal{F}_\psi = \int_{\Omega} \left\{ k_B T \left[ \psi \ln \left( \frac{\psi}{\psi_{\max}} \right) + (\psi_{\max} - \psi) \ln \left( 1 - \frac{\psi}{\psi_{\max}} \right) \right] + \psi \beta_\psi(\phi) \right\} \quad (3.87)$$

where  $\psi_{\max}$  is a maximum concentration such that  $\psi \in [0, \psi_{\max}]$ , and the solubility energy is given by

$$\beta_\psi(\phi) = -A_\psi \frac{(1 - \phi^2)^2}{4} + B_\psi \frac{\phi^2}{4}. \quad (3.88)$$

Here, the first term on the right hand side is a smooth approximation of a Dirac delta function centered at the interface, which makes it energetically favorable to dissolve surfactants there. Conversely, the last term penalises the presence of surfactant in either of the pure phases. The coefficients  $A_\psi, B_\psi$  are related to the adsorption rates. The resulting chemical potential (assuming non-ionic surfactants) is given by

$$g_\psi = k_B T \ln \frac{\psi}{\psi_{\max} - \psi} + \beta_\psi(\phi), \quad (3.89)$$

The dynamics is analogous to how chemical transport occurs:

$$\partial_t \psi_j + \mathbf{u} \cdot \nabla \psi_j = \nabla \cdot (M_\psi \nabla g_\psi), \quad (3.90)$$

except that the mobility is modelled as  $M_\psi(\psi) = M_{\psi,0}\psi(1 - \psi)$ . This was shown in<sup>[133]</sup> to yield the Langmuir adsorption isotherm. In precursor work of<sup>[133]</sup>, Van der Sman and Van der Graaf<sup>[451]</sup> showed that the Langmuir equation of state for the *measured* surface tension  $\gamma'$ ,

$$\gamma' - \gamma \sim k_B T \ln \left[ 1 - \frac{\psi}{\psi_{\max}} \right], \quad (3.91)$$

where  $\gamma$  is the equilibrium surface tension entering into the model, could be obtained with appropriately chosen coefficients.

For discussions on alternative phase-field models with soluble and insoluble surfactants, see e.g.<sup>[3,4,7,161]</sup>. Note also that in a similar manner as above, increased interface

conductivity can be modeled by supplementing the interpolation function  $D_j(\phi)$  with a similar delta function term at the interface as above.

In the review by Saville<sup>[396]</sup>, chemical reactions are an integral part to how the author arrives at the macroscopic model for electrohydrodynamics. Chemical reactions can trivially be included in the model, as was done originally by Campillo-Funollet et al.<sup>[79]</sup>. In Paper 5<sup>[265]</sup>, a single-phase model with reactions is considered. The formulation Saville<sup>[396]</sup> ends up with is of a leaky-dielectric type, except that net charge is described by a conservation law of the type

$$\partial_t \rho_e + \mathbf{u} \cdot \nabla \rho_e = \nabla \cdot (K(\phi) \nabla V), \quad (3.92)$$

where  $K$  is the conductivity. A corresponding phase-field model was presented by Eck et al.<sup>[128]</sup>, albeit a diffusive term was included for numerical purposes. As mentioned, such a model can be rigorously<sup>[399]</sup> derived from the full electrokinetic model (3.81) above, but the procedure is fairly cumbersome. Here, we do it instead heuristically by linearising the concentrations around  $c^{\text{ref}}$ , i.e.

$$c_j = c^{\text{ref}} + \delta c_j, \quad (3.93)$$

and truncating at the lowest order, assuming a weak electric field, which gives

$$\partial_t \delta c_j + \mathbf{u} \cdot \nabla \delta c_j = \nabla \cdot \left[ D_j(\phi) \nabla \delta c_j + \frac{D_j q_e z_j c^{\text{ref}}}{k_B T} \nabla V \right]. \quad (3.94)$$

Assuming  $D_j(\phi) = D(\phi)$  for all  $j$ , we multiply eq. (3.94) by  $q_e z_j$ , sum over  $j$  and obtain

$$\partial_t \rho_e + \mathbf{u} \cdot \nabla \rho_e = \nabla \cdot [D(\phi) \nabla \rho_e + K(\phi) \nabla V] \quad (3.95)$$

where we have identified the conductivity as  $K(\phi) = D(\phi) q_e^2 c^{\text{ref}} (k_B T)^{-1} \sum_{j=1}^N z_j^2$  (cf. eq. (3.63) and the expression there for  $K$ ). In this picture,  $\rho_e$  can be seen as a single chemical species associated with a modified free energy density  $\propto \rho_e^2$ . In the limit where we can neglect convection and diffusion, i.e. assume instantaneous steady-state, we obtain the following Laplace equation:

$$\nabla \cdot [K(\phi) \nabla V] = 0, \quad (3.96)$$

which yields  $V$  directly, and replaces all solute transport. This constitutes the leaky-dielectric approximation.

A phase-field model for leaky dielectrics was proposed by Lin et al.<sup>[258]</sup>, constituted by the normal phase-field equations, supplied by force terms in the momentum equation, due to the permittivity and conductivity gradients in the two phases. The electric gradient terms were only included in the momentum equation, not in the chemical potential, and hence the model is further from being thermodynamically consistent than that of Eck et al.<sup>[128]</sup>. However, such terms in the phase-field chemical potential can lead to  $O(\varepsilon)$  deviations from the pure phase values  $\phi = \pm 1$ <sup>[133,311]</sup> (also curved interfaces may lead to this<sup>[479]</sup>). A possible mitigation strategy is to omit the additional terms in the phase-field equation, but include them in the momentum equation—a consequence being that the model loses its dissipative property. However, as mentioned earlier, it is not clear whether the thermodynamic consistency for unphysically large interface widths poses a significant advantage with regards to convergence to the correct sharp-interface description, apart from being advantagous when constructing numerical schemes<sup>[403,404]</sup>.

### 3.4.3 Electrokinetic scaling of the equations

For both analytical and numerical purposes, it is useful to limit the problem to involving as few parameters as possible. Thus, we now nondimensionalize the equations, focusing in particular on the model (3.81) which also covers the special cases of single-phase electrohydrodynamics and pure two-phase flow. Dimensionless versions of physical variables are marked by a tilde, while reference values are marked with an asterisk (see also<sup>[263,264]</sup>). We let  $\tilde{t} = t/t^*$ ,  $\tilde{\rho} = \rho/\rho^*$ ,  $\tilde{\mathbf{u}} = \mathbf{u}/u^*$ ,  $\tilde{p} = p/p^*$ ,  $\tilde{\mu} = \mu/\mu^*$ ,  $\tilde{c}_j = c_j/c^*$ ,  $\tilde{V} = V/V^*$ ,  $\tilde{D}_{\pm} = D_{\pm}/D^*$ ,  $\tilde{\epsilon} = \epsilon_r/\epsilon^*$ , and  $\tilde{\gamma} = \gamma/\gamma^*$ . The spatial dimensions are scaled by a reference linear size  $R^*$ , such that  $\tilde{\mathbf{x}} = \mathbf{x}/R^*$ . The electrostatic potential  $V$  is scaled by a thermal voltage (cf. eq. (3.58)),

$$V^* = V_T = \frac{k_B T}{q_e}, \quad (3.97a)$$

while all other reference values are given by

$$t^* = \frac{R^*}{u^*}, \quad \rho^* = \frac{q_e c^* V_T}{(u^*)^2}, \quad D^* = u^* R^*, \quad p^* = q_e c^* V_T, \quad (3.97b)$$

$$\mu^* = \frac{q_e c^* V_T R^*}{u^*}, \quad \epsilon^* = \frac{q_e c^* (R^*)^2}{\epsilon_0 V_T}, \quad \gamma^* = q_e c^* V_T R^*. \quad (3.97c)$$

Altogether, this represents an invertible set of relations between the physical and dimensionless variables. Now, adopting the dimensionless variables and subsequently omitting the tildes, yields the model (3.81) with  $q_e = k_B T = 1$  and  $\epsilon_0 \epsilon_r \rightarrow \epsilon$ . This represents a simplification to the equations where the same physics is contained, which will be taken advantage of in the next section.

# 4

## NUMERICAL METHODOLOGY

---

For all geometries but the very simplest ones, computational methods must be employed to solve the governing equations. In particular, the problems under scrutiny must be discretized both in space and time. This chapter gives an overview of the numerical methodology employed in this project. We will first introduce the finite element method, which is the main spatial discretization strategy used. Secondly, we consider temporal discretization strategies. In particular, we propose a general numerical scheme that is applicable to most of the systems in this thesis. Thereafter, we present methods for the simplified case of single-phase flow. Finally, we present an overview of the numerical software *employed* and *developed* in this work.

### 4.1 THE FINITE ELEMENT METHOD

The finite element method (FEM) is a popular and efficient method for solving partial differential equations (PDEs) in arbitrary geometries. The method relies on discretizing the domain by dividing it into simpler, finite elements. In contrast to finite difference and finite volume methods, that typically seek to find discrete approximations to the *equations* that are to be solved, the FEM consists in approximating the *solution* itself. This is achieved using calculus of variations, and by expressing an approximate solution as a linear combination of basis functions that are compactly supported on the elements. In the FEM, the original PDE is converted into a weak formulation, which, by using the Galerkin method, can be turned into a linear system of equations. The Galerkin method provides a solution that minimizes an error residual between the approximate solution, found by the finite basis, and the true solution. The finite element method works on linear PDEs, but by appropriate linearization and iterated solutions (Newton or Picard iteration) it can be straightforwardly adapted to solve nonlinear problems.

We shall illustrate the above concepts with an exemplary problem. For a more thorough and technical introduction into the theory of FEM, the reader is referred to standard textbooks on the topic (e.g. [67,132,172]).

A fairly general PDE relevant to many of the PDEs described in this thesis,<sup>24</sup> can be stated in the following form. Find  $u \in \mathcal{U}$  such that

$$\mathcal{D}u \stackrel{\text{def}}{=} -\alpha u + \nabla \cdot (\mathbf{w}(\mathbf{x})u + k(\mathbf{x})\nabla u) = f(\mathbf{x}), \quad \text{for } \mathbf{x} \in \Omega, \quad (4.1)$$

$$u = f_D(\mathbf{x}), \quad \text{for } \mathbf{x} \in \partial\Omega_D, \quad (4.2)$$

$$\hat{\mathbf{n}} \cdot \nabla u = f_N(\mathbf{x}), \quad \text{for } \mathbf{x} \in \partial\Omega_N. \quad (4.3)$$

Here,  $\mathcal{U}$  is the function space where the solution  $u$  lives, and the fields  $\mathbf{w}(\mathbf{x})$ ,  $k(\mathbf{x})$ ,  $f(\mathbf{x})$  are taken only to depend on the spatial variable  $\mathbf{x} \in \Omega \subset \mathbb{R}^d$ , and not on  $u$ , while  $\alpha$  is a constant. The subdomains  $\partial\Omega_D$  and  $\partial\Omega_N$  denote, respectively, the Dirichlet and Neumann parts of the boundary  $\partial\Omega$  of the domain  $\Omega$ . We also let  $\hat{\mathbf{n}} \cdot \mathbf{w}(\mathbf{x}) = 0$  on  $\partial\Omega$ .

The inner product of two fields will be used recurrently in the forthcoming. It is denoted by  $(\bullet, \bullet)$ , and can be taken between a pair of scalars  $a, b$ ; vectors  $\mathbf{a}, \mathbf{b}$ ; or tensors

<sup>24</sup> For example, when  $\alpha, \mathbf{w}$  vanish, eq. (4.1) reduces to the Poisson equation, which arises many places in this work (Gauss' law for electrostatics, Darcy flow, pressure correction). Then,  $k$  is analogous to a space dependent permittivity/permeability and  $f$  is a space-dependent source term. It is also easy to see how eq. (4.1) can be turned into a temporally discretized advection-diffusion-reaction equation.

**A, B**—related to the integral over the domain  $\Omega$  respectively by

$$(a, b) = \int_{\Omega} ab, \quad (\mathbf{a}, \mathbf{b}) = \int_{\Omega} \mathbf{a} \cdot \mathbf{b}, \quad (\mathbf{A}, \mathbf{B}) = \int_{\Omega} \mathbf{A} : \mathbf{B}. \quad (4.4)$$

Now, we can find the variational form of eq. (4.1), by considering  $u$  as a *trial function* and multiplying eq. (4.1) by the *test function*  $v$  it and integrating over the domain,

$$(\mathcal{D}u, v) = -\alpha(u, v) - (\mathbf{w}u, \nabla v) - (k\nabla u, \nabla v) + \int_{\partial\Omega_N} kf_N v = (f, v), \quad (4.5)$$

where we have integrated by parts and inserted eq. (4.3). Note that Equation (4.5) holds for any  $v$ .

The discretized domain  $\Omega_h$  approximates the true domain  $\Omega$ , and consists of a *tesselation* of  $N_{\text{el}}$  finite elements  $\Omega_i$ , such that

$$\Omega_h = \bigcup_{i=1}^{N_{\text{el}}} \Omega_i. \quad (4.6)$$

These elements can be typically simplicials; i.e. triangles (2D) and tetrahedra (3D); but other shapes, such as quadrilaterals (2D) and hexahedra (3D), are also common<sup>[132]</sup>. Here, we will primarily be concerned with simplicials. These unit cells share vertices, edges, and faces (in 3D) with their neighbouring elements. An exemplary discretized two-dimensional domain is shown in fig. 4.1 (a). The discretized domain is usually called a mesh, and is typically unstructured. In the following, we consider a mesh with  $N_{\text{vert}}$  vertices,  $N_{\text{edge}}$  edges, and  $N_{\text{el}}$  elements.

We shall now briefly discuss ways of constructing a set of basis functions  $\varphi_j$  from the discretized mesh, i.e. which discrete function spaces the solution should belong to. The most common elements belong to the  $P_k$  family ( $k$  times differentiable), e.g.:<sup>25</sup>

$P_0$  — Piecewise constant basis functions. (Note that these may be of limited use alone as their derivative is zero.)

$P_1$  — Piecewise linear basis functions.

$P_2$  — Piecewise quadratic basis functions.

Generally,  $P_{k-1}$  elements yield  $k^{\text{th}}$  order spatial convergence. Using a  $P_0$  basis yields a set of  $N_{\text{el}}$  basis functions, while  $P_1$  yields  $N_{\text{vert}}$  basis functions.  $P_2$  elements have ‘nodal’ values also at the middle of each edge, such that a polynomial of order 2 can be uniquely fixed<sup>[132]</sup>, and thus contain  $N_{\text{vert}} + N_{\text{edge}}$  basis functions. In the  $P_k$  family, the basis functions are chosen such that  $\varphi_j(\mathbf{x}_i) = \delta_{ij}$  where  $\mathbf{x}_j$  are the positions of these nodes. An example of a single basis function from the common piecewise linear  $P_1$  element, is shown in fig. 4.1 (b). Note that the set of such ‘hat functions’ for all nodes constitutes the  $P_1$  basis for this domain. The generalization to three dimensions is straightforward, but harder to visualize.

We shall here employ a set of basis functions  $\varphi_i, i \in \{1, \dots, n\}$ , which in principle could represent all of the above elements. In the following, we use the Einstein convention, summing over repeated indices.

An approximation to the solution  $u$  of eq. (4.1) can be written as a linear combination of the basis functions:

$$u \simeq \hat{u} = U_i \varphi_i(\mathbf{x}), \quad (4.7)$$

where  $U_i$  are the hitherto unknown coefficients in this expansion. The Galerkin method now imparts letting the test functions belong to the same function space as  $\hat{u}$ . Thus,

$$v \simeq \hat{v} = V_i \varphi_i(\mathbf{x}). \quad (4.8)$$

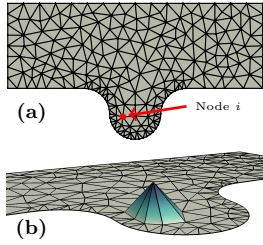


FIGURE 4.1: The finite element method in two dimensions. (a) Illustration of a discretized domain, i.e. a triangular mesh. (b) The  $P_1$  ‘hat function’  $\varphi_i$  associated with node  $i$  indicated in (a). The maximum of  $\varphi_i(\mathbf{x})$  is  $\varphi_i(\mathbf{x}_i) = 1$ , where  $\mathbf{x}_i$  is the location of node  $i$ .

<sup>25</sup> See also<sup>[19]</sup> or <https://www.femtable.org> for an overview of finite elements.

Now, we can insert these into the terms in eq. (4.5) to obtain

$$(\hat{u}, \hat{v}) = (\phi_i, \phi_j) U_i V_j, \quad (4.9a)$$

$$(\mathbf{w}\hat{u}, \nabla\hat{v}) = (\mathbf{w}\phi_i, \nabla\phi_j) U_i V_j, \quad (4.9b)$$

$$(k\nabla\hat{u}, \nabla\hat{v}) = (k\nabla\phi_i, \nabla\phi_j) U_i V_j, \quad (4.9c)$$

$$\int_{\partial\Omega_N} k f_N v = \int_{\partial\Omega_N} k f_N \phi_j V_j, \quad (4.9d)$$

$$(f, v) = (f, \phi_j) V_j. \quad (4.9e)$$

Since eq. (4.5) should hold for any  $\hat{v}$ , the equations resulting from inserting eq. (4.9) should be independent of the choice of  $V_j$ . Thus, eq. (4.5) becomes

$$\alpha(\phi_i, \phi_j) U_i + (\mathbf{w}\phi_i, \nabla\phi_j) U_i + (k\nabla\phi_i, \nabla\phi_j) U_i = \int_{\partial\Omega_N} k f_N \phi_j - (f, \phi_j), \quad (4.10)$$

We now define the matrix

$$\mathbf{A} = [A_{ij}], \quad \text{where } A_{ij} = \alpha(\phi_i, \phi_j) + (\mathbf{w}\phi_i, \nabla\phi_j) + (k\nabla\phi_i, \nabla\phi_j), \quad (4.11)$$

where the three contributing terms represent, respectively, the mass matrix, the advection matrix and the stiffness matrix. Further, the right hand side can be written as

$$\mathbf{b} = [b_j], \quad \text{where } b_j = \int_{\partial\Omega_N} k f_N \phi_j - (f, \phi_j), \quad (4.12)$$

and the vector of unknowns can be written as  $\mathbf{U} = [U_i]$ . Thus, eq. (4.10) becomes

$$\mathbf{AU} = \mathbf{b}, \quad (4.13)$$

which must be solved for  $\mathbf{U}$ . The numerical calculation of the elements of the matrix  $\mathbf{M}$  and right hand side vector  $\mathbf{b}$  in eq. (4.13), is called to *assemble* the system. In terms of computationa, this process can often be comparatively costly to solving the matrix system<sup>[320]</sup>.

### Mixed elements

It should be noted that to represent a PDE of order  $2k$ , one would expect that a discretized function space of (at least) order  $k$  is necessary, as this is the best balancing between trial and test functions that can be achieved by successive integration by parts. In the present work, this is particularly relevant for the fourth order phase-field equation, see eqs. (3.26c) and (3.26d). However, low-order elements can be used by introducing an auxiliary field, and employing *mixed* elements. For example, solving the equation

$$\nabla^4 u = f, \quad (4.14)$$

for  $u$  (with appropriate boundary conditions), would intuitively correspond to the following variational problem: Find  $u \in \mathcal{U}$  such that

$$(\nabla^2 u, \nabla^2 v) = (f, v), \quad (4.15)$$

for all  $v \in \mathcal{U}$ . Instead, one can introduce the auxiliary variable  $g = \nabla^2 w$ , which turns eq. (4.14) into

$$\nabla^2 u = g, \quad \nabla^2 g = f. \quad (4.16)$$

The corresponding variational form becomes: Find  $(u, g) \in \mathcal{U}' \times \mathcal{G}'$  such that

$$(\nabla u, \nabla v) = -(g, v), \quad (\nabla g, \nabla h) = -(f, h), \quad (4.17)$$

for all  $(v, h) \in \mathcal{U}' \times \mathcal{G}'$ . Here, the discrete approximations to the subspaces  $\mathcal{U}'$  and  $\mathcal{G}'$  can be of lower order than the approximation to the function space  $\mathcal{U}$  in eq. (4.15). It is then a trivial task to turn eq. (4.17) into a matrix equation of the form eq. (4.13).

### 4.1.1 Solvers and preconditioners

Having assembled the system, as stated in the form (4.13), the task is now to isolate the vector  $\mathbf{U}$  with as little computation—or as quickly—as possible. This is in general a task for numerical linear algebra routines. The most robust methods solve this *directly* (using lower–upper (LU) decomposition or Gaussian elimination). However, this is highly memory consuming for large systems and does not scale well with the number of unknowns. Better results are therefore achieved with methods that can exploit the structure of  $\mathbf{A}$ .

Since the basis functions have compact support, they are typically only nonzero in a small neighbourhood of a given node or element. Thus the involved inner products are predominantly zero, i.e., the resulting matrix  $\mathbf{M}$  is very sparse. Moreover, the bulk of the nonzero entries are found close to the diagonal.

Such matrix structures are often suitable for use with *iterative* Krylov subspace methods. It is not within the scope of this thesis to enter into the technical theory on Krylov subspaces and sequences—the interested reader is referred to literature on the field, e.g.<sup>[387]</sup>. We will only briefly outline some of the most popular methods. For symmetric, positive definite systems, the conjugate gradient (CG) method<sup>[188]</sup> is typically the optimal method. For symmetric systems, the minimal residual (MinRes) method<sup>[349]</sup> is a viable option. For less restrictive requirements to the system matrices, the more robust generalized minimal residual (GMRES) method<sup>[388]</sup>, or the biconjugate gradient stabilized (BiCGSTAB) method<sup>[452]</sup> can be used.

For these methods to converge, it is essential to use good *preconditioners*. This basically amounts to multiplying both sides of eq. (4.13) by a matrix  $\mathbf{P} \simeq \mathbf{A}^{-1}$  (the inverse of  $\mathbf{A}$ ) to bring the system matrix closer to the identity matrix, or, generally make the system easier to solve. Common preconditioning techniques include Jacobi preconditioning, algebraic multigrid (AMG), incomplete LU factorization (ILU), and successive over-relaxation (SOR). The choice of an appropriate preconditioner also depends on the choice of linear solver, and for large-scale applications, it is fundamental to access parallel implementations of the preconditioner–solver pair. A thorough overview of preconditioners and linear solvers, with emphasis on fluid-mechanical problems, can be found in the book by Elman et al.<sup>[132]</sup>.

### 4.1.2 Comparison to other methods

The main advantage of using the finite element method (FEM) is its versatility. The method is not restricted to a specific physical problem, and is intrinsically suited for a wide variety of physical models and problems. This includes elasticity and solid mechanics (where it originates from), advection and diffusion, fluid flow, and many more. Further, the method is not limited to specific mesh structures, but is formulated in terms of general discretized domains. This is in contrast to finite difference (FDM) and finite volume methods (FVM), which typically rely on structured meshes or grids. It is possible to extend FDM and FVM to unstructured grids, but it is not as intuitive as for the FEM<sup>[172]</sup>. In particular, FEM formulations on structured meshes often become equivalent to FDM or FVM stencils. Further, implicit or semi-implicit versions of all three problems typically reduce to solving a linear system of equations<sup>[241]</sup>. Gresho and Sani<sup>[172], sec. 1.7</sup> provide an interesting discussion on the relation between FEM and FVM.

Another advantage of the FEM is that it straightforwardly allows to construct numerical schemes where certain stability properties can be shown. In particular, implicit and semi-implicit schemes can be constructed with ease by using finite differences in time. Moreover, enforcing Neumann (or even Robin) boundary conditions in a FEM is straightforward, as they enter directly in the weak formulation. This is, e.g., particularly

useful for imposing contact angle boundary conditions in phase-field simulations.

Progress in recent years indicate that for incompressible flow, the finite element method is fully competitive with FVM<sup>[320]</sup> in terms of computational performance. Compared to the lattice Boltzmann method (LBM), FEM solves the actual PDEs while the LBM approximates them using kinetic theory. If steady-state solutions are sought, implicit or semi-implicit schemes are preferred, as larger time steps are allowed. For turbulent flow, however, the time-step restrictions may be of lesser importance, and explicit methods such as the LBM (where all interactions are local) may be advantageous for parallel scalability. However, unbiased comparisons of the various methods for a representative spectrum of problems, is in general hard to find. In part, it is also a question of implicit versus explicit methods. Implicit methods are more stable, but also tend to smear out the solution more; i.e. they are more dissipative. For other applications, such as for compressible flow, the FVM is possibly still more mature than the FEM<sup>[395]</sup>. The unstructured lattice Boltzmann method (ULBM) represents an extension of LBM to unstructured meshes, opening the way for the same geometric flexibility as found with the FEM (or FVM). However, the velocities must typically be interpolated on the unstructured meshes by using FVM or FEM methods, and thus the method loses some of its advantages.

Finally, it should be mentioned that the choice of basis functions in the Galerkin method need not be limited to the compactly supported functions employed in the FEM. In simple geometries with a high degree of symmetry, such as periodic channels, pipes, and fully periodic geometries, spectral (and spectral Galerkin) methods yield superior accuracy and efficiency. For example, Lee and Moser<sup>[250]</sup> presented direct numerical simulations of plane channel flow at impressively high Reynolds number using a Fourier basis in the streamwise and spanwise directions and a B-spline collocation method in the wall-normal direction. Another option is the use a Chebyshev basis in the wall-normal direction, see e.g.<sup>[319]</sup>. However, these methods cannot be easily adapted to more complicated geometries. An alternative, conceptually halfway between these two approaches is the spectral element method (which is used e.g. in the CFD code NEK5000<sup>[152]</sup>) but that shall not be evaluated here.

For two-phase flow simulations, including front-tracking, level-set, volume-of-fluid and phase-field methods, it is also possible to combine different methods. The methods typically need some Navier–Stokes solver to advect the fluids, but are not dependent on which method is used for this purpose. For example, Campillo-Funollet et al.<sup>[79]</sup> used a FVM on a dual grid to solve the convective terms, while using FEM on the diffusive terms; thus taking advantage of the strengths of both methods.

Having discussed spatial discretization strategies, we now proceed to temporal discretization strategies, which are often independent of the spatial method. In particular, we consider finite-difference integration in time.

## 4.2 A NUMERICAL SCHEME FOR TRANSIENT FLOW

To apply the models considered herein to realistic time-dependent problems, reliable time-discretization schemes are needed. The models covered in this thesis concern, in a general sense, the incompressible Navier–Stokes equations, in many cases coupled to external fields. The latter fields are either an arbitrary number of concentration fields, or a single phase field.

We can state the models in the following compact form:

$$\rho \partial_t \mathbf{u} + \mathbf{m} \cdot \nabla \mathbf{u} - \nabla \cdot [2\mu \mathbf{D}\mathbf{u}] + \nabla p = - \sum_{i=0}^N \psi_i \nabla g_i, \quad (4.18)$$

$$\nabla \cdot \mathbf{u} = 0, \quad (4.19)$$

$$\partial_t \psi_i + \mathbf{u} \cdot \nabla \psi_i - \nabla \cdot (K_i \nabla g_i) = 0, \quad (4.20)$$

$$\nabla \cdot (\varepsilon \nabla V) = -\rho_e, \quad (4.21)$$

with appropriate boundary conditions, where  $\psi_i$  are the transported scalar fields, i.e. the collection of all phase and concentration fields,

$$\psi_i = \begin{cases} \phi & \text{for } i = 0, \\ c_i & \text{for } i \in \{1, \dots, N\}. \end{cases} \quad (4.22)$$

The associated chemical potentials can be written as the general functionals

$$g_i = g_i[\{\psi_j\}_{j=0}^N, V] = \begin{cases} g_\phi & \text{for } i = 0, \\ g_{c_i} & \text{for } i \in \{1, \dots, N\}. \end{cases} \quad (4.23)$$

and the generalized mobilities can be defined by

$$K_i = \begin{cases} M(\phi) & \text{for } i = 0, \\ D_i(\phi)c_i & \text{for } i \in \{1, \dots, N\}. \end{cases} \quad (4.24)$$

The advecting momentum  $\mathbf{m}$  is, as before, given by eq. (3.29), such that the total density evolution can be written as

$$\partial_t \rho + \nabla \cdot \mathbf{m} = 0. \quad (4.25)$$

The coupled problem of fluid flow, transport of scalar fields, and electrostatics, is in general a hard problem to solve numerically. It is thus beneficial to split the problem into multiple substeps. Here, we separate out the fluid flow problem from the scalar transport, while still being able to prove the same energy stability property that is associated with the continuous problem.

As unconditionally stable schemes of second or higher temporal order still seems lacking for two-phase flow with unmatched density, we will consider the following temporally first-order scheme. In particular, the splitting between velocity and pressure, as seen below, introduces an  $O(\tau)$  error. The method is of arbitrary order in space, as it depends on the chosen finite element basis.

We will first present the step solving for the scalar fields, including the electric field, and subsequently the hydrodynamics step will be considered. We assume here for brevity that the dynamic boundary condition with no-slip (3.36), although the extension to a generalized Navier boundary condition (GNBC) (3.35) is straightforward (e.g. along the lines of<sup>[5]</sup>). To simplify the notation, we use the electrokinetic scaling of the model (3.81) outlined in section 3.4.3.

We consider schemes that use finite elements in space, and finite differences in time. Thus, we consider a discrete time step  $\tau$ , and denote for conciseness the first-order discrete time derivative by

$$\partial_\tau^- \mathcal{A}^k \stackrel{\text{def}}{=} \frac{\mathcal{A}^k - \mathcal{A}^{k-1}}{\tau}. \quad (4.26)$$

Finally, we use the shorthand notation that when a general quantity  $\mathcal{A}$  is evaluated at a timestep  $k$ , it is denoted by  $\mathcal{A}^k$ , e.g.,  $\mathcal{A}^k = \mathcal{A}(\phi^k)$ .

For completeness, we define the following finite element subspaces:

$$\mathbf{U}_h = (U_h)^d \quad \text{where} \quad U_h = \{v \in H^1(\Omega)\} \quad \text{for velocity,} \quad (4.27\text{a})$$

$$P_h = \{p \in L_0^2(\Omega)\} \quad \text{for pressure,} \quad (4.27\text{b})$$

$$\Phi_h = \{\phi \in H^1(\Omega)\} \quad \text{for scalar fields,} \quad (4.27\text{c})$$

$$G_h = \{g \in H^1(\Omega)\} \quad \text{for chemical potentials,} \quad (4.27\text{d})$$

$$\mathcal{U}_h = \{V \in H^1(\Omega)\} \quad \text{for the electrostatic potential.} \quad (4.27\text{e})$$

#### 4.2.1 Scalar transport step

The scalar transport step is given by the following discrete problem at each time step  $k$ . Assume that  $\psi_0^{k-1}, \dots, \psi_N^{k-1}, g_0^{k-1}, \dots, g_N^{k-1}, V^{k-1}, \mathbf{u}^{k-1}, p^{k-1}$  are given. Then, using eqs. (4.22) and (4.23), solve:

$$\partial_{\tau}^{-} \psi_j^k + \nabla \cdot (\mathbf{u}^* \psi_j^{k-1}) = \nabla \cdot (K_j^{k-1} \nabla g_j^k), \quad (4.28\text{a})$$

$$g_{\phi}^k = \chi \gamma \left[ \varepsilon^{-1} \overline{W'} - \varepsilon \nabla^2 \phi^k \right] + \sum_j \frac{\partial \beta_j}{\partial \phi} \bar{c}_j - \frac{1}{2} \frac{\partial \epsilon}{\partial \phi} |\nabla V^k|^2, \quad (4.28\text{b})$$

$$g_{c_j}^k = \bar{\alpha}' + \bar{\beta}_j + z_j V^k, \quad (4.28\text{c})$$

$$\nabla \cdot (\varepsilon^k \nabla V^k) = -\rho_e^k. \quad (4.28\text{d})$$

Here,

$$\mathbf{u}^* = \mathbf{u}^{k-1} - \frac{\tau}{\rho^{k-1}} \sum_j \psi_j^{k-1} \nabla g_j^k \quad (4.29)$$

is a forward-projected velocity, building on an idea by Minjeaud<sup>[305]</sup>. Moreover, we have introduced the following discretizations:

$\overline{W'}$  – A discrete approximation of the derivative of the Ginzburg–Landau double well potential,  $W'(\phi)$ , see eq. (3.28). Here, a convex-concave decomposition  $W(\phi) = W_+(\phi) - W_-(\phi)$  is used (see e.g.<sup>[404]</sup>):

$$\overline{W'} = W'_+(\phi^k) - W'_-(\phi^{k-1}) \quad (4.30)$$

where  $W_+(\phi) = (1 + \phi^4)/4$  and  $W_-(\phi) = \phi^2/2$ .

$\overline{f_w'}$  – A discrete approximation of the derivative of the wall energy interpolation function. Here, it is given by

$$\overline{f_w'} = \frac{1}{4} \left[ 3 - (\phi^k)^2 - \phi^k \phi^{k-1} - (\phi^{k-1})^2 \right]. \quad (4.31)$$

$\bar{c}_j$  – interpolated concentration  $\bar{c}_j = \omega c_j^k + (1 - \omega) c_j^{k-1}$ , where  $\omega \in [0, 1]$  is an arbitrary weighting coefficient.

$\bar{\beta}_j$  – interpolated solubility energy,  $\bar{\beta}_j = (1 - \omega) \beta_j^k + \omega \beta_j^{k-1}$ .

$\overline{\alpha'}$  – An approximation of the derivative of a generalized chemical energy  $\alpha(c)$ ; we use

$$\overline{\alpha'} = \alpha'(c_j^k) = \ln c_j^k, \quad (4.32)$$

where the last equality holds for standard Nernst–Planck transport.

These discretizations have been made in this way to satisfy a discrete energy dissipation law, which we will show in the coming sections.

### Weak form

For a finite-element implementation, a weak form of the above scheme must be found. The following variational problem corresponds to the scheme (4.28).  
Find  $(\psi_0^k, \dots, \psi_N^k, g_0^k, \dots, g_N^k, V^k) \in \Phi_h^{N+1} \times G_h^{N+1} \times \mathcal{U}_h$  such that

$$\left( \partial_\tau^- \psi_j^k, \xi_j \right) - \left( \mathbf{u}^* \psi_j^{k-1}, \nabla \xi_j \right) + \left( K_j^{k-1} \nabla g_j^k, \nabla \xi_j \right) = 0, \quad (4.33a)$$

$$\begin{aligned} \left( g_\phi^k, h_0 \right) &= \chi \gamma \varepsilon^{-1} (\overline{W'}, h_0) + \chi \gamma \varepsilon \left( \nabla \phi^k, \nabla h_0 \right) \\ &\quad + \int_{\partial\Omega} [\gamma \cos(\theta_{\text{eq}}) \overline{f'_w} + \Gamma^{-1} \partial_\tau^- \phi] h_0 \\ &\quad + \sum_j \left( \frac{\partial \beta_j}{\partial \phi} \bar{c}_j, h_0 \right) - \left( \frac{1}{2} \frac{\partial \epsilon}{\partial \phi} |\nabla V^k|^2, h_0 \right), \end{aligned} \quad (4.33b)$$

$$\left( g_{c_j}^k, h_j \right) = (\overline{\alpha'}, h_j) + (\overline{\beta}_j, h_j) + (z_j V^k, h_j), \quad (4.33c)$$

$$\left( \varepsilon^k \nabla V^k, \nabla U \right) = \left( \rho_e^k, U \right) + \int_{\partial\Omega} \sigma_e U, \quad (4.33d)$$

for all test functions  $(\xi_0, \dots, \xi_N, g_0, \dots, g_N, U) \in \Phi_h^{N+1} \times G_h^{N+1} \times \mathcal{U}_h$ .

#### 4.2.2 Fluid flow step

To solve the Navier–Stokes equations with a non-constant density, many approaches exist, specifically solving for velocity and pressure either in a coupled or in a decoupled manner. The present method is based on a decoupled *fractional-step* method, which has its roots back to the seminal works of Chorin<sup>[92,93]</sup>. The fluid flow step consists of three substeps: *velocity prediction*, *pressure correction*, and *velocity correction*. They are given in the following.

Assume that the scalar transport step (4.28) has been carried out, and thus

$$\psi_0^k, \dots, \psi_N^k, g_0^k, \dots, g_N^k, V^k, \mathbf{u}^{k-1}, p^{k-1}$$

are given. Then, carry out the following substeps.

- 1. Tentative velocity step:** Solve the following problem for the tentative velocity step  $\tilde{\mathbf{u}}^k$ .

$$\begin{aligned} \rho^{k-1} \frac{\tilde{\mathbf{u}}^k - \mathbf{u}^{k-1}}{\tau} + (\mathbf{m}^{k-1} \cdot \nabla) \tilde{\mathbf{u}}^k - \nabla \cdot (2\mu^k \mathbf{D}\tilde{\mathbf{u}}^k) + \nabla p^{k-1} \\ + \frac{1}{2} \tilde{\mathbf{u}}^k \left[ \partial_\tau^- \rho^k + \nabla \cdot \mathbf{m}^{k-1} \right] = - \sum_i \psi_i^{k-1} \nabla g_i^k, \end{aligned} \quad (4.34a)$$

with the Dirichlet boundary condition  $\tilde{\mathbf{u}}^k = \mathbf{0}$  on  $\partial\Omega$ . Here we have used

$$\mathbf{m}^k = \rho^k \mathbf{u}^k - \rho'(\phi) M^k \nabla g_\phi^k. \quad (4.34b)$$

Note also the presence of the last term in the right hand side of eq. (4.34a), which is an approximation of  $\mathbf{0}$ , cf. eq. (4.25). It is needed to satisfy a discrete energy law, as will be shown below.

2. **Pressure correction step:** Solve the following problem for the pressure  $p^k$ .

$$\frac{1}{\rho_0} \nabla^2 (p^k - p^{k-1}) = \frac{1}{\tau} \nabla \cdot \tilde{\mathbf{u}}^k, \quad (4.34c)$$

where  $\rho_0 = \min(\rho_1, \rho_2)$ . Here the artificial Neumann condition  $\mathbf{n} \cdot \nabla(p^k - p^{k-1}) = 0$  should be enforced.

3. **Velocity correction step:** To obtain the corrected velocity  $\mathbf{u}^k$ , solve

$$\rho^k \frac{\mathbf{u}^k - \tilde{\mathbf{u}}^k}{\tau} = -\nabla \left( p^k - p^{k-1} \right), \quad (4.34d)$$

with the Dirichlet boundary condition  $\mathbf{u}^k = \mathbf{0}$  on  $\partial\Omega$ .

*Weak form*

The following variational problem corresponds to the scheme (4.34) above.

1. *Tentative velocity step:* Find  $\tilde{\mathbf{u}}^k \in \mathbf{U}_h$  such that for all  $\mathbf{v} \in \mathbf{U}_h$ ,

$$\begin{aligned} & \left( \rho^{k-1} \frac{\tilde{\mathbf{u}}^k - \mathbf{u}^{k-1}}{\tau}, \mathbf{v} \right) + \left( (\mathbf{m}^{k-1} \cdot \nabla) \tilde{\mathbf{u}}^k, \mathbf{v} \right) + \left( 2\mu^k \mathbf{D}\tilde{\mathbf{u}}^k, \mathbf{D}\mathbf{v} \right) \\ & - \left( p^{k-1}, \nabla \cdot \mathbf{v} \right) + \frac{1}{2} \left( \tilde{\mathbf{u}}^k \partial_\tau \rho^k, \mathbf{v} \right) - \frac{1}{2} \left( \mathbf{m}^{k-1}, \nabla(\tilde{\mathbf{u}}^k \cdot \mathbf{v}) \right) \\ & = - \sum_i \left( \psi_i^{k-1} \nabla g_i^k, \mathbf{v} \right), \end{aligned} \quad (4.35a)$$

with the Dirichlet boundary condition  $\tilde{\mathbf{u}}^k = \mathbf{0}$  on  $\partial\Omega$ .

2. *Pressure correction step:* Find  $p^k \in P_h$  such that for all  $q \in P_h$ , we have

$$\left( \frac{1}{\rho_0} \nabla(p^k - p^{k-1}), \nabla q \right) = -\frac{1}{\tau} \left( \nabla \cdot \tilde{\mathbf{u}}^k, q \right). \quad (4.35b)$$

3. *Velocity correction step:* Find  $\mathbf{u}^k \in \mathbf{U}_h$  such that for all  $\mathbf{v} \in \mathbf{U}_h$ ,

$$\left( \rho^k \frac{\mathbf{u}^k - \tilde{\mathbf{u}}^k}{\tau}, \mathbf{v} \right) = \left( p^k - p^{k-1}, \nabla \cdot \mathbf{v} \right), \quad (4.35c)$$

which we solve by explicitly imposing the Dirichlet boundary condition  $\mathbf{u}^k = \mathbf{0}$  on  $\partial\Omega$ .

This completes the numerical time discretization scheme. Some remarks are in order:

- At each time step, the scalar transport equations (section 4.2.1) need to be solved *before* the hydrodynamic equations (section 4.2.2).
- The scalar transport equations (4.28) (or (4.33)) are *at least* weakly coupled through  $V^k$  and need to be solved simultaneously.
- Multiplying eq. (4.34d) by  $\tau/\rho^k$ , taking the divergence, and using eq. (4.34c), yields:

$$\nabla \cdot \mathbf{u}^k = \tau \nabla \cdot \left[ \left( \frac{1}{\rho_0} - \frac{1}{\rho^k} \right) \nabla \left( p^k - p^{k-1} \right) \right], \quad (4.36)$$

i.e., the scheme admits a small  $O(\tau^2)$  compressibility in the corrected velocity field. This might, however, stabilize the spatial method; see the discussion in section 4.3.

### 4.2.3 Energy stability

We now set out to show that there is a discrete energy law associated with the given scheme.

We start with the hydrodynamic part. First, we note that, using eq. (4.29), eq. (4.35a) can be written as

$$\begin{aligned} & \left( \rho^{k-1} \frac{\tilde{\mathbf{u}}^k - \mathbf{u}^*}{\tau}, \mathbf{v} \right) + \left( (\mathbf{m}^{k-1} \cdot \nabla) \tilde{\mathbf{u}}^k, \mathbf{v} \right) + \left( 2\mu^k \mathbf{D}\tilde{\mathbf{u}}^k, \mathbf{D}\mathbf{v} \right) \\ & - \left( p^{k-1}, \nabla \cdot \mathbf{v} \right) + \frac{1}{2} \left( \tilde{\mathbf{u}}^k \partial_\tau^- \rho^k, \mathbf{v} \right) - \frac{1}{2} \left( \mathbf{m}^{k-1}, \nabla(\tilde{\mathbf{u}}^k \cdot \mathbf{v}) \right) = 0. \end{aligned} \quad (4.37)$$

We let  $\mathbf{v} = \tilde{\mathbf{u}}^k$  in eq. (4.37):

$$\begin{aligned} & \frac{1}{2\tau} \left[ \left\| \sqrt{\rho^k} \tilde{\mathbf{u}}^k \right\|^2 - \left\| \sqrt{\rho^{k-1}} \mathbf{u}^* \right\|^2 \right] + \left\| \sqrt{2\mu^k} \mathbf{D}\tilde{\mathbf{u}}^k \right\|^2 - \left( p^{k-1}, \nabla \cdot \tilde{\mathbf{u}}^k \right) \\ & = -\frac{1}{2\tau} \left\| \sqrt{\rho^{k-1}} (\tilde{\mathbf{u}}^k - \mathbf{u}^*) \right\|^2, \end{aligned} \quad (4.38)$$

and test eq. (4.29) with  $\rho^{k-1} \mathbf{u}^* / \tau$ :

$$\begin{aligned} & \frac{1}{2\tau} \left\| \sqrt{\rho^{k-1}} \mathbf{u}^* \right\|^2 - \frac{1}{2\tau} \left\| \sqrt{\rho^{k-1}} \mathbf{u}^{k-1} \right\|^2 \\ & = - \sum_j \left( \psi_j^{k-1} \nabla g_j^k, \mathbf{u}^* \right) - \frac{1}{2\tau} \left\| \sqrt{\rho^{k-1}} (\mathbf{u}^* - \mathbf{u}^{k-1}) \right\|^2. \end{aligned} \quad (4.39)$$

Further, we let  $q = -\tau p^k$  in eq. (4.35b):

$$\left( \nabla \cdot \tilde{\mathbf{u}}^k, p^k \right) = -\frac{\tau}{2\rho_0} \left[ \left\| \nabla p^k \right\|^2 - \left\| \nabla p^{k-1} \right\|^2 + \left\| \nabla(p^k - p^{k-1}) \right\|^2 \right], \quad (4.40)$$

and put  $\mathbf{v} = \tilde{\mathbf{u}}^k$  in eq. (4.35c):

$$\frac{1}{2\tau} \left\| \sqrt{\rho^k} \mathbf{u}^k \right\|^2 - \frac{1}{2\tau} \left\| \sqrt{\rho^k} \tilde{\mathbf{u}}^k \right\|^2 - \frac{1}{2\tau} \left\| \sqrt{\rho^k} (\mathbf{u}^k - \tilde{\mathbf{u}}^k) \right\|^2 = \left( p^k - p^{k-1}, \nabla \cdot \tilde{\mathbf{u}}^k \right). \quad (4.41)$$

From eq. (4.34d), we find

$$\left\| \sqrt{\rho^k} (\mathbf{u}^k - \tilde{\mathbf{u}}^k) \right\|^2 = \tau^2 \left\| \frac{1}{\sqrt{\rho^k}} \nabla(p^k - p^{k-1}) \right\|^2. \quad (4.42)$$

Combining eqs. (4.38) to (4.42) we obtain:

$$\begin{aligned} \partial_\tau^- \mathcal{F}_{\mathbf{u}}^k = & - \left\| \sqrt{2\mu^k} \mathbf{D}\tilde{\mathbf{u}}^k \right\|^2 - \frac{1}{2\tau} \left\| \sqrt{\rho^{k-1}} (\tilde{\mathbf{u}}^k - \mathbf{u}^*) \right\|^2 - \frac{1}{2\tau} \left\| \sqrt{\rho^{k-1}} (\mathbf{u}^* - \mathbf{u}^{k-1}) \right\|^2 \\ & - \frac{\tau}{2} \left\| \sqrt{\frac{1}{\rho_0} - \frac{1}{\rho^k}} \nabla(p^k - p^{k-1}) \right\|^2 - \sum_j \left( \psi_j^{k-1} \nabla g_j^k, \mathbf{u}^* \right), \end{aligned} \quad (4.43)$$

where we have identified the *discrete* kinetic energy,

$$\mathcal{F}_{\mathbf{u}}^k = \frac{1}{2} \left\| \sqrt{\rho^k} \mathbf{u}^k \right\|^2 + \frac{\tau^2}{2\rho_0} \left\| \nabla p^k \right\|^2, \quad (4.44)$$

which contains an additional  $O(\tau^2)$  compressibility term compared to its continuous counterpart, eq. (3.40).

Now, we consider the evolution of the scalar fields. In the general case, eq. (4.33a) becomes, using  $\xi_j = g_j^k$ :

$$\left( \partial_\tau^- \psi_j^k, g_j^k \right) - \left( \mathbf{u}_j^* \psi_j^{k-1}, \nabla g_j^k \right) = - \left\| \sqrt{K_j^{k-1}} \nabla g_j^k \right\|^2. \quad (4.45)$$

For the phase field, we find, using  $h_0 = \partial_\tau^- \phi^k$  in eq. (4.33b):

$$\begin{aligned} \left( g_\phi^k, \partial_\tau^- \phi^k \right) &= \chi \gamma \varepsilon^{-1} \left( \overline{W'}, \partial_\tau^- \phi^k \right) + \chi \gamma \varepsilon \left( \nabla \phi^k, \nabla \partial_\tau^- \phi^k \right) + \partial_\tau^- \mathcal{F}_w^k \\ &+ \int_{\partial\Omega} [\Gamma^{-1} |\partial_\tau^- \phi|^2] + \sum_j \left( \bar{c}_j, \partial_\tau^- \beta_j^k \right) - \left( \frac{1}{2} |\nabla V^k|^2, \partial_\tau^- \epsilon^k \right). \end{aligned} \quad (4.46)$$

Here we have used that

$$\overline{f'_w} \partial_\tau^- \phi^k = \frac{1}{\tau} \left[ f_w(\phi^k) - f_w(\phi^{k-1}) \right], \quad (4.47)$$

and identified the discrete fluid-solid interface energy (cf. eq. (3.39)),

$$\mathcal{F}_w^k = \int_{\partial\Omega} \left[ \gamma_2 + \gamma \cos \theta_{eq} f_w(\phi^k) \right]. \quad (4.48)$$

Now, note that both  $W_\pm(\phi)$  are convex functions, i.e.  $W''_\pm(\phi) \geq 0$  for all  $\phi$ . By Taylor expansion, we find, using the mean value theorem,

$$W_+(\phi^k) = W_+(\phi^{k-1}) + W_+(\phi^k)(\phi^k - \phi^{k-1}) - \frac{1}{2}(\phi^k - \phi^{k-1})^2 W''_+(\bar{\phi}_+), \quad (4.49a)$$

$$W_-(\phi^k) = W_-(\phi^{k-1}) + W_-(\phi^{k-1})(\phi^k - \phi^{k-1}) + \frac{1}{2}(\phi^k - \phi^{k-1})^2 W''_-(\bar{\phi}_-), \quad (4.49b)$$

for some  $\bar{\phi}_\pm \in [\min(\phi^{k-1}, \phi^k), \max(\phi^{k-1}, \phi^k)]$ . We thus find

$$\left( \overline{W'}, \partial_\tau^- \phi^k \right) = \left( W'_+(\phi^k) - W'_-(\phi^{k-1}), \phi^k - \phi^{k-1} \right) \quad (4.50)$$

$$= \int_{\Omega} [W(\phi^k) - W(\phi^{k-1})] + \Delta W, \quad (4.51)$$

where  $\Delta W = \frac{1}{2}(\phi^k - \phi^{k-1})^2 (W''_+(\bar{\phi}_+) + W''_-(\bar{\phi}_-)) \geq 0$ . We also find that

$$\left( \nabla \phi^k, \nabla \partial_\tau^- \phi^k \right) = \frac{1}{2\tau} \left\| \nabla \phi^k \right\|^2 - \frac{1}{2\tau} \left\| \nabla \phi^{k-1} \right\|^2 + \frac{1}{2\tau} \left\| \nabla (\phi^k - \phi^{k-1}) \right\|^2. \quad (4.52)$$

For the chemical potential for the ions, we let  $h_j = \partial_\tau^- c_j^k$  in eq. (4.33c):

$$\left( g_{c_j}^k, \partial_\tau^- c_j^k \right) = \left( \overline{\alpha'}, \partial_\tau^- c_j^k \right) + \left( \bar{\beta}_j, \partial_\tau^- c_j^k \right) + \left( z_j V^k, \partial_\tau^- c_j^k \right), \quad (4.53)$$

where we find that

$$\left( \overline{\alpha'_j}, \partial_\tau^- c_j^k \right) = \int_{\Omega} \left[ \alpha_j(c_j^k) - \alpha_j(c_j^{k-1}) + \Delta \alpha_j \right] \quad (4.54)$$

where  $\bar{c}_j \in [\min(c_j^{k-1}, c_j^k), \max(c_j^{k-1}, c_j^k)]$  and the last term,  $\Delta \alpha_j = \frac{1}{2} \alpha''_j(\bar{c}_j)(c_j^k - c_j^{k-1})^2$  is non-negative since  $\alpha''_j(c) \geq 0$  for all  $c$ .

From eq. (4.33d) we find

$$\left( \varepsilon^k \nabla V^k, \nabla V^k \right) = \left( \rho_e^k, V^k \right) + \int_{\partial\Omega} \sigma_e V^k, \quad (4.55)$$

$$\left( \varepsilon^{k-1} \nabla V^{k-1}, \nabla V^k \right) = \left( \rho_e^{k-1}, V^k \right) + \int_{\partial\Omega} \sigma_e V^k, \quad (4.56)$$

which gives

$$\left( \varepsilon^k \nabla V^k - \varepsilon^{k-1} \nabla V^{k-1}, \nabla V^k \right) = \sum_j z_j \left( c_j^k - c_j^{k-1}, V^k \right). \quad (4.57)$$

Combining eqs. (4.45), (4.46), (4.51) to (4.54) and (4.57), and summing over  $j$  where appropriate, we obtain

$$\begin{aligned} \partial_\tau^- \left[ \mathcal{F}_\phi^k + \mathcal{F}_w^k + \sum_j \mathcal{F}_{c_j}^k + \mathcal{F}_V^k \right] &= \sum_j \left( \mathbf{u}_j^* \psi_j^{k-1}, \nabla g_j^k \right) - \sum_j \left\| \sqrt{K_j^{k-1}} \nabla g_j^k \right\|^2 \\ &\quad - \int_{\partial\Omega} [\Gamma^{-1} |\partial_\tau^- \phi|^2] - \int_\Omega \chi \gamma \varepsilon^{-1} \Delta W - \frac{\chi \gamma \varepsilon}{2\tau} \left\| \nabla (\phi^k - \phi^{k-1}) \right\|^2 \\ &\quad - \frac{1}{2\tau} \left\| \sqrt{\epsilon^{k-1}} (\nabla V^k - \nabla V^{k-1}) \right\|^2 - \sum_j \int_\Omega \Delta \alpha_j \end{aligned} \quad (4.58)$$

where we have used

$$\left( \bar{c}_j, \partial_\tau^- \beta_j^k \right) + \left( \bar{\beta}_j, \partial_\tau^- c_j^k \right) = \frac{1}{\tau} \left[ \beta_j^k c_j^k - \beta_j^{k-1} c_j^{k-1} \right], \quad (4.59)$$

and identified the following discrete free energy expressions:

$$\mathcal{F}_\phi^k = \chi \gamma \left[ \int_\Omega \varepsilon^{-1} W(\phi^k) + \frac{\varepsilon}{2} \left\| \nabla \phi^k \right\|^2 \right] \quad (4.60)$$

$$\mathcal{F}_{c_j}^k = \int_\Omega \left[ \alpha_j(c_j^k) + \beta_j^k c_j^k \right] \quad (4.61)$$

$$\mathcal{F}_V^k = \frac{1}{2} \left\| \sqrt{\epsilon^k} \nabla V^k \right\|^2. \quad (4.62)$$

These are the discrete counterparts of eqs. (3.38), (3.50) and (3.51), respectively.

Now, we are in a position to combine the above results. Summing eqs. (4.43) and (4.58), we obtain

$$\begin{aligned} \partial_\tau^- \mathcal{F}^k &= - \sum_j \left\| \sqrt{K_j^{k-1}} \nabla g_j^k \right\|^2 - \left\| \sqrt{2\mu^k} \mathbf{D}\tilde{\mathbf{u}}^k \right\|^2 - \int_{\partial\Omega} [\Gamma^{-1} |\partial_\tau^- \phi|^2] \\ &\quad - \int_\Omega \chi \gamma \varepsilon^{-1} \Delta W - \frac{\chi \gamma \varepsilon}{2\tau} \left\| \nabla (\phi^k - \phi^{k-1}) \right\|^2 - \frac{1}{2\tau} \left\| \sqrt{\epsilon^{k-1}} (\nabla V^k - \nabla V^{k-1}) \right\|^2 \\ &\quad - \sum_j \int_\Omega \Delta \alpha_j - \frac{1}{2\tau} \left\| \sqrt{\rho^{k-1}} (\tilde{\mathbf{u}}^k - \mathbf{u}^*) \right\|^2 \\ &\quad - \frac{1}{2\tau} \left\| \sqrt{\rho^{k-1}} (\mathbf{u}^* - \mathbf{u}^{k-1}) \right\|^2 - \frac{\tau}{2} \left\| \sqrt{\frac{1}{\rho_0} - \frac{1}{\rho^k}} \nabla (p^k - p^{k-1}) \right\|^2 \end{aligned} \quad (4.63)$$

where we have identified the total discrete energy,

$$\mathcal{F}^k = \mathcal{F}_\mathbf{u}^k + \mathcal{F}_\phi^k + \mathcal{F}_w^k + \sum_j \mathcal{F}_{c_j}^k + \mathcal{F}_V^k. \quad (4.64)$$

We observe that all terms on the right hand side of eq. (4.63) are negative; hence  $\partial_\tau^- \mathcal{F}^k \leq 0$ , i.e. a discrete counterpart of eq. (3.86) is satisfied. Comparing eqs. (3.86) and (4.63), we also note that only the three first terms in eq. (4.63) are present in eq. (3.86); the rest of the terms in eq. (4.63) represent numerical dissipation and are at least of order  $O(\tau)$ .

#### 4.2.4 Discussion

An advantage of using the above scheme is that it is highly *decoupled*: The hydrodynamic computation is decoupled from the scalar transport, and within the hydrodynamic subproblem, the computation of the velocity is decoupled from the pressure computation. This is achieved by a fractional step method, based on Chorin's method<sup>[92,93]</sup> and similar to that presented in<sup>[404]</sup> for pure two-phase flow. As noted, the method introduces a small numerical compressibility, see eq. (4.36), which also serves to stabilize the problem with regard to the Babuska–Brezzi criterion (see section 4.3 below). Furthermore, the discrete energy inequality, which is also an important property of the continuous version of the model, serves to limit the energy blowup that is often associated with the sharp gradients typically present in two-phase flow. The functional can possibly be used to prove convergence of the numerical scheme in the same way as done by Shen and Yang<sup>[404]</sup> for the case of pure two-phase flow, and more recently by Metzger<sup>[301]</sup> for a similar scheme to this.

A main disadvantage of this scheme is that all scalar fields must be solved simultaneously, and additionally, it requires using a nonlinear solver, for the discrete energy law to be satisfied. This may impart a FEM problem that is not necessarily easy to precondition and solve. Alternatively, a fully linear scheme where all nonlinear terms above are linearised around the variables at time step  $k - 1$  (and higher order terms are omitted) is presented in Paper 6<sup>[263]</sup>. Although free energy dissipation, as represented by eq. (4.63), can then not be guaranteed, the problem could be split between (i) computing the phase field, (ii) computing the chemical transport, and (iii) hydrodynamics. For the resulting subproblems (i) and (iii) there are efficient and robust solvers that can be used. For (ii) it has proven harder to solve the equations, in particular when the electric fields are so strong that we are well into the nonlinear electrokinetic regime ( $V \gtrsim V_T$ ).

Another disadvantage, compared to solving *all* equations (including hydrodynamics) simultaneously—i.e. using a fully implicit scheme—is that the operator splitting imparts an explicit inclusion of the advective velocity. This introduces a restriction on how large time steps can be used for the scheme to remain stable, governed by the Courant–Friedrichs–Lowy (CFL) criterion. Again, however, it is not straightforward to find robust and efficient preconditioners and solvers for this problem, and fully implicit schemes are also affiliated with excessive numerical dissipation.

Finally, we propose here a way to provide efficient energy-stable simulations, i.e. solving for the scalar transport values simultaneously. Within the scalar transport subproblem, the following Picard iteration should be carried out at each time step  $k$ .

1. Let the tentative variables  $\hat{\phi}_0^k = \phi^{k-1}$ ,  $\hat{V}_0^k = V^{k-1}$ ,  $\hat{c}_{j,0}^k = c_j^{k-1}$ , and let  $i = 1$ .
2. Solve the phase field equations linearized around  $\hat{\phi}_i^k$ , and obtain the tentative value  $\hat{\phi}_{i+1}^k$ .
3. Solve the electrostatic problem with the newly obtained  $\hat{\phi}_{i+1}^k$ , and obtain  $\hat{V}_{i+1}^k$ .
4. Solve the chemical transport problem with the new  $\hat{\phi}_{i+1}^k$ ,  $\hat{V}_{i+1}^k$ , and obtain  $\hat{c}_{j,i+1}^k$ .
5. Compute

$$\mathcal{E}_{i+1}^k = \sqrt{\left\| \hat{\phi}_{i+1}^k - \hat{\phi}_i^k \right\|^2 + \left\| \hat{V}_{i+1}^k - \hat{V}_i^k \right\|^2 + \sum_j \left\| \hat{c}_{j,i+1}^k - \hat{c}_{j,i}^k \right\|^2}. \quad (4.65)$$

If  $\mathcal{E}_{i+1}^k < \text{tol}$ , where tol is some tolerance, assign  $\phi^k = \hat{\phi}_{i+1}^k$ ,  $V^k = \hat{V}_{i+1}^k$ ,  $c_j^k = \hat{c}_{j,i+1}^k$ , and proceed to the next time step  $k + 1$ . Otherwise, increase  $i \leftarrow i + 1$  and go to step 2.

Steps 2–4 above are fairly standard procedures, as they require solving a sequence of decoupled linear equations. Nevertheless, when applicable, a Newton solver would converge in fewer iterations. However, with the iteration scheme above, effective reuse of matrices could be permitted in a finite element method, as outlined e.g. in<sup>[320]</sup> for a pure single-phase case, and in<sup>[119]</sup> for a two-phase model.

#### 4.2.5 Pure single-phase schemes

Now we consider the flow of a *pure* single-phase fluid, i.e. the flow is not coupled to any additional scalar fields. The scheme above reduces to the classical Chorin scheme when applied to a single-phase case, where  $\rho, \mu$  are taken to be constant. Then, the numerical problem reduces to sequentially solving

$$\rho \left( \frac{\tilde{\mathbf{u}}^k - \mathbf{u}^{k-1}}{\tau} + \mathbf{u}^{k-1} \cdot \nabla \tilde{\mathbf{u}}^k \right) - \mu \nabla^2 \tilde{\mathbf{u}}^k + \nabla p^{k-1} = \mathbf{0}, \quad (4.66a)$$

$$\nabla^2(p^k - p^{k-1}) = \frac{\rho}{\tau} \nabla \cdot \tilde{\mathbf{u}}^k, \quad (4.66b)$$

$$\rho \frac{\mathbf{u}^k - \tilde{\mathbf{u}}^k}{\tau} = -\nabla(p^k - p^{k-1}). \quad (4.66c)$$

Here, the first and last equations should be solved with the no-slip boundary condition,  $\tilde{\mathbf{u}}^k = \mathbf{0}$  and  $\mathbf{u}^k = \mathbf{0}$ , respectively. The pressure correction equation is typically solved with the artificial boundary condition  $\hat{\mathbf{n}} \cdot \nabla(p^k - p^{k-1}) = 0$ . A temporally second-order version of Chorin's method can be found by a modification of the above equations (4.66) to arrive at the following fractional step scheme<sup>[320]</sup>:

$$\rho \left( \frac{\tilde{\mathbf{u}}^k - \mathbf{u}^{k-1}}{\tau} + \mathbf{u}_{AB}^{k-1/2} \cdot \nabla \tilde{\mathbf{u}}_{CN}^{k-1/2} \right) - \mu \nabla^2 \tilde{\mathbf{u}}_{CN}^{k-1/2} + \nabla p^* = \mathbf{0}, \quad (4.67a)$$

$$\nabla^2(p^{k-1/2} - p^*) = \frac{\rho}{\tau} \nabla \cdot \tilde{\mathbf{u}}^k, \quad (4.67b)$$

$$\rho \frac{\mathbf{u}^k - \tilde{\mathbf{u}}^k}{\tau} = -\nabla(p^{k-1/2} - p^*) \quad (4.67c)$$

Here,  $\tilde{\mathbf{u}}_{CN}^{k-1/2} = (\tilde{\mathbf{u}}^k + \mathbf{u}^{k-1})/2$  is the Crank–Nicolson interpolated velocity, and  $\mathbf{u}_{AB}^{k-1/2} = (3\mathbf{u}^{k-1} - \mathbf{u}^{k-2})/2$  is the Adams–Bashforth projected convecting velocity. Equations (4.67a) and (4.67b) are solved in an inner loop, where, before each iteration,

<sup>26</sup> The initial  $p^{k-1/2}$  can be assigned by e.g. a projection  $p^{k-1/2} \leftarrow 2p^{k-3/2} - p^{k-5/2}$ . Hence, this scheme is called an incremental pressure correcting scheme (IPCS). A convergence criterion based on  $\|p^{k-1/2} - p^*\|$ , or a desired maximum number of iterations, is typically set. See also the review by Langtangen et al.<sup>[241]</sup> for an overview of methods for incompressible single-phase flow.

Assuming the inner loop is solved with high accuracy, such that  $p^* = p^{k-1/2}$ , we obtain from eq. (4.67c) that  $\tilde{\mathbf{u}}^k = \mathbf{u}^k$ . Inserting these expressions into eq. (4.67a), testing with  $\mathbf{u}_{CN}^k = \tilde{\mathbf{u}}_{CN}^k = (\mathbf{u}^k + \mathbf{u}^{k-1})/2$ , and as usual using the no-slip condition, we obtain

$$\frac{1}{2\tau} \rho \|\mathbf{u}^k\|^2 - \frac{1}{2\tau} \rho \|\mathbf{u}^{k-1}\|^2 = -\|2\mu \mathbf{D} \mathbf{u}_{CN}^{k-1/2}\|^2, \quad (4.68)$$

where we have also used that  $\nabla \cdot \mathbf{u}_{CN}^k = 0$ . Comparing to the first-order counterpart (4.43) (letting  $\mathbf{u}^* = \mathbf{u}^{k-1}$  and  $\rho^k = \rho$  and disregarding chemical potential terms) it is clear that the second-order scheme is less dissipative, while still retaining the sought energy stability. It is tempting to pursue such a direction for two-phase flow with density contrast, solute transport and electric fields, and it is trivial to construct schemes that are, at least, formally second order<sup>[403]</sup>. However, to the author's knowledge, even for two-phase flow with mass contrast it is an open question how to achieve energy stability, which again can allow for rigorous convergence results.

### 4.3 STEADY-STATE SCHEMES

For problems where a steady-state solution is sought, it is often undesirable to go through thousands of time steps to reach a steady state. Moreover, as seen from eq. (4.63), the steady state reached by a time-splitting scheme may contain spurious *numerical* dissipative terms of the order  $O(\tau)$ , and the artificial boundary condition on the pressure Poisson equation introduces an error  $O(\tau)$ <sup>[241]</sup>, sec. 5.1—which can be detrimental to the overall solution even when a higher-order method is used.

In this case, it might be worthwhile to solve for velocity and pressure in a coupled manner. For clarity, we consider the Stokes equation (3.17) for creeping flow, which we restate here,

$$-\mu \nabla^2 \mathbf{u} + \nabla p = \mathbf{f}, \quad (4.69)$$

$$\nabla \cdot \mathbf{u} = 0. \quad (4.70)$$

Here, we have added the constant body force  $\mathbf{f}$  to the right hand side of eq. (4.69). We impose the no-slip condition  $\mathbf{u} = \mathbf{0}$  on the boundary  $\partial\Omega$ .

Equation (4.69) can be written as the following *linear* variational problem. Find  $(\mathbf{u}, p) \in \mathbf{U}_h \times P_h$  such that

$$\mu (\nabla \mathbf{u}, \nabla \mathbf{v}) - (p, \nabla \cdot \mathbf{v}) = (\mathbf{f}, \mathbf{v}) \quad (4.71a)$$

$$(\nabla \cdot \mathbf{u}, q) = 0, \quad (4.71b)$$

for all test functions  $(\mathbf{v}, q) \in \mathbf{U}_h \times P_h$ . Solving and preconditioning this system remains an important area of research to this day. Particularly, this is relevant for cases where an accurate steady state is sought.

#### Finite element approximation

In the finite element method, as explained in section 4.1, we can expand the solution functions in a finite basis. For the velocity, we write the approximated solution as<sup>[241]</sup>

$$\mathbf{u} \simeq \hat{\mathbf{u}} = \sum_{j=1}^n \sum_{r=1}^{n_{\text{dim}}} U_{j,r} \mathbf{N}_j^r \quad (4.72)$$

where  $\mathbf{N}_j^r = N_j \hat{\mathbf{e}}_r$  ( $\hat{\mathbf{e}}_r$  are unit vectors), while the pressure can be approximated as

$$p \simeq \hat{p} = \sum_{j=1}^m P_j L_j. \quad (4.73)$$

Here,  $U_{r,j}$ ,  $P_j$  are constant coefficients, while  $N_j$ ,  $L_j$  are basis functions. Here, the velocity is represented by  $n \cdot n_{\text{dim}}$  unknowns ( $n_{\text{dim}}$  is the number of spatial dimensions) and the pressure is represented by  $m$  unknowns. Using the Galerkin method, as demonstrated in section 4.1, we can express (4.71) in terms of the basis functions. We then obtain the following equation sets:

$$\sum_{j=1}^n \mu (\nabla N_j, \nabla N_i) U_{j,r} - \sum_{k=1}^m (L_k, \partial_r N_i) P_k = (f_r, N_i), \quad (4.74a)$$

for  $r \in \{1, \dots, n_{\text{dim}}\}$ ,  
and  $i \in \{1, \dots, n\}$ ,

$$\sum_{r=1}^{n_{\text{dim}}} \sum_{i=1}^n (L_k, \partial_r N_i) U_{i,r} = 0, \quad \text{for } k \in \{1, \dots, m\}. \quad (4.74b)$$

Evidently, we can identify the inner products as the matrices  $\mathbf{A} = [A_{ij}]$  where  $A_{ij} = \mu(\nabla N_j, \nabla N_i)$ , and  $\mathbf{B}_r = [B_{ik,r}]$  where  $B_{ik,r} = -(\partial_r N_i, L_k)$ ; the source term vectors  $\mathbf{Q}_r = [Q_{r,i}]$  where  $Q_{r,i} = (f_r, N_i)$ ; and the vectors of unknowns  $\mathbf{U}_r = [U_{i,r}]$ ,  $\mathbf{P} = [P_i]$ . Here  $\mathbf{A}$  is an  $n \times n$  matrix,  $\mathbf{B}_r$  is a  $n \times m$  matrix,  $\mathbf{U}_r$  is an  $n$ -vector, and  $\mathbf{P}$  is an  $m$ -vector. By defining  $\mathbf{U} = [\mathbf{U}_1, \dots, \mathbf{U}_{n_{\text{dim}}}, \mathbf{P}]$  as the system vector of unknowns,  $\mathbf{Q} = [\mathbf{Q}_1, \dots, \mathbf{Q}_{n_{\text{dim}}}, \mathbf{0}_m]$  ( $\mathbf{0}_m$  is an  $m$ -dimensional zero vector) as the source term vector, and

$$\mathbf{M} = \begin{bmatrix} \mathbf{A} & & \mathbf{B}_1 \\ & \ddots & \vdots \\ & & \mathbf{A} & \mathbf{B}_{n_{\text{dim}}} \\ \mathbf{B}_1^T & \dots & \mathbf{B}_{n_{\text{dim}}}^T & \end{bmatrix} \quad (4.75)$$

as the  $(n \cdot n_{\text{dim}} + m) \times (n \cdot n_{\text{dim}} + m)$  system matrix, we can write the linear system as

$$\mathbf{M}\mathbf{U} = \mathbf{Q}. \quad (4.76)$$

Now, the main quest is to solve eq. (4.76), i.e. choose basis functions  $N_j, L_k$  such that  $\mathbf{M}$  is not singular. In this respect, the Babuska–Brezzi condition<sup>[67,68,241]</sup> is a central concept, which determines whether a finite element approximation is stable and leads to a uniquely defined solution vector  $\mathbf{U}$ . In practice, it imparts that a standard P<sub>1</sub>–P<sub>1</sub> discretization (of  $(\mathbf{u}, p)$ ), i.e. piecewise continuous basis functions on the discretized domain, cannot generally be used to solve the Stokes equations. The arguably most obvious choice is to use Taylor–Hood elements, which consists of P<sub>2</sub>–P<sub>1</sub> elements; i.e. piecewise quadratic basis functions for the velocity and piecewise linear basis functions for the pressure. This, however, leads to a larger number of unknowns, and in general, a large linear system that is hard to solve. The criterion also enables several other mixed element formulations, such as P<sub>k+1</sub>–P<sub>k</sub> for  $k > 1$ , and more advanced elements such as the MINI element, the “bubble” elements, and Crouzeix–Raviart elements. We will not discuss such methods here, and the interested reader is referred elsewhere<sup>[132,172]</sup>.

A more intuitive way of stabilizing the Stokes equations is to modify the governing equations, and include a mesh dependent parameter that ensures that convergence to the correct solution is obtained when the mesh is sufficiently refined, i.e. let the typical linear element size  $h \rightarrow 0$ . Such stabilization can enable the use of elements of the same order for both pressure and velocity, i.e. elements that would otherwise violate the Babuska–Brezzi criterion. When solving the Stokes equations numerically with elements that violate this criterion, the pressure field is usually found to be highly oscillatory. It is therefore consistent with physical intuition to add a term to the right hand side of eq. (4.70) that dampens out short-wavelength oscillations in the pressure field. Such a term can be expressed by

$$\nabla \cdot \mathbf{u} = \delta h^2(\mathbf{x}) \nabla^2 p, \quad (4.77)$$

where  $h(\mathbf{x})$  is a local mesh size, and  $\delta$  is parameter that is typically chosen heuristically. It is clear that the modification of the continuity equation, eq. (4.77), admits a compressibility proportional to  $\delta$ , i.e. the velocity field is no longer divergence free. In particular,  $\delta$  should be large enough to provide stable convergence, but small enough for the introduced compressibility to be unimportant for the final results.

The modification (4.77) leads to a resulting in a modification (from eq. (4.75)) of the system matrix  $\mathbf{M}$  in eq. (4.76):

$$\mathbf{M}_{\text{stab}} = \begin{bmatrix} \mathbf{A} & & \mathbf{B}_1 \\ & \ddots & \vdots \\ & & \mathbf{A} & \mathbf{B}_d \\ \mathbf{B}_1^T & \dots & \mathbf{B}_d^T & -\delta \mathbf{C} \end{bmatrix}, \quad (4.78)$$

where the  $m \times m$  matrix  $\mathbf{C} = [C_{ij}]$  is defined by  $C_{ij} = h^2 (\nabla L_i, \nabla L_j)$ . For sufficiently large  $\delta$ , the matrix  $\mathbf{M}_{\text{stab}}$  becomes nonsingular even for P<sub>1</sub>–P<sub>1</sub> elements.

The Babuska–Brezzi criterion is in general not only applicable to mixed elements and steady-state problems. It also applies to transient problems (the generalisation is straightforward), including those that impinge splitting between velocity and pressure. However, for splitting methods, such as that presented in section 4.2, a weak numerical compressibility is introduced,  $\nabla \cdot \mathbf{u} \propto \tau^2 \partial_t p$ , which can be seen from eq. (4.35b). This has a similar effect as the stabilization term (4.77) above, rendering simulations using P<sub>1</sub> elements for all fields possible. This can be a particularly viable alternative when the  $O(\tau)$  splitting error dominates. Finally, mixed element formulations that actually violate the Babuska–Brezzi criterion may also work well in practice. For instance, the P<sub>2</sub>–P<sub>0</sub> element has found wide use<sup>[241]</sup>. For more discussions on stabilization methods for single-phase fluid flow, see e.g.<sup>[172,241]</sup>.

#### 4.4 NUMERICAL SOFTWARE AND TOOLS

Computational tools are needed to numerically solve the discretized equations presented in the preceding sections. To consider the finite element method, the numerical tasks at hand include constructing meshes, computing basis functions, assembling system matrices (typically at each time step), preconditioning and solving the resulting sparse linear systems, and storing and analysing the data. Many of these steps are in themselves well-developed scientific topics, and hence it would be daunting task to implement everything from scratch. Luckily, there exist freely available numerical resources which allow to use highly optimized routines for all of these tasks. The obvious advantages of this approach is that one avoids ‘reinventing the wheel’ and the approach thus allows to obtain reliable results in a shorter amount of time—both in terms of implementation and simulation time. Obviously, this relies on the employed software to be trustworthy.

The importance of reproducibility in science was pointed out already by Boyle in the 17th century<sup>[402]</sup> pp. 82. Recently, an increased interest in reproducible research has emerged, particularly in computational science<sup>[75,135]</sup>. An essential component to reproducible science is transparency. For computational science, this imparts that the numerical codes should be available to the public, so that anyone can inspect and critically evaluate the validity of the tools with which results have been obtained. An important facilitator for development of such *open source* software has been the open version control system such as GIT<sup>[444]</sup> and MERCURIAL, combined with public code repositories such as GitHub and BitBucket.<sup>27</sup> In order to keep in line with this policy, we have opted both to *use* and *develop* open source codes.<sup>28</sup>

##### 4.4.1 FENICS

Most of the simulations presented in this thesis have been carried out within the finite element framework FENICS<sup>[272]</sup>. FENICS is an open-source computing platform for solving partial differential equations using the finite element method, which aims to automatize the discretization and assembly of the problems in question. The backend code is written in C++, while the features can be accessed using high-level PYTHON code. Since the bulk of the computation time in a finite element problem is spent on matrix assembly and linear solvers, the high-level PYTHON interface does not pose a significant cost in terms of efficiency<sup>[320]</sup>. Rather, it serves to cut time spent on code development, documentation, and maintenance. FENICS consists as a collection of dedicated components that together make setting up finite element problems straightforward. DOLFIN<sup>[273]</sup> is the C++/PYTHON interface to the computational backend of FENICS. The FENICS Form Compiler FFC<sup>[235]</sup>

<sup>27</sup> Not only does this provide a powerful and transparent change-tracking environment, and allow users to quickly update their code (by “pulling” from the repository); it invites users to interact, point out errors or shortcomings (file “issues”), and provide fixes or new features themselves (submit “pull requests”), which in turn can be incorporated into the main branch of the project by the code authors.

<sup>28</sup> Open science is also an important target for the Horizon 2020 programme of the European Commission<sup>[141]</sup>, a funding agent for the present project.

translates variational forms into efficient c++ code for FEM assembly. The discretized variational forms can be specified by users via the Unified Form Language (UFL)<sup>[10]</sup>. The Finite element Automatic Tabulator (FIAT)<sup>[234]</sup> generates various types of finite elements (including  $P_k$ ) elements. DIJITSO<sup>[11]</sup> is a just-in-time compiler for c++ code generated by PYTHON code.

Within a PYTHON script, FENiCS users can specify a mesh, set up finite element spaces, specify a weak form of the governing equations, and impose boundary conditions. The numerical problem is then automatically converted to a linear matrix system by the c++ backend. The computational backend interfaces to highly optimized linear solver libraries, such as PETSc<sup>[25]</sup>, HYPRE<sup>[142]</sup>, and TRILINOS<sup>[187]</sup>. Which linear solvers and preconditioners to use can be specified by the user. In particular, all the solvers and preconditioners mentioned in section 4.1 can be accessed through FENiCS, and additional preconditioners are found e.g. in FENAPACK<sup>[55]</sup>. In common with (and partly due to) its linear algebra backend, FENiCS is highly parallelized and developed with high-performance computing in mind. In particular, it uses the Message Parsing Interface (MPI) for parallel communication.

For a more thorough introduction to how FENiCS is used in practice, the reader is referred to the extensive tutorial by Langtangen and Logg<sup>[240]</sup>. In this project, FENiCS has been used as the underlying framework for solving the equations of elasticity, creeping flow, transient single-phase flow, and multiphase flow with electric fields and solutes, as we will see below.

#### 4.4.2 OASIS

The OASIS (Optimized And Stripped Solver) software, developed by Mortensen and Valen-Sendstad<sup>[320]</sup>, is a high-level, fast and flexible solver for the Navier–Stokes equations. OASIS is written entirely in PYTHON, built on top of the FENiCS platform, and heavily exploits its PETSc backend. The runtime of the solver has been shown to be dominated by Krylov solver iterations, underpinning the fact that the high-level PYTHON interface is insignificant to the overall performance. In particular, the solver was shown to yield similar efficiency as solvers written entirely in low level code, i.e. OPENFOAM<sup>[217]</sup> and CDP<sup>[86]</sup> by comparative simulations on the Abel supercomputer at the University of Oslo, and weak scaling was demonstrated up to 256 cores.

OASIS is distributed as a Python package and is modular by design. Several solvers, i.e. numerical schemes, given as separate Python scripts, are implemented in the code. These include Chorin’s method, i.e. eq. (4.66), and an optimized IPS3, i.e. eq. (4.67), and other methods. Problems, i.e. simulation cases, are implemented as separate PYTHON scripts in a similar manner, and user specific problems can be easily defined, for example by modifying some of the default problems to fit the needs of the user. A customized version of OASIS<sup>29</sup> used in this project was developed by the author jointly with MSc student Mads H. A. Madsen, whom the author co-advised during the spring of 2016.

<sup>29</sup> The code can be found on the GIT repository <https://github.com/gautelinga/Oasis/tree/nbiOasis>.

#### 4.4.3 BERNAISE

BERNAISE (Binary Electrohydrodynamic Solver) is a flexible, high-level finite element solver of two-phase electrohydrodynamic flow problems in complex geometries, which has been developed in this project<sup>[263]</sup>, in a joint venture with colleague Asger Bolet. Inspired by the famous sauce—and oil-in-water emulsion—Béarnaise<sup>30</sup>, the solver aims at solving problems involving the smallest constituents of such phases, namely small droplets of one phase immersed in another phase, possibly subject to chemical transport and electric fields. The basic version of the solver targets solving the phase-field model (3.81) as proposed by Campillo-Funollet et al.<sup>[79]</sup>, while other phase-field models can be

<sup>30</sup> The missing A in BERNAISE compared to the sauce stands for Adaptivity, which is at the present not an implemented feature.

integrated with ease. Employing a phase-field model, the solver is better suited to handle topological changes and moving contact lines than comparable sharp-interface models; cf.<sup>[43]</sup>. Several numerical schemes are implemented, which include coupled velocity and pressure computation, fractional-step methods, energy stable schemes and fully linear schemes. This permits simulations both in two and in three dimensions. The 3D version of the solver is fully iterative and demonstrated strong scaling up to about 40 cores on an in-house computing cluster.

BERNAISE is inspired by the OASIS solver, and is similar to the latter in both structure and implementation. This approach is chosen both in order to appeal to the same user base, and because it was the developers' opinion that the approach of OASIS is a sensible one. Many of the routine functions are similar, and problems and solvers can easily be implemented in a reminiscent<sup>31</sup> way by the user, i.e. by supplying single PYTHON scripts. Nevertheless, it is our hope and opinion that most users—familiar with OASIS or not—should easily arrive at a decent level in BERNAISE.

In addition to the simulation environment, BERNAISE comes with a set of utility tools. This includes post-processing tools for analysing data, producing figures, etc., a mesh generation utility, and a plotting utility.

The appended Paper 6<sup>[263]</sup> which documents the software, simulation method, and code validation, is described also section 5.3. Additionally, the code has been used for several of the other appended publications.

#### 4.4.4 Meshing tools

Although meshing was mentioned only in passing in section 4.1, it represents a genuinely hard and important problem. Unstructured meshes have the initially persuasive feature that they allow to represent parts of the domain with finer elements and thus allowing to obtain locally higher accuracy. However, for complex domains in 3D, constructing quality meshes is a challenging task. In many settings, such as in simulation of incompressible flow, 'bad' elements can deteriorate the solution, and lead to instabilities in otherwise stable methods<sup>[241]</sup>. Moreover, splitting schemes for transient flow are subject to the CFL criterion and therefore strongly inhibited by the smallest grid size (or specifically, the highest local Courant number).

The CGAL library<sup>[441]</sup> is an extensive c++ library for meshing in 2D and 3D, but is difficult to master. TETGEN<sup>[408]</sup> is another robust mesh generation tool with a more modest feature list. FENICS' built-in meshing tool, the PYTHON package MSHR<sup>[230]</sup> interfaces to both the above libraries. Another good PYTHON package is MESHPy<sup>[236]</sup>, which interfaces to TRIANGLE<sup>[405]</sup> for 2D meshes and above-mentioned TETGEN. Iso2MESH<sup>[143]</sup> is a MATLAB toolbox which both interfaces to CGAL and TETGEN, and contains several other features.

In this work, Iso2MESH was used to generate meshes from segmented X-ray microtomography data of a porous limestone (see section 5.2), using the interface to TETGEN to produce the surface mesh and the CGAL interface to produce the interior tetrahedra.

Periodic domains constitute an additional difficulty, as nodal values must be mapped exactly to the opposing sides. This is particularly relevant for constructing meshes for rough channel or pipe geometries. To do this, a meshing tool was developed in Python,<sup>32</sup> that takes an arbitrary (rough) surface as input and creates a periodic mesh from it. Using a combination of manually written routines for the edges, TRIANGLE (via MESHPy) for the flat (periodic) sides, and TETGEN for the interior tetrahedra, reasonably high-quality meshes could be obtained that were also fully periodic. As will become obvious in the next chapter, these routines were taken advantage of in both electrohydrodynamic and transitional flows.

<sup>31</sup> As the two codes simulate related, but in many ways quite different physical problems, significant differences in the code structure are necessary.

<sup>32</sup> Some of the meshing tools used in this project are available at the GIT repository <https://github.com/gautelinga/meshtools>.



# 5

## SUMMARY OF PAPERS

---

In this chapter, the research articles produced in this project are summarized. The papers are roughly organized into four overarching themes for which background material has been introduced in the previous chapters.

### 5.1 TURBULENT FRONTS IN PIPE FLOW

**PAPER 1:** Statistical mechanics of puff-splitting in the transition to pipe turbulence  
 Hong-Yan Shih, Gaute Linga, Grégoire Lemoult, Mukund, Vasudevan, Björn Hof, Joachim Mathiesen, and Nigel Goldenfeld  
 In preparation (2018)

Paper 1 concerns the spatio-temporal transition to turbulence in a smooth pipe, and starts off where the discussion in section 2.2.2 ended. As noted there, whether or not the transition belongs to the directed percolation universality class has been a long-standing puzzle in the community at the intersection between fluid mechanics and statistical physics. Recent experiments by Mukund and Hof<sup>[327]</sup> showed that even in (quasi-periodic) pipes of length  $7800d$  ( $d$  is pipe diameter), a continuous transition to turbulence could *not* be observed. Rather, a *discontinuous* behaviour was observed, from the point where all turbulence died out at  $\text{Re} \simeq 2020$ , shown in fig. 2.3 (d), to a point where turbulent puffs were ‘jammed’ in a crystalline state at  $\text{Re} \simeq 2060$ , shown in fig. 5.1 (a). This relied on the standard view of considering the turbulent fraction  $F$  as the order parameter and  $\text{Re}$  as the control parameter<sup>[28,29]</sup>. Moreover, knowledge from studies on directed percolation suggests that the critical point,  $\text{Re}_c$ , is somewhat higher than at the  $\text{Re}_x \simeq 2040$  found by Avila et al.<sup>[23]</sup> based on single-puff statistics<sup>[23,29,193]</sup>.<sup>33</sup> Here, we summarize and give some supplementary information to the appended preprint.

In this work, the main assumption is that the statistical properties of a puff depend (in average) only on the shear profile at its upstream front. In particular, the latter should depend only on the distance to the nearest neighbour upstream, and not on anything happening downstream of it. Thus, the dynamics are controlled only by *one-way* two-particle interactions. Moreover, the puffs can stochastically spontaneously split and decay with rates (or conversely, characteristic times) that depend only on  $\text{Re}$  and the distance  $\ell$  to its upstream neighbour, and the speed  $u$  at which they travel downstream is also only dependent on  $\ell$  and  $\text{Re}$ . Carefully executed experiments presented in this work show that, at fixed  $\text{Re}$ , both the decay times  $\tau_d$ , splitting times  $\tau_s$ , and downstream velocities  $u$ , can be described by the exponential<sup>34</sup> relations

$$\tau_d(\ell) = \tau_{d,\infty} \left[ 1 - a_d e^{-\ell/\lambda} \right], \quad \tau_s(\ell) = \tau_{s,\infty} \left[ 1 + a_s e^{-\ell/\lambda} \right], \quad (5.1)$$

$$u(\ell) = u_\infty \left[ 1 + b e^{-\ell/\lambda} \right], \quad (5.2)$$

*This manuscript addresses the spatio-temporal transition to turbulence in pipe flow. Results from Paper 1 were presented by the author at the conference Computational Methods in Water Resources, held in Saint-Malo, France, 3–7 June 2018.*

<sup>33</sup> However, as noted also by Avila et al.<sup>[23]</sup>, the splitting and decay rates change so abruptly around  $\text{Re}_x$  that  $\text{Re}_c$  is likely only be slightly larger.

<sup>34</sup> Which is perhaps not surprising given the exponential (in time) development of a Hagen–Poiseuille profile, see e.g.<sup>[321]</sup>.

where the parameters  $\tau_{d,\infty}$ ,  $\tau_{s,\infty}$ ,  $u_\infty$  are the single-puff properties. The first two,  $\tau_{d,\infty}$  and  $\tau_{s,\infty}$ , depend superexponentially on  $\text{Re}$  and can be obtained from<sup>[23]</sup>. The last,

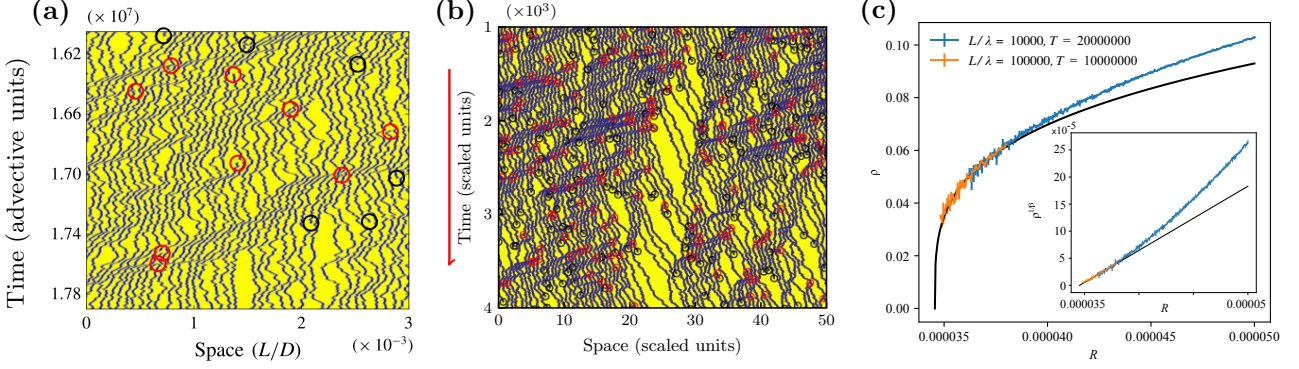


**FIGURE 5.1:** Puff-splitting in the transition to pipe turbulence. (a) The experiments by Mukund and Hof<sup>[327]</sup> above the critical point. (b) Simulations of the continuous model above the critical point. (c) Ensemble-averaged turbulent fraction in the steady-state.

$u_\infty$ , which has a weaker dependence on  $\text{Re}$  can be found from<sup>[30]</sup>. Finally, the amplification/reduction factors  $a_d$ ,  $a_s$ , and  $b$ , and the interaction distance  $\lambda$ , are empirical parameters found from the experiment. Now, the motion of puff  $i$  can be described by the Langevin equation

$$\frac{dx_i}{dt} = u(x_i - x_{i-1}) + \sqrt{D}\xi_i(t), \quad (5.3)$$

where  $x_i$  is the puff position, and  $i - 1$  is the upstream puff (to the left of  $i$ ) such that  $x_i > x_{i-1}$ . The noise  $\xi_i$  is taken to be uncorrelated and Gaussian, i.e.  $\langle \xi_i(t)\xi_j(t') \rangle = \delta_{ij}\delta(t - t')$ .  $D$  is a heuristic diffusion coefficient that represents the stochastic motion of puffs observed experimentally, and can be determined from experiments or direct numerical simulations. We assume periodic boundary conditions in the axial direction in a pipe with length  $L$ , and puffs can be removed ('decay') and spawned at the downstream end of another ('split') with rates  $\tau_d^{-1}, \tau_s^{-1}$ , respectively.

For numerical implementation purposes, and to limit the number of parameters to a minimum, it is useful to nondimensionalize the equations. First, we move into a reference frame moving at the mean speed of newly spawned puffs, i.e.  $\bar{U} = u_\infty(1 + b)$ . Then, we introduce new space and time variables denoted by tildes, through  $\tilde{x}_i = X\tilde{x}_i$  and  $t = T\tilde{t}$ , and correspondingly  $D = \tilde{D}X^2/T$ ,  $\tilde{\lambda} = X\lambda$ ,  $L = X\tilde{L}$ ,  $u = \tilde{u}X/T$ ,  $\tau_i = T\tilde{\tau}_i$ . Here,  $X$  and  $T$  are the spatial and temporal scales.

Equation (5.3) becomes

$$\frac{d\tilde{x}_i}{d\tilde{t}} = \tilde{u}(\tilde{x}_i - \tilde{x}_{i-1}) + \text{sgn}(X)\sqrt{\tilde{D}}\xi_i(\tilde{t}), \quad (5.4)$$

where we have used  $\xi_i(T\tilde{t}) = \xi_i(\tilde{t})/\sqrt{T}$ , and

$$\tilde{u}(\tilde{\ell}) = \frac{T u_\infty b}{X} \left[ e^{-\tilde{\ell}/\tilde{\lambda}} - 1 \right], \quad \tilde{\tau}_i(\tilde{\ell}) = \frac{\tau_{i,\infty}}{T} \left[ 1 - a_d e^{-\tilde{\ell}/\tilde{\lambda}} \right]. \quad (5.5)$$

It is practical to choose the time scale  $T = \tau_x = \tau_{d,\infty}(\text{Re}_x) = \tau_{s,\infty}(\text{Re}_x)$  where  $\text{Re}_x$  is the single-puff critical Reynolds number found by Avila et al.<sup>[23]</sup>. We also choose the spatial scale  $X = \tau_x u_\infty b(\text{Re}_x)$ . For convenience, and compliance with the next model, we omit the tildes, flip the sign of the  $x$ -axis and invert the order over the puff indices, so that  $x_{i+1} > x_i$ . Further, we introduce the simplified control parameter  $\varphi = \text{Re} - \text{Re}_x$ . We thus obtain eq. (5.4) with

$$u(\ell) = \alpha(\varphi) \left[ e^{-\ell/\lambda} - 1 \right], \quad \alpha(\varphi) = \frac{u_\infty b(\text{Re}_x + \varphi)}{u_\infty b(\text{Re}_x)}, \quad (5.6a)$$

$$\tau_i(\ell) = \beta_i(\varphi) \left[ 1 - a_d e^{-\ell/\lambda} \right], \quad \beta_i(\varphi) = \frac{\tau_{i,\infty}(\text{Re}_x + \varphi)}{\tau_{i,\infty}(\text{Re}_x)}. \quad (5.6b)$$

Here,  $\alpha(0) = \beta_i(0) = 1$ , and can be linearized around  $\varphi = 0$ .<sup>35</sup> This model, which we call the *continuous model*, captures the dynamics of puff interaction well.

The equations can be numerically integrated explicitly using the Itô formalism. At time step  $k$ , we calculate

$$\Delta x^* = \Delta t u(x_{i+1}^k - x^k) + \sqrt{D\Delta t}N(0, 1), \quad (5.7)$$

where  $\Delta t$  is the discrete time step, and  $N(0, 1)$  is an uncorrelated random number drawn from a Gaussian distribution with mean 0 and variance 1. The position is then updated by

$$x_i^{k+1} = x_i^k + \max(0, \min(\Delta x_i^*, x_{i+1}^k - x_i^k)), \quad (5.8)$$

to strictly avoid puffs passing each other. The integration is combined with an efficient double-linked list implementation in c++, where puffs are removed if  $P_d = 1 - e^{-\Delta t/\tau_d} > R_d$ , where  $R_d$  is a random number drawn from a uniform distribution in the interval  $(0, 1)$ .<sup>35</sup> Likewise, a puff is inserted into the list if  $P_s = 1 - e^{-\Delta t/\tau_s} > R_s$ , where  $R_s$  is another (uncorrelated) random number drawn from the same distribution as  $R_d$ . Since we are interested in ensemble properties, the optimal parallelization strategy is to run thousands of independent simulations simultaneously.

By coarse-graining the continuous model, a simplified lattice-based model can be obtained, which contains the basic phenomenology of puff interaction. The basic ingredients are splitting, decay, and propagation, which are all described by the rates  $\omega_s, \omega_d, p$ . In this picture, we are in a frame co-moving with the puffs going fastest downstream (as with the rescaled and shifted continuous model), and in this frame of reference, the puffs are propagating upstream.<sup>37</sup> If there are no puffs in front (i.e. upstream) of a given puff, the puff is free to move in that direction. If there is a puff in front of it, the puff cannot propagate, and a *queue* starts to form.

Readers who have experience with commuting to work by car, will probably recognize this dynamics from traffic congestion. Indeed, this lattice model is tightly connected to traffic models, namely those belonging to the class of asymmetric exclusion processes (ASEP)<sup>[94,184]</sup>. Such models have been well studied by statistical physicists<sup>[184]</sup>. In particular, the lattice model of puff dynamics is reminiscent of the totally asymmetric exclusion process (TASEP), in which only unidirectional motion is allowed. Puff dynamics displays, however, two notable differences from traffic applications: (i) “Cars” (or puffs) can spontaneously appear or disappear from the queue, and (ii) the boundary is periodic, i.e., the “cars” drive in circle. The lattice model is straightforward to implement, and the lattice sites can be set to be updated synchronously. The processes *split*, *decay*, and *propagate* can be picked in a random order at each discrete time step.

The mean field equation for this process is given by

$$\partial_t \langle n_i \rangle = -p \langle n_i(1 - n_{i+1}) \rangle + p \langle n_{i-1}(1 - n_i) \rangle - \omega_d \langle n_i \rangle + \omega_s \langle n_{i-1}(1 - n_i) \rangle \quad (5.9)$$

where  $n_i$  is the occupation number of site  $i$  of the lattice. Here, the first two terms represent propagation, and the last two represent decay and splitting, respectively. If  $p = 0$ , the model contains the four ingredients of DP: diffusion, de-coagulation, coagulation and annihilation<sup>[193]</sup>. We can identify e.g.  $\omega_s$  as a control parameter, such that the mean number of particles  $\rho = \langle n_i \rangle \sim (\omega_{s,c} - \omega_c)^\beta$ , where the exponent  $\beta$  is found in table 2.1.

By performing a Kramers–Moyal expansion to second order, a Fokker–Planck equation can be obtained, which again can be transformed to a Langevin equation representing the model. In this (further) coarse-grained continuum description, i.e.  $i \rightarrow x$ , the replacements

$$n_i \rightarrow \rho(x) \quad \text{and} \quad n_{i+1} \rightarrow \rho(x) + \partial_x \rho(x) + \frac{1}{2} \partial_x^2 \rho(x), \quad (5.10)$$

<sup>35</sup> The code is available at the Git repository <https://github.com/gautelinga/puffdyn>.

<sup>36</sup> Avila et al.<sup>[23]</sup> gave the functional form  $\tau_i(\varphi) = \exp(\exp(a_i \varphi - b_i))$  for  $i \in \{s, d\}$ , including numerical values for the parameters  $a_i, b_i$ . Thus,  $\tau_i$  are rapidly growing analytic functions. The linear range may however be very narrow, as seen by Taylor expansion of  $\tau_i$ . Using the values from<sup>[23]</sup>, we find that the contribution of the second order term is of the order 10% when  $\varphi/\text{Re}_x \simeq 2\%$ .

<sup>37</sup> This is also the correct way of looking at it, according to Barkley<sup>[29]</sup>; by viewing the puff motion as an interface propagation phenomenon.

must be made, leading to the equation

$$\begin{aligned}\partial_t \rho = & -\omega_d \rho + \frac{1}{2}(p + \omega_s) \partial_x^2 \rho - (p + \omega_s) \partial_x \rho + \omega_s \rho (1 - \rho) \\ & + (2p + \omega_s) \rho \partial_x \rho - \frac{\omega_s}{2} \rho \partial_x^2 \rho + \sqrt{\rho(1 - \rho)} \xi,\end{aligned}\quad (5.11)$$

where  $\xi(x, t)$  is a white noise, such that  $\langle \xi(x, t) \xi(x', t') \rangle = \delta(x - x') \delta(t - t')$ . Compared to the corresponding Langevin equation for DP, eq. (5.11) contains two terms proportional to  $\sim \rho \partial_x^j \rho$  where  $j = 1, 2$ , which in TASEP models lead to shocks or ‘traffic jams.’ The question is now whether the presence of these terms change the universality class away from DP. By a renormalization group argument outlined in the appended preprint, it can be shown that these terms are indeed irrelevant at the DP fixed point.

To test this prediction, numerical simulations were carried out both for the continuous model and the lattice model. The experimental values provide a basis for the parameters in the continuous model, while in the lattice models the parameters are chosen more heuristically. Nevertheless, universal dynamics should not be *sensitively* dependent on the details of the implementation. Figure 5.1 (a) shows the puff dynamics in the experiment by Mukund and Hof<sup>[327]</sup>, and in fig. 5.1 (b) we show corresponding simulations with the continuum model. The similarity between the two is striking, in particular with regard to how waves of puff repulsion propagate through the system. This behaviour is also captured in the discrete model, but in a more coarse-grained way. In this picture, the typical interaction distance  $\lambda$  in the continuous model, which presumably is proportional to a puff size, should correspond to a lattice unit. By carefully accounting for finite size effects, the DP scaling  $\rho \sim \varphi^\beta$  could be reproduced with both models. For the continuous model a system size  $L/\lambda = 10^5$  (and a simulation time  $T/\tau_x = 5 \cdot 10^4$ ) was required to obtain a reasonable scaling range, see fig. 5.1 (c).

In light of these insights, we can reinterpret the results of Mukund and Hof<sup>[327]</sup>. It is clear that with a puff interaction distance  $\lambda \simeq 15d$  (estimated from experiments), the system size  $L = 7800d$  corresponds to  $L/\lambda \simeq 500$ , which is nearly three orders of magnitude smaller than what we needed to obtain an acceptable range numerically. Knowing that asymptotically close to the critical point, the equilibration time diverges, it seems clear that an experimental measurement would be hard. A simple extrapolation from the continuous simulations carried out here, indicates that a system size of at least  $L \sim 10^5 d$  and a simulation time of  $T \sim 10^{11}$  advective units would be necessary ( $\tau_x \sim 10^7$  advective units, from<sup>[23]</sup>). As a large ensemble is needed to obtain robust results, this might pose significant challenges to realize experimentally.

**REMAINING WORK** The experimental work needs to be included in the manuscript. Furthermore, it would strengthen the paper to give a more quantitative prediction on how large systems and simulation times would be required to observe the DP scaling in an actual experiment.

**CONTRIBUTIONS** For the first paper, the idea of probing the large-scale behaviour by using ‘two-particle’ puff statistics was conceived by Lemoult. The experiments were carried out by Mukund and Hof. Goldenfeld, Shih, Mathiesen and I developed an independent model and made through discussions the connection to the TASEP model. Lemoult, Mathiesen and I implemented different versions of the lattice model and carried out simulations. Lemoult and I developed independent versions of the continuous molecular dynamics model and carried out simulations. Goldenfeld and Shih derived the Langevin equation from the lattice model, and performed the renormalization group analysis. The manuscript in the appended state, was written mainly by Goldenfeld, with

input from the other authors, while the section on the continuous model was written by me.

## 5.2 FLOW IN FRACTURED AND POROUS MEDIA

*These papers concern flow in disordered geophysical media. Paper 2 concerns the mechanical coupling between creeping flow and solid stress in an evolving porous medium, while Paper 3 focuses on the role of unsteady flow on the transport properties in a fracture. Paper 2 was the basis for an oral presentation at the EGU General Assembly, Vienna, 2016, while a preliminary version of the second paper formed the basis for a poster presentation at the AGU General Assembly, New Orleans, 2017.*

- PAPER 2: Self-similar distributions of fluid velocity and stress heterogeneity in a dissolving porous limestone  
 Gute Linga, Joachim Mathiesen, and François Renard  
*Journal of Geophysical Research: Solid Earth* **122**, 1726–1743 (2017)
- PAPER 3: Transitional flow in self-affine rough fractures  
 Gute Linga, Luiza Angheluta, and Joachim Mathiesen  
 In preparation (2018).

As mentioned in section 2.1.1, the disordered microstructure of porous rocks is known to cause a strong heterogeneity in local flow rates and solid stress. Accordingly, an evolving microstructure will have consequences on the distributions of fluid flow and stress in the solid. In Paper 2, we consider numerically the coupling between fluid flow and solid stress in a dissolving porous limestone sample. The aim of the study is to assess (i) how an imposed fluid flow through the pore space can affect the stress distribution in the solid, and (ii) how an evolving microstructure can affect the same distribution, and (iii) how dissolution in the rock can modify the flow heterogeneity. The simulation set-up is shown in fig. 5.2 (a).

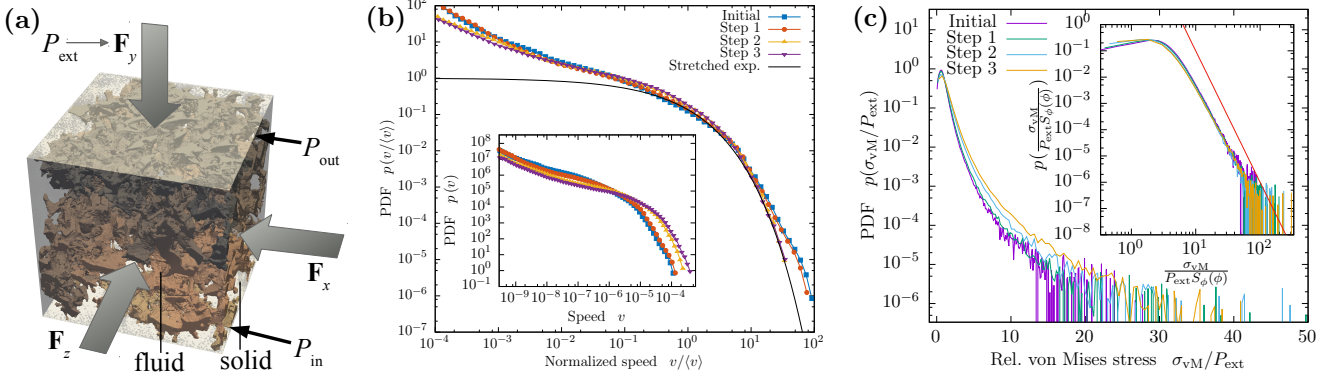
The starting point for the investigation is the experiments by Noiriel et al.<sup>[342, 343]</sup>, where an acidic fluid was injected into a core sample of porous limestone in multiple rounds, leading to dissolution and porosity increase. The sample was imaged using X-ray microtomography at each stage of dissolution. Noiriel generously provided to the authors segmented three-dimensional images (consisting of fluid and solid voxels) at four stages of dissolution, with porosities  $\phi$  ranging from 0.09 to 0.2. The segmented data was then post-processed, and unstructured meshes were generated of the sample at each dissolution stage (see section 4.4.4).

To model the coupling between the fluid flow and the state of stress in the solid, two main approximations are made. The first is to assume creeping flow, i.e. the Stokes equations (3.17) is assumed to hold. This assumption, which amounts to  $\text{Re} \ll 1$ , can also be verified based on parameters from the actual experiment Noiriel et al.<sup>[342]</sup>. The second assumption is to consider *quasi-static* deformation; i.e., the time-scale of geometry change is considered to be slow, so that we can seek equilibrium solutions to the elastic problem. The assumption also imparts a *one-way coupling* from the fluid to solid: we assume that the effect of fluid flow and external forces is so small that the geometry does not deform enough for the velocity field to be affected. In particular, locally infinitesimal displacements of the solid matrix are assumed, and linear elasticity should be a valid description.

The assumptions imply that the Stokes equations need to be solved in a constant geometry, with the no-slip conditions at the pore wall, and with pressure boundary conditions at the inlet and outlet. As demonstrated in section 3.1.2, this is then a linear problem, and the velocity can be shown to be dependent solely on the *geometry* on the one hand, and (is proportional to) the pressure difference on the other hand. A similar linear relation holds for the pressure distribution, and accordingly for the fluid stress tensor. It is thus only necessary to perform *one* accurate steady-state solution in each mesh, and the solution for all pressure conditions can be found by a trivial rescaling. The boundary conditions entering the elasticity problem are given by the traction on the pore walls due to fluid flow and pressure.

Elastostatics is described by

$$\nabla \cdot \boldsymbol{\sigma}_s = \mathbf{0}, \quad (5.12)$$



where the  $\sigma_s$  is the solid stress tensor, and external body forces have been neglected. Equation (5.12) is analogous to Stokes equations for creeping flow, except that it is not supplied by a divergence criterion. In linear elasticity, the stress tensor is given by

$$\sigma_s[\mathbf{d}] = \frac{E}{1+\nu} \left[ \mathbf{D}\mathbf{d} + \frac{\nu}{1-2\nu} \nabla \cdot \mathbf{d} \right], \quad (5.13)$$

where  $\mathbf{d}(\mathbf{x})$  is the displacement vector,  $E$  is Young's modulus and  $\nu$  is the Poisson ratio. The strain tensor is given by  $\mathbf{D}\mathbf{d} = \text{sym}(\nabla\mathbf{d})$  (analogously to its fluid counterpart, the strain *rate* tensor  $\mathbf{D}\mathbf{u}$ ). In our set-up, eq. (5.12) is subjected to external loading on the outer boundary, along with internal stress from the fluid, in order to mimic experimental settings. Hence, we are left with solving a set of linear equations for a range of parameters.

With respect to the fluid phase, the results show that for the porosity range considered, the permeability  $k$  varies over more than an order of magnitude, and can be well described by a power law  $k \sim \phi^\beta$  where  $\beta \simeq 4$ . This is consistent with observations in the literature (see section 2.1.1, but contrary to the Kozeny–Carman relation<sup>[84,85,237]</sup>). Secondly, we find that the probability density functions of velocity (sampled over volume) can be described by a stretched exponential function with exponent 1/2 (see eq. (2.18) in section 2.2.1). The distributions are shown in fig. 5.2 (b). Moreover, even though the porosity varies by a factor two, and the permeability varies by a factor 10, the distributions can be collapsed onto the essentially same master curve by rescaling with the mean velocity. Whether these observations are a result of e.g. preferential dissolution in dominant channels, or of more generic nature, remains an open question.

By analyzing the pressure and viscous stress, we show that the contribution to the traction by pressure (normal stress) is dominant over that by viscous shear by an order of magnitude. Probability density functions of the *invariants* of the stress tensor (mechanical pressure and von Mises stress) also display a heavy tail, consistently with e.g.<sup>[244]</sup>, and for all considered loading and flow conditions, they can be collapsed onto the same universal curve, cf. fig. 5.2 (c). With regard to the von Mises stress, which is often used as a fracture criterion, the heavy tail of the distribution implies that a small increase in dissolution and fluid flow rate can bring a large number of ‘sites’ in the rock across a critical threshold. Hence, if these results can be extrapolated to other rocks, they could provide an additional explanation of the sensitivity of rocks to failure under slight changes of stress.

The stress that a flowing fluid exerts on the confining boundaries is directly related to the flow resistance, and thus the friction factor. In Paper 3, we disregard the state of stress in the solid, and abandon the paradigm of creeping flow. As documented in section 2.2.1, most numerical studies have considered steady-state flow, either creeping

FIGURE 5.2: Flow and stress in a dissolving porous limestone, reprinted from<sup>[261]</sup>. (a) Schematic setup of the problem. (b) Probability density functions of the velocity sampled over the pore space, rescaled by mean velocity. A stretched exponential decay is plotted alongside the data. The inset shows the raw data. (c) Probability density functions of von Mises stress in the solid. The inset shows how the distributions collapse when rescaled by their means.

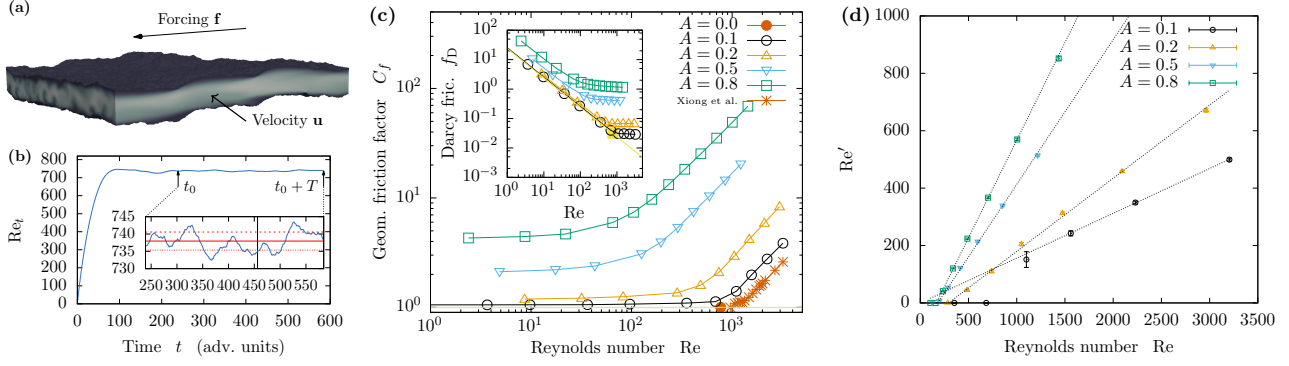


**FIGURE 5.3:** Transitional flow in self-affine rough channels, from<sup>[262]</sup>. (a) A snapshot from a simulation. (b) The instantaneous Reynolds number as a function of time. Inset: a close up of the sampling time in the steady state. (c) Geometric friction factor as a function of Reynolds number. Inset: Darcy friction factor. (d) The fluctuation-based Reynolds number, indicating the presence of turbulence, as a function of (fluxed-based) Reynolds number.

or laminar. Despite its apparent industrial relevance, unsteady, transitional flow in three dimensional fractures is largely unexplored. In this study, we consider a simple and generic fracture geometry that consists of a periodic self-affine surface (see eq. (2.7)) that has been shifted vertically by a distance  $d$  to form a rough model fracture joint. The main research questions underlying the investigations can be summarized as the following: (i) What is the impact of a generic roughness on the transport properties of a channel geometry? (ii) What is the effect of velocity fluctuations? (iii) How is the laminar–turbulent transition in such channels affected by including a boundary roughness?

To construct a mesh for the fracture joint, we generate a periodic self-affine surface  $h$ , parametrized in terms of  $(x, y) \in [0, 10d] \times [0, 10d]$ . This forms the lower boundary of the flow geometry. The same surface, shifted by a distance  $d$  along the  $z$ -axis, forms the upper boundary, and the flow is confined to the slab between these two boundaries. Since a self-affine surface does not have an intrinsic length scale, we define the roughness amplitude  $A$  as the root-mean-square height undulations of the surface  $h(x, y)$ . Here, we consider the four roughness amplitudes  $A \in \{0.1d, 0.2d, 0.5d, 0.8d\}$  with the same self-affine realization.

Fluid flow in the spanwise and streamwise periodic domain is enforced using a fixed uniform body force  $\mathbf{f} = f\hat{\mathbf{x}}$ , and the Navier–Stokes equations (3.14) are integrated in time using an incremental pressure-correction scheme (see eq. (4.67) in section 4.2.5) in a modified OASIS solver (see section 4.4.2 and ref.<sup>[320]</sup>). Simulations are run until a steady state is reached, either in an absolute or in a statistical sense; the latter for unsteady flow. The instantaneous flow rate  $u_x(t)$  can then be computed, and a flux-based Reynolds number can be measured by averaging it in time (indicated by an overline), i.e.

$$\text{Re} = \frac{\rho \bar{u} d}{\mu}, \quad (5.14)$$

In fig. 5.3 (a) an instantaneous snapshot of a typical simulation is shown, and in fig. 5.3 (b) we display the development of the instantaneous Reynolds number  $\text{Re}_t$  (based on  $u_x(t)$  instead of the time-averaged  $\bar{u}_x$ ). In fig. 5.3 (c) we show the *geometric friction factor*, defined by

$$C_f = \frac{f d^2}{12 \mu \bar{u}} \quad (5.15)$$

as a function of  $\text{Re}$ , for all four considered roughness amplitudes  $A$ . This quantity has the property that it equals  $C_f = 1$  in the double limit  $\text{Re}, A \rightarrow 0$ , and can be seen as an inverse permeability relative to plane Poiseuille flow. The inset of the fig. 5.3 (c) shows the same data, but plots instead the Darcy friction factor  $f_D = 2fd/\rho u^2$  versus  $\text{Re}$ .

As discussed in section 2.2.1, the Forchheimer law is often used to describe relationships between friction loss and flow rates. In this work, we find that a generalized

Forchheimer equation, which takes into a finite crossover region between the scaling  $C_f \sim \text{constant}$  for  $\text{Re} \ll \text{Re}_c$ , and  $C_f \sim \text{Re}$  for  $\text{Re} \gg \text{Re}_c$ , fits the data well. This leads us to identify a critical Reynolds number  $\text{Re}_c$ , which quantifies the point where nonlinear flow sets in, and a purely geometric friction  $C_{f,0}$ . The latter two quantities depend on the roughness  $A$ , and lead to a reasonable data collapse for the data shown in fig. 5.3 (c). However, nonlinear friction is not synonymous with unsteadiness, and to assess the effect of transitional flow, we perform a Reynolds decomposition of the flow field,

$$\mathbf{u}'(\mathbf{x}, t) = \mathbf{u}(\mathbf{x}, t) - \bar{\mathbf{u}}(\mathbf{x}), \quad (5.16)$$

to obtain the velocity fluctuations  $\mathbf{u}'(\mathbf{x}, t)$ . Here,  $\mathbf{u}(\mathbf{x}, t)$  is the transient flow field, and  $\bar{\mathbf{u}}(\mathbf{x}) = \overline{\mathbf{u}(\mathbf{x}, t)}$  is the time-averaged flow field, sampled over a time period in the steady state as indicated in fig. 5.3 (b). Now, taking the time and space average of the squared velocity fluctuations,  $q = \langle |\mathbf{u}'(\mathbf{x}, t)|^2 \rangle$ , we obtain an indicator of the global turbulent intensity as the fluctuation-based Reynolds number  $\text{Re}' = \rho\sqrt{qd}/\mu$ . In fig. 5.3 (d), we show the fluctuation-based Reynolds number  $\text{Re}'$  plotted against the flux-based Reynolds number  $\text{Re}$  for all roughness amplitudes  $A$ . We observe that the relation between the two quantities is linear beyond a certain *second* critical Reynolds number  $\text{Re}_{c,q}$ . For sufficiently high roughness, this linear relation extends down to  $\text{Re}'$ , indicating a supercritical transition to turbulence, while for low  $\text{Re}$ , the transition is subcritical. This suggests that at a certain roughness amplitude  $A$ , the transition changes character from subcritical to supercritical.

Further, given that  $\text{Re}_{c,q}$  and  $\text{Re}_c$  are of comparable magnitude, we conclude that transitional flow may play a significant role in fracture flow, and must be accounted for in simulations on larger scales when roughness and flow rates are sufficiently high.

**REMAINING WORK** It would strengthen the results in Paper 3 to provide a more quantitative investigation of the suggested change of the transition from sub- to supercritical. Further, the robustness of the results to the particular realization of a self-affine surface, and secondly, to the streamwise and spanwise scale of the periodic domain, should be assessed. Numerical simulations investigating this are underway. Finally, it would be useful to estimate the quantitative contribution of the fluctuations to the friction factor.

**CONTRIBUTIONS** For the first paper, I wrote most of the manuscript, carried out simulations and analysed data. Renard initiated the study and wrote significant parts of the introduction and discussion. Renard and Mathiesen contributed in discussions and interpretation of the results.

The second manuscript was written by me, and I carried out simulations and analysed data. Angheluta and Mathiesen participated in discussions and in interpretation of results.

### 5.3 ELECTROHYDRODYNAMICS

These four papers concern fluid flow with solutes and electric fields. Papers 4 and 5 deal with single-phase electrohydrodynamics, while Papers 6 and 7 deal with two-phase systems. Some of this work was the basis for an invited talk by Mathiesen at AGU General Assembly, New Orleans, 2017. Some of this work was also presented in the thesis by Bolet<sup>[57]</sup>.

- PAPER 4:** Electrohydrodynamic channeling effects in narrow fractures and pores  
Asger Bolet, Gaute Linga, and Joachim Mathiesen  
*Physical Review E* **97**, 043114 (2018)
- PAPER 5:** Transient electrohydrodynamic flow with concentration-dependent fluid properties: modelling and energy-stable numerical schemes  
Gaute Linga, Asger Bolet, and Joachim Mathiesen  
Submitted to *Journal of Computational Physics* (2018)
- PAPER 6:** Bernaise: A flexible framework for simulating two-phase electrohydrodynamic flows in complex domains  
Gaute Linga, Asger Bolet, and Joachim Mathiesen  
Submitted (2018)
- PAPER 7:** Controlling wetting with electrolytic solutions: Phase-field simulations of a droplet-conductor system  
Gaute Linga, Asger Bolet, and Joachim Mathiesen  
*Physical Review E* **98**, 013101 (2018)

In Paper 4, we consider steady-state single-phase flow in a charged model microfracture. As mentioned briefly in section 2.1.1, the inherent nonlinearity of the governing equations has imparted that most numerical studies having been limited to geometries with a high degree of symmetry, such as 2D geometries<sup>[150,151]</sup> or axisymmetric cylindrical capillaries of finite length<sup>[286,287]</sup>. Here, we consider full three-dimensional simulations in a model fracture or narrow pore. Even simpler than the self-affine geometry in which we studied transitional flow (see section 5.2), we consider here a periodic channel where the bottom surface is sinusoidally undulated along the spanwise direction (see fig. 5.4).

We are here interested in electroviscous *flow channeling*, i.e. how fluid flow is directed to or from narrow parts of the channel, in the presence of a surface charge. This effect can have consequences for both transport on larger scales and surface growth in geological systems. We investigate the (i) impact of the Debye length  $\lambda_D$  (which characterises the extent of the electric double layer, see section 3.3), relative to the fracture aperture  $d$ , and (ii) the additional impact of the undulation amplitude on the flow channeling. The steady-state Stokes–Poisson–Nernst–Planck equations are solved using a hybrid algorithm similar to that proposed by Mitscha-Baude et al.<sup>[309]</sup>. The algorithm combines a Picard iteration scheme in an outer loop, splitting between the Stokes and the Poisson–Nernst–Planck subproblems. Here, the solver alternates between a linear solver for the linear Stokes problem, and a nonlinear solver for the Poisson–Nernst–Planck problem, which uses a Newton method in an inner loop. The method is detailed in the paper, and the problem is solved using FEniCS, with preconditioning using FENAPACK<sup>[55]</sup>. To quantify the flow channeling relative to the reference case of vanishing Debye length, we define the *relative asymmetry* (Eq. (29) in the paper). We find that compared to the case without surface charge, the flux can be reduced in the narrowest regions by up to 5%, and locally up to 10% velocity can be observed. Thus ridges may be more prone to precipitation than valleys, leading to even more pronounced channeling.

In Paper 5, we consider modelling of transient single-phase electrohydrodynamic flow. The model is derived by considering the single-phase electrohydrodynamic energy functional similar to that stated in eq. (3.49):

$$\mathcal{F} = \int_{\Omega} \left[ \frac{1}{2} \rho |\mathbf{u}|^2 + \sum_{j=1}^N M_j + \frac{1}{2} \epsilon |\mathbf{E}|^2 - \rho \mathbf{x} \cdot \mathbf{a}_{\text{grav}} \right]. \quad (5.17)$$

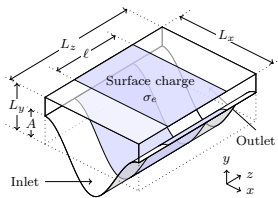
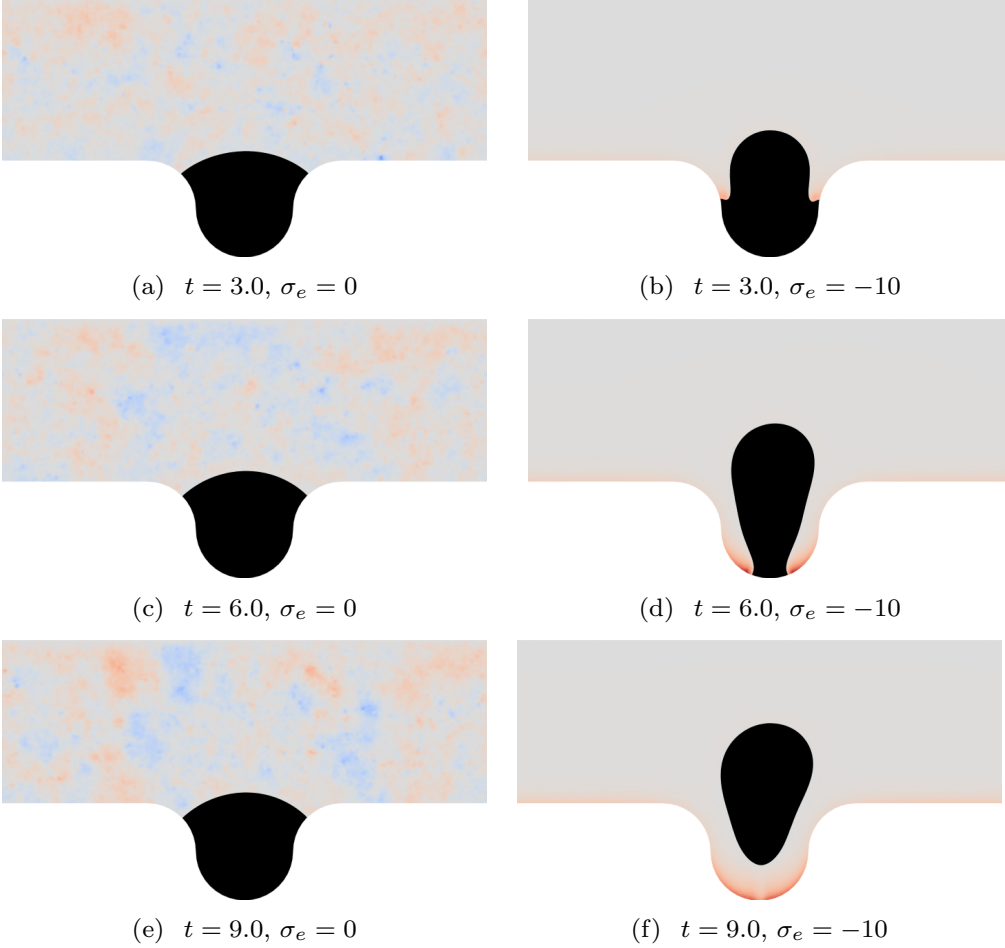


FIGURE 5.4: Sketch of the model microfracture or pore, wherein electrohydrodynamic channeling effects are studied. Reprinted from<sup>[58]</sup>.



**FIGURE 5.5:** Snapshots of simulations of a dead-end pore under a shear flow. The black phase (“oil”) does not contain solutes, and the other phase (“water”) contains a symmetric monovalent electrolyte. The color indicates net charge, red is positive and blue is negative. The left column shows a simulation without surface charge (and hence only numerical noise can be seen of the charge field), while the right column shows a simulation *with* surface charge. Reprinted from<sup>[263]</sup>.

Here, the added last term represents gravitational energy, and  $M_j$  is a generalized chemical energy. In contrast to the modelling in section 3.3, fluid parameters such as density, permittivity, and viscosity, are allowed to depend on the concentration fields, and we allow for chemical reactions to occur. We determine the chemical fluxes and the induced body force by using the Onsager variational principle in a similar way as in Refs.<sup>[2,79]</sup>. For the resulting model, we propose a set of energy-stable numerical schemes, similar to the more general scheme presented in section 4.2. The numerical schemes are implemented in BERNASE, and validated in the last part of the paper.

In Paper 6, we present BERNASE, which was already described in section 4.4.3, a framework for simulating two-phase electrohydrodynamics in complex geometries. The literature and background for the modelling approach is introduced in the first part of the paper. The basic model<sup>[79]</sup> is then presented, whereupon we present two numerical schemes: (i) a fully implicit scheme, and (ii) an alternative linear, decoupled scheme which splits the problem into three subproblems, as outlined in section 4.2. The latter scheme is validated through numerical simulations. First, the convergence of the scheme towards the theoretical profile of the phase-field interface is verified in both space and time. While, to our knowledge, no analytical reference solutions are available for dynamical simulations of two-phase electrohydrodynamics with soluble species, phase-field models can (in contrast to sharp-interface models) provide such solutions if augmented by appropriate source terms. This is known as the *method of manufactured solution*, which constitutes a powerful tool for validating numerical implementations. To this end, we present an electrohydrodynamic Taylor–Green vortex to address the temporal and spatial convergence, and find satisfactory convergence results. Finally,

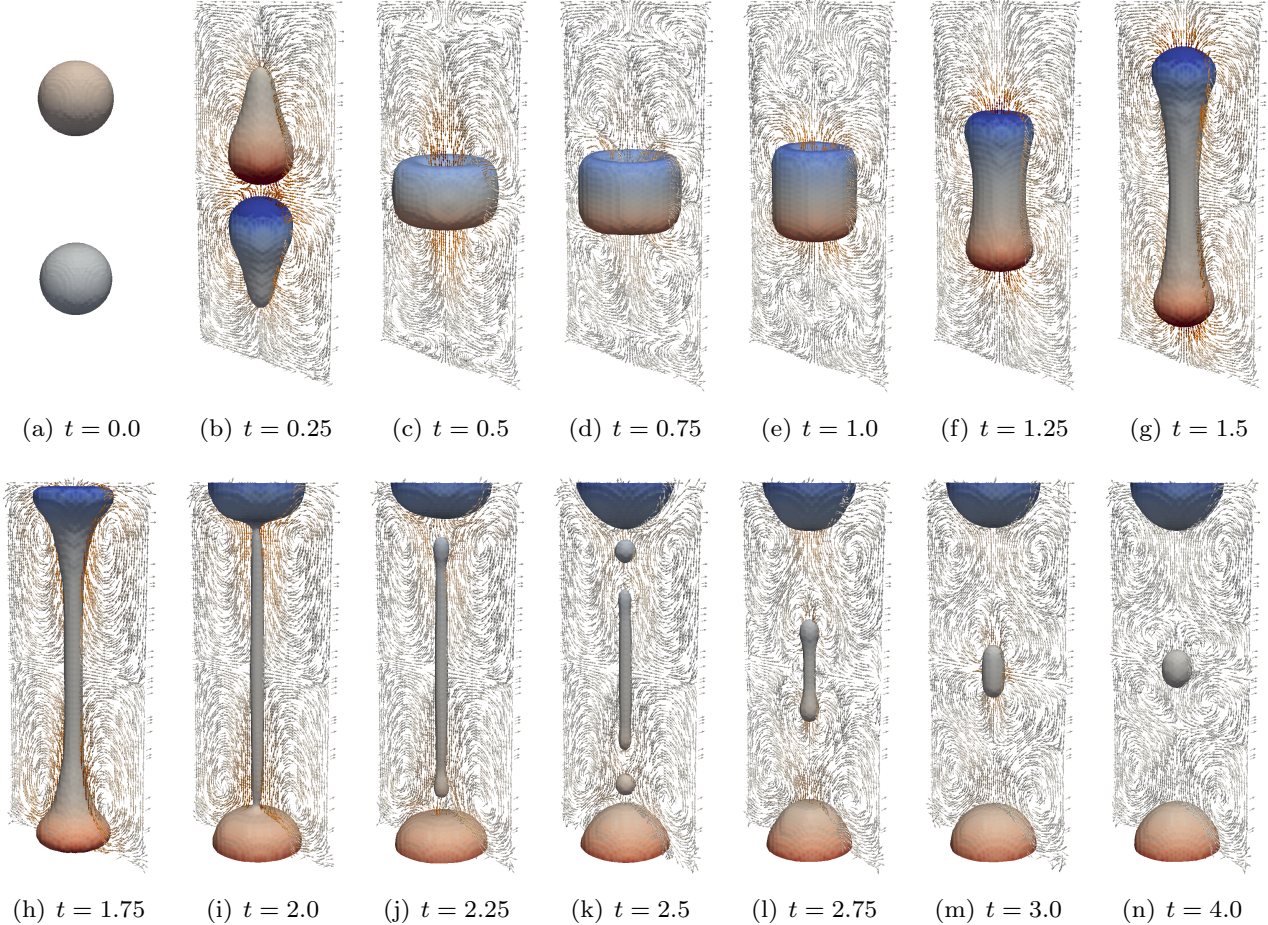


**FIGURE 5.6:** Coalescence and break-up of charged droplets, simulated using BERNNAISE. Reprinted from<sup>[263]</sup>.

convergence from the solution of the equations with finite interface thickness  $\varepsilon$  to the sharp-interface description in the limit  $\varepsilon \rightarrow 0^+$  is verified by comparison to a high-resolution reference solution. In a final part, we demonstrate two possible applications of the framework. First, we consider the expulsion of a droplet of one phase (“oil”) which is placed in a dead-end pore, where another phase (“water”) flows above. This should be a familiar set-up for readers who still remember section 1.2.

As shown in fig. 5.5, with shear flow and without any electrohydrodynamic effects, the droplet is stuck in the pore. By including electrohydrodynamic effects, a thin film of water is drawn into the pore and expels the oil droplet from the pore and releases it in the bulk flow. Although the parameter values used in the simulations are not real values, the results indicate that such a minimal model of electrochemical interactions at the pore scale can be a contributing factor to the enhanced oil recovery observed when injecting water of a particular salinity into porous rocks (see e.g.<sup>[145,179,192,382]</sup>). Secondly, we demonstrate that the code can be applied to studying droplet breakup and coalescence in full 3D, as shown in fig. 5.6.

In Paper 2, we quantitatively inspect the wetting properties of a single droplet of one phase sitting on an electrode, surrounded by a second phase. A potential drop is imposed across the system, and changes the wetting properties of the droplet, i.e. the contact angle. This set-up is fairly well-studied in terms of conducting liquids and relatively strong fields, in the context of electrowetting-on-dielectric (EWOD) devices. Here, we consider weak fields and a dissolved binary electrolyte in the surrounding fluid. We also consider an insulated electrode where no net current is allowed to pass through the system. Important theoretical progress in describing this system was achieved by Monroe

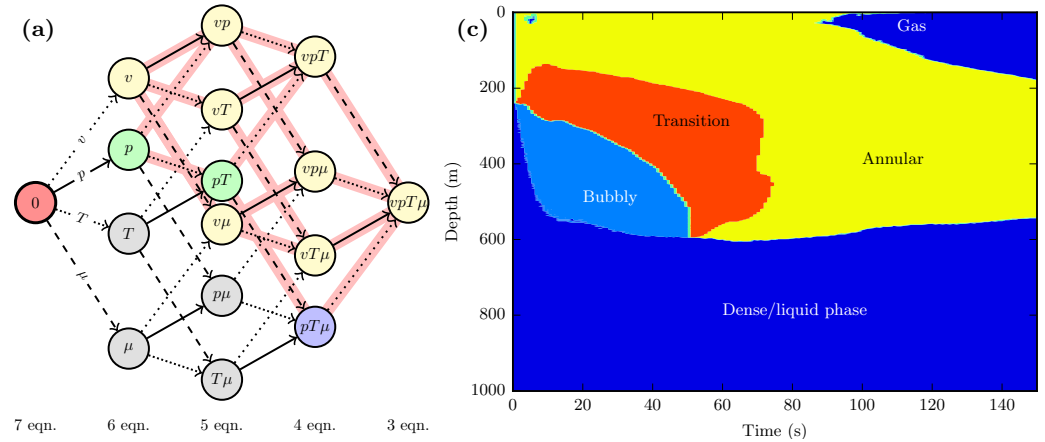
et al.<sup>[314, 315]</sup>, who used non-linear Poisson–Boltzmann theory to obtained an expression for the total Gibbs free energy of a so-called ITIES<sup>38</sup> system. They assumed that the Debye length was small enough to assume that one-dimensional back-to-back distributions could describe the chemical and potential distributions (and for the contact line region to be neglected), and by an energy minimization they obtained an expression for the dependence of the *apparent* contact angle (see section 2.1.3) on the applied potential and system parameters. In this work, we propose a heuristic generalization (or simplification) of the latter theory to concern a pure droplet phase. Dynamical simulations carried out using BERNAISE for a range of realistic parameters indicate that the theory well describes the apparent contact angle, and allows us to fit the only phenomenological dependence that appears in the theoretical description. From the simulations, we deduce an effective boundary condition that can be used in simulations on a larger scale, where the electric double layer is not fully resolved.

**CONTRIBUTIONS** In the first paper, all authors took part in designing the study. The numerical program used to carry out most of the simulations was written by Bolet, with input from me. Bolet performed most of the simulations, and I constructed the meshes, performed complementary simulations and theory, and contributed in discussions.

The remaining papers were written mainly be me. The topics studied in the papers are results of discussions with Bolet, who also wrote some sections in the last paper, and performed some of the code validation. Both Bolet and Mathiesen contributed with discussions and feedback on the manuscripts.

<sup>38</sup> Interface between two immiscible electrolyte solutions; where no ions can cross the fluid-fluid interface.

**FIGURE 5.7:** Theory and application of homogenized two-phase flow models. (a) The hierarchy of non-equilibrium two-phase flow models; reprinted from [259]. (b) Flow regimes in a CO<sub>2</sub> injection well during a blow-out scenario; reprinted from [260].



#### 5.4 HOMOGENIZED MODELS FOR TWO-PHASE FLOW

PAPER 8: A hierarchy of non-equilibrium two-phase flow models

Gaute Linga and Tore Flåtten

Submitted to *ESAIM: Proceedings & Surveys* (2018).

PAPER 9: A two-fluid model for vertical flow applied to CO<sub>2</sub> injection wells

Gaute Linga and Halvor Lund

*International Journal of Greenhouse Gas Control* **51**, 71–80 (2016)

*These two papers concern homogenized models for two-phase flow, which are typically applied to pipe flow.*

*Flåtten presented paper 8 at the Workshop on Compressible Multiphase Flows: Derivation, closure laws, thermodynamics, Strasbourg, May 2018. Most of the work forming the basis of this section was carried out before starting the PhD project, but the papers were completed during the course of the period.*

<sup>39</sup> That is, in the limit of instantaneously equal phase velocities, which makes the eigenstructure analytically tractable

In Paper 8, we start out with the Baer–Nunziato model<sup>[24]</sup>, and consider the relaxation processes discussed in section 3.2.3. From this, we can derive a hierarchy of relaxation models for two-phase flow with equilibrium in one or more of the variables pressure, temperature, chemical potential, and velocity. We review the resulting hierarchy, derive the remaining models and provide expressions for the sound velocities of the models.<sup>39</sup> In the context of two-phase flow models, the subcharacteristic condition implies that the fluid-mechanical speed of sound is reduced by every equilibrium assumption. We show, using simple techniques, that this condition is everywhere respected in the hierarchy, in the analytically tractable limit of equal phase velocities. This analytical result is supported numerically by plots of the model speeds of sound for the entire hierarchy, using data from two industrially relevant two-phase mixtures.

Paper 9 is of a more applied nature, and concerns modelling and simulation of two-phase flow in an injection well for CO<sub>2</sub>. The model, which assumes equilibrium in pressure, temperature and chemical potential, incorporates correlations for interface friction, wall friction and heat condition based on flow regimes (see section 2.1.3), and employs the accurate industrial Span–Wagner equation of state for CO<sub>2</sub><sup>[417]</sup>. We apply the model to studying sudden blowout and shut-in cases, in a well configuration chosen to resemble the Sleipner CO<sub>2</sub> injection well. The model is simulated numerically using a finite volume method detailed in the paper.

**CONTRIBUTIONS** The first paper was written by me, and I carried out the analysis. Flåtten contributed in designing the research, contributed in discussions, gave comments on the manuscript, and verified the analysis.

The second paper was written jointly with Lund. Both authors took part in development and implementation of the model and method, running simulations and writing of the paper.

# 6

## CLOSING REMARKS

---

It is now time to revisit the blunt question asked in the opening lines of the introduction: How does fluid flow through rocks? Although it is apparent that this question touches upon many scientific disciplines, and poses neither a *single* nor a *simple* answer, the author is of the opinion that some insights have been provided through the work presented in this thesis. Perhaps more importantly, the results provided lay the foundations for ensuing research that could potentially continue in many directions.

The unifying theme has been numerically resolving fluid flows with disordered interfaces. In one aspect, fluid flows near complex solid boundaries, i.e. fluid-solid interfaces, have been considered, spanning from laminar flow in an evolving porous medium, through high-Reynolds number flows in rough model fractures, to electrohydrodynamic flow over charged surfaces. Another aspect concerns the propagation of turbulent–laminar interfaces, i.e. turbulent fronts. A third aspect is the concurrent motion of fluid–fluid interfaces, which has been investigated also in the presence of electrohydrodynamic effects. Although these interfacial flows are governed by inherently different mechanisms, where the role of inertia and the time scale of interface motion varies strongly, the theory describing them, and the tools used to explore them, bear many similarities.

In this work, the research output has been threefold: We have contributed with (i) physical modelling, (ii) development of numerical methods and tools, and (iii) applications of the developed models and methods.

In the part of the work concerning single-phase transitional flow, we have developed a model that could help resolve the conundrum regarding Pomeau’s hypothesis on the universality class of the transition to turbulence in pipe flow. Also in fracture flow, the laminar–turbulent transition was investigated. Here, the friction factor was found to be sensitive to the roughness, leading to unsteady transitional flow accompanying the departure from linear friction. By numerically investigating the solid stress due to flow in a porous rock under dissolution, we observed a heavy-tailed distribution that could be useful to explaining how sensitive rocks are to slight increases in loading or fluid pressure.

In the part of the work concerning two-phase and electrohydrodynamic flows, multiple flow phenomena have been considered. This includes a numerical investigation of flow channeling in microfractures, wetting behaviour of droplets subject to electric fields, modelling of flow with concentration-dependent fluid properties, an analysis of a hierarchy of homogenized two-phase flow models, and modelling and simulation of a CO<sub>2</sub> injection well. Numerical methods that could provide efficient and robust simulations of electrohydrodynamic and interfacial flows have been developed.

Finally, and perhaps most prominently, the BERNASE framework for simulating two-phase electrohydrodynamic flow has been developed and documented. It is our hope that this framework can be of use not only for studying geophysically relevant settings, but also to be a useful tool to the microfluidics community, where many researchers rely on using proprietary (and to some extent *black-box*) software.

## 6.1 OUTLOOK

Having experienced the ups and downs of a project with a broad focus, it has occurred to me that project management and planning skills might be underrated assets in (at least some parts of) academia. An optimum of scientific quality and productivity—relative to the workload—would, in the author’s opinion, be obtained with a narrower focus and more rigid planning. On the other hand, perfect is the enemy of good. The broad scope (and the accompanying heavy workload) has, at least for the author, opened connections between topics that would otherwise seem less apparent.

It is my sincere hope that the work contained in this thesis will be helpful to others. In the following, I give some suggestions for avenues of future research, particularly with emphasis on the limitations of the present work.

**TRULY EVOLVING MICROSTRUCTURE:** With regard to the work presented in Papers 2 and 3, on single-phase flow in disordered geometries, it would be a natural step onwards to abandon the *one-way coupling* from the solid to fluid phase. The solid phase, and thus the accessible space for the fluid, would then deform due to fluid motion. This could occur due to dissolution or precipitation processes, either including a thermodynamic description, or along the lines of Hawkins et al.<sup>[181, 182]</sup>, where the solid grows proportionally to a concentration gradient. A part of the author’s stay at the University of Oslo was dedicated to developing a phase-field model for interface evolution incorporating solid stress into the thermodynamic description. This essentially couples an Asaro–Tiller–Grinfeld instability (see e.g.<sup>[228, 229]</sup>) to fluid flow. Evolving the microstructure by a sharp-interface method<sup>[17, 18, 338]</sup> would also be a possibility. However, precipitation kinetics becomes harder to model, since the precipitated solid need not inherit the state of stress from the solid it is precipitated onto; see e.g.<sup>[127]</sup> for a relevant discussion on crystal growth in confinement. A simpler approach is that taken by Jäger et al.<sup>[213, 214]</sup> where interface evolution is driven by deposition and erosion depending on the tangential shear force.

**FLOW AND STRESS DISTRIBUTIONS:** A limitation of the work presented in Paper 2 is that it is unclear whether the results can be extrapolated to other rocks, and to other deformation mechanisms than dissolution. A different mechanism of deformation would be fracturing of a rock, and an investigation of flow and stress evolution is underway in collaboration with François Renard at the University of Oslo.

Another open question concerns the observed “universal” stretched-exponential or power-exponential distribution of velocity<sup>[293]</sup> in porous media, and how much information about the pore geometry is necessary to predict the velocity (and stress) distribution. It seems likely that the ‘distance’ (in porosity) from the percolation threshold might determine the range of power-law scaling. Moreover, the effects on the distributions of wall slip, which could be important at the nanoscale<sup>[31]</sup>, and inertia, which could be important at larger scales, remain, to the author’s knowledge, open questions.

**PHASE-FIELD MODELLING:** The phase-field modelling considered herein, and the related numerics, could be improved in many ways. Although fairly complicated (at least in terms of number of fields and equations), the model in the state presented in the current thesis, constitutes an idealised representation of electrohydrodynamics. Real systems are usually dirty. As such, many possibly important effects have been neglected in the present work, including electrochemical reactions at the fluid-solid interface, thermal gradients, surfactants or other large molecules at the fluid-fluid interface (which could imply elastic effects<sup>[137]</sup>), and boundary inhomogeneities, to name a few. It would therefore be important to properly benchmark the models against experiments and/or

*ab initio* simulations. (It was briefly outlined in section 3.4.2 how to include surfactants, but no proper testing of this has yet been done.)

Another avenue would be to extend the model, with and without electrohydrodynamics, to encompassing more than two fluid phases. It is possible that augmenting the three-phase model by Minjeaud<sup>[305]</sup> with electrohydrodynamics is not particularly challenging, but extending that formulation to more than three phases (even without electrohydrodynamics) is known to be a non-trivial task. It could also be useful for simulation of many relevant systems, to let the third phase be a solid phase, such that interface evolution with two fluid phases could be simulated. By evolving the solid interface, one should then be able model electrodeposition<sup>[338]</sup> in the single-phase limit; relevant phase-field modelling approaches can be found in Refs.<sup>[181,182,473]</sup>.

**NUMERICAL METHODS:** The general scheme for two-phase electrohydrodynamics was presented and shown to be energy stable in section 4.2 and should thus provide robust solutions without energy blow-up. However, it is possible that these schemes introduce *too much* dissipation, i.e. that they require unnecessarily fine mesh and small time steps to reproduce the continuum equations. Another point in question is whether phase-field models (with finite interface thickness) in themselves may be overly dissipative compared to the sharp-interface equations which they are meant to represent. In particular, a critical evaluation of (i) which weighted averages should be used for the fluid properties across the interface, and (ii) how to model the phase-field mobility, should be carried out.

A limitation of the schemes presented here is that they are only first-order in time. It would be desirable to obtain higher-order temporal accuracy, and as shown e.g. in<sup>[403]</sup>, it is easy to construct schemes that are *formally* second-order using a backward differencing formula (BDF). However, it has not yet been possible to construct second-order schemes with the desired energy stability.

Finally, the solvers implemented in BERNASE could be optimized heavily, especially in terms of reusing system matrices along the lines of ref.<sup>[320]</sup> and in particular ref.<sup>[119]</sup>, possibly in combination with the Picard iteration scheme outlined in section 4.2.

**HEAT AND SOLUTE TRANSPORT:** In the spirit of e.g.<sup>[333–335]</sup>, it would be interesting both from a fundamental and a geothermal engineering point of view to extend investigate heat transfer both in 3D and to higher Re flows, particularly in fractures. This would, as a first approximation, amount to a one-way coupling of incompressible fluid flow to a *passive* scalar temperature field (much like how a passive concentration field is described herein). The natural first investigative steps would then be to seek the dependence of the Nusselt number, Nu (which measures the ratio of convective to conductive heat transfer), on the Reynolds number Re.

Another topic, which has drawn much attention both by the author, collaborators and others, is that of passive tracer transport in disordered media. In contrast to the concentration *fields* described previously in this thesis, we are here concerned with ensembles of particles advected solely by the velocity field  $\mathbf{u}$  (not by diffusion), similar to how tracer statistics is studied in turbulence. Early efforts on simplified models were reviewed by Bouchaud and Georges<sup>[63]</sup>, while the recent access to high-fidelity simulation tools and high-resolution tomography data of natural rocks has revived the subject and complemented the early models with direct simulations in a variety of real and synthetic porous geometries. The displacement of particles has been observed to be superdiffusive (in the direction of forcing) and subdiffusive (in the direction normal to forcing), see e.g.<sup>[199,226,246,275]</sup>. This is closely connected to the wide distribution of velocities in such geometries, as manifested in the Eulerian velocity PDFs. In 2D (synthetic) and 3D (synthetic and natural) systems, continuous-time random walks have

provided a framework for describing such transport<sup>[158]</sup>. While homogeneous porous media is well understood<sup>[254–256,256]</sup>, less is certain for dense and heterogeneous porous media, in particular close to the percolation point. However, as a numerical velocity field is only approximately divergence free, simulations in such geometries cause the problems that passive tracers can be spuriously ‘adsorbed’ to the boundary. This is particularly relevant for very narrow pore throats, and raises doubts about the validity of the results of e.g. Kang et al.<sup>[226]</sup>. As a first step, numerical solvers must be properly tested against pore network models, where quasi-analytical reference solutions can be found. Our preliminary results were reported in<sup>[186]</sup>, but are omitted here.

Solute transport in fractures has also been studied<sup>[122]</sup>, but many unanswered questions remain. In this respect, it would be interesting to study solute transport in 3D self-affine fractures at higher Re; in particular, can the results of Bouquain et al.<sup>[64]</sup> be generalized or extended to such geometries?

**TURBULENT FRONTS IN ROUGH PIPES:** As mentioned in section 2.1.2, flow in rough pipes has been extensively investigated in the fully turbulent regime, and transitional flows in smooth pipes have been studied for many years. However, little work has concerned the intersection of these two often separate areas—transitional flow in rough pipes—even though both roughness and transitional flows may appear in the context of blood flow in our bodies<sup>[238]</sup>. A reason for this being uncharted territory might be that it is extremely challenging to numerically resolve turbulent flow in large domains in the presence of complex boundaries, as spectral methods are not easily applicable to these settings (see section 4.1.2). Numerically, even lifetime statistics of puffs, at least close to criticality, may be out of reach for direct numerical simulations. It would therefore be a natural first step to investigate the speeds of turbulent fronts of single puffs and slugs in rough pipes, similar to the smooth-pipe study by Barkley et al.<sup>[30]</sup>. In this respect, the experiments by Cerbus et al.<sup>[87]</sup>, who essentially measured the friction factor of single puffs and slugs, would be interesting to compare with.

**SPATIO-TEMPORAL TRANSITION TO TURBULENCE:** The Barkley model<sup>[28–30]</sup> has provided great qualitative insight into the transition to turbulence in pipe flow. Moreover, it can also *quantitatively* describe most features of the spatio-temporal dynamics near the transition. However, this relies on fitting a set of model parameters to resemble the observations from experiments or direct numerical simulations. As discussed by Barkley<sup>[29]</sup>, a first-principles derivation of a macroscopic model (Barkley model or similar) for the transition is still lacking. The ‘holy grail’ is to predict, for example, front speeds from the Navier–Stokes equations. Another point to add, is the lack of an equivalent of the Barkley model for e.g. plane Poiseuille flow, which could help in understanding off-critical transitional flow in that system.

In this work, we studied transitional flow in fractures, but as demonstrated e.g. in Paper 1, the *really interesting* dynamics occurs in the study of collective motion of turbulent structures. By considering ensembles of large systems, thus, one might be able to investigate whether adding a ‘quenched randomness’ such as boundary roughness (possibly different from self-affine) may push shear flows out of the directed-percolation universality class.<sup>40</sup>

<sup>40</sup> Similar to how adding a quenched noise to the Kardar–Parisi–Zhang equation<sup>[227]</sup> changes its universality class<sup>[231]</sup>.

Investigations in this direction are already underway. Notably, the direct numerical simulation study by Ishida et al.<sup>[206]</sup> with transitional flow in the presence of several types of (effectively modelled) roughness displayed a richer phase diagram (in terms of flow regimes) than what has been observed for smooth-walled transitional flow. For large systems, however, computations are incredibly demanding. It is likely that the approach mainly taken in this project; involving unstructured meshes (explicitly representing

the boundary) and using the finite element method, is *not* the way to proceed for large systems. Instead, spectral methods on structured grids which *effectively* incorporate the rough boundary as a body force (see<sup>[77,206]</sup>) would likely lead to significant computational speedup.

**APPLICATIONS OF BERNASE:** The simulation framework developed in this project enables many possible applications, one of which being electrowetting, as shown in Paper<sup>[264][264]</sup>. Another interesting application could be to study phase separation kinetics (spinodal decomposition) in the presence of an electric field; related to the original motivation of Hohenberg and Halperin<sup>[196]</sup> to introduce their ‘Model H’ phase-field model. Droplet motion, coalescence, break-up, and pinch-off, particularly in the presence of solid surfaces and electrokinetic effects, would all provide interesting studies. Such effects are now possible to simulate efficiently in full 3D, in contrast to earlier studies which have often been limited to axisymmetric geometries; cf.<sup>[43]</sup> and related publications. Finally, we hope that, in time (and with possibly more validation, testing, and incorporation of necessary additional features), the framework could be used by the microfluidics community for prototyping and optimizing lab-on-a-chip devices.



## BIBLIOGRAPHY

---

- [1] U. J. F. Aarsnes, T. Flåtten, and O. M. Aamo. Review of two-phase flow models for control and estimation. *Annu. Rev. Control.*, 42:50–62, 2016. doi: 10.1016/j.arcontrol.2016.06.001.
- [2] H. Abels, H. Garcke, and G. Grün. Thermodynamically consistent, frame indifferent diffuse interface models for incompressible two-phase flows with different densities. *Math. Models Methods Appl. Sci.*, 22(03):1150013, 2012. doi: 10.1142/S0218202511500138.
- [3] H. Abels, H. Garcke, K. F. Lam, and J. Weber. Two-phase flow with surfactants: Diffuse interface models and their analysis. In *Transport Processes at Fluidic Interfaces*, pages 255–270. Springer, 2017.
- [4] S. Aland. Phase field models for two-phase flow with surfactants and biomembranes. In *Transport Processes at Fluidic Interfaces*, pages 271–290. Springer, 2017.
- [5] S. Aland and F. Chen. An efficient and energy stable scheme for a phase-field model for the moving contact line problem. *Int. J. Numer. Methods Fluids*, 81(11):657–671, 2016. doi: 10.1002/fld.4200.
- [6] S. Aland, S. Boden, A. Hahn, F. Klingbeil, M. Weismann, and S. Weller. Quantitative comparison of Taylor flow simulations based on sharp-interface and diffuse-interface models. *Int. J. Numer. Methods Fluids*, 73(4):344–361, 2013. doi: 10.1002/fld.3802.
- [7] S. Aland, A. Hahn, C. Kahle, and R. Nürnberg. Comparative simulations of Taylor flow with surfactants based on sharp-and diffuse-interface methods. In *Transport Processes at Fluidic Interfaces*, pages 639–661. Springer, 2017.
- [8] R. Allan and S. Mason. Particle behaviour in shear and electric fields I. Deformation and burst of fluid drops. *Proc. Royal Soc. A.*, 267(1328):45–61, 1962. doi: 10.1098/rspa.1962.0082.
- [9] J. Allen, M. Shockling, G. Kunkel, and A. Smits. Turbulent flow in smooth and rough pipes. *Philos. Trans. R. Soc. A.*, 365(1852):699–714, 2007. doi: 10.1098/rsta.2006.1939.
- [10] M. S. Alnæs, A. Logg, K. B. Ølgaard, M. E. Rognes, and G. N. Wells. Unified form language: A domain-specific language for weak formulations of partial differential equations. *ACM Trans. Math. Softw.*, 40(2):9, 2014. doi: 10.1145/2566630.
- [11] M. S. Alnæs, G. N. Wells, and J. Ring. Dijitso: Github repository. <https://bitbucket.org/fenics-project/dijitso/>, 2018.
- [12] C. B. Amos, P. Audet, W. C. Hammond, R. Bürgmann, I. A. Johanson, and G. Blewitt. Uplift and seismicity driven by groundwater depletion in central California. *Nature*, 509(7501):483, 2014. doi: 10.1038/nature13275.
- [13] D. M. Anderson, G. B. McFadden, and A. A. Wheeler. Diffuse-interface methods in fluid mechanics. *Annu. Rev. Fluid Mech.*, 30(1):139–165, 1998. doi: 10.1146/annurev.fluid.30.1.139.
- [14] H. Andrä, N. Combaret, J. Dvorkin, E. Glatt, J. Han, M. Kabel, Y. Keehm, F. Krzikalla, M. Lee, C. Madonna, et al. Digital rock physics benchmarks – Part II: Computing effective properties. *Comput. Geosci.*, 50:33–43, 2013. doi: 10.1016/j.cageo.2012.09.008.
- [15] J. Andrade Jr, M. Almeida, J. Mendes Filho, S. Havlin, B. Suki, and H. Stanley. Fluid flow through porous media: the role of stagnant zones. *Phys. Rev. Lett.*, 79(20):3901, 1997. doi: 10.1103/PhysRevLett.79.3901.
- [16] J. Andrade Jr, U. Costa, M. Almeida, H. Makse, and H. Stanley. Inertial effects on fluid flow through disordered porous media. *Phys. Rev. Lett.*, 82(26):5249, 1999. doi: 10.1103/PhysRevLett.82.5249.

- [17] L. Angheluta, E. Jettestuen, J. Mathiesen, F. Renard, and B. Jamtveit. Stress-driven phase transformation and the roughening of solid-solid interfaces. *Phys. Rev. Lett.*, 100(9):096105, 2008. doi: 10.1103/PhysRevLett.100.096105.
- [18] L. Angheluta, E. Jettestuen, and J. Mathiesen. Thermodynamics and roughening of solid-solid interfaces. *Phys. Rev. E*, 79(3):031601, 2009. doi: 10.1103/PhysRevE.79.031601.
- [19] D. N. Arnold and A. Logg. Periodic table of the finite elements. *SIAM News*, 47(9):212, 2014.
- [20] C. H. Arns, M. A. Knackstedt, W. V. Pinczewski, and E. J. Garboczi. Computation of linear elastic properties from microtomographic images: Methodology and agreement between theory and experiment. *Geophysics*, 67(5):1396–1405, 2002. doi: 10.1190/1.1512785.
- [21] C. Arson and T. Vanorio. Chemomechanical evolution of pore space in carbonate microstructures upon dissolution: Linking pore geometry to bulk elasticity. *J. Geophys. Res. Solid Earth*, 120(10): 6878–6894, 2015. doi: 10.1002/2015JB012087.
- [22] H. Auradou, G. Drazer, J.-P. Hulin, and J. Koplik. Permeability anisotropy induced by the shear displacement of rough fracture walls. *Water Resour. Res.*, 41(9):W09423, 2005. doi: 10.1029/2005WR003938.
- [23] K. Avila, D. Moxey, A. de Lozar, M. Avila, D. Barkley, and B. Hof. The onset of turbulence in pipe flow. *Science*, 333(6039):192–196, 2011. doi: 10.1126/science.1203223.
- [24] M. Baer and J. Nunziato. A two-phase mixture theory for the deflagration-to-detonation transition (DDT) in reactive granular materials. *Int. J. Multiph. Flow*, 12(6):861–889, 1986. doi: 10.1016/0301-9322(86)90033-9.
- [25] S. Balay, S. Abhyankar, M. F. Adams, J. Brown, P. Brune, K. Buschelman, L. Dalcin, V. Eijkhout, W. D. Gropp, D. Kaushik, M. G. Knepley, D. A. May, L. C. McInnes, K. Rupp, B. F. Smith, S. Zampini, H. Zhang, and H. Zhang. PETSc web page. <http://www.mcs.anl.gov/petsc>, 2017. URL <http://www.mcs.anl.gov/petsc>.
- [26] A.-L. Barabási and H. E. Stanley. *Fractal concepts in surface growth*. Cambridge University Press, 1995.
- [27] A. J. Bard and L. R. Faulkner. *Electrochemical methods: fundamentals and applications*, volume 2. Wiley, New York, 2 edition, 2001.
- [28] D. Barkley. Simplifying the complexity of pipe flow. *Phys. Rev. E*, 84(1):016309, 2011. doi: 10.1103/PhysRevE.84.016309.
- [29] D. Barkley. Theoretical perspective on the route to turbulence in a pipe. *J. Fluid Mech.*, 803:P1, 2016. doi: 10.1017/jfm.2016.465.
- [30] D. Barkley, B. Song, V. Mukund, G. Lemoult, M. Avila, and B. Hof. The rise of fully turbulent flow. *Nature*, 526:550–553, 2015. doi: 10.1038/nature15701.
- [31] J.-L. Barrat and L. Bocquet. Large slip effect at a nonwetting fluid-solid interface. *Phys. Rev. Lett.*, 82 (23):4671, 1999. doi: 10.1103/PhysRevLett.82.4671.
- [32] J. Baygents and D. Saville. The circulation produced in a drop by an electric field: a high field strength electrokinetic model. In *AIP Conf. Proc.*, volume 197, pages 7–17. AIP, 1990.
- [33] M. Z. Bazant. Electrokinetics meets electrohydrodynamics. *J. Fluid Mech.*, 782:1–4, 2015. doi: 10.1017/jfm.2015.416.
- [34] M. Z. Bazant, K. Thornton, and A. Ajdari. Diffuse-charge dynamics in electrochemical systems. *Phys. Rev. E*, 70(2):021506, 2004. doi: 10.1103/PhysRevE.70.021506.
- [35] D. Beamish and R. Peart. Electrokinetic geophysics: a review. *Terra Nova*, 10(1):48–55, 1998. doi: 10.1046/j.1365-3121.1998.00160.x.
- [36] J. Bear, C.-F. Tsang, and G. De Marsily. *Flow and contaminant transport in fractured rock*. Academic Press, 1993.
- [37] G. Beni and S. Hackwood. Electro-wetting displays. *Appl. Phys. Lett.*, 38(4):207–209, 1981. doi: 10.1063/1.92322.

- [38] G. Beni and M. Tenan. Dynamics of electrowetting displays. *J. Appl. Phys.*, 52(10):6011–6015, 1981. doi: 10.1063/1.329822.
- [39] B. Berge. Electrocapillarité et mouillage de films isolants par l'eau. *C. R. Acad. Sci. IIB*, 317(2):157–163, 1993.
- [40] B. Berkowitz. Characterizing flow and transport in fractured geological media: A review. *Adv. Water Resour.*, 25(8-12):861–884, 2002. doi: 10.1016/S0309-1708(02)00042-8.
- [41] Y. Bernabé and A. Revil. Pore-scale heterogeneity, energy dissipation and the transport properties of rocks. *Geophys. Res. Lett.*, 22(12):1529–1532, 1995. doi: 10.1029/95GL01418.
- [42] I. Berre, F. Doster, and E. Keilegavlen. Flow in fractured porous media: A review of conceptual models and discretization approaches. arXiv:1805.05701, 2018.
- [43] J. Berry, M. Davidson, and D. J. Harvie. A multiphase electrokinetic flow model for electrolytes with liquid/liquid interfaces. *J. Comput. Phys.*, 251:209–222, 2013. doi: 10.1016/j.jcp.2013.05.026.
- [44] E. Bertrand, D. Bonn, D. Broseta, H. Dobbs, J. Indekeu, J. Meunier, K. Ragil, and N. Shahidzadeh. Wetting of alkanes on water. *J. Pet. Sci. Eng.*, 33(1-3):217–222, 2002. doi: 10.1016/S0920-4105(01)00191-7.
- [45] E. Besterman and R. Creese. Waller—pioneer of electrocardiography. *Br. Heart J.*, 42(1):61, 1979.
- [46] D. Bestion. The physical closure laws in the cathare code. *Nuclear Engineering and Design*, 124(3):229–245, 1990. doi: 10.1016/0029-5493(90)90294-8.
- [47] B. Bijeljic, A. H. Muggeridge, and M. J. Blunt. Pore-scale modeling of longitudinal dispersion. *Water Resour. Res.*, 40(11), 2004. doi: 10.1029/2004WR003567.
- [48] B. Bijeljic, A. Raeini, P. Mostaghimi, and M. J. Blunt. Predictions of non-fickian solute transport in different classes of porous media using direct simulation on pore-scale images. *Phys. Rev. E*, 87(1):013011, 2013. doi: 10.1103/PhysRevE.87.013011.
- [49] M. A. Biot. General theory of three-dimensional consolidation. *J. Appl. Phys.*, 12(2):155–164, 1941. doi: 10.1063/1.1712886.
- [50] M. A. Biot. Theory of elasticity and consolidation for a porous anisotropic solid. *J. Appl. Phys.*, 26(2):182–185, 1955. doi: 10.1063/1.1721956.
- [51] M. A. Biot. Theory of propagation of elastic waves in a fluid-saturated porous solid. I. Low frequency range. *J. Acoust. Soc. Am.*, 28(2):168–178, 1956. doi: 10.1121/1.1908239.
- [52] M. A. Biot. Theory of propagation of elastic waves in a fluid-saturated porous solid. II. Higher frequency range. *J. Acoust. Soc. Am.*, 28(2):179–191, 1956. doi: 10.1121/1.1908241.
- [53] E. Bjørklund. The level-set method applied to droplet dynamics in the presence of an electric field. *Comput. Fluids*, 38(2):358–369, 2009. doi: 10.1016/j.compfluid.2008.04.008.
- [54] T. Blake and J. Haynes. Kinetics of liquid-liquid displacement. *J. Colloid Interface Sci.*, 30(3):421–423, 1969. doi: 10.1016/0021-9797(69)90411-1.
- [55] J. Blechta and M. Řehoř. Fenapack. <https://github.com/blechta/fenapack>, 2018.
- [56] M. J. Blunt, B. Bijeljic, H. Dong, O. Gharbi, S. Iglesias, P. Mostaghimi, A. Paluszny, and C. Pentland. Pore-scale imaging and modelling. *Adv. Water Resour.*, 51:197–216, 2013. doi: 10.1016/j.advwatres.2012.03.003.
- [57] A. Bolet. *Electrohydrodynamics in one and two phases*. PhD thesis, Niels Bohr Institute, University of Copenhagen, 2018.
- [58] A. Bolet, G. Linga, and J. Mathiesen. Electrohydrodynamic channeling effects in narrow fractures and pores. *Phys. Rev. E*, 97:043114, 2018. doi: 10.1103/PhysRevE.97.043114.
- [59] D. Bonamy, L. Ponson, S. Prades, E. Bouchaud, and C. Guillot. Scaling exponents for fracture surfaces in homogeneous glass and glassy ceramics. *Phys. Rev. Lett.*, 97(13):135504, 2006. doi: 10.1103/PhysRevLett.97.135504.

- [60] D. Bonn, J. Eggers, J. Indekeu, J. Meunier, and E. Rolley. Wetting and spreading. *Rev. Mod. Phys.*, 81(2):739, 2009. doi: 10.1103/RevModPhys.81.739.
- [61] E. Bouchaud. Scaling properties of cracks. *J. Phys. Condens. Matter*, 9(21):4319, 1997. doi: 10.1088/0953-8984/9/21/002.
- [62] E. Bouchaud, G. Lapasset, and J. Planes. Fractal dimension of fractured surfaces: a universal value? *Europhys. Lett.*, 13(1):73, 1990. doi: 10.1209/0295-5075/13/1/013.
- [63] J.-P. Bouchaud and A. Georges. Anomalous diffusion in disordered media: statistical mechanisms, models and physical applications. *Phys. Rep.*, 195(4-5):127–293, 1990. doi: 10.1016/0370-1573(90)90099-N.
- [64] J. Bouquain, Y. Méheust, D. Bolster, and P. Davy. The impact of inertial effects on solute dispersion in a channel with periodically varying aperture. *Phys. Fluids*, 24(8):083602, 2012. doi: 10.1063/1.4747458.
- [65] BP. BP Statistical Review of World Energy 2017, 2017.
- [66] J. Brackbill, D. B. Kothe, and C. Zemach. A continuum method for modeling surface tension. *J. Comput. Phys.*, 100(2):335–354, 1992. doi: 10.1016/0021-9991(92)90240-Y.
- [67] S. C. Brenner and L. R. Scott. *The Mathematical Theory of Finite Element Methods*. Springer Science & Business Media, 3 edition, 2008.
- [68] F. Brezzi. On the existence, uniqueness and approximation of saddle-point problems arising from Lagrangian multipliers. *R.A.I.R.O. Analyse Numérique*, 8(R2):129–151, 1974. doi: 10.1051/m2an/197408R201291.
- [69] S. Briggs, B. W. Karney, and B. E. Sleep. Numerical modeling of the effects of roughness on flow and eddy formation in fractures. *J. Rock Mech. Geotechnical Eng.*, 9(1):105–115, 2017. doi: 10.1016/j.jrmge.2016.08.004.
- [70] S. R. Broadbent and J. M. Hammersley. Percolation processes: I. Crystals and mazes. In *Math. Proc. Camb. Philos. Soc.*, volume 53, pages 629–641. Cambridge University Press, 1957.
- [71] G. O. Brown. The history of the Darcy–Weisbach equation for pipe flow resistance. In *Environmental and Water Resources History*, pages 34–43. American Society of Civil Engineers, 2003.
- [72] S. R. Brown. Fluid flow through rock joints: the effect of surface roughness. *J. Geophys. Res. Solid Earth*, 92(B2):1337–1347, 1987. doi: 10.1029/JB092iB02p01337.
- [73] D. J. Brush and N. R. Thomson. Fluid flow in synthetic rough-walled fractures: Navier–Stokes, Stokes, and local cubic law simulations. *Water Resour. Res.*, 39(4):SBH, 2003. doi: 10.1029/2002WR001346.
- [74] H. Bruus. *Theoretical microfluidics*, volume 18. Oxford University Press, 2008.
- [75] J. B. Buckheit and D. L. Donoho. Wavelab and reproducible research. In *Wavelets and statistics*, pages 55–81. Springer, 1995.
- [76] T. Bultreys, W. De Boever, and V. Cnudde. Imaging and image-based fluid transport modeling at the pore scale in geological materials: A practical introduction to the current state-of-the-art. *Earth-Sci. Rev.*, 155:93–128, 2016. doi: 10.1016/j.earscirev.2016.02.001.
- [77] A. Busse and N. D. Sandham. Parametric forcing approach to rough-wall turbulent channel flow. *J. Fluid Mech.*, 712:169–202, 2012. doi: 10.1017/jfm.2012.408.
- [78] J. W. Cahn and J. E. Hilliard. Free energy of a nonuniform system. I. interfacial free energy. *J. Chem. Phys.*, 28(2):258–267, 1958. doi: 10.1063/1.1744102.
- [79] E. Campillo-Funollet, G. Grün, and F. Klingbeil. On modeling and simulation of electrokinetic phenomena in two-phase flow with general mass densities. *SIAM J. Appl. Math.*, 72(6):1899–1925, 2012. doi: 10.1137/120861333.
- [80] M. B. Cardenas, D. T. Slottke, R. A. Ketcham, and J. M. Sharp. Effects of inertia and directionality on flow and transport in a rough asymmetric fracture. *J. Geophys. Res. Solid Earth*, 114(B6), 2009. doi: 10.1029/2009JB006336.

- [81] A. Carlson. *Capillarity and dynamic wetting*. PhD thesis, KTH Royal Institute of Technology, 2012.
- [82] A. Carlson, M. Do-Quang, and G. Amberg. Modeling of dynamic wetting far from equilibrium. *Phys. Fluids*, 21(12):121701, 2009. doi: 10.1063/1.3275853.
- [83] A. Carlson, G. Bellani, and G. Amberg. Universality in dynamic wetting dominated by contact-line friction. *Phys. Rev. E*, 85(4):045302, 2012. doi: 10.1103/PhysRevE.85.045302.
- [84] P. C. Carman. Fluid flow through granular beds. *Trans. Inst. Chem. Eng.*, 15:150–166, 1937. doi: 10.1016/S0263-8762(97)80003-2.
- [85] P. C. Carman. *Flow of gases through porous media*. Academic Press, 1956.
- [86] CDP. CDP: the Unstructured LES Code. <https://web.stanford.edu/group/cits/research/combustor/cdp.html>, 2004.
- [87] R. T. Cerbus, C.-c. Liu, G. Gioia, and P. Chakraborty. Laws of resistance in transitional pipe flows. *Phys. Rev. Lett.*, 120(5):054502, 2018. doi: 10.1103/PhysRevLett.120.054502.
- [88] H.-C. Chang and L. Y. Yeo. *Electrokinetically driven microfluidics and nanofluidics*. Cambridge University Press, 2010.
- [89] M. Chantry, L. S. Tuckerman, and D. Barkley. Universal continuous transition to turbulence in a planar shear flow. *J. Fluid Mech.*, 824:R1, 2017. doi: 10.1017/jfm.2017.405.
- [90] D. L. Chapman. A contribution to the theory of electrocapillarity. *Philos. Mag.*, 25(148):475–481, 1913. doi: 10.1080/14786440408634187.
- [91] R.-C. Chen and J.-L. Liu. An iterative method for adaptive finite element solutions of an energy transport model of semiconductor devices. *J. Comput. Phys.*, 189(2):579–606, 2003. doi: 10.1016/S0021-9991(03)00247-X.
- [92] A. J. Chorin. A numerical method for solving incompressible viscous flow problems. *J. Comput. Phys.*, 2(1):12–26, 1967. doi: 10.1016/0021-9991(67)90037-X.
- [93] A. J. Chorin. Numerical solution of the Navier–Stokes equations. *Math. Comp.*, 22(104):745–762, 1968. doi: 10.1090/S0025-5718-1968-0242392-2.
- [94] T. Chou, K. Mallick, and R. Zia. Non-equilibrium statistical mechanics: from a paradigmatic model to biological transport. *Rep. Prog. Phys.*, 74(11):116601, 2011. doi: 10.1088/0034-4885/74/11/116601.
- [95] A. Clauset, C. R. Shalizi, and M. E. Newman. Power-law distributions in empirical data. *SIAM Rev.*, 51(4):661–703, 2009. doi: 10.1137/070710111.
- [96] C. Colebrook and C. White. Experiments with fluid friction in roughened pipes. *Proc. Royal Soc. A*, 161(906):367–381, 1937. doi: 10.1098/rspa.1937.0150.
- [97] D. Coles. Interfaces and intermittency in turbulent shear flow. *Mécanique de la Turbulence*, 108: 229–248, 1962.
- [98] J. Cooper, L. Stamford, and A. Azapagic. Shale gas: a review of the economic, environmental, and social sustainability. *Energy Technology*, 4(7):772–792, 2016. doi: 10.1002/ente.201500464.
- [99] A. Costa. Permeability-porosity relationship: A reexamination of the Kozeny–Carman equation based on a fractal pore-space geometry assumption. *Geophys. Res. Lett.*, 33(2):L02318, 2006. doi: 10.1029/2005GL025134.
- [100] F. G. Cottrell and J. B. Speed. Separating and collecting particles of one liquid suspended in another liquid, 1911. US Patent 987, 115.
- [101] R. Cox. The dynamics of the spreading of liquids on a solid surface. Part 1. Viscous flow. *J. Fluid Mech.*, 168:169–194, 1986. doi: 10.1017/S0022112086000332.
- [102] A. D. Craik. George Gabriel Stokes on water wave theory. *Annu. Rev. Fluid Mech.*, 37:23–42, 2005. doi: 10.1146/annurev.fluid.37.061903.175836.
- [103] E. Custodio. Trends in groundwater pollution: loss of groundwater quality and related services. Technical report, Groundwater Governance, 2013.

- [104] T. J. Danielson. Transient multiphase flow: past, present, and future with flow assurance perspective. *Energy Fuels*, 26(7):4137–4144, 2012. doi: 10.1021/ef300300u.
- [105] A. Darbyshire and T. Mullin. Transition to turbulence in constant-mass-flux pipe flow. *J. Fluid Mech.*, 289:83–114, 1995. doi: 10.1017/S0022112095001248.
- [106] H. Darcy. *Les fontaines publiques de la ville de Dijon*. Victor Dalmont, Paris, 1856.
- [107] H. Darcy. *Recherches expérimentales relatives au mouvement de l'eau dans les tuyaux*, volume 1. Mallet-Bachelier, 1857.
- [108] S. S. Datta, H. Chiang, T. S. Ramakrishnan, and D. A. Weitz. Spatial fluctuations of fluid velocities in flow through a three-dimensional porous medium. *Phys. Rev. Lett.*, 111:064501, Aug 2013. doi: 10.1103/PhysRevLett.111.064501.
- [109] C. David, T.-F. Wong, W. Zhu, and J. Zhang. Laboratory measurement of compaction-induced permeability change in porous rocks: Implications for the generation and maintenance of pore pressure excess in the crust. *Pure. Appl. Geophys.*, 143(1-3):425–456, 1994. doi: 10.1007/BF00874337.
- [110] P. de Anna, T. Le Borgne, M. Dentz, A. M. Tartakovsky, D. Bolster, and P. Davy. Flow intermittency, dispersion, and correlated continuous time random walks in porous media. *Phys. Rev. Lett.*, 110(18):184502, 2013. doi: 10.1103/PhysRevLett.110.184502.
- [111] R. de Boer. Highlights in the historical development of the porous media theory: toward a consistent macroscopic theory. *Appl. Mech. Rev.*, 49(4):201–262, 1996. doi: 10.1115/1.3101926.
- [112] J. A. de Chalendar, C. Garing, and S. M. Benson. Pore-scale modelling of Ostwald ripening. *J. Fluid Mech.*, 835:363–392, 2018. doi: 10.1017/jfm.2017.720.
- [113] P.-G. de Gennes. Wetting: statics and dynamics. *Rev. Mod. Phys.*, 57(3):827, 1985. doi: 10.1103/RevModPhys.57.827.
- [114] I. E. M. de Graaf. *Limits to global groundwater consumption: Effects on groundwater levels and river low flows*. PhD thesis, Utrecht University, 2016.
- [115] P. Debye and E. Hückel. Zur theorie der elektrolyte. I. Gefrierpunktserniedrigung und verwandte erscheinungen. *Phyz. Z.*, 24(9):185–206, 1923.
- [116] P. Debye and E. Hückel. Zur theorie der elektrolyte. II. Das grenzgesetz für die elektrische leitfähigkeit. *Phyz. Z.*, 24(9):185–206, 1923.
- [117] A. Delesse. Procede mecanique pour determiner la composition des roches. *Ann. Min.*, 13:379–388, 1848.
- [118] H. Ding, P. D. Spelt, and C. Shu. Diffuse interface model for incompressible two-phase flows with large density ratios. *J. Comput. Phys.*, 226(2):2078–2095, 2007. doi: 10.1016/j.jcp.2007.06.028.
- [119] S. Dong and J. Shen. A time-stepping scheme involving constant coefficient matrices for phase-field simulations of two-phase incompressible flows with large density ratios. *J. Comput. Phys.*, 231(17):5788–5804, 2012. doi: 10.1016/j.jcp.2012.04.041.
- [120] J. Douglas Jr and T. Arbogast. Dual porosity models for flow in naturally fractured reservoirs. In *Dynamics of Fluids in Hierarchical Porous Media*, pages 177–221. Academic Press London, UK, 1990.
- [121] G. Drazer and J. Koplik. Permeability of self-affine rough fractures. *Phys. Rev. E*, 62(6):8076, 2000. doi: 10.1103/PhysRevE.62.8076.
- [122] G. Drazer and J. Koplik. Transport in rough self-affine fractures. *Phys. Rev. E*, 66(2):026303, 2002. doi: 10.1103/PhysRevE.66.026303.
- [123] D. A. Drew. Mathematical modeling of two-phase flow. *Annu. Rev. Fluid Mech.*, 15(1):261–291, 1983. doi: 10.1146/annurev.fl.15.010183.001401.
- [124] D. A. Drew and S. L. Passman. *Theory of multicomponent fluids*, volume 135. Springer, 2006.
- [125] W. Durham and B. Bonner. Self-propping and fluid flow in slightly offset joints at high effective pressures. *J. Geophys. Res. Solid Earth*, 99(B5):9391–9399, 1994. doi: 10.1029/94JB00242.

- [126] E. Dussan. On the spreading of liquids on solid surfaces: static and dynamic contact lines. *Annu. Rev. Fluid Mech.*, 11(1):371–400, 1979. doi: 10.1146/annurev.fl.11.010179.002103.
- [127] D. K. Dysthe. Shaping the interface – interactions between confined water and the confining solid. In *Transport and Reactivity of Solutions in Confined Hydrosystems*, pages 199–212. Springer, 2014.
- [128] C. Eck, M. Fontelos, G. Grün, F. Klingbeil, and O. Vantzos. On a phase-field model for electrowetting. *Interface Free Bound.*, 11(2):259–290, 2009. doi: 10.4171/IFB/211.
- [129] M. Eckert. The troublesome birth of hydrodynamic stability theory: Sommerfeld and the turbulence problem. *Eur. Phys. J. H.*, 35(1):29–51, 2010. doi: 10.1140/epjh/e2010-00003-3.
- [130] D. Edwards, M. Shapiro, P. Bar-Yoseph, and M. Shapira. The influence of Reynolds number upon the apparent permeability of spatially periodic arrays of cylinders. *Phys. Fluids A*, 2(1):45–55, 1990. doi: 10.1063/1.857691.
- [131] S. Ehrenberg, G. Eberli, M. Keramati, and S. Moallemi. Porosity-permeability relationships in inter-layered limestone-dolostone reservoirs. *AAPG Bulletin*, 90(1):91–114, 2006. doi: 10.1306/08100505087.
- [132] H. C. Elman, D. J. Silvester, and A. J. Wathen. *Finite elements and fast iterative solvers: with applications in incompressible fluid dynamics*. Numerical Mathematics and Scientific Computation, 2014.
- [133] S. Engblom, M. Do-Quang, G. Amberg, and A.-K. Tornberg. On diffuse interface modeling and simulation of surfactants in two-phase fluid flow. *Commun. Comput. Phys.*, 14(4):879–915, 2013. doi: 10.4208/cicp.120712.281212a.
- [134] S. Ergun. Fluid flow through packed columns. *Chem. Eng. Prog.*, 48:89–94, 1952.
- [135] Å. Ervik. *Multiscale modelling using molecular dynamics and interfacecapturing methods for two-phase flow simulation of droplets covered with surfactants or asphaltenes, and applications to electrocoalescence*. PhD thesis, NTNU, 2016.
- [136] Å. Ervik, K. Y. Lervåg, and S. T. Munkejord. A robust method for calculating interface curvature and normal vectors using an extracted local level set. *J. Comput. Phys.*, 257:259–277, 2014. doi: 10.1016/j.jcp.2013.09.053.
- [137] Å. Ervik, M. O. Lysgaard, C. Herdes, G. Jim'enez-Serratos, E. A. Müller, S. T. Munkejord, and B. Müller. A multiscale method for simulating fluid interfaces covered with large molecules such as asphaltenes. *J. Comput. Phys.*, 327:576 – 611, 2016. doi: 10.1016/j.jcp.2016.09.039.
- [138] L. Euler. Principe généraux de l'état d'équilibre des fluides. *Mémoires de l'Académie des Sciences de Berlin*, pages 217–273, 1757.
- [139] L. Euler. Anleitung zur naturlehre. *Opera postuma mathematica et physica, Bd*, pages 1–2, 1762.
- [140] L. Euler. *Lettres à une princesse d'Allemagne sur divers sujet de physique et de philosophie*. St. Petersbourg: Imprimerie de l'Academie Imperiale des Sciences, 1768.
- [141] European Commission. Horizon 2020, work programme 2017–2018, 2017.
- [142] R. D. Falgout and U. M. Yang. hypre: A library of high performance preconditioners. In *International Conference on Computational Science*, pages 632–641. Springer, 2002.
- [143] Q. Fang and D. A. Boas. Tetrahedral mesh generation from volumetric binary and grayscale images. In *Biomedical Imaging: From Nano to Macro, 2009. ISBI'09. IEEE International Symposium on*, pages 1142–1145. IEEE, 2009.
- [144] J. T. Fanning. *A Practical Treatise on Water-supply Engineering: Relating to the Hydrology, Hydrodynamics, and Practical Construction of Water-works, in North America. With Numerous Tables and Illustrations*. D. Van Nostrand, 1877.
- [145] S. J. Fathi, T. Austad, and S. Strand. “Smart water” as a wettability modifier in chalk: the effect of salinity and ionic composition. *Energy Fuels*, 24(4):2514–2519, 2010. doi: 10.1021/ef901304m.
- [146] J. Feder. *Fractals*. Springer, 2013.

- [147] A. Fernández, G. Tryggvason, J. Che, and S. L. Ceccio. The effects of electrostatic forces on the distribution of drops in a channel flow: Two-dimensional oblate drops. *Phys. Fluids*, 17(9):093302, 2005. doi: 10.1063/1.2043147.
- [148] P. J. M. Ferrer, T. Flåtten, and S. T. Munkejord. On the effect of temperature and velocity relaxation in two-phase flow models. *ESAIM Math. Model. Numer. Anal.*, 46(2):411–442, 2012. doi: 10.1051/m2an/2011039.
- [149] A. Fick. Ueber diffusion. *Ann. Phys.*, 170(1):59–86, 1855. doi: 10.1002/andp.18551700105.
- [150] E.-A. Fiorentino, R. Toussaint, and L. Jouniaux. Lattice Boltzmann modelling of streaming potentials: variations with salinity in monophasic conditions. *Geophys. J. Int.*, 205(1):648–664, 2016. doi: 10.1093/gji/ggw041.
- [151] E.-A. Fiorentino, R. Toussaint, and L. Jouniaux. Two-phase lattice Boltzmann modelling of streaming potentials: influence of the air-water interface on the electrokinetic coupling. *Geophys. J. Int.*, 208(2): 1139–1156, 2016. doi: 10.1093/gji/ggw417.
- [152] P. Fischer, J. Kruse, J. Mullen, H. Tufo, J. Lottes, and S. Kerkemeier. Nek5000. <https://nek5000.mcs.anl.gov/community/>, 2018.
- [153] T. Flåtten and H. Lund. Relaxation two-phase flow models and the subcharacteristic condition. *Math. Models Methods Appl. Sci.*, 21(12):2379–2407, 2011. doi: 10.1142/S0218202511005775.
- [154] H. Fletcher. My work with Millikan on the oil-drop experiment. *Physics Today*, 35(6):43–47, 1982. doi: 10.1063/1.2915126.
- [155] P. J. Flory. Molecular size distribution in three dimensional polymers. I. Gelation. *J. Am. Chem. Soc.*, 63(11):3083–3090, 1941. doi: 10.1021/ja01856a061.
- [156] P. H. Forchheimer. Wasserbewegung durch boden. *Zeitz. Ver. Duetch Ing.*, 45:1782–1788, 1901.
- [157] M. Fourar, G. Radilla, R. Lenormand, and C. Moyne. On the non-linear behavior of a laminar single-phase flow through two and three-dimensional porous media. *Adv. Water Resour.*, 27(6):669–677, 2004. doi: 10.1016/j.advwatres.2004.02.021.
- [158] I. Fouzon and M. Holzner. Solvable continuous-time random walk model of the motion of tracer particles through porous media. *Phys. Rev. E*, 94(2):022132, 2016. doi: 10.1103/PhysRevE.94.022132.
- [159] A. C. Fowler and A. C. Fowler. *Mathematical models in the applied sciences*, volume 17. Cambridge University Press, 1997.
- [160] A. Frumkin, A. Gorodetskaya, B. Kabanov, and N. Nekrasov. Electrocapillary phenomena and the wetting of metals by electrolytic solutions, i. *I. Phys Z. Sowjetunion*, 1:255–339, 1932.
- [161] H. Garcke, K. F. Lam, and B. Stinner. Diffuse interface modelling of soluble surfactants in two-phase flow. [arXiv:1303.2559](https://arxiv.org/abs/1303.2559), 2013.
- [162] J. W. Gibbs. A method of geometrical representation of the thermodynamic properties by means of surfaces. *Trans. Conn. Acad. Arts Sci.*, pages 382–404, 1873.
- [163] R. Gill, M. J. Harbottle, J. Smith, and S. Thornton. Electrokinetic-enhanced bioremediation of organic contaminants: A review of processes and environmental applications. *Chemosphere*, 107:31–42, 2014. doi: 10.1016/j.chemosphere.2014.03.019.
- [164] N. Goldenfeld. Roughness-induced critical phenomena in a turbulent flow. *Phys. Rev. Lett.*, 96(4): 044503, 2006. doi: 10.1103/PhysRevLett.96.044503.
- [165] N. Goldenfeld and H.-Y. Shih. Turbulence as a problem in non-equilibrium statistical mechanics. *J. Stat. Phys.*, 167:575–594, 2017. doi: 10.1007/s10955-016-1682-x.
- [166] N. Goldenfeld, N. Guttenberg, and G. Gioia. Extreme fluctuations and the finite lifetime of the turbulent state. *Phys. Rev. E*, 81(3):035304, 2010. doi: 10.1103/PhysRevE.81.035304.
- [167] L. G. Gouy. Sur la constitution de la charge électrique à la surface d'un électrolyte. *C. R. Hebdo. Seances Acad. Sci.*, 149:354–357, 1909.

- [168] L. G. Gouy. Sur la constitution de la charge électrique à la surface d'un électrolyte. *J. Phys. Theor. Appl.*, 9(1):457–468, 1910. doi: 10.1051/jphystap:019100090045700.
- [169] D. C. Grahame. The electrical double layer and the theory of electrocapillarity. *Chem. Rev.*, 41(3):441–501, 1947. doi: 10.1021/cr60130a002.
- [170] P. Grassberger. On phase transitions in Schlägl's second model. *Z. Phys. B*, 47(4):365–374, 1982. doi: 10.1007/BF01313803.
- [171] J.-P. Gratier, P. Favreau, and F. Renard. Modeling fluid transfer along California faults when integrating pressure solution crack sealing and compaction processes. *J. Geophys. Res. Solid Earth*, 108(B2):2104, 2003. doi: 10.1029/2001JB000380.
- [172] P. M. Gresho and R. L. Sani. *Incompressible flow and the finite element method*. John Wiley & Sons, 1998.
- [173] Y. Guglielmi, F. Cappa, J. P. Avouac, P. Henry, and D. Elsworth. Seismicity triggered by fluid injection-induced aseismic slip. *Science*, 348:1224–1226, 2015. doi: 10.1126/science.aab0476.
- [174] I. Gunnarsson and S. Arnórsson. Impact of silica scaling on the efficiency of heat extraction from high-temperature geothermal fluids. *Geothermics*, 34(3):320–329, 2005. doi: 10.1016/j.geothermics.2005.02.002.
- [175] R. Gutfraind and A. Hansen. Study of fracture permeability using lattice gas automata. *Transp. Porous Media*, 18(2):131–149, 1995. doi: 10.1007/BF01064675.
- [176] R. A. Guyer and H. A. Kim. Theoretical model for fluid-solid coupling in porous materials. *Phys. Rev. E*, 91(4):042406, 2015. doi: 10.1103/PhysRevE.91.042406.
- [177] G. Hagen. Ueber die bewegung des wassers in engen cylindrischen röhren. *Ann. Phys.*, 122(3):423–442, 1839.
- [178] F. H. Harlow and J. E. Welch. Numerical calculation of time-dependent viscous incompressible flow of fluid with free surface. *Phys. Fluids*, 8(12):2182–2189, 1965. doi: 10.1063/1.1761178.
- [179] T. Hassenkam, C. S. Pedersen, K. Dalby, T. Austad, and S. L. S. Stipp. Pore scale observation of low salinity effects on outcrop and oil reservoir sandstone. *Colloids Surf. A*, 390(1):179–188, 2011. doi: 10.1016/j.colsurfa.2011.09.025.
- [180] F. Hauksbee. *Physico-mechanical Experiments on Various Subjects: Containing an Account of Several Surprizing Phaenomena Touching Light and Electricity, Producible on the Attrition of Bodies. With Many Other Remarkable Appearances, Not Before Observ'd. Together with the Explanations of All the Machines,(the Figures of which are Curiously Engrav'd on Copper) and Other Apparatus Us'd in Making the Experiments.* R. Brugis, 1709.
- [181] C. Hawkins, L. Angheluta, Ø. Hammer, and B. Jamtveit. Precipitation dendrites in channel flow. *Europhys. Lett.*, 102(5):54001, 2013. doi: 10.1209/0295-5075/102/54001.
- [182] C. Hawkins, L. Angheluta, and B. Jamtveit. Hydrodynamic shadowing effect during precipitation of dendrites in channel flow. *Phys. Rev. E*, 89(2):022402, 2014. doi: 10.1103/PhysRevE.89.022402.
- [183] R. A. Hayes and B. J. Feenstra. Video-speed electronic paper based on electrowetting. *Nature*, 425(6956):383, 2003. doi: 10.1038/nature01988.
- [184] D. Helbing. Traffic and related self-driven many-particle systems. *Rev. Mod. Phys.*, 73(4):1067, 2001. doi: 10.1103/RevModPhys.73.1067.
- [185] C. H. Hendon. Brewing a great cup of coffee depends on chemistry and physics. The Conversation. <https://theconversation.com/brewing-a-great-cup-of-coffee-depends-on-chemistry-and-physics-84473>, 2017.
- [186] A. Hernandez-Garcia. *Numerical simulations and mathematical models of flows in complex geometries*. PhD thesis, Niels Bohr Institute, University of Copenhagen, 2016.
- [187] M. A. Heroux, R. A. Bartlett, V. E. Howle, R. J. Hoekstra, J. J. Hu, T. G. Kolda, R. B. Lehoucq, K. R. Long, R. P. Pawłowski, E. T. Phipps, et al. An overview of the Trilinos project. *ACM Trans. Math. Softw.*, 31(3):397–423, 2005. doi: 10.1145/1089014.1089021.

- [188] M. R. Hestenes and E. Stiefel. *Methods of conjugate gradients for solving linear systems*, volume 49. NBS Washington, DC, 1952.
- [189] D. R. Hewitt, J. S. Nijjer, M. G. Worster, and J. A. Neufeld. Flow-induced compaction of a deformable porous medium. *Phys. Rev. E*, 93(2):023116, 2016. doi: 10.1103/PhysRevE.93.023116.
- [190] R. J. Hill, D. L. Koch, and A. J. Ladd. The first effects of fluid inertia on flows in ordered and random arrays of spheres. *J. Fluid Mech.*, 448:213–241, 2001. doi: 10.1017/S0022112001005936.
- [191] R. J. Hill, D. L. Koch, and A. J. Ladd. Moderate-Reynolds-number flows in ordered and random arrays of spheres. *J. Fluid Mech.*, 448:243–278, 2001. doi: 10.1017/S0022112001005936.
- [192] E. Hilner, M. P. Andersson, T. Hassenkam, J. Matthiesen, P. Salino, and S. L. S. Stipp. The effect of ionic strength on oil adhesion in sandstone – the search for the low salinity mechanism. *Sci. Rep.*, 5: 9933, 2015. doi: 10.1038/srep09933.
- [193] H. Hinrichsen. Non-equilibrium critical phenomena and phase transitions into absorbing states. *Adv. Phys.*, 49(7):815–958, 2000. doi: 10.1080/00018730050198152.
- [194] H. Hinrichsen. On possible experimental realizations of directed percolation. *Braz. J. Phys.*, 30(1): 69–82, 2000. doi: 10.1590/S0103-97332000000100007.
- [195] B. Hof, A. De Lozar, M. Avila, X. Tu, and T. M. Schneider. Eliminating turbulence in spatially intermittent flows. *Science*, 327(5972):1491–1494, 2010. doi: 10.1126/science.1186091.
- [196] P. C. Hohenberg and B. I. Halperin. Theory of dynamic critical phenomena. *Rev. Mod. Phys.*, 49(3): 435, 1977. doi: 10.1103/RevModPhys.49.435.
- [197] H. Holmås. *Numerical simulation of waves in two-phase pipe flow using 1D two-fluid models*. PhD thesis, Faculty of Mathematics and Natural Sciences, University of Oslo, 2008.
- [198] K. E. Holter, B. Kehlet, A. Devor, T. J. Sejnowski, A. M. Dale, S. W. Omholt, O. P. Ottersen, E. A. Nagelhus, K.-A. Mardal, and K. H. Pettersen. Interstitial solute transport in 3D reconstructed neuropil occurs by diffusion rather than bulk flow. *Proc. Natl. Acad. Sci.*, 114(37):9894–9899, 2017. doi: 10.1073/pnas.1706942114.
- [199] M. Holzner, V. L. Morales, M. Willmann, and M. Dentz. Intermittent Lagrangian velocities and accelerations in three-dimensional porous medium flow. *Phys. Rev. E*, 92(1):013015, 2015. doi: 10.1103/PhysRevE.92.013015.
- [200] J.-J. Huang, H. Huang, and X. Wang. Wetting boundary conditions in numerical simulation of binary fluids by using phase-field method: some comparative studies and new development. *Int. J. Numer. Methods Fluids*, 77(3):123–158, 2015. doi: 10.1002/fld.3975.
- [201] C. Huh and L. Scriven. Hydrodynamic model of steady movement of a solid/liquid/fluid contact line. *J. Colloid Interface Sci.*, 35(1):85–101, 1971. doi: 10.1016/0021-9797(71)90188-3.
- [202] M. Hultmark, M. Vallikivi, S. Bailey, and A. Smits. Turbulent pipe flow at extreme Reynolds numbers. *Phys. Rev. Lett.*, 108(9):094501, 2012. doi: 10.1103/PhysRevLett.108.094501.
- [203] H. E. Huppert and J. A. Neufeld. The fluid mechanics of carbon dioxide sequestration. *Annu. Rev. Fluid Mech.*, 46:255–272, 2014. doi: 10.1146/annurev-fluid-011212-140627.
- [204] IEA. Energy technology perspectives 2014, 2014.
- [205] T. Ihle and D. Kroll. Stochastic rotation dynamics: a Galilean-invariant mesoscopic model for fluid flow. *Phys. Rev. E*, 63(2):020201, 2001. doi: 10.1103/PhysRevE.63.020201.
- [206] T. Ishida, G. Brethouwer, Y. Duguet, and T. Tsukahara. Laminar-turbulent patterns with rough walls. *Phys. Rev. Fluids*, 2(7):073901, 2017. doi: 10.1103/PhysRevFluids.2.073901.
- [207] T. Ishido and H. Mizutani. Experimental and theoretical basis of electrokinetic phenomena in rock-water systems and its applications to geophysics. *J. Geophys. Res. Solid Earth*, 86(B3):1763–1775, 1981. doi: 10.1029/JB086iB03p01763.
- [208] M. Ishii and T. Hibiki. *Thermo-fluid dynamics of two-phase flow*. Springer, 2010.

- [209] S. Izbasch. O filtracii v kropnozernstom materiale. Leningrad, USSR, 1931.
- [210] J. Jackel, S. Hackwood, and G. Beni. Electrowetting optical switch. *Appl. Phys. Lett.*, 40(1):4–5, 1982. doi: 10.1063/1.92920.
- [211] D. Jacqmin. Calculation of two-phase Navier–Stokes flows using phase-field modeling. *J. Comput. Phys.*, 155(1):96–127, 1999. doi: 10.1006/jcph.1999.6332.
- [212] D. Jacqmin. Contact-line dynamics of a diffuse fluid interface. *J. Fluid Mech.*, 402:57–88, 2000. doi: 10.1017/S0022112099006874.
- [213] R. Jäger, M. Mendoza, and H. J. Herrmann. Channelization in porous media driven by erosion and deposition. *Phys. Rev. E*, 95(1):013110, 2017. doi: 10.1103/PhysRevE.95.013110.
- [214] R. Jäger, M. Mendoza, and H. J. Herrmann. Mechanism behind erosive bursts in porous media. *Phys. Rev. Lett.*, 119(12):124501, 2017. doi: 10.1103/PhysRevLett.119.124501.
- [215] B. Jamtveit and Ø. Hammer. Sculpting of rocks by reactive fluids. *Geochem. Perspect.*, 1:341–477, 2012.
- [216] H.-K. Janssen. On the nonequilibrium phase transition in reaction-diffusion systems with an absorbing stationary state. *Z. Phys. B*, 42(2):151–154, 1981. doi: 10.1007/BF01319549.
- [217] H. Jasak, A. Jemcov, Z. Tukovic, et al. OpenFOAM: A C++ library for complex physics simulations. In *International workshop on coupled methods in numerical dynamics*, volume 1000, pages 1–20. IUC Dubrovnik, Croatia, 2007.
- [218] L. Jasinski and M. Dabrowski. The effective transmissivity of a plane-walled fracture with circular cylindrical obstacles. *J. Geophys. Res. Solid Earth*, 123(1):242–263, 2018. doi: 10.1002/2017JB014509.
- [219] L. Jasinski, D. Sangaré, P. Adler, V. Mourzenko, J.-F. Thovert, N. Gland, and S. Békri. Transport properties of a Bentheim sandstone under deformation. *Phys. Rev. E*, 91(1):013304, 2015. doi: 10.1103/PhysRevE.91.013304.
- [220] M. Javadi, M. Sharifzadeh, K. Shahriar, and Y. Mitani. Critical Reynolds number for nonlinear flow through rough-walled fractures: The role of shear processes. *Water Resour. Res.*, 50(2):1789–1804, 2014. doi: 10.1002/2013WR014610.
- [221] I. Jensen. Low-density series expansions for directed percolation: I. a new efficient algorithm with applications to the square lattice. *Journal of Physics A: Mathematical and General*, 32(28):5233, 1999. doi: 10.1088/0305-4470/32/28/304.
- [222] F. Jiang and T. Tsuji. Changes in pore geometry and relative permeability caused by carbonate precipitation in porous media. *Phys. Rev. E*, 90(5):053306, 2014. doi: 10.1103/PhysRevE.90.053306.
- [223] C. Jin, P. Langston, G. Pavlovskaya, M. Hall, and S. Rigby. Statistics of highly heterogeneous flow fields confined to three-dimensional random porous media. *Phys. Rev. E*, 93(1):013122, 2016. doi: 10.1103/PhysRevE.93.013122.
- [224] Y. Jin, J. Dong, X. Zhang, X. Li, and Y. Wu. Scale and size effects on fluid flow through self-affine rough fractures. *Int. J. Heat Mass Transf.*, 105:443–451, 2017. doi: 10.1016/j.ijheatmasstransfer.2016.10.010.
- [225] V. Joekar-Niasar and S. Hassanizadeh. Analysis of fundamentals of two-phase flow in porous media using dynamic pore-network models: A review. *Crit. Rev. Environ. Sci. Technol.*, 42(18):1895–1976, 2012. doi: 10.1080/10643389.2011.574101.
- [226] P. K. Kang, P. Anna, J. P. Nunes, B. Bijeljic, M. J. Blunt, and R. Juanes. Pore-scale intermittent velocity structure underpinning anomalous transport through 3-D porous media. *Geophys. Res. Lett.*, 41(17): 6184–6190, 2014. doi: 10.1002/2014GL061475.
- [227] M. Kardar, G. Parisi, and Y.-C. Zhang. Dynamic scaling of growing interfaces. *Phys. Rev. Lett.*, 56(9): 889, 1986. doi: 10.1103/PhysRevLett.56.889.
- [228] K. Kassner and C. Misbah. A phase-field approach for stress-induced instabilities. *Europhys. Lett.*, 46(2):217, 1999. doi: 10.1209/epl/i1999-00247-9.
- [229] K. Kassner, C. Misbah, J. Müller, J. Kappey, and P. Kohlert. Phase-field modeling of stress-induced instabilities. *Phys. Rev. E*, 63(3):036117, 2001. doi: 10.1103/PhysRevE.63.036117.

- [230] B. Kehlet. Mshr: Git repository. <https://bitbucket.org/fenics-project/mshr>, 2018.
- [231] D. A. Kessler, H. Levine, and Y. Tu. Interface fluctuations in random media. *Phys. Rev. A*, 43(8):4551, 1991. doi: 10.1103/PhysRevA.43.4551.
- [232] J. Kim. Phase-field models for multi-component fluid flows. *Commun. Comput. Phys.*, 12(3):613–661, 2012. doi: 10.4208/cicp.301110.040811a.
- [233] B.J. Kirby. *Micro-and nanoscale fluid mechanics: transport in microfluidic devices*. Cambridge University Press, 2010.
- [234] R. C. Kirby. Algorithm 839: Fiat, a new paradigm for computing finite element basis functions. *ACM Trans. Math. Softw.*, 30(4):502–516, 2004. doi: 10.1145/1039813.1039820.
- [235] R. C. Kirby and A. Logg. A compiler for variational forms. *ACM Trans. Math. Softw.*, 32(3):417–444, 2006. doi: 10.1145/1163641.1163644.
- [236] A. Klöckner. Meshpy. <https://mathematician.de/software/meshpy/>, 2018.
- [237] J. Kozeny. Über kapillare leitung der wasser in boden. *Royal Academy of Science, Vienna, Proc. Class I*, 136:271–306, 1927.
- [238] D. N. Ku. Blood flow in arteries. *Annu. Rev. Fluid Mech.*, 29(1):399–434, 1997. doi: 10.1146/annurev.fluid.29.1.399.
- [239] H. Lan, C. D. Martin, and B. Hu. Effect of heterogeneity of brittle rock on micromechanical extensile behavior during compression loading. *J. Geophys. Res. Solid Earth*, 115(B1):B01202, 2010. doi: 10.1029/2009JB006496.
- [240] H. P. Langtangen and A. Logg. *Solving PDEs in Python*. Springer, 2017. ISBN 978-3-319-52461-0. doi: 10.1007/978-3-319-52462-7.
- [241] H. P. Langtangen, K.-A. Mardal, and R. Winther. Numerical methods for incompressible viscous flow. *Adv. Water Resour.*, 25(8–12):1125–1146, 2002. doi: 10.1016/S0309-1708(02)00052-0.
- [242] P. S. Laplace. *Traité de mécanique céleste. Supplément au dixième livre*, volume 4. Crapelet, 1805.
- [243] D. Lasseux, A. A. Abbasian Arani, and A. Ahmadi. On the stationary macroscopic inertial effects for one phase flow in ordered and disordered porous media. *Phys. Fluids*, 23(7):073103, 2011. doi: 10.1063/1.3615514.
- [244] H. Laubie, F. Radjai, R. Pellenq, and F.-J. Uhlmann. Stress transmission and failure in disordered porous media. *Phys. Rev. Lett.*, 119(7):075501, 2017. doi: 10.1103/PhysRevLett.119.075501.
- [245] B. Lautrup. *Physics of continuous matter: exotic and everyday phenomena in the macroscopic world*. CRC Press, 2004.
- [246] T. Le Borgne, M. Dentz, and J. Carrera. Lagrangian statistical model for transport in highly heterogeneous velocity fields. *Phys. Rev. Lett.*, 101(9):090601, 2008. doi: 10.1103/PhysRevLett.101.090601.
- [247] T. Le Borgne, M. Dentz, and E. Villermaux. Stretching, coalescence, and mixing in porous media. *Phys. Rev. Lett.*, 110(20):204501, 2013. doi: 10.1103/PhysRevLett.110.204501.
- [248] L. Lebon, L. Oger, J. Leblond, J. Hulin, N. Martys, and L. Schwartz. Pulsed gradient NMR measurements and numerical simulation of flow velocity distribution in sphere packings. *Phys. Fluids*, 8(2):293–301, 1996. doi: 10.1063/1.869307.
- [249] J. Lee and C.-J. Kim. Surface-tension-driven microactuation based on continuous electrowetting. *J. Microelectromech. Syst.*, 9(2):171–180, 2000. doi: 10.1109/84.846697.
- [250] M. Lee and R. D. Moser. Direct numerical simulation of turbulent channel flow up to  $Re_\tau \approx 5200$ . *J. Fluid Mech.*, 774:395–415, 2015. doi: 10.1017/jfm.2015.268.
- [251] L. Leger and J. Joanny. Liquid spreading. *Rep. Prog. Phys.*, 55(4):431, 1992. doi: 10.1088/0034-4885/55/4/001.
- [252] G. Lemoult, L. Shi, K. Avila, S. V. Jalikop, M. Avila, and B. Hof. Directed percolation phase transition to sustained turbulence in Couette flow. *Nat. Phys.*, 12(3):254–258, 2016. doi: 10.1038/nphys3675.

- [253] K. Y. Lervåg. *Calculation of interface curvatures with the level-set method for two-phase flow simulations and a second-order diffuse-domain method for elliptic problems in complex geometries*. PhD thesis, Norges teknisk-naturvitenskapelige universitet, Fakultet for ingeniørvitenskap og teknologi, Institutt for energi-og prosessteknikk, 2013.
- [254] D. Lester, G. Metcalfe, and M. Trefry. Anomalous transport and chaotic advection in homogeneous porous media. *Phys. Rev. E*, 90(6):063012, 2014. doi: 10.1103/PhysRevE.90.063012.
- [255] D. R. Lester, G. Metcalfe, and M. G. Trefry. Is chaotic advection inherent to porous media flow? *Phys. Rev. Lett.*, 111:174101, Oct 2013. doi: 10.1103/PhysRevLett.111.174101.
- [256] D. R. Lester, M. Dentz, and T. Le Borgne. Chaotic mixing in three-dimensional porous media. *J. Fluid Mech.*, 803:144–174, 2016. doi: 10.1017/jfm.2016.486.
- [257] V. G. Levich. *Physicochemical hydrodynamics*. Prentice Hall, 1962.
- [258] Y. Lin, P. Skjetne, and A. Carlson. A phase field model for multiphase electro-hydrodynamic flow. *Int. J. Multiph. Flow*, 45:1–11, 2012. doi: 10.1016/j.ijmultiphaseflow.2012.04.002.
- [259] G. Linga and T. Flåtten. A hierarchy of non-equilibrium two-phase flow models. arXiv:1804.05241, 2018.
- [260] G. Linga and H. Lund. A two-fluid model for vertical flow applied to CO<sub>2</sub> injection wells. *Int. J. Greenh. Gas Con.*, 51:71–80, 2016. doi: 10.1016/j.ijggc.2016.05.009.
- [261] G. Linga, J. Mathiesen, and F. Renard. Self-similar distributions of fluid velocity and stress heterogeneity in a dissolving porous limestone. *J. Geophys. Res. Solid Earth*, 122(3):1726–1743, 2017. doi: 10.1002/2016JB013536.
- [262] G. Linga, L. Angheluta, and J. Mathiesen. Transitional flow in self-affine rough channels. unpublished, 2018.
- [263] G. Linga, A. Bolet, and J. Mathiesen. Bernaise: A flexible framework for two-phase electrohydrodynamic flow. submitted, 2018.
- [264] G. Linga, A. Bolet, and J. Mathiesen. Controlling wetting with electrolytic solutions: Phase-field simulations of a droplet-conductor system. *Phys. Rev. E*, 98:013101, 2018. doi: 10.1103/PhysRevE.98.013101.
- [265] G. Linga, A. Bolet, and J. Mathiesen. Transient electrohydrodynamic flow with concentration-dependent fluid properties: modelling and energy-stable numerical schemes. submitted, 2018.
- [266] H. Linga. *Measurements of two-phase flow details: non-intrusive methods applied to slug and dispersed flows*. PhD thesis, Norges Tekniske Høgskole, 1992.
- [267] G. Lippmann. *Relations entre les phénomènes électriques et capillaires*. PhD thesis, Sorbonne, 1875.
- [268] J.-L. Liu and B. Eisenberg. Numerical methods for a Poisson–Nernst–Planck–Fermi model of biological ion channels. *Phys. Rev. E*, 92(1):012711, 2015. doi: 10.1103/PhysRevE.92.012711.
- [269] T. S. Lo and J. Koplik. Suspension flow and sedimentation in self-affine fractures. *Phys. Fluids*, 24(5):053303, 2012. doi: 10.1063/1.4717529.
- [270] T. S. Lo and J. Koplik. Channeling and stress during fluid and suspension flow in self-affine fractures. *Phys. Rev. E*, 89(2):023010, 2014. doi: 10.1103/PhysRevE.89.023010.
- [271] D. Lo Jacono, F. Plouraboué, and A. Bergeon. Weak-inertial flow between two rough surfaces. *Phys. Fluids*, 17(6):063602, 2005. doi: 10.1063/1.1923347.
- [272] A. Logg, K.-A. Mardal, and G. Wells. *Automated solution of differential equations by the finite element method: The FEniCS book*, volume 84. Springer Science & Business Media, 2012.
- [273] A. Logg, G. N. Wells, and J. Hake. DOLFIN: A C++/Python finite element library. In *Automated Solution of Differential Equations by the Finite Element Method*, pages 173–225. Springer, 2012.
- [274] J. López-Herrera, S. Popinet, and M. Herrada. A charge-conservative approach for simulating electrohydrodynamic two-phase flows using volume-of-fluid. *J. Comput. Phys.*, 230(5):1939–1955, 2011. doi: 10.1016/j.jcp.2010.11.042.

- [275] C. P. Lowe and D. Frenkel. Do hydrodynamic dispersion coefficients exist? *Phys. Rev. Lett.*, 77: 4552–4555, Nov 1996. doi: 10.1103/PhysRevLett.77.4552.
- [276] J. Lowengrub and L. Truskinovsky. Quasi-incompressible Cahn–Hilliard fluids and topological transitions. *Proc. Royal Soc. A*, 454(1978):2617–2654, 1998. doi: 10.1098/rspa.1998.0273.
- [277] H.-W. Lu, K. Glasner, A. Bertozzi, and C.-J. Kim. A diffuse-interface model for electrowetting drops in a hele-shaw cell. *J. Fluid Mech.*, 590:411–435, 2007. doi: 10.1017/S0022112007008154.
- [278] H. Lund. A hierarchy of relaxation models for two-phase flow. *SIAM J. Appl. Math.*, 72(6):1713–1741, 2012. doi: 10.1137/12086368X.
- [279] H. Lund. *Relaxation models for two-phase flow with applications to CO<sub>2</sub> transport*. PhD thesis, Norges teknisk-naturvitenskapelige universitet, Fakultet for ingeniørvitenskap og teknologi, Institutt for energi-og prosessteknikk, 2013.
- [280] L. Lundgaard, G. Berg, S. Ingebrigtsen, and P. Atten. Electrocoalescence for oil-water separation: Fundamental aspects. In J. Sjöblom, editor, *Emulsions and emulsion stability*, pages 549–592. Taylor & Francis, 2006.
- [281] R. Maex. On the Nernst–Planck equation. *J. of Integr. Neurosci.*, 16(1):73–91, 2017. doi: 10.3233/JIN-170008.
- [282] B. B. Mandelbrot, D. E. Passoja, and A. J. Paullay. Fractal character of fracture surfaces of metals. *Nature*, 308(5961):721, 1984. doi: 10.1038/308721a0.
- [283] P. Manneville. On the transition to turbulence of wall-bounded flows in general, and plane Couette flow in particular. *Eur. J. Mech. B Fluids*, 49:345–362, 2015. doi: 10.1016/j.euromechflu.2014.03.017.
- [284] P. Manneville. Transition to turbulence in wall-bounded flows: Where do we stand? *Mechanical Engineering Reviews*, 3(2):15–00684, 2016. doi: 10.1299/mer.15-00684.
- [285] P. Mansfield and B. Issa. Fluid transport in porous rocks. I. EPI studies and a stochastic model of flow. *J. Magn. Reson., Ser A*, 122(2):137 – 148, 1996. ISSN 1064-1858. doi: 10.1006/jmra.1996.0189.
- [286] A. Mansouri, C. Scheuerman, S. Bhattacharjee, D. Y. Kwok, and L. W. Kostiuk. Transient streaming potential in a finite length microchannel. *J. Colloid Interface Sci.*, 292(2):567–580, 2005. doi: 10.1016/j.jcis.2005.05.094.
- [287] A. Mansouri, S. Bhattacharjee, and L. W. Kostiuk. Transient electrokinetic transport in a finite length microchannel: currents, capacitance, and an electrical analogy. *J. Phys. Chem. B*, 111(44):12834–12843, 2007. doi: 10.1021/jp074386c.
- [288] R. Matin. *From Pore Scale to Turbulent Flow with the Unstructured Lattice Boltzmann Method*. PhD thesis, Niels Bohr Institute, University of Copenhagen, 2016.
- [289] R. Matin, M. K. Misztal, A. Hernández-García, and J. Mathiesen. Evaluation of the finite element lattice Boltzmann method for binary fluid flows. *Comput. Math. Appl.*, 74(2):281–291, 2017. doi: 10.1016/j.camwa.2017.04.027.
- [290] R. Matin, M. K. Misztal, A. Hernández-García, and J. Mathiesen. Finite-element lattice Boltzmann simulations of contact line dynamics. *Phys. Rev. E*, 97(1):013307, 2018. doi: 10.1103/PhysRevE.97.013307.
- [291] J. M. Matter, M. Stute, S. Ó. Snæbjörnsdóttir, E. H. Oelkers, S. R. Gislason, E. S. Aradottir, B. Sigfusson, I. Gunnarsson, H. Sigurdardóttir, E. Gunnlaugsson, et al. Rapid carbon mineralization for permanent disposal of anthropogenic carbon dioxide emissions. *Science*, 352(6291):1312–1314, 2016. doi: 10.1126/science.aad8132.
- [292] M. Matyka, A. Khalili, and Z. Koza. Tortuosity-porosity relation in porous media flow. *Phys. Rev. E*, 78(2):026306, 2008. doi: 10.1103/PhysRevE.78.026306.
- [293] M. Matyka, J. Gołembiewski, and Z. Koza. Power-exponential velocity distributions in disordered porous media. *Phys. Rev. E*, 93:013110, Jan 2016. doi: 10.1103/PhysRevE.93.013110.
- [294] P. Meakin and A. M. Tartakovsky. Modeling and simulation of pore-scale multiphase fluid flow and reactive transport in fractured and porous media. *Rev. Geophys.*, 47(3):3002, 2009. doi: 10.1029/2008RG000263.

- [295] Y. Méheust and J. Schmittbuhl. Flow enhancement of a rough fracture. *Geophys. Res. Lett.*, 27(18):2989–2992, 2000. doi: 10.1029/1999GL008464.
- [296] Y. Méheust and J. Schmittbuhl. Geometrical heterogeneities and permeability anisotropy of rough fractures. *J. Geophys. Res. Solid Earth*, 106(B2):2089–2102, 2001. doi: 10.1029/2000JB900306.
- [297] Y. Méheust and J. Schmittbuhl. Scale effects related to flow in rough fractures. *Pure. Appl. Geophys.*, 160:1023–1050, 2003. doi: 10.1007/PL00012559.
- [298] C. Mei and J.-L. Auriault. The effect of weak inertia on flow through a porous medium. *J. Fluid Mech.*, 222:647–663, 1991. doi: 10.1017/S0022112091001258.
- [299] J. Melcher and G. Taylor. Electrohydrodynamics: a review of the role of interfacial shear stresses. *Annu. Rev. Fluid Mech.*, 1(1):111–146, 1969. doi: 10.1146/annurev.fl.01.010169.000551.
- [300] A. Meseguer and L. N. Trefethen. Linearized pipe flow to Reynolds number  $10^7$ . *J. Comput. Phys.*, 186(1):178–197, 2003. doi: 10.1016/S0021-9991(03)00029-9.
- [301] S. Metzger. On stable, dissipation reducing splitting schemes for two-phase flow of electrolyte solutions. *Numer. Algorithms*, pages 1–30, 2018. doi: 10.1007/s11075-018-0530-2.
- [302] S. Mhatre, V. Vivacqua, M. Ghadiri, A. Abdullah, M. Al-Marri, A. Hassanpour, B. Hewakandamby, B. Azzopardi, and B. Kermani. Electrostatic phase separation: A review. *Chem. Eng. Res. Des.*, 96:177–195, 2015. doi: 10.1016/j.cherd.2015.02.012.
- [303] S. A. Miller. Fluid-mediated influence of adjacent thrusting on the seismic cycle at parkfield. *Nature*, 382(6594):799, 1996. doi: 10.1038/382799a0.
- [304] R. A. Millikan. On the elementary electrical charge and the avogadro constant. *Phys. Rev.*, 2(2):109, 1913. doi: 10.1103/PhysRev.2.109.
- [305] S. Minjeaud. An unconditionally stable uncoupled scheme for a triphasic Cahn–Hilliard/Navier–Stokes model. *Numer. Methods Partial Differ. Equ.*, 29(2):584–618, 2013. doi: 10.1002/num.21721/full.
- [306] S. Mirjalili, S. Jain, and M. Dodd. Interface-capturing methods for two-phase flows: An overview and recent developments. Annual research briefs, Center for Turbulence Research, 2017.
- [307] M. K. Misztal, A. Hernandez-Garcia, R. Matin, D. Müter, D. Jha, H. O. Sørensen, and J. Mathiesen. Simulating anomalous dispersion in porous media using the unstructured lattice Boltzmann method. *Frontiers in Physics*, 3:50, 2015. doi: 10.3389/fphy.2015.00050.
- [308] M. K. Misztal, A. Hernandez-Garcia, R. Matin, H. O. Sørensen, and J. Mathiesen. Detailed analysis of the lattice Boltzmann method on unstructured grids. *J. Comput. Phys.*, 297:316–339, 2015. doi: 10.1016/j.jcp.2015.05.019.
- [309] G. Mitscha-Baude, A. Buttinger-Kreuzhuber, G. Tulzer, and C. Heitzinger. Adaptive and iterative methods for simulations of nanopores with the PNP–Stokes equations. *J. Comput. Phys.*, 338:452–476, 2017. doi: 10.1016/j.jcp.2017.02.072.
- [310] H. Mizutani, T. Ishido, T. Yokokura, and S. Ohnishi. Electrokinetic phenomena associated with earthquakes. *Geophys. Res. Lett.*, 3(7):365–368, 1976. doi: 10.1029/GL003i007p00365.
- [311] D. Mokbel, H. Abels, and S. Aland. A phase-field model for fluid-structure-interaction. *J. Comput. Phys.*, 372:823–840, 2018. doi: 10.1016/j.jcp.2018.06.063.
- [312] J. Monaghan. Smoothed particle hydrodynamics and its diverse applications. *Annu. Rev. Fluid Mech.*, 44:323–346, 2012. doi: 10.1146/annurev-fluid-120710-101220.
- [313] A. S. Monin and A. M. Yaglom. *Statistical fluid mechanics, volume II: mechanics of turbulence*, volume 2. Courier Corporation, 2013.
- [314] C. W. Monroe, L. I. Daikhin, M. Urbakh, and A. A. Kornyshev. Electrowetting with electrolytes. *Phys. Rev. Lett.*, 97:136102, Sep 2006. doi: 10.1103/PhysRevLett.97.136102.
- [315] C. W. Monroe, L. I. Daikhin, M. Urbakh, and A. A. Kornyshev. Principles of electrowetting with two immiscible electrolytic solutions. *J. Phys. Condens. Matter*, 18(10):2837, 2006. doi: 10.1088/0953-8984/18/10/009.

- [316] L. F. Moody. Friction factors for pipe flow. *Trans. ASME*, 66:671–684, 1944.
- [317] A. Morin. *Mathematical modelling and numerical simulation of two-phase multi-component flows of CO<sub>2</sub> mixtures in pipes*. PhD thesis, Norges teknisk-naturvitenskapelige universitet, Fakultet for ingeniørvitenskap og teknologi, Institutt for energi-og prosessteknikk, 2012.
- [318] A. Morin and T. Flåten. A two-fluid four-equation model with instantaneous thermodynamical equilibrium. *ESAIM Math. Model. Numer. Anal.*, 50(4):1167–1192, 2016. doi: 10.1051/m2an/2015074.
- [319] M. Mortensen. A spectral-Galerkin turbulent channel flow solver for large-scale simulations. *arXiv:1701.03787*, 2017.
- [320] M. Mortensen and K. Valen-Sendstad. Oasis: A high-level/high-performance open source Navier-Stokes solver. *Comput. Phys. Commun.*, 188:177–188, 2015. doi: 10.1016/j.cpc.2014.10.026.
- [321] N. A. Mortensen and H. Bruus. Universal dynamics in the onset of a Hagen–Poiseuille flow. *Phys. Rev. E*, 74(1):017301, 2006. doi: 10.1103/PhysRevE.74.017301.
- [322] M. Moura. *Burst dynamics in quasi-2D disordered systems: experiments on porous media two-phase flows*. PhD thesis, Department of Physics, University of Oslo, 2016.
- [323] V. V. Mourzenko, J.-F. Thovert, and P. M. Adler. Permeability of a single fracture; validity of the Reynolds equation. *J. Phys. II*, 5(3):465–482, 1995. doi: 10.1051/jp2:1995133.
- [324] F. Mugele. Fundamental challenges in electrowetting: from equilibrium shapes to contact angle saturation and drop dynamics. *Soft Matter*, 5(18):3377–3384, 2009. doi: 10.1039/B904493K.
- [325] F. Mugele and J.-C. Baret. Electrowetting: from basics to applications. *J. Phys. Condens. Matter*, 17(28):R705, 2005. doi: 10.1088/0953-8984/17/28/R01.
- [326] F. Mugele, M. Duits, and D. Van den Ende. Electrowetting: a versatile tool for drop manipulation, generation, and characterization. *Adv. Colloid Interface Sci.*, 161(1):115–123, 2010. doi: 10.1016/j.cis.2009.11.002.
- [327] V. Mukund and B. Hof. The critical point of the transition to turbulence in pipe flow. *J. Fluid Mech.*, 839:76–94, 2018. doi: 10.1017/jfm.2017.923.
- [328] S. T. Munkejord, M. Hammer, and S. W. Løvseth. CO<sub>2</sub> transport: Data and models – a review. *Applied Energy*, 169:499–523, 2016. doi: 10.1016/j.apenergy.2016.01.100.
- [329] R. Natalini. Recent mathematical results on hyperbolic relaxation problems. Preprint of IAC, CNR, 1998.
- [330] C. Navier. Mémoire sur les lois du mouvement des fluides. *Mémoires de l'Académie Royale des Sciences de l'Institut de France*, 6(1823):389–440, 1823.
- [331] W. Nernst. Zur kinetik der in lösung befindlichen körper. *Z. Phys. Chem.*, 2(1):613–637, 1888.
- [332] W. Nernst. Die elektromotorische wirksamkeit der jonen. *Z. Phys. Chem.*, 4(1):129–181, 1889.
- [333] A. Neuville, R. Toussaint, and J. Schmittbuhl. Hydrothermal coupling in a self-affine rough fracture. *Phys. Rev. E*, 82(3):036317, 2010. doi: 10.1103/PhysRevE.82.036317.
- [334] A. Neuville, R. Toussaint, and J. Schmittbuhl. Hydraulic transmissivity and heat exchange efficiency of open fractures: a model based on lowpass filtered apertures. *Geophys. J. Int.*, 186(3):1064–1072, 2011. doi: 10.1111/j.1365-246X.2011.05126.x.
- [335] A. Neuville, E. G. Flekkøy, and R. Toussaint. Influence of asperities on fluid and thermal flow in a fracture: A coupled lattice Boltzmann study. *J. Geophys. Res. Solid Earth*, 118(7):3394–3407, 2013. doi: 10.1002/jgrb.50256.
- [336] C. Neuzil and J. V. Tracy. Flow through fractures. *Water Resour. Res.*, 17(1):191–199, 1981. doi: 10.1029/WR017i001p00191.
- [337] C. P. Nielsen and H. Bruus. Concentration polarization, surface currents, and bulk advection in a microchannel. *Phys. Rev. E*, 90(4):043020, 2014. doi: 10.1103/PhysRevE.90.043020.

- [338] C. P. Nielsen and H. Bruus. Sharp-interface model of electrodeposition and ramified growth. *Phys. Rev. E*, 92(4):042302, 2015. doi: 10.1103/PhysRevE.92.052310.
- [339] J. Nikuradse. Strömungsgesetze in rauhen rohren. In *Forschungsheft auf dem Gebiete des Ingenieurwesens*, volume 361. VDI-Verlag, 1933.
- [340] R. H. Nochetto, A. J. Salgado, and S. W. Walker. A diffuse interface model for electrowetting with moving contact lines. *Math. Models Methods Appl. Sci.*, 24(01):67–111, 2014. doi: 10.1142/S0218202513500474.
- [341] C. Noiri. Resolving time-dependent evolution of pore-scale structure, permeability and reactivity using x-ray microtomography. *Rev. Mineral Geochim.*, 80:247–285, 2015. doi: 10.2138/rmg.2015.80.08.
- [342] C. Noiri, P. Gouze, and D. Bernard. Investigation of porosity and permeability effects from microstructure changes during limestone dissolution. *Geophys. Res. Lett.*, 31(24):L24603, 2004. doi: 10.1029/2004GL021572.
- [343] C. Noiri, D. Bernard, P. Gouze, and X. Thibault. Hydraulic properties and microgeometry evolution accompanying limestone dissolution by acidic water. *Oil & gas science and technology*, 60(1):177–192, 2005. doi: 10.2516/ogst:2005011.
- [344] A. Obliger, M. Jardat, D. Coelho, S. Bekri, and B. Rotenberg. Pore network model of electrokinetic transport through charged porous media. *Phys. Rev. E*, 89(4):043013, 2014. doi: 10.1103/PhysRevE.89.043013.
- [345] C. T. O’Konski and H. C. Thacher Jr. The distortion of aerosol droplets by an electric field. *J. Phys. Chem.*, 57(9):955–958, 1953. doi: 10.1021/j150510a024.
- [346] A. P. Oron and B. Berkowitz. Flow in rock fractures: The local cubic law assumption reexamined. *Water Resour. Res.*, 34(11):2811–2825, 1998.
- [347] S. Osher and J. A. Sethian. Fronts propagating with curvature-dependent speed: algorithms based on Hamilton–Jacobi formulations. *J. Comput. Phys.*, 79(1):12–49, 1988. doi: 10.1016/0021-9991(88)90002-2.
- [348] Pacific Institute. Water Conflict Chronology. <http://www.worldwater.org/chronology.html>, 2018.
- [349] C. C. Paige and M. A. Saunders. Solution of sparse indefinite systems of linear equations. *SIAM J. Numer. Anal.*, 12(4):617–629, 1975. doi: 10.1137/0712047.
- [350] H. Pellat. Force agissant à la surface de séparation de deux diélectriques. *C. R. Hebd. Séances Acad. Sci.*, 119:675, 1894.
- [351] H. Pellat. Mesure de la force agissant sur les diélectriques liquides non électrisés placés dans un champ élittique. *C. R. Hebd. Séances Acad. Sci.*, 119:691, 1895.
- [352] J. Pereira Nunes, M. Blunt, and B. Bijeljic. Pore-scale simulation of carbonate dissolution in micro-ct images. *J. Geophys. Res. Solid Earth*, 121:558–576, 2016. doi: 10.1002/2015JB012117.
- [353] C. S. Peskin. The immersed boundary method. *Acta Numerica*, 11:479–517, 2002. doi: 10.1017/S0962492902000077.
- [354] N. H. Pham, R. S. Voronov, N. R. Tummala, and D. V. Papavassiliou. Bulk stress distributions in the pore space of sphere-packed beds under darcy flow conditions. *Phys. Rev. E*, 89(3):033016, 2014. doi: 10.1103/PhysRevE.89.033016.
- [355] M. Planck. Ueber die erregung von electricität und wärme in electrolyten. *Ann. Phys.*, 275(2):161–186, 1890. doi: 10.1002/andp.18902750202.
- [356] M. Planck. Ueber die potentialdifferenz zwischen zwei verdünnten lösungen binärer electrolyte. *Ann. Phys.*, 276(8):561–576, 1890. doi: 10.1002/andp.18902760802.
- [357] J. Plateau. Experimental and theoretical researches into the figures of equilibrium of a liquid mass without weight. *Philos. Mag.*, 38(257):445–455, 1869. doi: 10.1080/14786445708642346.
- [358] F. Plouraboué, P. Kurowski, J.-P. Hulin, S. Roux, and J. Schmittbuhl. Aperture of rough cracks. *Phys. Rev. E*, 51(3):1675, 1995. doi: 10.1103/PhysRevE.51.1675.

- [359] O. Plümper, A. Botan, C. Los, Y. Liu, A. Malthe-Sørenssen, and B. Jamtveit. Fluid-driven metamorphism of the continental crust governed by nanoscale fluid flow. *Nat. Geosci.*, 10(9):685, 2017. doi: 10.1038/ngeo3009.
- [360] J. L. M. Poiseuille. Recherches expérimentales sur le mouvement des liquides dans les tubes de très-petits diamètre. *C. R. Acad. Sci.*, 12:112–15, 1841.
- [361] M. Pollack, A. Shenderov, and R. Fair. Electrowetting-based actuation of droplets for integrated microfluidics. *Lab Chip*, 2(2):96–101, 2002. doi: 10.1039/b110474h.
- [362] Y. Pomeau. Front motion, metastability and subcritical bifurcations in hydrodynamics. *Physica D*, 23 (1-3):3–11, 1986. doi: 10.1016/0167-2789(86)90104-1.
- [363] Y. Pomeau. The long and winding road. *Nat. Phys.*, 12(3):198, 2016. doi: 10.1038/nphys3684.
- [364] L. Ponson, H. Auradou, M. Pessel, V. Lazarus, and J.-P. Hulin. Failure mechanisms and surface roughness statistics of fractured Fontainebleau sandstone. *Phys. Rev. E*, 76(3):036108, 2007. doi: 10.1103/PhysRevE.76.036108.
- [365] S. Popinet. Numerical models of surface tension. *Annu. Rev. Fluid Mech.*, 50(1):49–75, 2018. doi: 10.1146/annurev-fluid-122316-045034.
- [366] S. R. Pride and F. Morgan. Electrokinetic dissipation induced by seismic waves. *Geophysics*, 56(7): 914–925, 1991. doi: 10.1190/1.1443125.
- [367] R. F. Probstein. *Physicochemical hydrodynamics: an introduction*. John Wiley & Sons, 2005.
- [368] A. Prosperetti and G. Tryggvason. *Computational methods for multiphase flow*. Cambridge University Press, 2009.
- [369] J. Qian, H. Zhan, W. Zhao, and F. Sun. Experimental study of turbulent unconfined groundwater flow in a single fracture. *J. Hydrol.*, 311(1-4):134–142, 2005. doi: 10.1016/j.jhydrol.2005.01.013.
- [370] J. Qian, H. Zhan, S. Luo, and W. Zhao. Experimental evidence of scale-dependent hydraulic conductivity for fully developed turbulent flow in a single fracture. *J. Hydrol.*, 339(3-4):206–215, 2007. doi: 10.1016/j.jhydrol.2007.03.015.
- [371] T. Qian, X.-P. Wang, and P. Sheng. Molecular scale contact line hydrodynamics of immiscible flows. *Phys. Rev. E*, 68(1):016306, 2003. doi: 10.1103/PhysRevE.68.016306.
- [372] T. Qian, X.-P. Wang, and P. Sheng. Power-law slip profile of the moving contact line in two-phase immiscible flows. *Phys. Rev. Lett.*, 93(9):094501, 2004. doi: 10.1103/PhysRevLett.93.094501.
- [373] T. Qian, X.-P. Wang, and P. Sheng. A variational approach to moving contact line hydrodynamics. *J. Fluid Mech.*, 564:333–360, 2006. doi: 10.1017/S0022112006001935.
- [374] D. Quéré. Wetting and roughness. *Annu. Rev. Mater. Res.*, 38:71–99, 2008. doi: 10.1146/annurev.matsci.38.060407.132434.
- [375] G. Quincke. Ueber eine neue art elektrischer ströme. *Ann. Phys.*, 183(5):1–47, 1859. doi: 10.1002/andp.18591830502.
- [376] L. Rayleigh. On the theory of surface forces. II. Compressible fluids. *Philos. Mag.*, 33(201):209–220, 1892. doi: 10.1080/14786449208621456.
- [377] W. Ren and W. E. Boundary conditions for the moving contact line problem. *Phys. Fluids*, 19(2): 022101, 2007. doi: 10.1063/1.2646754.
- [378] F. Reuss. Charge-induced flow. *Proceedings of the Imperial Society of Naturalists of Moscow*, 1809, 3: 327–344, 1809.
- [379] A. Revil, H. Schwaeger, L. Cathles, and P. Manhardt. Streaming potential in porous media: 2. theory and application to geothermal systems. *J. Geophys. Res. Solid Earth*, 104(B9):20033–20048, 1999. doi: 10.1029/1999JB900090.
- [380] O. Reynolds. An experimental investigation of the circumstances which determine whether the motion of water shall be direct or sinuous, and of the law of resistance in parallel channels. *Philos. Trans. R. Soc.*, 174:935–982, 1883. doi: 10.1098/rstl.1883.0029 2053-9223.

- [381] O. Reynolds. On the theory of lubrication and its application to Mr. Beauchamp Tower's experiments, including an experimental determination of the viscosity of olive oil. *Philos. Trans. R. Soc.*, 177: 157–234, 1886. doi: 10.1098/rstl.1886.0005.
- [382] A. RezaeiDoust, T. Puntervold, S. Strand, and T. Austad. Smart water as wettability modifier in carbonate and sandstone: A discussion of similarities/differences in the chemical mechanisms. *Energy Fuels*, 23(9):4479–4485, 2009. doi: 10.1021/ef900185q.
- [383] C. L. Rice and R. Whitehead. Electrokinetic flow in a narrow cylindrical capillary. *J. Phys. Chem.*, 69(11):4017–4024, 1965. doi: 10.1021/j100895a062.
- [384] J. R. Rice and M. P. Cleary. Some basic stress diffusion solutions for fluid-saturated elastic porous media with compressible constituents. *Rev. Geophys.*, 14(2):227–241, 1976. doi: 10.1029/RG014i002p00227.
- [385] S. Rojas and J. Koplik. Nonlinear flow in porous media. *Phys. Rev. E*, 58(4):4776, 1998. doi: 10.1103/PhysRevE.58.4776.
- [386] S. Roux, J. Schmittbuhl, J.-P. Villette, and A. Hansen. Some physical properties of self-affine rough surfaces. *Europhys. Lett.*, 23(4):277, 1993. doi: 10.1209/0295-5075/23/4/007.
- [387] Y. Saad. *Iterative methods for sparse linear systems*, volume 82. SIAM, 2003.
- [388] Y. Saad and M. H. Schultz. Gmres: A generalized minimal residual algorithm for solving nonsymmetric linear systems. *SIAM J. Sci. and Stat. Comput.*, 7(3):856–869, 1986. doi: 10.1137/0907058.
- [389] E. H. Saenger, F. Enzmann, Y. Keehm, and H. Steeb. Digital rock physics: Effect of fluid viscosity on effective elastic properties. *Journal of Applied Geophysics*, 74(4):236–241, 2011. doi: 10.1016/j.jappgeo.2011.06.001.
- [390] M. Sahimi. Flow phenomena in rocks: from continuum models to fractals, percolation, cellular automata, and simulated annealing. *Rev. Mod. Phys.*, 65(4):1393, 1993. doi: 10.1103/RevModPhys.65.1393.
- [391] M. Sahimi. *Applications of percolation theory*. CRC Press, 2014.
- [392] H. Salwen, F. W. Cotton, and C. E. Grosch. Linear stability of Poiseuille flow in a circular pipe. *J. Fluid Mech.*, 98(2):273–284, 1980. doi: 10.1017/S0022112080000146.
- [393] M. Sano and K. Tamai. A universal transition to turbulence in channel flow. *Nat. Phys.*, 12:249–254, 2016. doi: 10.1038/nphys3659.
- [394] R. Saurel and R. Abgrall. A multiphase Godunov method for compressible multifluid and multiphase flows. *J. Comput. Phys.*, 150(2):425–467, 1999. doi: 10.1006/jcph.1999.6187.
- [395] R. Saurel and C. Pantano. Diffuse-interface capturing methods for compressible two-phase flows. *Annu. Rev. Fluid Mech.*, 50(1), 2018. doi: 10.1146/annurev-fluid-122316-050109.
- [396] D. A. Saville. Electrohydrodynamics: the Taylor–Melcher leaky dielectric model. *Annu. Rev. Fluid Mech.*, 29(1):27–64, 1997. doi: 10.1146/annurev.fluid.29.1.27.
- [397] R. Scardovelli and S. Zaleski. Direct numerical simulation of free-surface and interfacial flow. *Annu. Rev. Fluid Mech.*, 31(1):567–603, 1999. doi: 10.1146/annurev.fluid.31.1.567.
- [398] J. Schmittbuhl, F. Schmitt, and C. Scholz. Scaling invariance of crack surfaces. *J. Geophys. Res. Solid Earth*, 100(B4):5953–5973, 1995. doi: 10.1029/94JB02885.
- [399] O. Schnitzer and E. Yariv. The Taylor–Melcher leaky dielectric model as a macroscale electrokinetic description. *J. Fluid Mech.*, 773:1–33, 2015. doi: 10.1017/jfm.2015.242.
- [400] R. B. Schoch, J. Han, and P. Renaud. Transport phenomena in nanofluidics. *Rev. Mod. Phys.*, 80(3):839, 2008. doi: 10.1103/RevModPhys.80.839.
- [401] J. A. Sethian and P. Smereka. Level set methods for fluid interfaces. *Annu. Rev. Fluid Mech.*, 35(1): 341–372, 2003. doi: 10.1146/annurev.fluid.35.101101.161105.
- [402] S. Shapin. The experimental philosophy and its institutions. In *The Scientific Revolution*, chapter 3, pages 72–100. Wiley-Blackwell, 2008.

- [403] J. Shen and X. Yang. A phase-field model and its numerical approximation for two-phase incompressible flows with different densities and viscosities. *SIAM J. Sci. Comput.*, 32(3):1159–1179, 2010. doi: 10.1137/09075860X.
- [404] J. Shen and X. Yang. Decoupled, energy stable schemes for phase-field models of two-phase incompressible flows. *SIAM J. Numer. Anal.*, 53(1):279–296, 2015. doi: 10.1137/140971154.
- [405] J. R. Shewchuk. Triangle: Engineering a 2D quality mesh generator and delaunay triangulator. In M. C. Lin and D. Manocha, editors, *Applied Computational Geometry: Towards Geometric Engineering*, volume 1148 of *Lecture Notes in Computer Science*, pages 203–222. Springer-Verlag, 1996.
- [406] H.-Y. Shih, T.-L. Hsieh, and N. Goldenfeld. Ecological collapse and the emergence of travelling waves at the onset of shear turbulence. *Nat. Phys.*, 12:245–248, 2015. doi: 10.1038/nphys3548.
- [407] I. A. Shiklomanov. Appraisal and assessment of world water resources. *Water International*, 25:11–32, 2000. doi: 10.1080/02508060008686794.
- [408] H. Si. Tetgen, a delaunay-based quality tetrahedral mesh generator. *ACM Trans. Math. Softw.*, 41(2): 11:1–11:36, 2015. ISSN 0098-3500. doi: 10.1145/2629697.
- [409] R. Sibson. Implications of fault-valve behaviour for rupture nucleation and recurrence. *Tectonophysics*, 211(1-4):283–293, 1992. doi: 10.1016/0040-1951(92)90065-E.
- [410] M. Siena, M. Riva, J. Hyman, C. L. Winter, and A. Guadagnini. Relationship between pore size and velocity probability distributions in stochastically generated porous media. *Phys. Rev. E*, 89(1):013018, 2014. doi: 10.1103/PhysRevE.89.013018.
- [411] A. Siria, M.-L. Bocquet, and L. Bocquet. New avenues for the large-scale harvesting of blue energy. *Nat. Rev. Chem.*, 1(1):0091, 2017. doi: 10.1038/s41570-017-0091.
- [412] E. Skjetne, A. Hansen, and J. Gudmundsson. High-velocity flow in a rough fracture. *J. Fluid Mech.*, 383:1–28, 1999. doi: 10.1017/S0022112098002444.
- [413] M. v. Smoluchowski. Contribution to the theory of electro-osmosis and related phenomena. *Bull. Int. Acad. Sci. Cracovie*, 3:184–199, 1903.
- [414] M. v. Smoluchowski. Zur theorie der elektrischen kataphorese und der oberflächenleitung. *Phyz. Z.*, 6:529–531, 1905.
- [415] J. H. Snoeijer and B. Andreotti. Moving contact lines: scales, regimes, and dynamical transitions. *Annu. Rev. Fluid Mech.*, 45:269–292, 2013. doi: 10.1146/annurev-fluid-011212-140734.
- [416] A. Solbrå, A. W. Bergersen, J. van den Brink, A. Malthe-Sørenssen, G. T. Einevoll, and G. Halnes. A Kirchhoff-Nernst-Planck framework for modeling large scale extracellular electrodiffusion surrounding morphologically detailed neurons. *bioRxiv*, page 261107, 2018. doi: 10.1101/261107.
- [417] R. Span and W. Wagner. A new equation of state for carbon dioxide covering the fluid region from the triple-point temperature to 1100 k at pressures up to 800 mpa. *J. Phys. Chem. Ref. Data*, 25(6): 1509–1596, 1996. doi: 10.1063/1.555991.
- [418] T. M. Squires and S. R. Quake. Microfluidics: Fluid physics at the nanoliter scale. *Rev. Mod. Phys.*, 77 (3):977, 2005. doi: 10.1103/RevModPhys.77.977.
- [419] V. Srinivasan, V. K. Pamula, and R. B. Fair. An integrated digital microfluidic lab-on-a-chip for clinical diagnostics on human physiological fluids. *Lab Chip*, 4(4):310–315, 2004. doi: 10.1039/b403341h.
- [420] D. Stauffer and A. Aharony. *Introduction to percolation theory*. CRC Press, 1994.
- [421] O. Stern. Zur theorie der elektrolytischen doppelschicht. *Berichte der Bunsengesellschaft für physikalische Chemie*, 30(21-22):508–516, 1924. doi: 10.1002/bbpc.192400182.
- [422] W. H. Stockmayer. Theory of molecular size distribution and gel formation in branched-chain polymers. *J. Chem. Phys.*, 11(2):45–55, 1943. doi: 10.1063/1.1723803.
- [423] G. G. Stokes. On the theories of the internal friction of fluids in motion, and of the equilibrium and motion of elastic solids. *Trans. Cambridge Philos. Soc.*, 8:287–319, 1845.

- [424] A. Strickler. *Beiträge zur Frage der Geschwindigkeitsformel und der Rauhigkeitszahlen für Ströme, Kanäle und geschlossene Leitungen*. Mitteilungen des Amtes für Wasserwirtschaft, 1923.
- [425] S. Succi. *The Lattice Boltzmann Equation: For Complex States of Flowing Matter*. Oxford University Press, 2018.
- [426] Y. Sui, H. Ding, and P. D. M. Spelt. Numerical simulations of flows with moving contact lines. *Annu. Rev. Fluid Mech.*, 46:97–119, 2014. doi: 10.1146/annurev-fluid-010313-141338.
- [427] M. Sussman and E. G. Puckett. A coupled level set and volume-of-fluid method for computing 3D and axisymmetric incompressible two-phase flows. *J. Comput. Phys.*, 162(2):301–337, 2000. doi: 10.1006/jcph.2000.6537.
- [428] M. Sussman, P. Smereka, and S. Osher. A level set approach for computing solutions to incompressible two-phase flow. *J. Comput. Phys.*, 114(1):146–159, 1994. doi: 10.1006/jcph.1994.1155.
- [429] S. P. Sutera and R. Skalak. The history of Poiseuille’s law. *Annu. Rev. Fluid Mech.*, 25(1):1–20, 1993. doi: 10.1146/annurev.fl.25.010193.000245.
- [430] H. L. Swinney and J. P. Gollub. *Hydrodynamic instabilities and the transition to turbulence*. Oxford University Press, 1981.
- [431] K. A. Takeuchi, M. Kuroda, H. Chaté, and M. Sano. Directed percolation criticality in turbulent liquid crystals. *Phys. Rev. Lett.*, 99(23):234503, 2007. doi: 10.1103/PhysRevLett.99.234503.
- [432] L. Talon, H. Auradou, and A. Hansen. Permeability estimates of self-affine fracture faults based on generalization of the bottleneck concept. *Water Resour. Res.*, 46(7):W07601, 2010. doi: 10.1029/2009WR008404.
- [433] L. Talon, H. Auradou, and A. Hansen. Permeability of self-affine aperture fields. *Phys. Rev. E*, 82(4):046108, 2010. doi: 10.1103/PhysRevE.82.046108.
- [434] P. Talwani and S. Acree. Pore pressure diffusion and the mechanism of reservoir-induced seismicity. *Pure. Appl. Geophys.*, 122:947–965, 1984. doi: 10.1007/BF00876395.
- [435] L. Tanner. The spreading of silicone oil drops on horizontal surfaces. *Journal of Physics D: Applied Physics*, 12(9):1473, 1979. doi: 10.1088/0022-3727/12/9/009.
- [436] G. Taylor. Studies in electrohydrodynamics. I. The circulation produced in a drop by electrical field. *Proc. Royal Soc. A*, 291(1425):159–166, 1966. doi: 10.1098/rspa.1966.0086.
- [437] K. E. Teigen and S. T. Munkejord. Sharp-interface simulations of drop deformation in electric fields. *IEEE T. Dielect. El. In.*, 16(2), 2009. doi: 10.1109/TDEI.2009.4815181.
- [438] K. E. Teigen and S. T. Munkejord. Influence of surfactant on drop deformation in an electric field. *Phys. Fluids*, 22(11):112104, 2010. doi: 10.1063/1.3504271.
- [439] K. E. Teigen, P. Song, J. Lowengrub, and A. Voigt. A diffuse-interface method for two-phase flows with soluble surfactants. *J. Comput. Phys.*, 230(2):375 – 393, 2011. ISSN 0021-9991. doi: 10.1016/j.jcp.2010.09.020.
- [440] H. Tennekes, J. L. Lumley, J. Lumley, et al. *A first course in turbulence*. MIT press, 1972.
- [441] The CGAL Project. *CGAL User and Reference Manual*. CGAL Editorial Board, 4.8 edition, 2016. URL <http://doc.cgal.org/4.8/Manual/packages.html>.
- [442] R. Thompson. The seismic electric effect. *Geophysics*, 1(3):327–335, 1936. doi: 10.1190/1.1437119.
- [443] G. Tomar, D. Gerlach, G. Biswas, N. Alleborn, A. Sharma, F. Durst, S. Welch, and A. Delgado. Two-phase electrohydrodynamic simulations using a volume-of-fluid approach. *J. Comput. Phys.*, 227(2):1267 – 1285, 2007. doi: 10.1016/j.jcp.2007.09.003.
- [444] L. Torvalds and J. Hamano. Git: Fast version control system. <http://git-scm.com>, 2005.
- [445] S. Torza, R. Cox, and S. Mason. Electrohydrodynamic deformation and bursts of liquid drops. *Phil. Trans. R. Soc. Lond. A*, 269(1198):295–319, 1971. doi: 10.1098/rsta.1971.0032.
- [446] D. J. Tritton. *Physical fluid dynamics*. Springer Science & Business Media, 2012.

- [447] G. Tryggvason, R. Scardovelli, and S. Zaleski. *Direct numerical simulations of gas–liquid multiphase flows*. Cambridge University Press, 2011.
- [448] V. Tzelepis, K. N. Moutsopoulos, J. N. Papaspyros, and V. A. Tsirhirtzis. Experimental investigation of flow behavior in smooth and rough artificial fractures. *J. Hydrol.*, 521:108–118, 2015. doi: 10.1016/j.jhydrol.2014.11.054.
- [449] S. O. Unverdi and G. Tryggvason. A front-tracking method for viscous, incompressible, multi-fluid flows. *J. Comput. Phys.*, 100(1):25–37, 1992. doi: 10.1016/0021-9991(92)90307-K.
- [450] M. Vallet, B. Berge, and L. Vovelle. Electrowetting of water and aqueous solutions on poly (ethylene terephthalate) insulating films. *Polymer*, 37(12):2465–2470, 1996. doi: 10.1016/0032-3861(96)85360-2.
- [451] R. Van der Sman and S. Van der Graaf. Diffuse interface model of surfactant adsorption onto flat and droplet interfaces. *Rheologica acta*, 46(1):3–11, 2006. doi: 10.1007/s00397-005-0081-z.
- [452] H. A. Van der Vorst. Bi-CGSTAB: A fast and smoothly converging variant of Bi-CG for the solution of nonsymmetric linear systems. *SIAM J. Sci. and Stat. Comput.*, 13(2):631–644, 1992. doi: 10.1137/0913035.
- [453] J. D. van der Waals. *Over de Continuiteit van den Gas-en Vloeistofoestand*. PhD thesis, University of Leiden, 1873.
- [454] J. D. van der Waals. The thermodynamic theory of capillarity under the hypothesis of a continuous variation of density. *J. Stat. Phys.*, 20(2):200–244, 1893. doi: 10.1007/BF01011514.
- [455] O. Voinov. Hydrodynamics of wetting. *Fluid Dynamics*, 11(5):714–721, 1976. doi: 10.1007/BF01012963.
- [456] A. G. Volkov, D. Deamer, D. Tanelian, and V. Markin. Electrical double layers at the oil/water interface. *Progress in surface science*, 53(1):1–134, 1996. doi: 10.1016/S0079-6816(97)82876-6.
- [457] H. von Helmholtz. Ueber einige gesetze der vertheilung elektrischer ströme in körperlichen leitern mit anwendung auf die thierisch-elektrischen versuche. *Ann. Phys.*, 165(6):211–233, 1853.
- [458] H. von Helmholtz. Studien über electrische grenzschichten. *Ann. Phys.*, 243(7):337–382, 1879.
- [459] C. von Terzaghi. *Erdbaumechanik auf bodenphysikalischer Grundlage*. Deuticke, 1925.
- [460] R. S. Voronov, S. B. VanGordon, V. I. Sikavitsas, and D. V. Papavassiliou. Distribution of flow-induced stresses in highly porous media. *Appl. Phys. Lett.*, 97(2):024101, 2010. doi: 10.1063/1.3462071.
- [461] J. O. Waldestrand and S. Evje. A multiphase model for exploring tumor cell migration driven by autologous chemotaxis. *Chem. Eng. Sci.*, 2018. doi: 10.1016/j.ces.2018.06.076.
- [462] A. D. Waller. A demonstration on man of electromotive changes accompanying the heart’s beat. *J. Physiol.*, 8(5):229–234, 1887. doi: 10.1113/jphysiol.1887.sp000257.
- [463] M. Wang, Y.-F. Chen, G.-W. Ma, J.-Q. Zhou, and C.-B. Zhou. Influence of surface roughness on nonlinear flow behaviors in 3D self-affine rough fractures: Lattice Boltzmann simulations. *Adv. Water Resour.*, 96:373–388, 2016. doi: 10.1016/j.advwatres.2016.08.006.
- [464] J. L. Weisbach. *Lehrbuch der Ingenieur-und Maschinen-Mechanik: Theoretische Mechanik*, volume 1. Druck und Verlag von Friedrich Vieweg und Sohn, 1845.
- [465] S. Whitaker. Flow in porous media i: A theoretical derivation of Darcy’s law. *Transp. Porous Media*, 1(1):3–25, 1986. doi: 10.1007/BF01036523.
- [466] S. Whitaker. The Forchheimer equation: a theoretical development. *Transp. Porous Media*, 25(1): 27–61, 1996. doi: 10.1007/BF00141261.
- [467] K. Wojtacki, L. Lewandowska, P. Gouze, and A. Lipkowski. Numerical computations of rock dissolution and geomechanical effects for CO<sub>2</sub> geological storage. *Int. J. Numer. Anal. Methods Geomech.*, 39: 482–506, 2015. doi: 10.1002/nag.2316.
- [468] R. Woltmann. *Beyträge zur hydraulischen Architektur*. Dritter Band, Johann Christian Dietrich, Göttingen, 1794.
- [469] World Energy Council. World energy resources. Technical report, World Energy Council, 2016.

- [470] I. Wygnanski and F. Champagne. On transition in a pipe. Part 1. The origin of puffs and slugs and the flow in a turbulent slug. *J. Fluid Mech.*, 59(2):281–335, 1973. doi: 10.1017/S0022112073001576.
- [471] I. Wygnanski, M. Sokolov, and D. Friedman. On transition in a pipe. Part 2. The equilibrium puff. *J. Fluid Mech.*, 69(2):283–304, 1975. doi: 10.1017/S0022112075001449.
- [472] X. Xiong, J. Tao, S. Chen, and L. Brandt. Turbulent bands in plane-Poiseuille flow at moderate Reynolds numbers. *Phys. Fluids*, 27(4):041702, 2015. doi: 10.1063/1.4917173.
- [473] Z. Xu and P. Meakin. Phase-field modeling of solute precipitation and dissolution. *J. Chem. Phys.*, 129(1):014705, 2008. doi: 10.1063/1.2948949.
- [474] Y. Yan and J. Koplik. Flow of power-law fluids in self-affine fracture channels. *Phys. Rev. E*, 77(3):036315, 2008. doi: 10.1103/PhysRevE.77.036315.
- [475] C. Yang and D. Li. A method of determining the thickness of liquid-liquid interfaces. *Colloids Surf. A*, 113(1-2):51–59, 1996. doi: 10.1016/0927-7757(96)03544-3.
- [476] Q. Yang, B. Q. Li, and Y. Ding. 3D phase field modeling of electrohydrodynamic multiphase flows. *Int. J. Multiph. Flow*, 57:1–9, 2013. doi: 10.1016/j.ijmultiphaseflow.2013.06.006.
- [477] Q. Yang, B. Q. Li, J. Shao, and Y. Ding. A phase field numerical study of 3D bubble rising in viscous fluids under an electric field. *Int. J. Heat Mass Transf.*, 78:820–829, 2014. doi: 10.1016/j.ijheatmasstransfer.2014.07.039.
- [478] T. Young. An essay on the cohesion of fluids. *Philos. Trans. R. Soc.*, 95:65–87, 1805. doi: 10.1098/rstl.1805.0005.
- [479] P. Yue, C. Zhou, and J. J. Feng. Spontaneous shrinkage of drops and mass conservation in phase-field simulations. *J. Comput. Phys.*, 223(1):1–9, 2007. doi: 10.1016/j.jcp.2006.11.020.
- [480] A. Zein, M. Hantke, and G. Warnecke. Modeling phase transition for compressible two-phase flows applied to metastable liquids. *J. Comput. Phys.*, 229(8):2964–2998, 2010. doi: 10.1016/j.jcp.2009.12.026.
- [481] J. Zhang and D. Y. Kwok. A 2D lattice Boltzmann study on electrohydrodynamic drop deformation with the leaky dielectric theory. *J. Comput. Phys.*, 206(1):150–161, 2005. doi: 10.1016/j.jcp.2004.11.032.
- [482] X. Zhang, M. A. Knackstedt, and M. Sahimi. Fluid flow across mass fractals and self-affine surfaces. *Physica A*, 233(3-4):835–847, 1996. doi: 10.1016/S0378-4371(96)00203-8.
- [483] E. K. Zholkovskij, J. H. Masliyah, and J. Czarnecki. An electrokinetic model of drop deformation in an electric field. *J. Fluid Mech.*, 472:1–27, 2002. doi: 10.1017/S0022112002001441.
- [484] R. W. Zimmerman and I.-W. Yeo. Fluid flow in rock fractures: From the Navier–Stokes equations to the cubic law. In *Dynamics of fluids in fractured rock*, pages 213–224. American Geophysical Union, 2013.
- [485] L. Zou. *Numerical modeling of fluid flow and solute transport in rock fractures*. PhD thesis, KTH Royal Institute of Technology, 2016.
- [486] L. Zou, L. Jing, and V. Cvetkovic. Roughness decomposition and nonlinear fluid flow in a single rock fracture. *Int. J. Rock Mech. Min. Sci.*, 75:102–118, 2015. doi: 10.1016/j.ijrmms.2015.01.016.
- [487] L. Zou, L. Jing, and V. Cvetkovic. Shear-enhanced nonlinear flow in rough-walled rock fractures. *Int. J. Rock Mech. Min. Sci.*, 97:33–45, 2017. doi: 10.1016/j.ijrmms.2017.06.001.
- [488] P.-E. Øren, S. Bakke, and R. Held. Direct pore-scale computation of material and transport properties for north sea reservoir rocks. *Water Resour. Res.*, 43(12):W12S04, 2007. ISSN 1944-7973. doi: 10.1029/2006WR005754.





